Investigation of the effects and impacts of selective composition modifications on the precipitation kinetics and creep resistance of the 12 wt.%Cr steel X12CrCoWVNb 11-2-2

Dissertation of
Francisca Méndez Martín

Submitted for the degree of
Doktor der technischen Wissenschaften
(Doctor of technical sciences)

Faculty of Mechanical Engineering

Graz University of Technology **Institute for Materials Science and Welding**

in collaboration with:

Institute for Electron Microscopy

Para mi Padre y Madre

Preface

This dissertation is submitted for the Doctoral degree at the Graz University of Technology under the supervision of Univ.-Prof. Dipl.-Ing. Dr.mont. Horst H. Cerjak. This work has been carried out at the Institute for Materials Science and Welding in collaboration with the Institute for Electron Microscopy. The project was started at June 2006 until October 2010, and it has been founded by Vallourec and Mannesmann Tubes.

Different courses have been attended related with the main topic of this project, to get a wide overview of the energy systems in the world on one hand, and on the other hand, to have an extensive knowledge in all used experimental techniques.

The work here set it out is original and no other than the declared sources / resources have been used for this work. I have explicitly marked all material, which has been quoted either literally or by content from the used sources.

Francisca Méndez Martín

October 2010

Acknowledgements

I would like to express my grateful to Univ.-Prof. Dipl.-Ing. Dr.mont. Horst H. Cerjak for his patience and supervision, my gratitude for his comments and his support on the outgoing of this project.

I would like to express my gratitude to Prof. Hans-Olof Andrén of Chalmers University, Sweden, for acting as assessor of this dissertation.

I would like also thanks to Ao.Univ.-Prof. Dipl.-Ing. Dr.techn. Gerald Kothleitner for introducing me in the art of electron microscopy. He showed me that, in the background of each electron microscope image, there is a strong effort, many hours of work and knowledge.

I would like also thanks to Univ.-Prof. Dipl.-Ing. Dr.techn. Ernst Kozeschnik, developer of MatCalc software. Prof. Kozeschnik introduced me in a completely unknown world for me before, simulation of precipitation kinetics in 9-12 %Cr steels.

Further thanks to Univ.-Prof. Dipl.-Ing. Dr.techn. Priv.-Doz. Christof Sommitsch for his support on the final steps of this thesis.

This work was supported by Vallourec & Mannesmann Tubes and I would like to express my gratitude to Dipl.-Ing. Hahn, who strongly supported this work with critical comments that motivated me on the progress of this thesis. As well as to Dr. Bendick from Salzgitter Mannesmann Forschung for providing me with helpful discussions and supporting this project with the material that have been investigated.

I would like particular thanks to Dr. Mihaela Albu, to Dr. Bernhard Sonderegger and to Dr. Peter Mayr, without their support, explanations and their guide through this work, this thesis would never be possible. They showed me different ways to approach a research problem and the need to be persistent to accomplish any goal. They have become not only excellent teachers also perfect work colleagues and dear friends.

I would like to express my gratitude to the laboratory group of the Institute for Materials Science and Welding and Institute for Electron Microscopy, specially Gernot Stöfan and Manuel Paller who helped and guided me on my experimental tests. I would like also thanks to Dr. Mitsche, who performed the EBSD measurements presented in this thesis.

Any project depends on the efforts of many different people, and this project is no exception. I would like to thank the Institute for Materials Science and Welding and the Institute for Electron Microscopy, all members in general for their help and support during the preparation of this thesis.

Last but not least, I thank my family for their support, and their understanding, even when they are so far away from me in distance, they have been always on my side and they were giving me the enough encouragement for the realization of this project.

Me gustaría agradecer con especial atención a mi padre y madre a los cuales les dedico esta tesis, por su especial apoyo y comprensión.

Abstract / Kurzfassung

The advanced operating conditions for steam power plants require materials with higher steam oxidation resistance and creep strength and 9 – 12 wt.%Cr tempered martensitic steels are excellent candidates. Nevertheless, a breakdown of creep strength has been observed associated with changes in the microstructure of the material. Microstructure analyses together with simulations in MatCalc software are excellent tools for the evaluation of the relationship between microstructural changes and the corresponding mechanical properties, such as creep.

The goal of this project is to determine the microstructural evolution of the creep resistant 12 %Cr steel X12CrCoWVNb 11-2-2 during creep and thermal ageing, with particular focus on the precipitation kinetics. The combination of experimental investigation methods (different techniques of electron microscopy) and precipitation modelling (thermokinetic calculations) is leading to a better understanding of the parameters governing the creep resistance. Intended results of the project are proposals for the modification of the chemical composition and/or the parameters of the heat treatment of the steel in order to increase the creep resistance.

Die anspruchsvollen Betriebsbedingungen in Dampfkraftwerken erfordern Materialien mit hoher Oxidations- und Kriechbeständigkeit. Aus diesem Grund sind martensitische 9 – 12 wt.%Cr Stähle hervorragend dafür geeignet. Die Abnahme der Kriechbeständigkeit wird mit Veränderungen in der Mikrostruktur des Materials in Verbindung gebracht. Mikrostrukturanalysen zusammen mit Simulationen der Mikrostrukturentwicklung mit der Software MatCalc sind hervorragende Methoden für die Evaluierung der Beziehung zwischen mikrostrukturellen Veränderungen und den entsprechenden mechanischen Eigenschaften, wie zum Beispiel das Kriechverhalten.

Das Ziel dieser Arbeit ist die Bestimmung der mikrostrukturellen Entwicklung des warmfestem 12 %Cr Stahl X12CrCoWVNb 11-2-2 während dem Kriechen und bei alleiniger thermischer Belastung mit besonderem Fokus auf die Ausscheidungskinetik. Die Kombination von experimentellen Untersuchungsmethoden (verschiedene Techniken der Elektronenmikroskopie) und Ausscheidungsmodellierung (thermokinetische Berechnungen) führt zu einem besseren Verständnis der Einflussparameter, die die Kriechfestigkeit bestimmen. Die Ergebnisse dieser Arbeit sollen dabei die Grundlage für die Modifizierung der chemischen Zusammensetzung und/oder der Wärmebehandlungsparameter dieser Stahlsorten darstellen, mit dem Ziel die Kriechfestigkeit zu erhöhen.

Content

1. Introduction

In a fossil fuel power plant, the chemical energy stored in fossil fuels and oxygen of the air is converted into electrical energy for continuous use and distribution [1]. Due to a linear relationship between efficiency in the power plant and environmentally damaging gases emissions, reductions of these pollutants are possible with increasing the efficiency in the power plant by: improving its design, optimise the thermal cycles or by increasing the steam parameters [2]. However, to achieve these higher efficiencies, boiler and turbines as well as their components have to work at high pressures and temperatures (221 bar, 600℃ or higher) [3] on the new generation of steam power plants at supercritical (SC) and ultrasupercritical (USC) conditions.

These high service conditions need materials with high creep strength and oxidation resistance. Low alloyed steels, austenitic steels, nickel based superalloys together with 9-12 wt.%Cr tempered martensitic steels are used nowadays in the development of boilers and steam turbines. Austenitic steels have higher creep and oxidation resistance, as well as nickel bases superalloys, together with a higher price compared to tempered martensitic 9-12 wt.%Cr steels. Because of the higher costs of austenitic and nickel base superalloys, new world-wide projects focus on the expansion of the application of tempered martensitic 9-12 wt.%Cr steels. Figure 1.1 represents how European projects like COST attempt to expand the application range of these Cr-steels.

Tempered martensitic 9-12 wt.%Cr steels are favoured for thick walled components in USC power plants. They have excellent thermo physical properties such as: low coefficient of thermal expansion, high thermal conductivity, as well as, a low-price [2] [4] [5] [6] [7] [8] [9]. Nevertheless, these steels show a drop in the creep resistance after about 10^4 h of service. One reason for this deterioration is microstructural changes: precipitates coarsen and dissolve, martensite laths broaden etc [10].

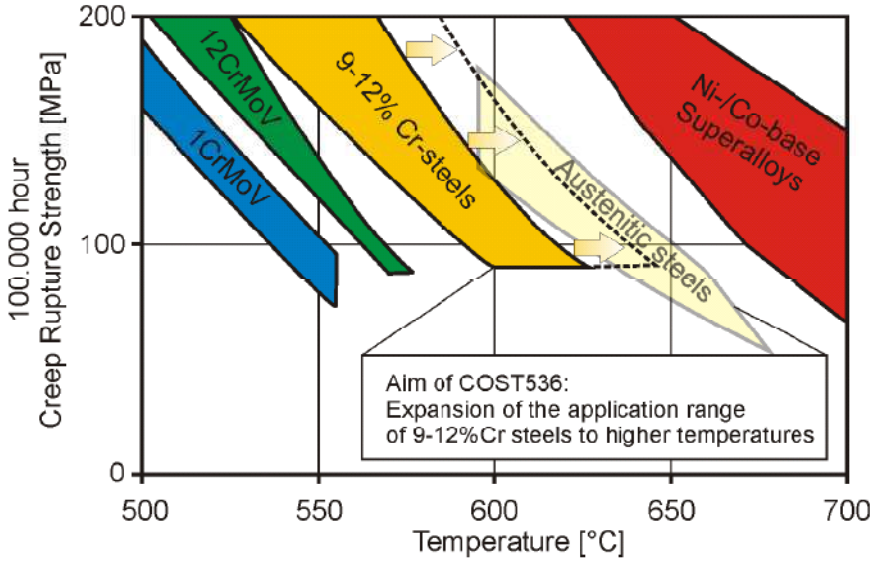

Figure 1.1. Temperature range application of the different used materials in thermal power plants. Dashed line represents the expansion of the range for application of Cr steels, which is under development in world-wide projects [9].

The motive of this work is the study of the microstructure evolution in the high chromium (12 wt.%Cr) tempered martensitic steel grade X12CrCoWVNb 11-2-2, developed by Vallourec & Mannesmann tubes (V&M) with better oxidation resistance properties, compared with 9 wt.%Cr containing steel grades i.e. P91, P92. Full microstructure characterization evolution, from as-received to different creep and thermal aged conditions, should help to understand the mechanisms responsible for the decrease in the creep strength of these types of steel grades. Modelling and simulations of its microstructure should be performed parallel in order to improve existing databases. This will support the possibility of prediction of the behaviour of new or modified chemical compositions and heat treatments without the necessity of running long creep tests, saving costs and time.

2. Objectives

9 wt.%Cr tempered martensitic steels were developed due to their lower thermal expansion and higher thermal conductivity as well as lower costs compared with austenitic steels. However, oxidation resistance, fabricability as well as weldability are parameters that have to be considered for the development of new tempered martensitic steel grades. For this reason to improve the oxidation resistance, chromium content was increased up to 12 wt.%. Nevertheless, the consequences of the chromium increase have been detrimental for the creep resistance.

Experimental investigations using the most advanced microscopy techniques are used for a full microstructure characterization of the investigated 12 wt.%Cr steel tempered martensitic X12CrCoWVNb 11-2-2, in order to evaluate the relation between microstructural changes and creep strength. Transmission electron microscopy (TEM), scanning electron microscopy (SEM) together with electron energy loss spectrometry (EELS), energy filtered transmission electron microscopy (EFTEM), energy dispersive X-ray analysis (EDX), convergent beam electron diffraction (CBED), selected area electron diffraction (SAED) and electron backscatter diffraction (EBSD) techniques are used for the characterization of the microstructure evolution of the X12CrCoWVNb 11-2-2 material at different creep test conditions as well as subgrain size, martensite lath size and prior austenite grain size.

Moreover, possible chemical composition adjustments that have been performed in these martensitic steels in the last decades of the century are based on the trial error method. This method is used currently for possible adjustments of the chemical composition as well as annealing temperatures, but long term creep tests for the study of the creep strength of the materials are always needed. Because of that effect, use modelling and simulation of microstructural changes is an enormous helpful tool for the prediction of new chemical compositions as well as new heat treatments to save time and costs. MatCalc software helps in the development of these steel grades, although, for this task, accurate databases are needed. With the output of the experimental results in this project, adjustments of the thermodynamic parameters in databases can be done, and reliable databases can be developed.

The final goal of this project is to clarify the behaviour of the 12 wt.%Cr tempered martensitic steel X12CrCoWVNb 11-2-2 provided by Salzgitter Mannesmann Forschung (SZMF) and Vallourec & Mannesmann Tubes, in order to develop optimised high chromium steels with creep strength level of P91 and P92 steels and increased oxidation resistance. The investigation of the base material as well as creep tested at different temperatures and stresses allow the evaluation of the microstructure and creep properties during time. Furthermore, simulations of the thermal history of this steel grade with new chemical composition and annealing temperatures for the improvement of the creep strength should be achieved.

3. Literature Review

PART I Power Plants and 9-12 wt.%Cr Tempered Martensitic Steels

3.1. 9-12 wt.%Cr tempered martensitic steels development for components in steam power plants

For the increase of the efficiency in steam power plants, steam temperatures and pressures should be increased. In order to achieve these conditions new heat resistant steels are needed, which have to satisfy conditions such as: oxidation resistance, high ductility under creep conditions, fabricability, high thermal efficiency, reduced costs and life expectancy of at least 200000 h [11]. Nevertheless, creep strength is one of the most significant factors, limiting the service life of these new heat resistance steels.

Strong efforts have been paid in the development of tempered martensitic steels for components in steam power plants, due to their low coefficient of thermal expansion and high thermal conductivity compared with austenitic steels [2] [4] [5] [6] [7] [8] [9]. For the development of these new materials for thick components in power plants, several international collaborations were started in the last century in USA (EPRI), Japan (EPDC) and Europe (COST). In the progress of these projects, several improvements in creep resistance were arranged, but still none of the developed steel grades meet the needs for its use at 650℃ (10^5 h creep rupture strength at 650℃, oxidation resistance, weldability and creep rupture strength of welded joints, thermal fatigue impact properties and hot workability) [12].

A number of steel grades have been developed over the last decades: steel X22CrMoV 12 1 (12 wt.%Cr) based its creep strength on solution hardening and precipitation of $M_{23}C_6$ carbides and its application in power plants was successful up to 566℃. P91 steel (9 wt.%Cr) developed in USA (used up to 600℃), increased the creep resistance because the precipitation of fine distributed MX precipitates (VN and Nb(CN)). Nevertheless, due to the low-chromium content, around 9 wt.%, the use of different coatings systems to improve the corrosion resistance are needed. Another improvement in creep strength was shown by the P92 steel (9 wt.%Cr). The addition of about 0.003 wt.%B and an increased W content of about 1.8 wt.% gave thermally stabile $M_{23}(C,B)_6$ precipitates and a higher amount of the Laves phase which enable an increase in service temperatures up to about 630℃.

Because of the different results obtained at the different steels, the alloying principles (MX precipitation, $M_{23}(C,B)_6$, increased W content) were used (or are used) for the development of new 12 wt.%Cr tempered martensitic steels, up to 620℃-650℃, to increase creep and oxidation resistance. However, a drop in the creep resistance of these steels can still be observed due to microstructure instabilities [12]. Figure 3.1 represents the changes of the microstructure in tempered martensitic steels due to the changes in the chemical composition of the different developed steels in the different international projects mentioned above.

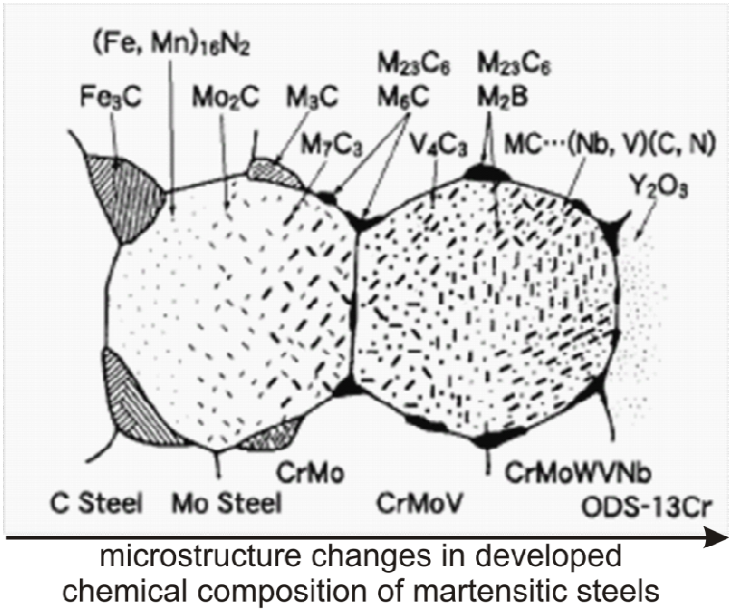

*Figure 3.1. Representation of the different microstructures changes due to the developed chemical compostion of martensitic steels for their use at high temperature and pressures in steam power plants [*13*].*

3.2. Microstructure of 9-12 wt.%Cr tempered martensitic steels

For service in power plant stations, low thermal expansion, low elastic modulus (which implies low thermal stress) and high thermal conductivity are needed. When using materials with these characteristics it is possible to avoid problems such as corrosion cracking caused by thermal stress or the need to use expansion loops or joints due to dimensional changes (expansions/contractions) [12]. In addition, these three properties are directly related with the bonding of atoms. The steel has metallic bonding, but for tempered martensitic steels, the matrix has a BCC structure and for austenitic steels a FCC structure. In other words, the FCC structure is more densely packed and the distance between atoms is shorter than for BCC structure. This means stronger attracting forces between atoms which has an effect in:

- Higher Young's modulus for austenitics steels due to this shorter distance between atoms, which implies higher thermal stresses for austenitics steels compared with tempered martensitic steels.
- The number density of mobile electrons is related with the thermal conductivity. Because the smaller inter-atomic distance in austenitic steels, the attraction between the nuclei and the electrons is stronger and the mobility of mobile electrons is much lower than for tempered BCC martensitic steels. Therefore, the thermal conductivity of austenitic steels is lower than that of tempered martensitic steels [12].
- The coefficient of thermal expansion for austenitic steels is higher than for tempered martensitic steels. The stronger the interaction between atoms, the higher is the bond energy. For tempered martensitic and austenitic steels, this bonding is the same (bonding between iron atoms) but the length is different. The FCC structure is denser than the BCC structure; hence, there is a higher thermal expansion coefficient for austenitic steels [12].

Nevertheless, the microstructure of 9-12 wt.%Cr tempered martensitic steels and alloys in general are also dependent on the chemical composition, heat treatment and manufacturing process. After casting, the material is heated up until austenitization temperature (normally around ~1100℃) where the matrix is fully austenitic. Following, the material is cooled (in many cases, air cooling), and a martensitic transformation occurs. The martensitic structure has a high density of dislocations, due to the

transformation from austenite to martensite is a non-diffusional process and the carbon remains trapped in the ferritic-martensitic structure, increasing the stress in the structure and the number of dislocations [14]. To improve the ductility of the martensitic structure, a tempering is performed to relieve stress, and a tempered martensitic structure is obtained.

As a result of the heat treatment as well as of the service conditions different precipitates populations nucleate, grow and coarse. Figure 3.2 shows the main changes of the precipitates populations in 9-12 %Cr tempered martensitic steels after heat treatment and thermal aging. In the as-received (after heat treatment) condition, the material shows finely distributed precipitates that after temperature exposure for long time evolve to coarse phases. This causes a detrimental effect for the creep strength.

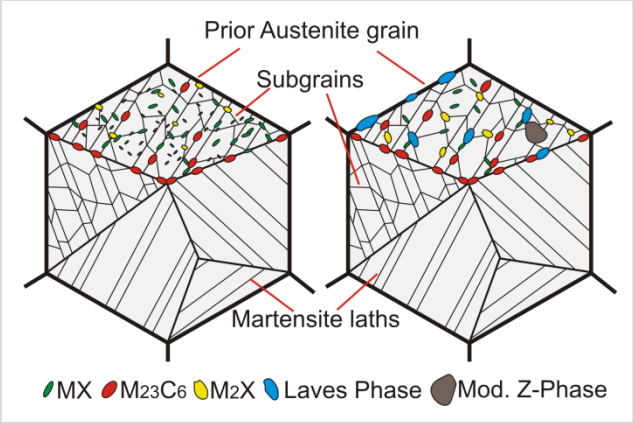

Figure 3.2. Evolution of the different precipitates populations in 9-12 wt.%Cr tempered martensitic steels: as-received condition (left), thermally aged condition (right) [15].

The most common precipitates types in 9-12 wt.%Cr tempered martensitic steels are:

- M_7C_3 {$(Fe,Cr,Mo)_7C_3$}: It is an orthorhombic chromium rich phase with a high-coarsening rate, which is replaced by the $M_{23}C_6$ during the heat treatment.
- $M_{23}C_6$ {$(Cr,Fe,Mo,W)_{23}(C,B)_6$}: It is a fcc chromium rich phase as well, which precipitates mainly at the prior austenite grain boundaries, subgrain boundaries and martensite lath boundaries. As have been investigated in NIMS by Dr. Abe [16] the addition of boron stabilizes the coarsening of the $M_{23}C_6$ particles by an enrichment of boron.
- BN: It has hexagonal crystal structure. Boron is added, in these steels, because of the decrease in the coarsening rate of the $M_{23}C_6$ phase and because stabilize the prior austenite grain boundaries. However, inappropriate additions of boron and nitrogen can promote the precipitation of boron nitrides, which are hindering this effect [17].
- MX: NbC {(Nb,V)(C,N)} and VN {(V,Nb)(N,C)}: These precipitates are finely distributed in the material and are hindering the movement of the dislocations. They have a low-coarsening rate at elevated temperatures, which produce an increase of the creep resistance. NbC, with a fcc crystal structure, precipitate already at the austenitization regime and hinder the austenite grain coarsening. VN, also with fcc crystal structure, precipitates at the tempering regime. However, this phase can transform [18] to mod. Z-phase, decreasing the precipitation strengthening which is not compensated from the new phase.
- M_2N {$(Cr,V,Fe)_2N$}: With a hexagonal crystal structure precipitates mainly at the grain boundaries as well as in the matrix and have a higher coarsening rate than the MX phase.
- Mod. Z-phase {Cr(Nb,V)N}: This phase is a complex nitride with a tetragonal crystal structure. Its precipitation is responsible of the dissolution of the fine dispersed MX particle, which is one of the possible reasons for the drop in creep strength in 9-12 wt.%Cr tempered martensitic steels [18].

- Laves phase {$(Fe,Cr,Si)_2(MoW)$}: Mo and W rich phase, is an intermetallic phase with a hexagonal crystal structure, which precipitates after a short time of service.

Because of the need to perform a heat treatment and to obtain a tempered martensitic structure, austenite or ferrite stabilizing elements are needed. Each alloying element will have a specific effect in the properties or behaviour of the material. Cr, Mo, W, Si and V are ferrite stabilizing elements. Chromium, in 9-12 wt.%Cr tempered martensitic steels, improves the corrosion and oxidation resistance. The Molybdenum and Tungsten are increasing the strength of the matrix by solid solution strengthening. However, after short time of service, an intermetallic phase (Laves phase) rich in these two elements precipitate. The Silicon is added to remove the oxygen during poring and solidification and also to increase the oxidation resistance. This element increases the precipitation hardening effect due to changes in the ferrite lattice parameter. The vanadium precipitates as MX phase, which hinders the movement of dislocations during service, due to it is finely distributed in the matrix.

On the other hand, austenite stabilizing elements (Ni, Co, Mn, C, N) are added to avoid the formation of δ-ferrite phase, which decrease the toughness of the material [19]. Nickel and Cobalt stabilize the austenite regime and manganese reduces the critical cooling rate. Carbon precipitates as carbides and increases the strength and the hardenability. Moreover, nitrogen precipitates as fine dispersed MX phases, which hinder movement of dislocations during service (VN).

PART II Creep, Microscopy Techniques and MatCalc Software

3.3. Creep

Creep can be defined as a time-dependent plastic deformation caused by dislocation movements and diffusion. The stress that produces a given rate of creep at a specified temperature is called *Creep Strength,* and is strongly dependant on temperature and stress. The general equation for creep is:

$$\frac{d\varepsilon}{dt} = \frac{C\sigma^m}{d^b} e^{\frac{-Q}{kT}}$$

where ε is the creep strain, C is a constant dependent on the material and the particular creep mechanism, m and b are exponents dependent on the creep mechanism, Q is the activation energy of the creep mechanism, σ is the applied stress, d is the grain size of the material, k is Boltzmann's constant, and T is the absolute temperature.

At high stresses, the creep is controlled by the movement of dislocations (Dislocation Creep) in the slip plane. Because the material contains defects (i.e. vacancies, precipitates, and solute atoms) the movement of the dislocation can be hindered. However, at high temperatures, vacancies can diffuse and the dislocations can move and climb allowing the deformation. The diffusion can be described as:

$$D = D_o \exp\left(-\frac{Q}{RT}\right)$$

where D is the diffusion rate, D_o is a constant, Q is the activation energy for atomic motion, R is the universal gas constant and T is the absolute temperature. Thus, diffusion-controlled mechanisms will have a significant effect on high temperature mechanical properties and performances. For example, dislocation climb, concentration of vacancies, new slip systems, and grain boundary sliding all are diffusion-controlled and will affect the behaviour of materials at high temperatures. In addition, corrosion or oxidation mechanisms, which are diffusion-rate dependent, will have an effect on the life time of materials at high temperatures [20].

Recovery and recrystallisation processes can also have a strong influence in creep even when they are not deformation systems. In these processes, rearrangement of dislocation occurs changing the number of dislocations and the subgrain size, affecting or changing the properties of the materials.

Figure 3.3 represents a typical creep curve diagram. Strain versus time is plotted, and three zones can be observed, the primary (I) creep, the secondary (II) or stationary creep and the tertiary (III) creep. At the primary stage, there is a decrease on the free dislocations. At the secondary creep, there is a balance between the decrease of free dislocation and generation of new dislocations. Finally, at the tertiary stage the creep rate increases because the decrease of cross section in the material. Nevertheless, tempered martensitic steels do not show this behaviour at higher temperatures or loads. These steels grades typically show only two stages, the primary and one, which is together secondary and tertiary.

In these tempered martensitic steel grades, high numbers of dislocations are produced due to the diffusionless transformation from austenite to martensite. To hinder the movement of these dislocations and therefore, increase creep resistance, barriers are introduced that can stop the movement of the dislocations. Precipitates, martensite lath boundaries and prior austenite grain boundaries hinder the movement of the dislocations and thus improve the creep strength. Figure 3.4 shows different mechanisms of how the dislocations can interact with the precipitates. Nevertheless, processes like recovery or recrystallization of the matrix and dissolution of precipitates occur and the dislocations can move free, producing a decrease of their number and thus a decrease in the creep strength.

There are four different basic ways to improve the creep resistance in steels: work hardening, solid solution strengthening, precipitation hardening and grain boundary strengthening [12]. For *solid solution hardening,* atoms with larger atomic sizes than iron are added like alloying elements (i.e. Mo or W). In addition, it is possible to hinder the movement of the dislocations by adding interstitial atoms such as nitrogen. *Precipitation hardening and grain boundary strengthening* can improve the creep resistance through precipitation of finely distributed precipitates particles (i.e. MX) in the matrix, stabilizing the free dislocations, or hindering the coarsening of grains and laths (i.e.$M_{23}C_6$, M_6C, M_7C_3, MX and M_2X, Fe_2(Mo,W) Laves phase). Another mechanism to improve creep resistance is to *increase the number of dislocations* in the matrix. This can be controlled through the heat treatment. The transformation from austenite to martensite and afterward the consequent tempering produced around 1-10x10^{14} m^{-2} dislocations in the matrix in 9-12 wt.%Cr tempered martensitic steels.

During all research projects that have been carried out around the world several hypothesis have been proposed for the decrease of creep strength of 9-12 wt.%Cr tempered martensitic steels:

- Dissolution of the finely distributed MX particles due to the formation of mod. Z-phase precipitates. This has a strong effect in 12 wt.%Cr tempered martensitic steels [12][21][22][23].
- Preferential recovery near prior austenite grain boundaries [12].
- Coarsening of $M_{23}C_6$ [12].
- Excess of dislocation coming from a low tempering temperature [12].
- Effect of delta ferrite [12].

However, there is currently no satisfactory solution to overcome the decrease of creep strength in 9-12 wt.%Cr tempered martensitic steel grades, which allow using these materials at the needed high temperatures and steam pressures, in order to increase the efficiency in USC power plants.

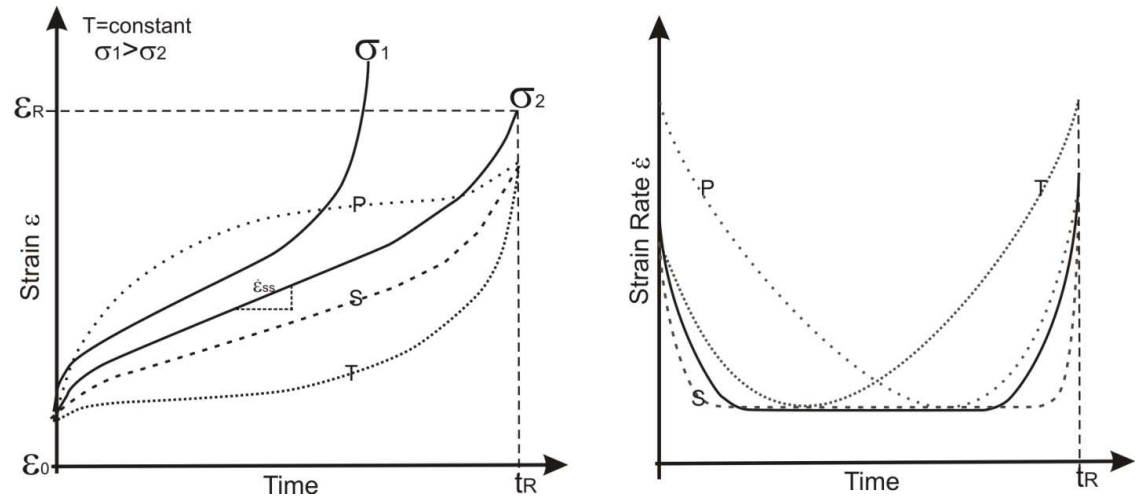

Figure 3.3. Creep curves at fix temperature and different stresses (left image) [12][24]. This graph represents the primary (I) creep, the secondary (II) or stationary creep and the tertiary (III) creep. ε_0 represents the initial strain, due to the initial application of load, normally elastic strain. ε_R represents the strain at rupture, t_R the time to rupture and $\dot{\varepsilon}_{SS}$ the mean creep rate. Dashed lines marked with P, S and T indicates how creep may be primary-dominated (P), secondary-dominated (S) or tertiary-dominated (T). The typical creep rate curve as a function of time at constant temperature is represented in the right image.

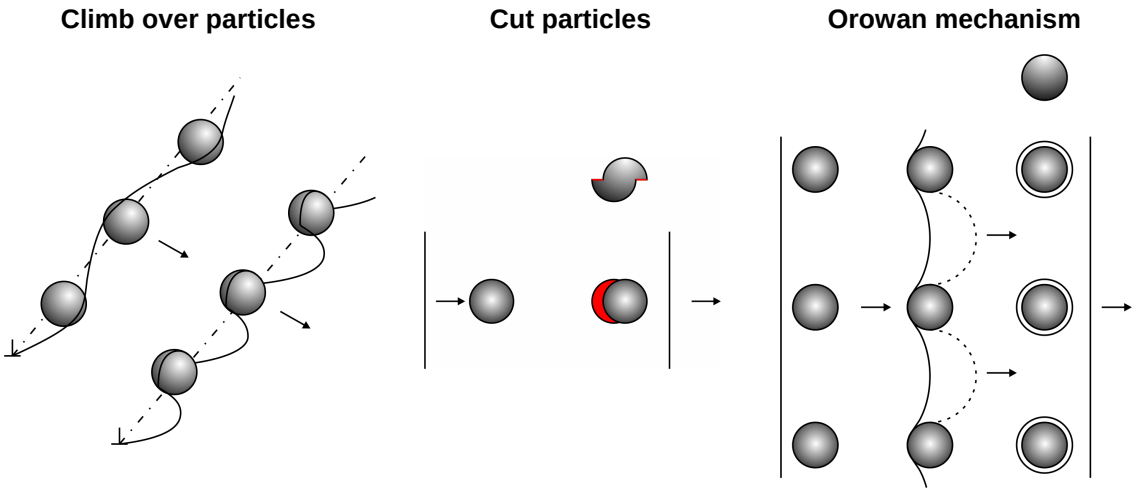

Figure 3.4. Schematic illustration [25], representing the interactions between precipitates and dislocations. Due to these interactions the movement of the dislocation can be hindered and the strength of the material increases (precipitation hardening).

3.4. Microscopy techniques: description

In the development of this project several microscopy techniques have been used for the study of the microstructure of the 12 wt.%Cr tempered martensitic steel X12CrCoWVNb 11-2-2. Optical microscopy, transmission electron microscopy and scanning electron microscopy techniques were used. Figure 3.5 represents the main parts of an optical microscope (OM), transmission electron microscope (TEM) and scanning electron microscope (SEM).

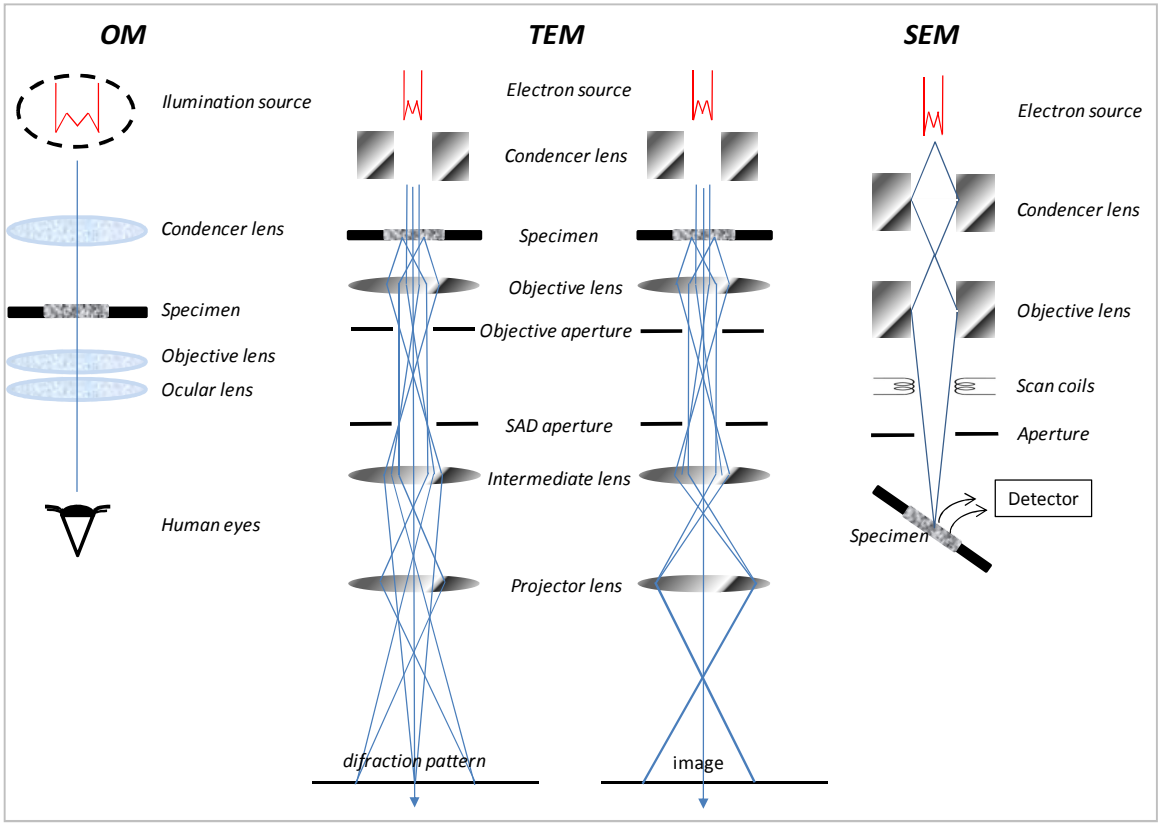

Figure 3.5. Three main microscopes have been used for the study of the macroscopic and microscopic features: optical microscope (OM), transmission electron microscope (TEM) and scanning electron microscope (SEM). The main parts of each one are here represented.

In the next sections, a brief description of the different microscopy techniques is going to be presented.

3.4.1. Optical Microscope (OM)

These types of microscopes reveal the microstructure of the material with some limitations. They have a resolution of about 200 nm (0.2 µm) due to the wave length of light (0.4-0.7 µm), which limits the possibility to study particles smaller than 200 nm. Because of that further investigations of the different precipitates phases of the studied steel (X12CrCoWVNB 11-2-2) were carried out with different electron microscopy techniques, TEM and SEM microscopes. However, this technique is useful for the characterization of the matrix structure (i.e. prior austenite grain size) as well as the identification and quantification of δ-ferrite.

3.4.2. Transmission Electron Microscopy (TEM)

Because of the lower wavelength radiation of electrons compared with the visible light (used in OM), in TEM microscopes the spatial resolution is improved and features down to less than 1 nm can be investigated.

In the TEM (see Figure 3.5), electrons emitted from a tungsten hairpin cathode or a LaB_6 source, are focused in an electron transparent specimen (thickness <100nm) and a system of condenser lenses and apertures are adjusted to illuminate the sample with a parallel beam. The electrons interact with the specimen and are recombined by the objective lenses to form an image (in the image plane) or a diffraction pattern (in the back focal plane). The image or the diffraction patter is projected into the fluorescent screen and recorded by a digital system (e.g. CCD camera) using the intermediate lenses and with the projector lenses the magnification can be modified. When TEM is operated in diffraction mode

the diffraction pattern is imaged onto the screen and by inserting an aperture (SAED) the area to be characterized can be restricted [26]. Important considerations have to be done with the different electron sources, apertures, lenses and its aberrations, pumps, specimen holders, resolution and magnification. At this point of time, the author of this thesis recommend “Transmission Electron Microscopy“ book [27] where detailed information can be found.

When the high energy electron beam (100-400 keV) interacts with the specimen several range of signals are produced, see Figure 3.6.

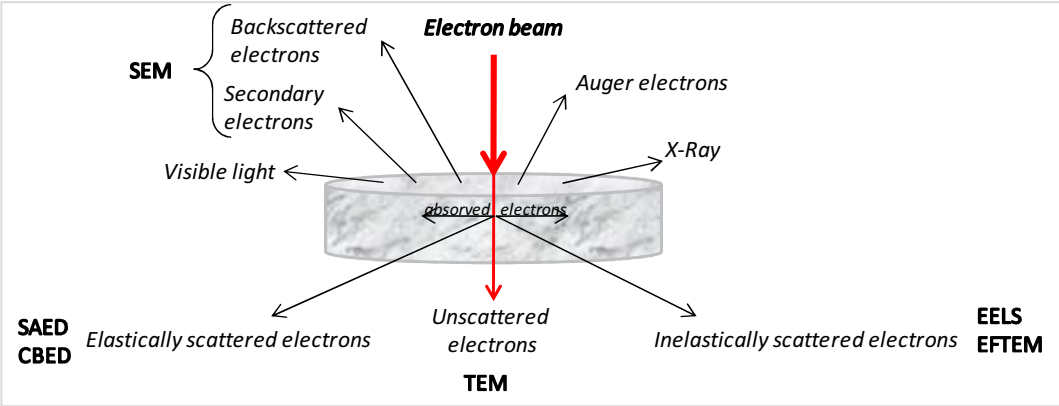

Figure 3.6. Signals generated when the high energy electron beam interact with the specimen.

The secondary electrons and backscattered electrons are mainly used to form images in Scanning Electron Microscopes and are going to be defined in the next chapter.

When working with TEM, the unscattered electrons, the elastically scattered electrons and the inelastically scattered electrons can be used for specimen characterization. The unscattered electrons correspond to the electrons of the direct beam. The electrons elastically scattered are electrons that have no lose of energy by interacting with the specimen and are coherent to the incident beam. On the other hand the inelastically scattered electrons have lost energy due to interaction electron-electron with the specimen. Auger electrons, excitation of secondary electrons, phonons, plasmons or X-ray emissions are all of them inelastic scattered electrons.

Electron Energy Loss Spectroscopy (EELS) and Energy Filtering Transmission Electron Microscopy (EFTEM).

The inner shell electrons in one atom have the lowest energy near the nucleus (K or L shell). They have very sharply defined energies, and they are localized. On the other hand, the outer electrons have the highest energy (i.e. with the lowest binding energy). Depending on the position of the electrons, the energy needed to move them, or to kick them out is different, and this is how techniques like EDX or EELS can be used to characterize the different elements into the different precipitates present in the analysed specimen.

In EELS, the electrons that have been inelastically scattered represent information about the electronic structure of the specimen atoms and reveal information of their nature and their bonding [26]. Using this technique, the inelastic scattered electrons are separated according to their energy, which can be done electrostatically and/or magnetically [26]. The EELS-spectrometer used in this thesis consists of a magnetic prism. This prism is basically an electromagnet, which produces a magnetic field perpendicular to the incoming beam. This prism can be placed after the phosphor screen of the TEM and has different functions. However, one of the most notable is that the electrons are spatially dispersed according to their kinetic energy (i.e. energy losses). The electrons with higher energy loses are deflected strongly and appear at the end of the spectra. The EEL spectrum can be acquired in two different ways; the method

used in this work has been by parallel-acquisition EELS (PEELS). Moreover, for the acquisition of spectra and images the Gatan Imaging Filter (GIF) has been used. The GIF is a PEELS with additional lenses and with an energy selecting slit after the prism and a CCD-detector [26]. The main components of the GIF are shown in Figure 3.7. The magnetic prism, with a bending angle of 90°, produces a spectra free of second order aberrations. Inside of this prism a drift tube is located for calibration or for moving the spectra which is electrically isolated. Using the energy slit, the energy interval that is contributing to the filtered image can be selected. Following, the quadrupole-sextupole is located where is possible to project an image of the spectrum, onto the CCD camera, or a compensation for the energy dispersion of the magnet is done and a magnified image of the specimen onto the CCD camera is projected. In the first mode, an spectra is obtain, in the second an image containing electrons of a specific energy selected by the slit is produced [26].

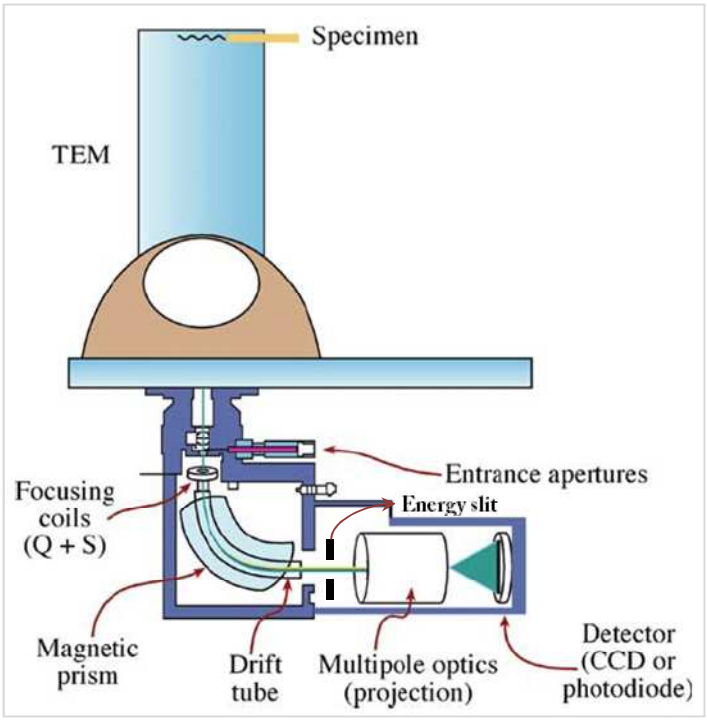

Figure 3.7. Schematic diagram of the GIF main components [27].

The energy loss spectrum, obtained using EELS technique, can be divided in three principal parts, as shown in Figure 3.8, the zero loss peak, the low loss energy spectrum and the high loss energy spectrum. The zero loss peak contains information about the electrons that have no loss of energy. However, this peak contains also phonon-scattered electrons and electrons that have suffered small energy losses. At the low loss energy spectrum, information about the beam electrons that have interacted with conduction and /or valence bands can be obtained. The energy border of a low energy loss spectrum is set at up to 50 eV of energy loss. The high loss energy spectrum (energy losses higher than 50 eV) contains information from inelastic interactions with the inner or core shells electrons. Therefore, the elemental composition and maps can be extracted from these spectra. When one electron coming from the beam, transfers the necessary energy to a core shell electron to move it outside the attractive field of the nucleus, the atom is ionized, and the beam's electron has ionization losses, which are characteristic of the involved atom. The electrons that are located in levels near the nucleus will need much more energy for ejection, also if Z (atomic number) increases [27]. In EELS ionizations edges from K, L, M etc. shell electrons are detected. Figure 3.9 shows the possible edges in the energy loss spectrum due to core

shell ionization. For example, the L shell, have electrons in 2s or 2p orbitals. If one electron is ionizated from 2p, in the spectra an L2 or L3 edge will appear. Sometimes is impossible to distinguish between both edges, then it is called L2,3.

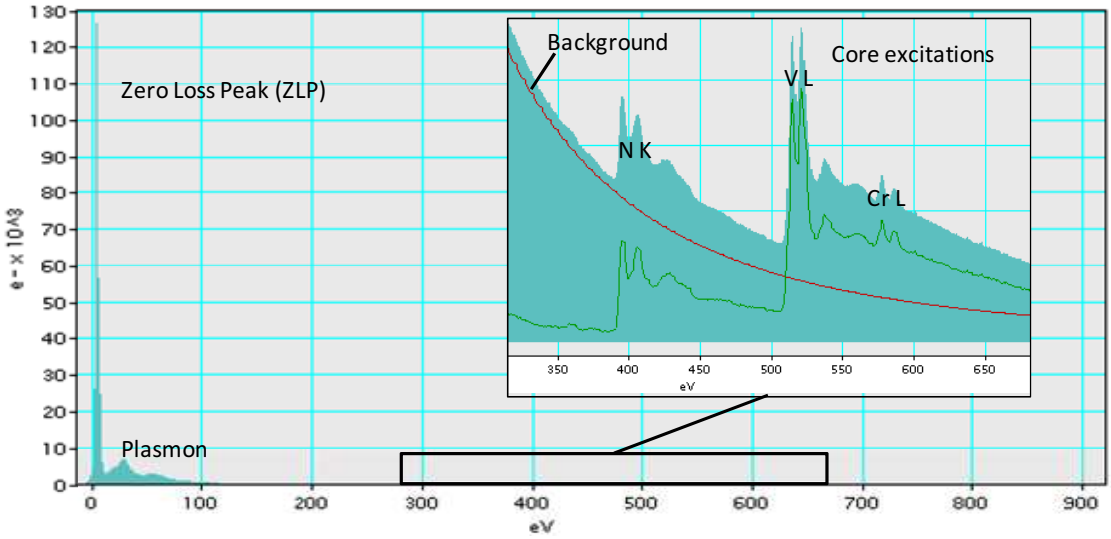

Figure 3.8. EELS spectrum of a mod. Z-phase precipitate indicating the main parts forming the spectrum.

For the analysis of solids, atoms integrated into a crystal lattice, the ionization edges are superimposed. In this case, the edge shows a fine structure due to the bonding effects (energy loss near edge structure ELNES). Figure 3.9 shows how the fine structure of the nitrogen edge can change due to changes in the crystal structure of the analysed particles [28]. With EDX technique information of the elemental composition is obtained, but with EELS and ELNES also information about the bonding can be studied. ELNES technique is highly sensitive to changes in the bonding, or the valence state, of the atom. Because of this, it is possible to use this technique as a fingerprinting approach.

In 9–12 wt.%Cr tempered martensitic steels, nitrides (MX, M_2X and modified Z-phase ((Cr,V,Nb,Fe)N)) are of particular interest because of their different contribution to the creep strength of the material, but these three phases show the same elemental composition (Cr, V, Nb, N). That is why to differ between these phases the energy-loss near edge structure (ELNES) of the nitrogen ionisation K edge has been used [28], see Figure 3.9. While VN is face centred cubic, Cr_2N is hexagonally close packed and the mod. Z-phase features a tetragonally distorted bcc lattice the differences in the N-K ELNES are obvious and the EELS technique can be used to differ between these phases without need to perform diffraction measurements.

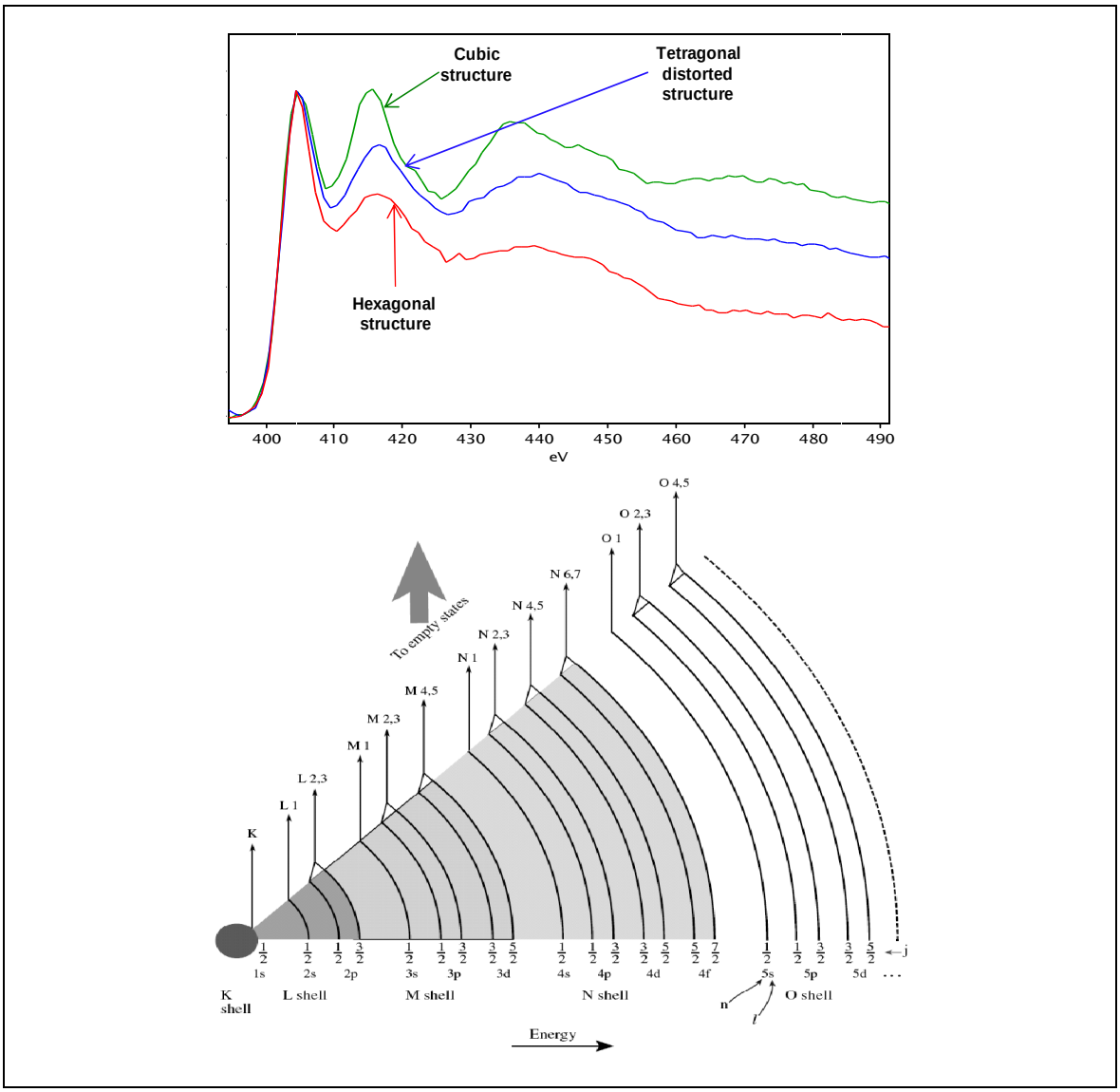

Figure 3.9. ELNES studies of the nitrogen peak for the study of three different phases in the X12CrCoWVNb 11-2-2 steel. Green line corresponds to the nitrogen of a cubic structure in a VN, blue for a mod. Z-phase and red for a Cr_2N (upper image) [28].The possible edges in the energy loss spectrum due to core shell ionization (lower image [27]).

When recording EELS, a narrow slit, located at the spectrometer image plane, can select the electrons that have lost specific energy (selected by the user). The electrons that go though the slit are detected and an image can be formed [27], this is how EFTEM technique is working. The slit width is variable and the narrower the slit allows a better energy resolution to be obtained, but on the other side, this produces a low amount of signal. Moreover, the background signal is normally higher than the ionization signal. Two methods are usually used to remove this signal the two or three windows technique, see Figure 3.10.

By the *elemental maps* technique (three windows technique), two images (pre-edge1 and pre-edge2) are recorded before the ionization edge, the background then being calculated and extracted from the image recorded at the energy of the maximum of absorption peak caused by the inner shell ionization (post-edge). This technique allows quantitative analysis, nevertheless some diffraction contrasts can still be present, to avoid this diffraction contrasts ratio mapping is performed.

In the *jump ratio* technique (two windows technique), an image is recorded using electrons at the energy of the maximum of absorption peak caused by a particular inner shell ionization (post-edge) and is divided by and image recorded just before the ionization energy (pre-edge).

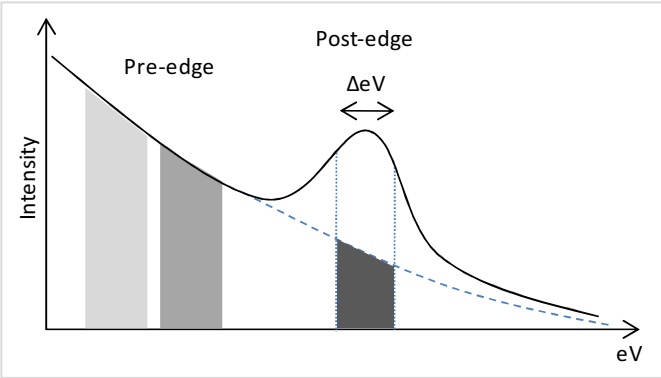

Figure 3.10. Two pre-edge windows and one post-edge window are used for acquirement of elemental maps. In the two pre-edge window the background signal can be calculated and removed from the post-edge signal. This method allows chemical quantification of the different detected elements in one particle [27].

Using this two or three window method, elemental images or ratio images can be obtained; mapping only the desired energy indicated by the user. Figure 3.11 represents the vanadium, chromium and nitrogen maps for a same position in the studied 12 wt.%Cr tempered martensitic steel. The different phases can be identified with this technique, and a colour Red Green Blue (RGB) map can be created out of the three different maps.

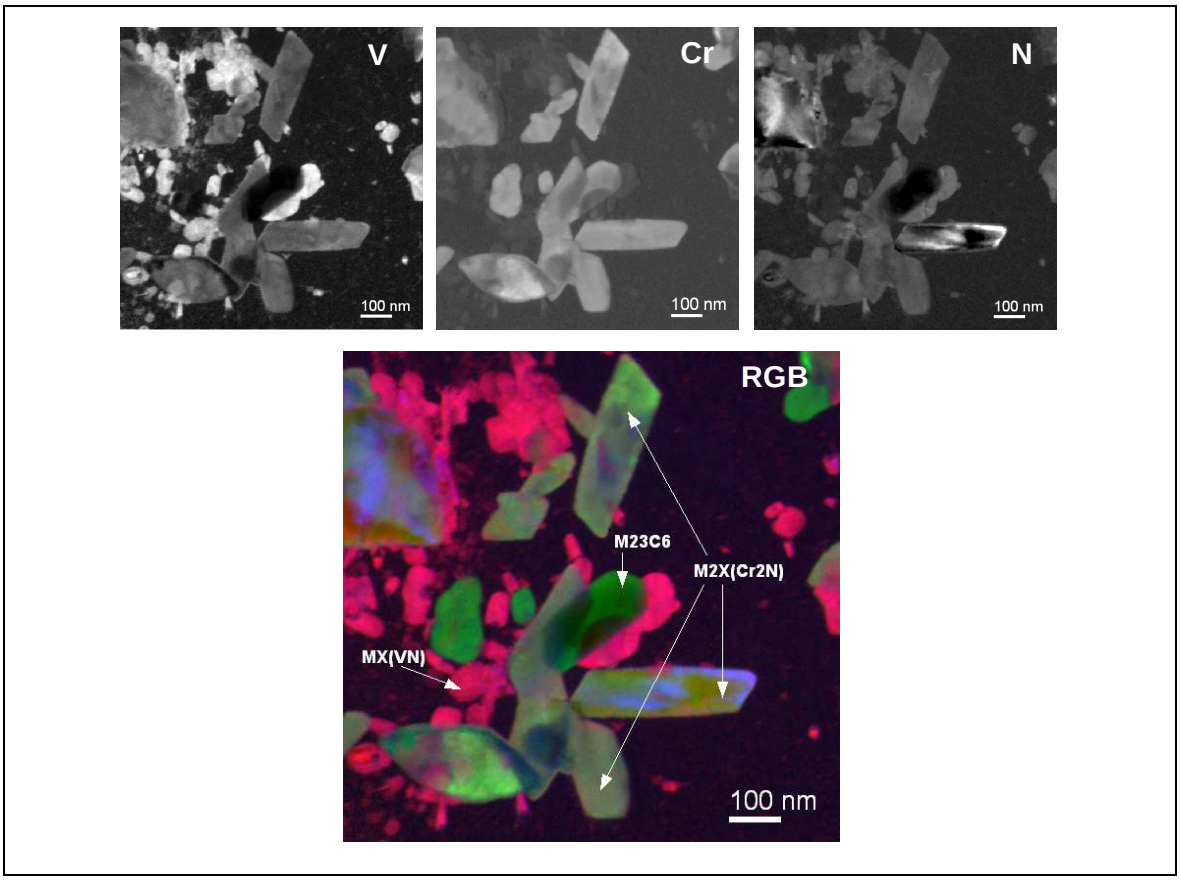

Figure 3.11. Three EFTEM images from vanadium, chromium and nitrogen elements and RGB reconstruction of the maps, where red is vanadium, green is chromium and blue is nitrogen.

Scatter Diagrams

Another helpful technique, used in the completion of this thesis, was the scatter diagrams for the identification of different phases in one image, Hofer et al. [29]. First, a bivariate or two-dimensional scatter diagram is produced by plotting the frequency of occurrence of intensity values for one image against the second related map, central image from Figure 3.12. The scatter diagrams can be displayed as images, where the axes correspond to the intensity ranges and brightness that will be used to indicate the frequency of occurrence. These diagrams present clusters, which may represent distinct chemical phases. To indicate which phase corresponds in the maps into the scatter diagram, it is necessary to mark the clusters with a digital mask on the computer screen. Afterwards, a traceback algorithm indicates in the image the pixels that have generated a count on the marked cluster [30]. Figure 3.12 represents the calculation of the phase diagrams for the investigated material X12CrCoWVNB 11-2-2. It can be clearly distinguished in form of a phase diagram the different phases present in the RGB image.

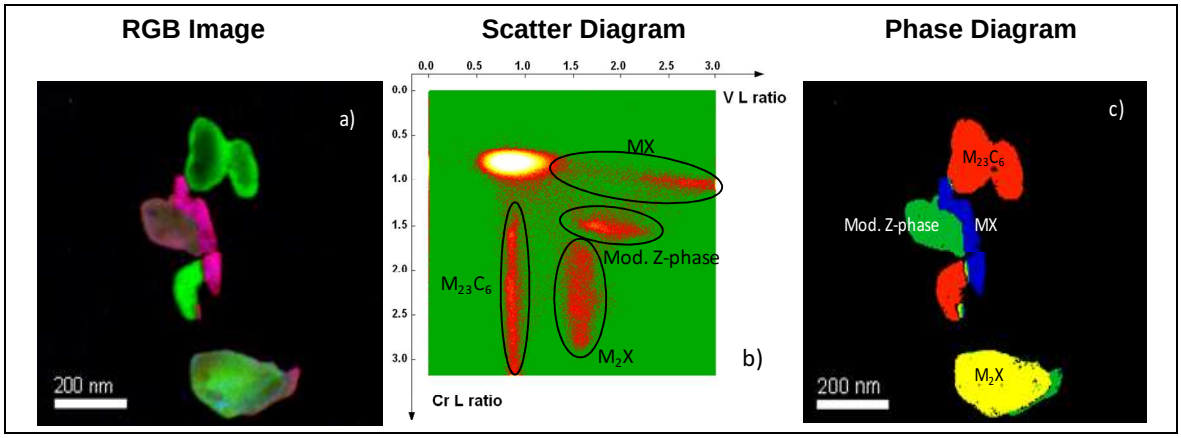

Figure 3.12. RGB (red=vanadium, green=chromium, blue=nitrogen) image from a 12 wt.%Cr X12CrCoWVNb 11-2-2 steel in a extraction replica sample (a). The different precipitates phases have been identified through the bivariate scatter diagram (b) showing clustering of the different precipitates according their vanadium and chromium ratio (c).

X-ray spectroscopy (EDX)

The X-rays are electromagnetic radiation its energy depends in the inner shell energies, which increase with the element number (Z). For X-ray spectroscopy, the incident beam knocks electrons out of the occupied states in the atom, leaving empty states. Afterwards, an electron from another occupied state move to the empty state vacancy in the ionised shell emitting an X-ray that can be detected, see Figure 3.13. This technique can be used complementary to EELS technique.

The EDX detector generates a charge pulse proportional to the X-ray energy, and afterwards it is converted into a voltage. The signal is then amplified through a field effect transistor, isolated from other pulses, amplified and then identified electronically as resulting from an X-ray of specific energy. As last step, a digitized signal is stored in a channel assigned to that energy in a multi channel analyzer. Different detectors are available on the market. Depending on each one, the possibilities to detect the elements of the periodic table are limited, and other factors like increased absorption within the specimen make light elements in EDX not detectable or difficult to detect. In those cases, the application of EELS is advisable [31].

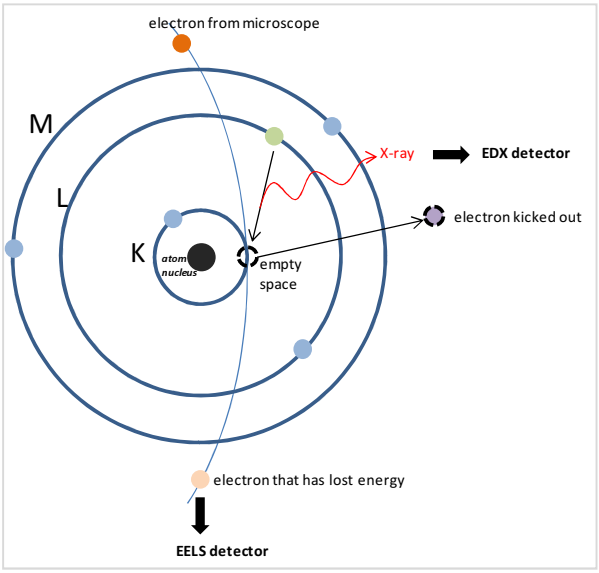

Figure 3.13. Schematic representation of the electron K, L and M shell of an atom. Representation of the different electron types that can be detected via EDX or EELS [31].

3.4.3. Scanning electron microscopy (SEM)

The scanning electron microscope (SEM) works similar to TEM. Electron gun, condenser lenses and other systems (like vacuum) are similar. While in TEM, the electrons are going through the specimen and provide information about the internal structure, in SEM the surface or near surface, of bulk specimens are studied. This is one of the big differences between these two techniques. In a SEM microscope, thick specimens are used for the analysis and only secondary electron and backscattered electrons can be detected, see Figure 3.14. Sometimes an X-ray detector is used for chemical analysis. The electrons, arriving from the beam penetrate into the specimen (interaction volume) where the different inelastic scatterings produce the different radiations (secondary or backscattered electrons). The radiation that will be detected is the one that escape from the specimen (see Figure 3.14).

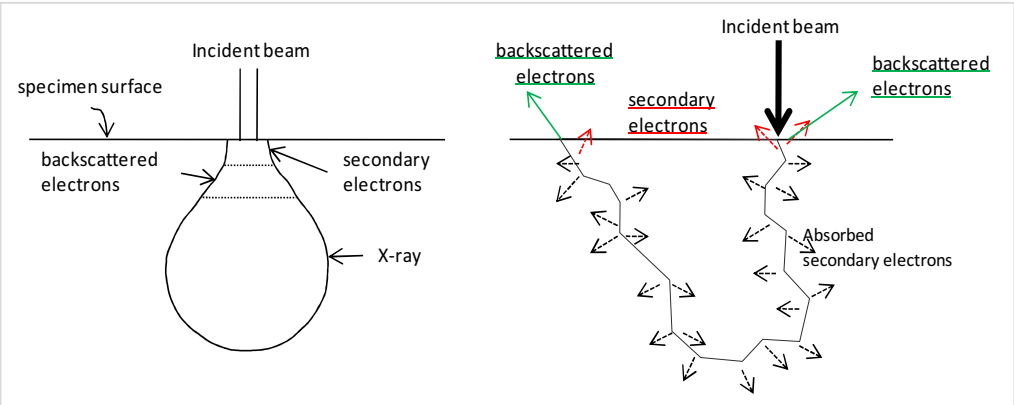

Figure 3.14. Interaction volume (left) and different types of electrons that can be mainly detected in the SEM (right) [31].

Figure 3.5 shows a schematic diagram of the main components in a SEM microscope. The electrons are generated at the source (normally tungsten filament, or field emission gun) and then accelerated from 1 keV to 30 keV. Afterwards, the condenser lenses focus the electron beam, arriving at the specimen with a

diameter of around 2-10 nm. The electron beam is then scanned across the specimen (by the scan coil) and the detector counts the number of low energy secondary or backscattered electrons provided from each point on the sample surface [31]. Parallel, the spot of a cathode ray tube is scanned across the screen. The brightness of the cathode ray tube spot is modulated by the amplified current from the secondary/backscattered electrons detector.

In SEM, the image is built up sequentially during the scan, image point (pixel) by image point (pixel). Because of that, if two features want to be separated they have to occupy different pixels. The resolution on SEM microscopes is depending on the size of the incident beam, the size of the cathode ray tube and the pixel size on the specimen. Topographic images are obtained with secondary electrons, but more useful are the composition images, information that is provided by the backscattered electrons. The numbers of secondary and backscattered electrons are strongly dependent on the atomic number of the specimen.

Electron backscattered diffraction (EBSD)

Also crystallographic information can be obtained with SEM microscopes. Electron backscattered diffraction (EBSD) permits the analysis of a specimen in SEM via diffraction. The electrons, from the electron beam, in a crystalline solid can be scattered in all directions elastically and inelastically. In this case, it is always electrons that follow the Bragg's law ($\lambda = 2\mathrm{d}\sin\theta$)[1] and the diffracted radiation is forming two cone's surfaces. Because of the electron wavelength and the lattice interplanar spacing into Bragg's law, these cones have an upper angle of near 180°. This indicates that these cones are almost flat and a pair of parallel conic sections results, which are so straight, that they look likes parallel lines on the view screen; these lines are the so called Kikuchi lines (Kikuchi bands) [32], see Figure 3.15. The distance between these lines is an angular distance 2θ which is proportional to the interplanar spacing in the atomic lattice. Thus, the Kikuchi pattern is a representation of all angular relationships in a crystal. Where the Kikuchi lines (the bands) intersect is defined as the zone axis, which represents the normal to a plane in the sample. Afterwards, an index to each zone axis is associated [32], and subsequently the orientation of the crystal can be determined. By scanning (in our case using a hexagonal grid) an extended amount of maps is obtained and evaluated, giving information on the microtexture, sample morphology or grain orientation and grain boundary. For more detailed information about EBSD technique, the author wants to recommend [32].

[1] λ correspond to the incident electron wavelength, d is the interplanar distance in the atomic lattice and θ is the angle between the incident beam and the scattering planes.

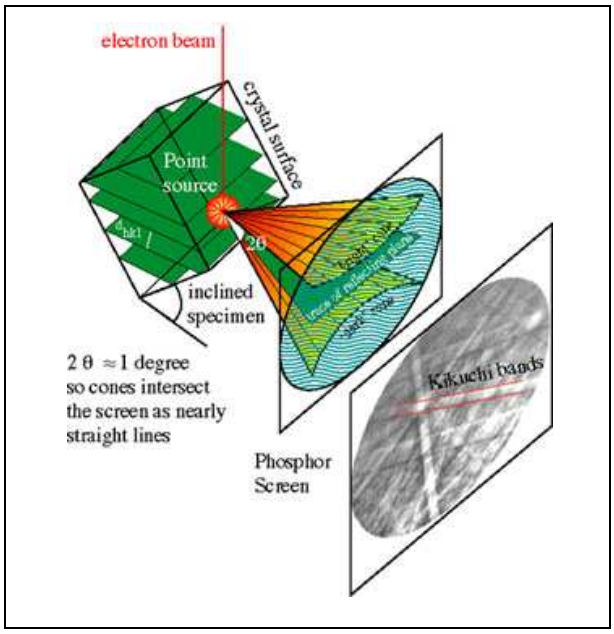

Figure 3.15 Formation of a backscattered Kikuchi bands [33].

3.5. Modelling / Simulations: Software MatCalc

For the study of the creep properties of 9-12 wt.%Cr tempered martensitic steels, long term creep tests have to be performed, and experimental investigations of the microstructure evolution during creep are time and capital consuming. To reduce costs and time the use of computer models that can predict these changes is important for the development and optimization of these materials. Many approaches have been published to model the precipitation kinetics in multi-component systems and some of them are summarised in [34].

MatCalc[2] stands for 'Materials Calculator' and some of the features of this software are: standard thermodynamic and diffusion databases (CALPHAD), equilibrium and non-equilibrium thermodynamics, microsegregation simulation (Scheil-type), multi-component precipitation kinetics, heat treatment of complex materials and some more. Equilibrium phases, as well as the kinetics of precipitate nucleation, precipitate growth and coarsening can be simulated. Prediction of the microstructural evolution for complex alloys is one of the goals of this software. However, for this task, reliable databases are necessary [35][36][37][38].

MatCalc, as well as ThermoCalc[3], are able to calculate the thermodynamic equilibrium of a system, and for that, the so called CALPHAD (CALculation of Phase Diagrams) approach is used. This method uses analytic expressions of Gibbs energies of every phase and every composition. The Gibbs energy of the individual phases is modelled as a function of temperature, composition, and sometimes pressure. Having this information, the equilibrium is simply calculated by a minimization of the energy [39].

In addition, MatCalc is able to simulate/calculate multicomponent precipitation kinetics as well as the software DICTRA[4] (Diffusion Controlled TRAnsformations), with a big difference. The different models in DICTRA are based on a solution of the multicomponent diffusion equations [40]. Balance equations are established and assuming equilibrium in the phase interface, it is possible to calculate the diffusive fluxes. Thermo-Calc can calculate the equilibrium under fixed temperatures and pressures. With a local thermodynamic equilibrium together with the calculation of the moving phase boundary, the kinetics of diffusion controlled phase transformations is calculated. This is how DICTRA works [41][42]. However, in DICTRA software due to the

[2] www.matcalc.at

[3] ThermoCalc AB, Stockholm, Sweden

[4] ThermoCalc AB, Stockholm, Sweden

complexity of calculating the thermodynamic equilibrium in the phase interface for systems with more elements only systems with a maximum of 4 components can be calculated. On the other hand, MatCalc is based on the thermodynamic extremal principle of maximum entropy production; the system evolves towards the maximum entropy and minimum Gibbs energy. In this way, the thermodynamic forces are formulated in terms of chemical potentials and the thermodynamic and kinetic databases are the input parameters, allowing calculations of complex systems with more than 4 components [42].

One of the first tasks that are needed for working with MatCalc software is to know the chemical composition of the studied alloy and its heat treatment. Afterwards, the nucleation site for each precipitate phase is needed.

MatCalc microstructure is simulated as solid bodies, which can represent austenitic and ferritic microstructure and can be shrunk and stretched to simulate martensitic lath structures. The number of nucleation sites is calculated for each of these solid bodies according to formulas described in [34]. Every nucleation site represents a different energy level which has important influences on nucleation, and afterwards, but less important, for growth and coarsening of the precipitates. Some of the nucleation sites in MatCalc are defined as:

-Grain boundaries (GB).
-Subgrain boundaries (SG).
-Other precipitates or inclusions.
-Atoms on a dislocation line (D).
-Single bulk atoms (B)

The next important parameter for the definition of the matrix system is the dislocation density. Three different matrixes are defined in the system for 9-12 wt.%Cr tempered martensitic steels: ferrite, austenite and martensite where this phase is defined as ferrite with higher dislocation density.

The software MatCalc package is based on the classical nucleation theory and how the software describes the evolution of the radii and of the chemical composition of individual precipitates can be found in several publications [36][37]. The nucleation rate *J*, as well as the total free energy *G* of the system, and the critical nucleation energy ΔG^*, are calculated as:

$$J_{SS} = Z\beta^* N_C \exp\left(-\frac{\Delta G^*}{kT}\right)\exp\left(-\frac{\tau}{t}\right) = J_s \exp\left(-\frac{\tau}{t}\right) \quad [42]$$

$$G = \sum_{i=1}^{n} N_{0i}\mu_{0i} + \sum_{k=1}^{m} \frac{4\pi\rho_k^3}{3}\left(\lambda_k + \sum_{i=1}^{n} c_{ki}\mu_{ki}\right) + \sum_{k=1}^{m} 4\pi\rho_k^2\gamma_k \quad [42]$$

$$\Delta G^* = \frac{16\pi}{3}\frac{\gamma^3}{F^2} \quad [42]$$

Where the *Z* is the Zeldovich factor, β^* is the atomic attachment rate, N_c is the number of potential nucleation, *k* is the Boltzmant constant, *T* is the absolute temperature, *t* is the time and τ the incubation time. Moreover, N_{0i} and μ_{0i} are the number of moles and chemical potentials of component i and, μ_{ki} and c_{ki} the chemical potential and the concentration of component i in the precipitate k, ρ_k is the radius and γ_k the interfacial energy and λ_k takes into account elastic and plastic energy contributions. *F* is the effective driving force [42]. All these equations are well defined in Computation Materials Enginering, chapter 6 [43]. Considering that during growth of a precipitate, diffusion inside the precipitate, diffusion in the matrix and interface movement occurs and applying the extreme principle (maximum entropy) it is possible to describe the change of the radius and the chemical composition of the different precipitates phases [42].

Interfacial energy γ [Jm^{-2}] and area [m^2] between precipitate and bulk material are of high importance parameters for the kinetics calculations. These parameters are related with the nucleation, growth and coarsening of precipitates. These values are dependant of many variables like: crystallography of precipitate and matrix, misorientations between them or chemical composition of the involved phases,

and are normally unknown. An approximation for the interfacial energy is considered in MatCalc and is denoted as effective interfacial energy [34].

In systems where the thermodynamic data is well known, the kinetics simulations can be performed with good success. When the thermodynamic database is inaccurate, the kinetic simulation will not correspond to the experimental findings [42] [44]. In this case the databases have to be improved by experimental investigations.

PART III X12CrCoWVNb 11- 2-2 steel

3.6. Development of the base material: X12CrCoWVNb 11-2-2

Out of the positive results presented on the steel T/P91, developed in the USA, Vallourec and Mannesmann Tubes (V&M) initiate a new R&D project for the development of a new tempered martensitic steel, with improved oxidation resistance, increasing the chromium content from 9 to 12 wt.%, for application up to 650℃ [45]. Following this aim, the X12CrCoWVNb 11-2-2 steel was produced.

The X12CrCoWVNb 11-2-2 material originates from the development of seven laboratory heats with various chemical compositions, all of them with a minimum of 11.2 wt.%Cr to improve oxidation resistance. Out of the 7 lab heats, one of them was chosen due to the best metallurgical results and oxidation behaviour. Thereafter, V&M proceeded with the industrial production of three heats (heat1, heat2, heat3) based on this laboratory heat [45][46][47]. Table 3.1 represents the different heats produced by V&M defining the production process, quantity and the obtained products. From Heat 1 and 2, three different products were produced and for Heat 3 only two.

The main alloying concept of this steel was the addition of 12 wt.%Cr to improve oxidation resistance as commented above. Moreover, vanadium, niobium and nitrogen were added to obtain precipitation strengthening, due to the precipitation of fine distributed MX particles. Carbon, silicon, molybdenum, tungsten, cobalt, boron and manganese were added to optimise final properties [45][48].

Table 3.1. Industrial production of X12CrCoWVNb 11-2-2 [46], grey marked areas indicate the investigated base material.

Steel plants	*Process*	*Quantity tons*	*Round bar*	*Mills*	*Process*	*Products*
Heat 1	Electric Arc Furnace – Vacuum degassing	20	Ingot Forging	A	Continuous mandrel rolling	Tubes 60.3 x 8.8 mm
				E	Push bench	Tubes 51 x 4 mm
			Ingot	B	Pierce and pilger rolling	Pipes 406.4 x 35 mm
Heat 2		80	Continuous Casting + Forging	A	Continuous mandrel rolling	Tubes 38 x 6.3 mm 38 x 7.1 mm 44.5 x 10 mm 51 x 4 mm
				E	Push bench	Tubes 51 x 4 mm
				C	Continuous mandrel rolling	Tubes 140 x 12 mm
Heat 3		65	Ingot	D	Pierce and draw rolling	Pipes 460 x 80 mm
				B	Pierce and pilger rolling	Pipes 460 x 60 mm

V&M started a creep program with these three heats at different temperatures between 575℃ to 650℃ and different stress levels. Material in as-received condition (after casting, rolling and heat treatment) of all three heats, and thermally aged and creep loaded of Heat 1, have been studied in this project. Figure 3.16 represents the creep curve graph of X12CrCoWVNb 11-2-2 Heat 1 at 575℃, 600℃ and 625℃. Following, the Figure 3.17 shows the CCT diagram of the material. Finally, Figure 3.18 represents the strain rate curves and strain curves respectively for X12CrCoWVNb 11-2-2 material at the different tested temperatures.

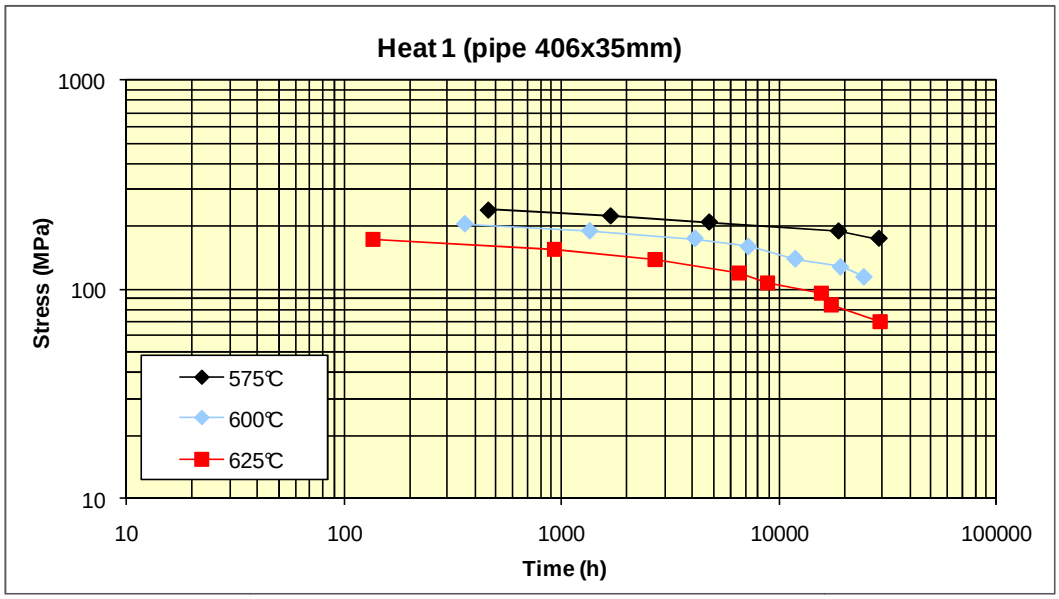

Figure 3.16. Creep curve graph for X12CrCoWVNb 11-2-2 Heat 1 material at 575℃, 600℃ and 625℃ [data provided by V&M].

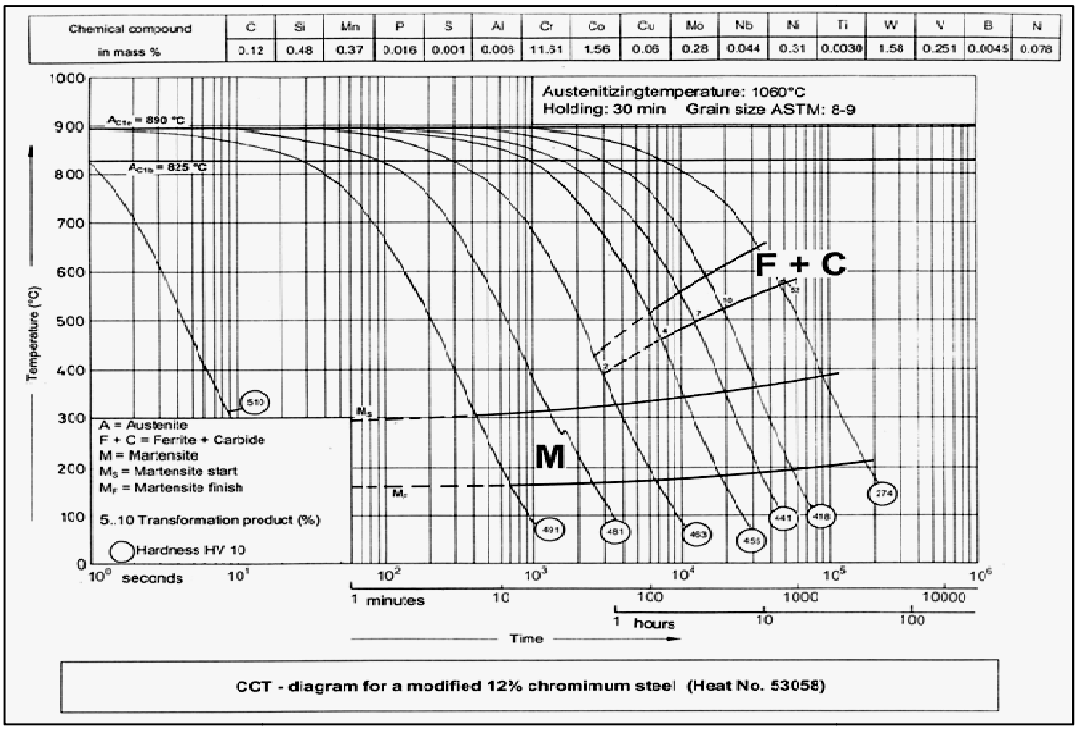

Figure 3.17. CCT diagram for X12CrCoWVNb 11-2-2 material [data provided by V&M].

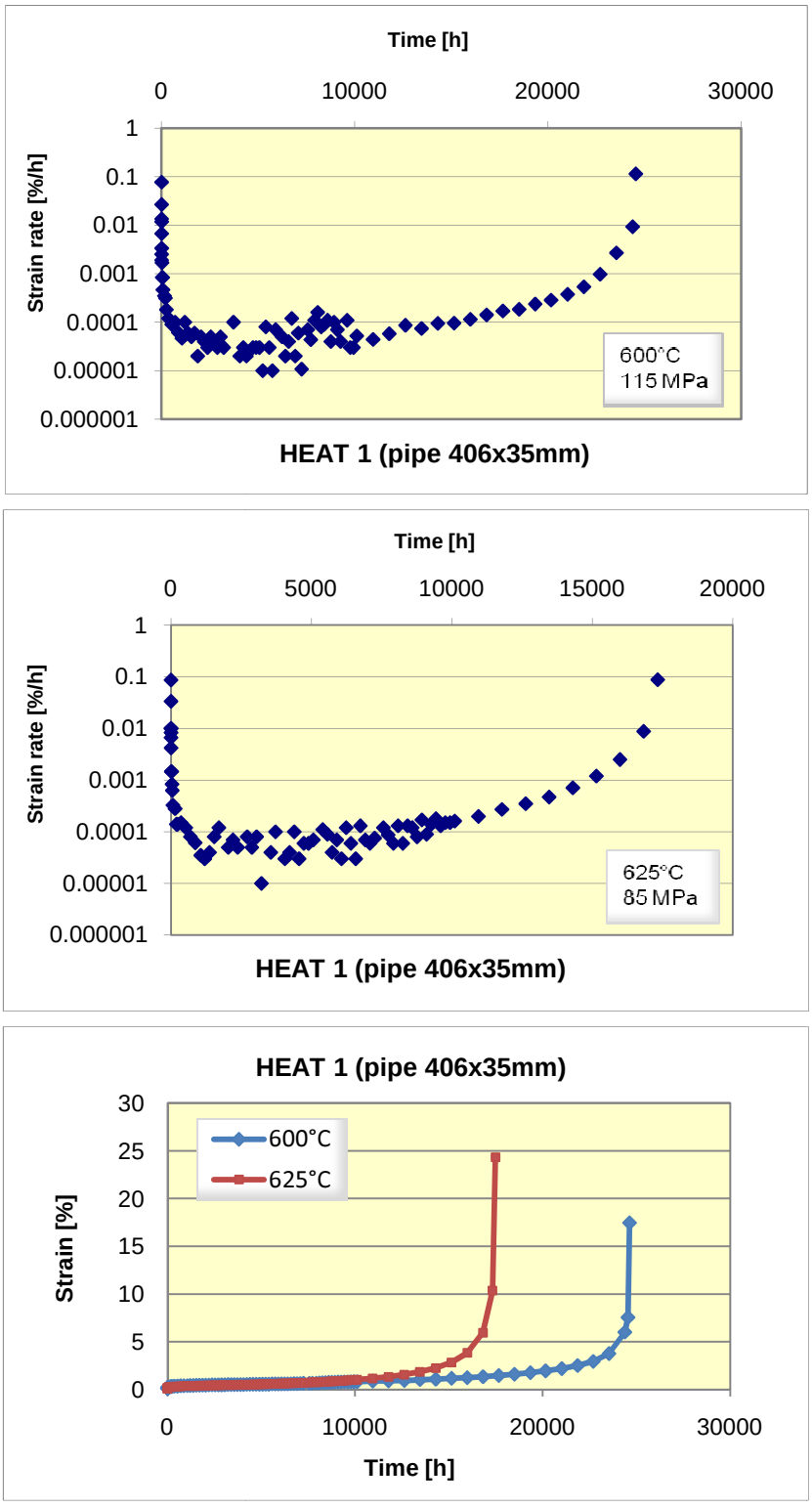

Figure 3.18. Strain rate and strain curves for X12CrCoWVNb 11-2-2 Heat 1 material at 600℃ and 625℃ [data provided by V&M].

3.7. Precedent microstructural studies of the material X12CrCoWVNb 11-2-2

X12CrCoWVNb 11-2-2 material steel was developed by V&M with the main goal of improve the creep resistance level (at the level of P91 and P92) with improved oxidation resistance due to the higher chromium content, 12 wt.%Cr. Different precedent investigations have been performed in this material by different investigations groups in the outgoing of the COST Action 536_Alloy Design Group program.

AGH University of Science and Technology of Cracow, the Centre of Excellence for Materials Characterization by Electron Microscopy [49] TEM microstructure characterization of annealed and creep deformed X12CrCoWVNb 11-2-2 steel performed. This group investigated subgrain size, dislocation density and mean large carbide size at different tempered and creep loaded X12CrCoWVNb 11-2-2 materials tested at 625℃. A summary of the results obtained is presented in Table 3.2. The TEM investigations were performed on thin foils and extraction replicas samples from the head and gauge length of the creep tested specimens.

Table 3.2. Microstructural parameters based on the TEM investigations of the X12CrCoWVNb 11-2-2 steel after annealing and creep deformation at 625˚C, obtained by the AGH University of Science and Technology, Prof. Aleksandra Czyrska-Filemonowicz [49].

Material Condition	Mean subgrain size [µm]	Dislocation density [m^{-2}]	Mean large carbide size [µm]
Specimen 426-7 annealed at 625˚C / 2706 h	0.60±0.20	2.60 ±0.43×10^{14}	0.14 ±0.10
Specimen 426-7 creep deformed at 625˚C / 140 MPa / 2706 h	0.82±0.35	1.92 ±0.54×10^{14}	0.17 ±0,08
Specimen 412-4 annealed at 625˚C / 15788 h	0.70±0.23	2.09 ±0.74×10^{14}	0.24 ±0.11
Specimen 412-4 creep deformed at 625˚C / 96 MPa / 15788 h	0.93±0.32	1.34 ±0.89×10^{14}	0.28 ±0.08

Technical University of Denmark (TUD) [50] performed also investigations on the X12CrCoWVNb 11-2-2 creep exposed material at 625℃ after 15788 h. TEM investigations were performed in extraction carbon replicas and mod. Z-phase, VN, NbC, Cr_2N, $Fe_2(W, Mo)$ and $Cr_{23}C_6$ were identified via EDS measurements. An experimental estimation of the quantity the mod. Z-phase was performed in different Cr containing tempered martensitic steels observed in this study X12CrCoWVNb 11-2-2 steel was classified as steel by which high mod. Z-phase content. The observed high quantity of mod. Z-phase was assumed to be one of the main reasons for the drop in creep resistance observed in this material.

4. Investigated Material: X12CrCoWVNb 11-2-2

The investigated material X12CrCoWVNb 11-2-2 was produced and delivered by V&M and SZFM at different conditions. X12CrCoWVNb 11-2-2 Heat 1, Heat 2 and Heat 3 variants, with a chemical composition presented in Table 4.1 were delivered in as-received condition after casting and heat treatment (see Table 4.2). Figure 4.1 shows different macrographs of the material in as-received condition. Moreover, the X12CrCoWVNb 11-2-2 Heat 1 variant was investigated after creep test exposure (see Figure 4.2), at different temperatures and stresses. In Table 4.3 is listed the different specimens that have been received in the outgoing of this project as well as the: creep testing temperature, creep testing stress, time to rupture, elongation and reduction's area of the creep tested specimens together with the different designated acronyms.

For the evaluation of the different specimens, to each sample an acronym has been assigned, see Table 4.4. The acronyms are defined as following:

- For the specimens in as-received condition:
  - AS: is indicating that the material is studied in as-received condition, after casting, rolling and heat treatment.
  - H: indicated which Heat variant is studied: Heat 1 (H1), Heat 2 (H2) and Heat 3 (H3).
  - Moreover, P or T is indicated: P for Pipe and T for Tube, indicating if the specific Heat was used for the production of pipes or tubes.
- For the specimens creep tested:
  - TA or CL: indicating if the specimen is investigated in thermally aged (TA) condition or in creep loaded (CL) condition.
  - Following, the creep tested temperature is defined: 575 for 575℃, 600 for 600℃ and 625 for 625℃.
  - The heat variant that has been studied is indicated by: H1P for Heat 1 pipe, H2T for Heat 2 tube and H3P for Heat 3 pipe.
  - If the evaluated specimen is TA, the rupture time is indicated as: dash and the rupture time in hours.
  - If the evaluated specimen is CL, the testing stress and the rupture time are indicated as: dash and stress in MPa, and dash and time to rupture in hours.

Table 4.1. Chemical composition (wt.%) of all three heats.

Heat	*Si*	*Mn*	*P*	*S*	*Al*	*Cu*	*Cr*	*Ni*
Ind. Heat 1 BGH	0.490	0.350	0.018	0.001	0.008	0.080	11.500	0.290
Ind. Heat 2 SSV	0.450	0.320	0.015	0.002	0.012	0.045	11.250	0.260
Ind. Heat 3 Bous	0.480	0.180	0.018	0.002	0.010	0.080	11.250	0.230

Heat	*Mo*	*W*	*V*	*B*	*Nb*	*Co*	*N*	*C*
Ind. Heat 1 BGH	0.290	1.500	0.260	0.0049	0.050	1.620	0.066	0.115
Ind. Heat 2 SSV	0.240	1.440	0.260	0.0044	0.047	1.550	0.055	0.106
Ind. Heat 3 Bous	0.270	1.440	0.230	0.0035	0.051	1.500	0.053	0.110

Table 4.2. Heat treatment of the three X12CrCoWVNb 11-2-2 heats variants.

Ind. Heat 1 BGH (20 t) pipe 406.4x35mm: heat treatment of 1060℃ 30 min a.c. + 780℃ 2 h a. c.
Ind. Heat 2 SSV (80 t) tube 140x10: heat treatment of 1060℃ 30 min a.c. + 780℃ 2 h a. c.
Ind. Heat 3 Bous (65 t) pipe 460x80: heat treatment of 1080℃ 30 min a.c. + 780℃ 4 h a. c.

Table 4.3. Investigated samples and the corresponding creep conditions.

Sample condition	Studied Samples: Acronym	Material	Temp. [℃]	Stress [MPa]	Time to rupture [h]	Rupture	
						Elongation [%]	Reduc. Area [%]
as-received	ASH1P, ASH2T and ASH3T	Heat 1 , Heat 2 and Heat 3	-	-	-	-	-
thermally aged 575℃ 18726 h	TA575H1P-18726	Heat 1 Pipe	575	190	18726	16.0	68.0
creep load 575℃ 190 MPa 18726 h	CL575H1P-190-18726						
thermally aged 600℃ 4137 h	TA600H1P-4137	Heat 1 Pipe	600	175	4137	20.9	79.2
creep load 600℃ 175 MPa 4137 h	CL600H1P-175-4137						
thermally aged 600℃ 24639 h	TA600H1P-24639	Heat 1 Pipe	600	115	24639	17.5	69.0
creep load 600℃ 115 MPa 24639 h	CL600H1P-115-24639						
thermally aged 625℃ 17487 h	TA625H1P-17487	Heat 1 Pipe	625	85	17487	24.3	72.0
creep load 625℃ 85 MPa 17487 h	CL625H1P-85-17487						
thermally aged 625℃ 28983 h	TA625H1P-28983	Heat 1 Pipe	625	70	28983	21.9	65.2
creep load 625℃ 70 MPa 28983 h	CL625H1P-70-28983						

Table 4.4. Definition of the specimen acronyms.

Sample condition	Acronym
as-received Heat 1 pipe	ASH1P
as-received Heat 2 tube	ASH2T
as-received Heat 3 pipe	ASH3P
thermally aged 575℃ 18726 h	TA575H1P-18726
creep load 575℃ 190 MPa 18726 h	CL575H1P-190-18726
thermally aged 600℃ 4137 h	TA600H1P-4137
creep load 600℃ 175 MPa 4137 h	CL600H1P-175-4137
thermally aged 600℃ 24639 h	TA600H1P-24639
creep load 600℃ 115 MPa 24639 h	CL600H1P-115-24639
thermally aged 625℃ 17487 h	TA625H1P-17487
creep load 625℃ 85 MPa 17487 h	CL625H1P-85-17487
thermally aged 625℃ 28983 h	TA625H1P-28983
creep load 625℃ 70 MPa 28983 h	CL625H1P-70-28983

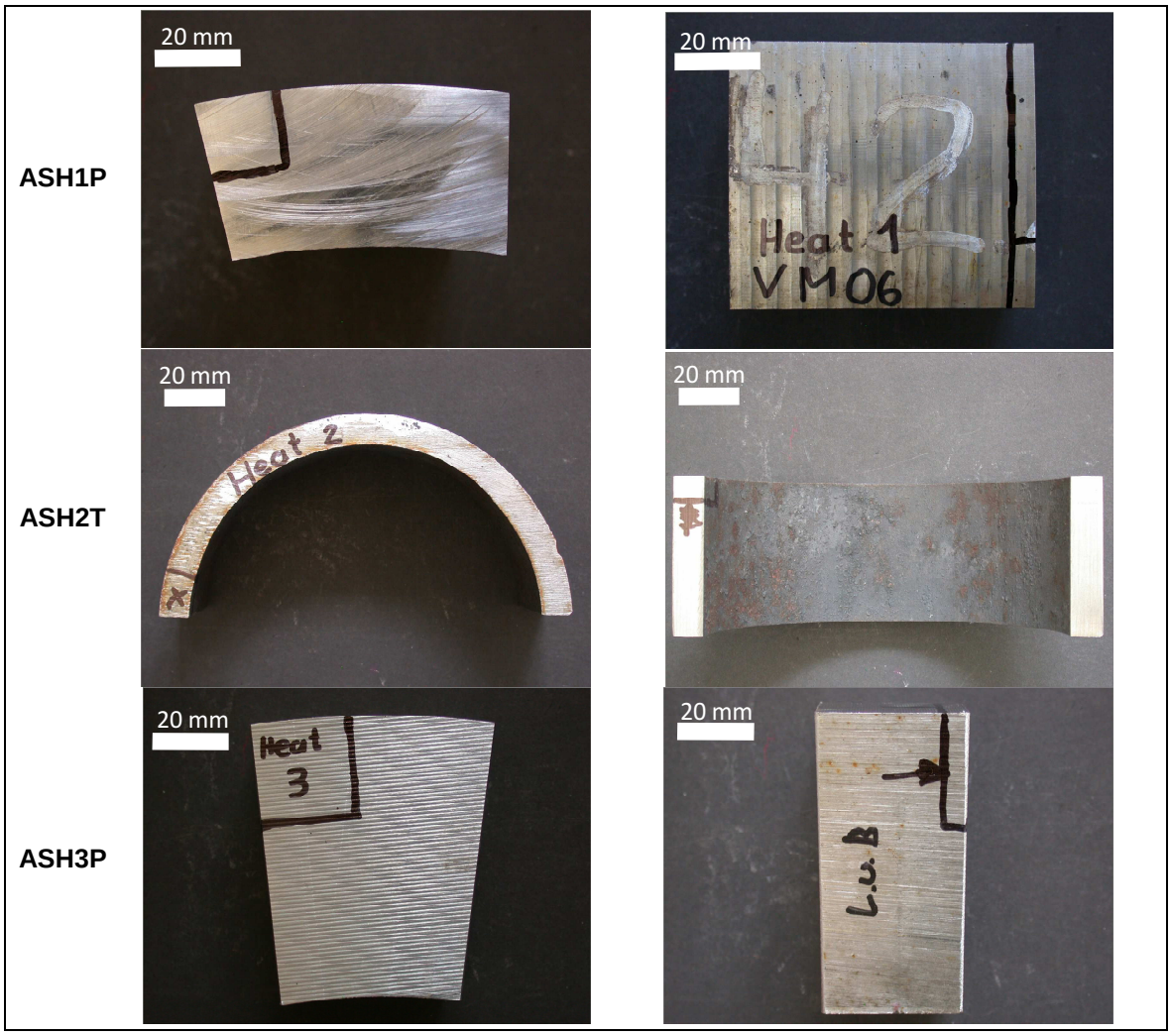

Figure 4.1. Macrographs of the received base material sample X12CrCoWVNb 11-2-2.

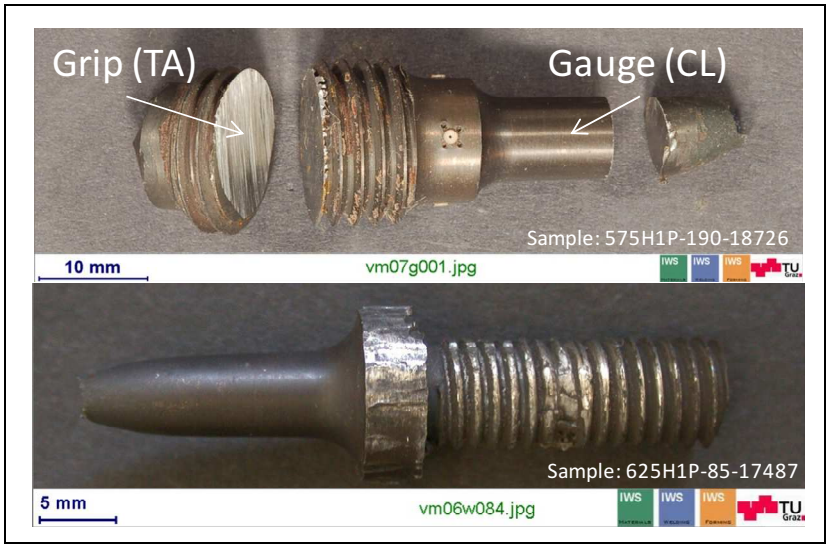

Figure 4.2. Macrograph of the received creep tested specimens: 575H1P-190-18726 and 625H1P-95-17497 from X12CrCoWVNb 11-2-2 Heat 1 variant. The analyzed thermally aged (TA) material was cut from the grip portion of the specimen, and the creep loaded (CL) from the gauge.

5. Experimental Procedure

The main focus of the experimental investigations was to obtain a fully microstructure characterization of the 12 wt.%Cr tempered martensitic X12CrCoWVNb 11-2-2 steel. Following this goal the most advanced electron microscopy techniques as: TEM, EFTEM, EELS, EDX and EBSD, were used. Table 5.1 summarises the different used techniques for each sample condition of the X12CrCoWVNb 11-2-2 steel.

Table 5.1. Definition of the different used techniques for the microstructure characterization of the X12CrCoWVNb 11-2-2 steel variants. See definition of the acronyms technique in section 12.

Acronym	*Sample Condition*	*Used Technique*
ASH1P	as-received	› OM › TEM: EFTEM, EELS, ELNES, EDX, SAD, CBED › SEM: EBSD
ASH2T	as-received	› OM
ASH3P	as-received	› OM
TA575H1P-18726	thermally aged 575℃ 18726h	› TEM: EFTEM, EELS, ELNES, EDX, SAD, CBED › SEM: EBSD
CL575H1P-190-18726	creep load 575℃ 190MPa 18726h	
TA600H1P-4137	thermally aged 600℃ 4137h	
TA600H1P-24639	thermally aged 600℃ 24639h	› OM › TEM: EFTEM, EELS, ELNES, EDX, SAD, CBED › SEM. EBSD
CL600H1P-115-24639	creep load 600℃ 115MPa 24639h	
TA625H1P-17487	thermally aged 625℃ 17487h	› TEM: EFTEM, EELS, ELNES, EDX, SAD, CBED › SEM: EBSD
CL625H1P-85-17487	creep load 625℃ 85MPa 17487h	
TA625H1P-28983	thermally aged 625℃ 28983h	

5.1. Optical Microscopy (OM)

Via optical microscopy, the base metal microstructure of X12CrCoWVNb 11-2-2 Heat 1 to 3 in as-received condition has been studied. The samples were cut to an appropriate size and embedded on a cold-curing resin. Afterwards, the surface to be investigated was grounded with SiC paper down to grit 4000 and polished with diamond suspension using a cloth coated with 3 and 1 µm. After polishing, the samples were etched with a modified LBII etchant (colour etchant: 100 ml distilled water, 0.75 g ammonium hydrogen fluoride, 0.90 g potassium disulfide) to reveal the microstructure. The images were obtained using a Reichert MeF3 optical microscope. Complementary to this investigation also microhardness tests were performed by using a pyramid-shaped indenter made of diamond, measuring the two diagonals of the impression made by the indenter in µm in order to identify δ-ferrite phase.

5.2. Electron Microscopy Investigations

The main creep strength mechanism used in the alloy design of X12CrCoWVNb 11-2-2 steel has been the precipitation of finely distributed precipitates [45] [46] of the nanometre size. Because of that, the characterization of these phases by the used of optical microscopes is not enough, due to its spatial resolution limitations. Instead, electron microscopy investigations were performed to characterize the microstructure of the material in a micro and nano-scale. For this characterization, TEM and SEM

microscopes have been used in collaboration with the Austrian Centre for Electron Microscopy and Nanoanalysis (FELMI) at Graz University of Technology.

Out of the promising results of the X12CrCoWVNb 11-2-2 Heat 1 steel, this variant was chosen for electron microscopy investigations. A fully microstructure characterization was performed in the as-received condition (ASH1P) as well as in the different thermal aged (TA) and creep loaded (CL) specimens.

5.2.1. Sample preparation

For electron microscopy investigations, different sample preparations were used to study the different features in the microstructure.

5.2.1.1. For Transmission Electron Microscopy (TEM)

Two samples preparation for TEM investigations were used, ion milled and/or extraction replica of the gauge and grip portion of the specimens; Table 5.2 lists which sample preparation was used for each sample condition.

Table 5.2. Conditions of the sample preparation.

Acronym	***Sample condition***	***Prepared Specimen***
ASH1P	as-received	ion milled and extraction replica
TA575H1P-18726	thermally aged 575℃ 18726h	ion milled
CL575H1P-190-18726	creep load 575℃ 190MPa 18726h	extraction replica
TA600H1P-4137	thermally aged 600℃ 4137h	ion milled
TA600H1P-24639	thermally aged 600℃ 24639h	ion milled and extraction replica
CL600H1P-115-24639	creep load 600℃ 115MPa 24639h	ion milled and extraction replica
TA625H1P-17487	thermally aged 625℃ 17487h	ion milled
CL625H1P-85-17487	creep load 625℃ 85MPa 17487h	ion milled and extraction replica
TA625H1P-28983	thermally aged 625℃ 28983h	ion milled and extraction replica

<u>Ion milled sample preparation</u>

Ion milled samples were used for a quantification of the mean radius, volume fraction and number density of the different precipitate types in the material. In this case, a 3 mm disc from the base material is cut using an Ultrasonic Disc Cutter (Gatan). Afterwards, an initial thinning, between 100 µm and 300 µm thickness, in the Diamantblattsäge ISOMET 1000 (Buehler) is done. Next preparation step is a pre-polishing with 3 different suspensions, first a 6 µm diamond suspension, second with ¼ µm diamond suspension and third with Al_2O_3 suspension of 0.05 µm, on one of the sample´s sides. Mechanical dimpling is carried out in the central region from the other side of the disc, in the Dimple Grinder 656 (Gatan), to get a thickness of 10-15 µm in the central position. Final thinning of the sample until producing a hole in the middle of the specimen with argon ions, in PIPS, Model 691; 4 kV, $4x10^{-4}$ Pa is last process, see Figure 5.1.

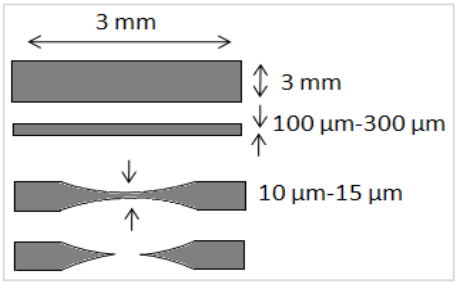

Figure 5.1. Ion milled sample preparation.

Extraction replica sample preparation

In this case, the extraction replica specimens were used for a chemical quantification of the different precipitates phases. For these samples, a disc of 3 mm diameter is cut and grinded until 30 µm thickness. Afterwards, the disc is polished with the same three suspensions as for ion milled specimens. Subsequently, the specimen is submerged into a solution (45mL Glycerine, 15mL nitric acid, 30mL HCl) for four minutes in order to remove some matrix (image 2 from Figure 5.2). Later the specimen is covered with a carbon amorphous film (160 Å thickness) and etched again in the same solution for 12 h at room temperature. Following, the specimen is cleaned with water and deposited on a copper grid.

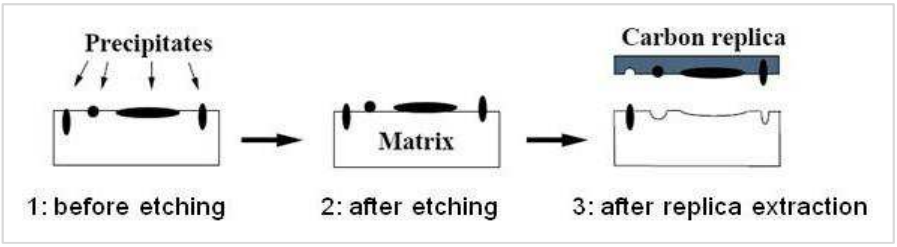

Figure 5.2. Extraction replica sample preparation description.

The advantage of using this technique compared with ion milled specimens is the better statistics in the chemical quantification of the different precipitates, due to the matrix is removed from the sample. However, as a disadvantage, some types of precipitates can dissolve with the etching. Additionally, precipitates can overlap, for example, near the grain boundaries, where there is a high-number density of precipitates, making interferences in the chemical analysis. In this case, it is necessary to evaluate positions, where this overlap is minimised.

5.2.1.2. For Electron Backscatter Diffraction (EBSD)

In order to obtain EBSD-measurements with high quality a routine, which was introduced by Katrakova and Mücklich [51], of the specimens preparation is applied. The specimens are embedded cylindrically in bakelite (Technovit 4071, diameter 2.5 cm, height 1 cm). After surface grinding and fine grinding down to a granulation of 7 µm, the specimen surface is polished in three steps with a diamond paste of 6 µm, 1 µm and 0.25 µm granulation a few minutes each. The final polishing step is carried out on a MiniMet® polisher (Buehler LTD.) with an alkaline colloidal silica solution (0.04 µm granulation) for 2 h. The surface of the encapsulant is covered with a conductive silver layer, and the specimen itself is conducted with a carbon strip to avoid charging during the long analysis time.

5.2.2. Transmission Electron Microscopy: online and offline methods

Electron microscopy measurements were performed using a Philips CM20/Scaning TEM (STEM) equipped with a Gatan imaging filter (GIF). The microscope was operated at 200 kV with a LaB_6 cathode. The spectra were recorded in image mode, to minimise sample contamination, with the slow scan CCD camera integrated in the GIF at dispersion of 1 eV/channel and an energy resolution of about 1.5 eV. All images and spectra were processed with Gatan's Digital Micrograph, and were corrected for dark current and gain variations. A good compromise in terms of signal to noise ratio was found by using a 200 µm condenser aperture (beam convergence angle α = 6.4 mrad) and a 40 µm objective aperture (acceptance half angle β = 7.6 mrad). Unfiltered and filtered (zero loss) images were recorded, in order to obtain thickness maps of the different studied positions of the ion milled and extraction replicas specimens.

5.2.2.1. EFTEM, EELS, EDX and image analysis

Energy filtered transmission electron microscopy (EFTEM) was performed in order to image the precipitates either on replicas or within thin foils. The elemental (three-window method) and ratio (two-window method) maps for B-K, C-K, N-K, V-L23, Cr-L23, Fe-L23, Nb-M45, Mo-M45 and W-O23 were recorded with the intention to evaluate the different precipitates phases present at the studied position. The energy windows, which were used, are presented in Table 5.3.

Table 5.3. Energy windows for the different analyzed elements in EFTEM.

Z	*Element*	*Edge*	*E [eV]*	*Post edge [eV]*	*Pre edge 1 [eV]*	*Pre edge 2 [eV]*	*Slit width*	*Acquisition times[s]*
5	**B**	K	188.0	4	12	5	8	3-5
6	**C**	K	283.8	8	26	10	16	5
7	**N**	K	401.6	10	32	12	20	30
23	**V**	L2,3	513.0	5	15	5	10	30
24	**Cr**	L2,3	574.0	5	15	5	10	30
26	**Fe**	M2,3	54.0	5	9	4	5	1
41	**Nb**	M4,5	204.6	50	5		10	3-10
42	**Mo**	M4,5	227.0	166	3		6	5-10
74	**W**	O2,3	36.0	5	3		4	1

For the chemical analysis of precipitates, EELS and EDX spectra were analysed. For the chemical quantification of the EELS spectra, core-loss analysis of the elemental edges from the EELS spectra Nb-M45, C-K, N-K, V-L23, O-K, Cr-L23 and Fe-L23 were used. To reduce the effect of multiple scattering, the spectra were acquired only from very thin particles, which were then analysed with the log-ratio technique [52]. The thicknesses were in the range 0.2–0.5 times the inelastic mean free path. Using MLS fit method [28] the chemical composition of the different nitrides was quantified out of the EEL spectra. Additionaly, EDX spectra were recorded in STEM mode, with a probe diameter of about 7 nm, using a Noran HPGe detector with an ultra thin window. However, using EELS technique, light elements could be detected and quantified more accurately than with EDX.

EDX spectra have been chemical quantified by using standard background modelling and peak area integration. However, for conversion into concentrations, experimental sensitivity factors, measured relative to silicon, were used [53]. With EDX only the metal content of the phase is quantified and considering stoichiometric phases the chemical composition of the precipitate is calculated.

Difficulties on the differenciation of nitrides, mod. Z-phase, M_2X and MX phases were found due to similarities in their chemical compositions and diffraction measurements were needed, see Table 5.4. SAD (Selected Aperture Diffraction) and CBED (Convergent Beam Electron Diffraction) techniques were used for the identification of the crystal structure of the nitrides: mod. Z-phase, M_2X and MX. However, diffraction measurements are time consuming measurements making their use for analysing each single precipitate, impossible. Because of that, ELNES technique (see description of this technique on section 3.4.2 of the literature review) was used to characterize the different precipitate types. The energy-loss near edge structure (ELNES) of the nitrogen ionisation K edge was used to identify the different type of nitride particles [54].

Table 5.4 summarizes the different crystallographic structures of the different nitrides as well as the mean containing chemical elements. In Figure 5.3 is shown the EEL spectra from the MX, M_2X and mod. Z-phase where it is possible to observe the different vanadium contents between these three particles. In addition, the fine structure of the nitrogen peak reveals some differences. The fine structure of the nitrogen peak is related with the hybridization of the different atom's orbital. The first peak of the nitrogen, corresponds to the hybridization of the 3d orbital from the metal (e.g. Cr, Fe) with 2p of the non metal (e.g. N, C). The second peak corresponds to the hybridization of the 4s and 4p orbital from the metal with 2p of the non metal. Finally, the third peak of the nitrogen corresponds to the hybridization of the 2p and 3d orbital from the metal with the 1s of the non metal. Therefore, the fine structure of the nitrogen peak is related with the crystal structure of the different phases.

Table 5.4. Comparison of the crystal structure and composition of MX, M_2X and mod. Z-phase precipitates.

Precipitate	Structure	Parameter [Å]	Composition
M_2X	Hexagonal	a, b = 4.760 c = 4.444	$(Cr,V)_2N$
MX	FCC	a, b, c = 4.139	(V,Nb)(N,C)
Mod. Z-phase	Tetragonal	a, b = 2.86; c = 7.39	(Cr,V,Nb)(N)

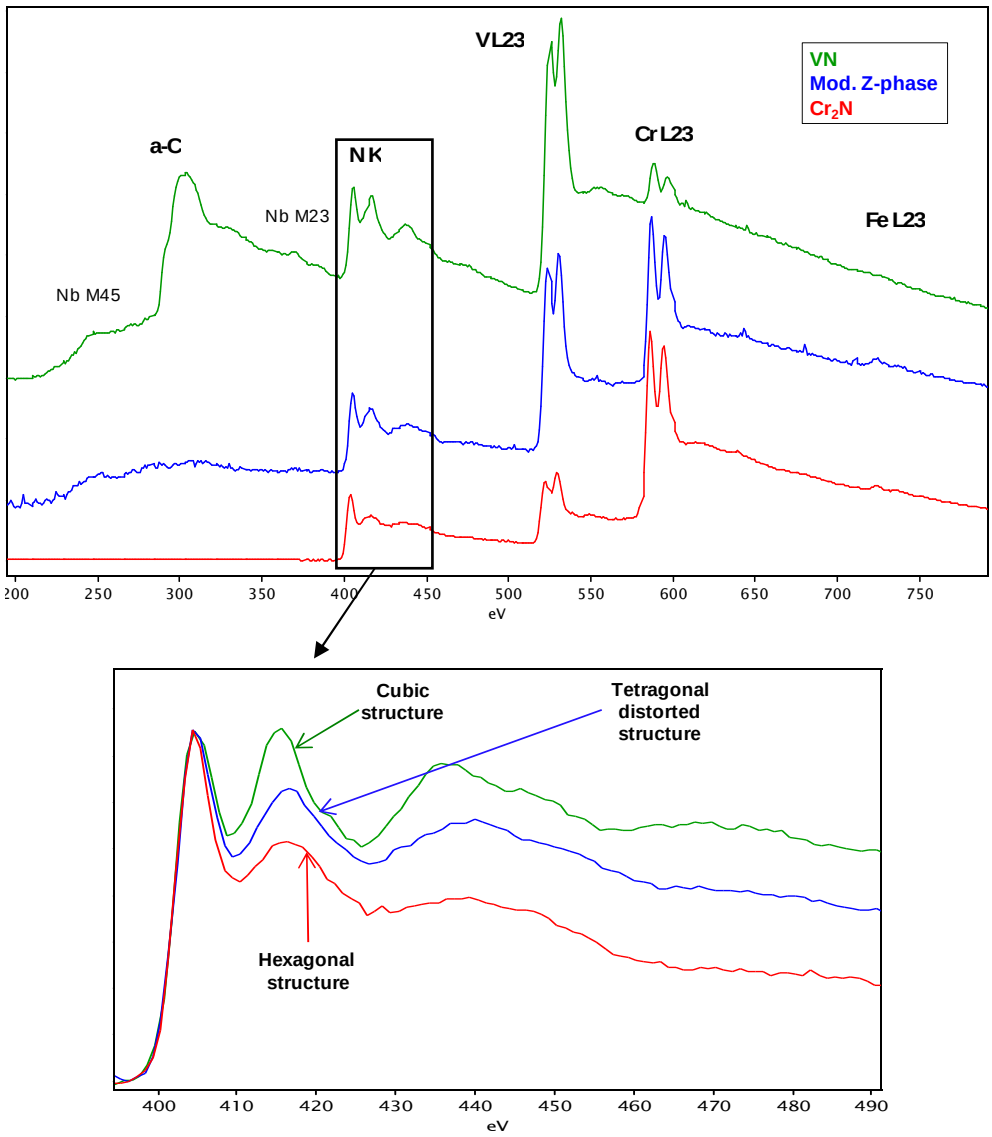

Figure 5.3. ELNES fine structure of nitrogen for three different precipitates: MX, M_2X and mod. Z-phase.

5.2.2.2. Precipitates Quantification

The ion milled specimens were used for quantitative analysis of precipitate parameters such as: mean diameter, number density and volume fraction. Because these parameters cannot be directly observed on the specimens, stereological methods were used. New advanced correction methods of the existing methods from Cahn and Nutting [55] and Hättestrand and Andren [56] have been published by Sonderegger in [57]. The mean diameter, the number density and the volume fraction were calculated using the mention method and the used equations are presented in Table 5.5.

Table 5.5. Equations for calculating the volume fraction of the precipitates, the mean diameter and the number density [57].

Mean diameter: $\bar{d} = \frac{\sum d_i \ w_{sample,i}}{\sum_i w_{sample,i}} = \frac{\sum_i d_i \left[\frac{t_i}{t_i + d_i}\right]}{\sum_i \left[\frac{t_i}{t_i + d_i}\right]}$

Volume fraction: $f_V = \frac{V_V}{V_{sample}} = \frac{1}{A_{sample}} \sum_i A_i \left(\frac{\frac{2d_{m,i}}{t_i}}{\frac{2d_{m,i}}{t_i} + 3} \right)$

Number density: $N_V = \frac{1}{A_{sample}} \sum_{i=1..N_A} \left(\frac{1}{t_i + d_{m,i}} \right)$

$\bar{d}$=diameter
d_m= mean measured diameter of all precipitates
$d_{m,i}$= mean measured diameter of precipitate i
A_i= projected area of precipitate i in the micrographs
t_i= sample thickness at position of precipitate i.
V_V= volume of the precipitates

EFTEM images were used for the calculation of these parameters. The precipitates were visualized by producing the chromium and vanadium elemental distributions micrographs. Using Digital Micrograph software the area of the different precipitates was measured and the precipitate size, phase fraction and number density were calculated via the previous formulas. For the analysis, also the thickness of the analysed position were considered and calculated. The relative thickness maps were produced from an unfiltered image and a zero-loss image of each studied position.

5.2.3. Scanning Electron Microscopy: Electron Backscatter Diffraction (EBSD)

With EBSD technique, it was possible to determine the positions and size of the martensite lath boundaries, subgrain boundaries and prior austenite grain boundaries.

All measurements were performed on a Zeiss DSM 982 Gemini equipped with an EBSD-system from EDAX-TSL. The microscope was operated with an accelerating voltage of E0 = 20 keV and a specimen current of Isp = 2.8 nA. Three magnifications were chosen for the investigation of each sample: 500 (step size: 0.6 µm), 2000 (step size: 0.15 µm) and 10000 (step size: 0.04 µm). The used step size permitted a resolution, which was high enough to resolve single martensite laths, and low enough to receive proper statistic by covering a high number of laths in one investigation field. To make sure no misinterpreted pixels were considered in the examinations, only subgrains and laths greater than the area of 5 Pixels were counted. Because of the higher number of pixel-neighbour pairs (6 instead of 4), hexagonal rastering was chosen in order to get a higher counting rate for misorientations and therefore, better statistical significance. EBSD patterns were generated within a small interaction volume located at the surface of a sample with a penetration depth typically less than 50-100nm.

For finding and analysing grain boundaries, the misorientation (Rodriguez Angle) between two neighbouring measurement points is calculated [15]. Angles below 1.5° are below the detection limit of the microscope and cannot be characterized. Small misorientations (1.5-20°) are characteristic for subgrain boundaries, large misorientations (>50°) for martensite laths [15] [58] [59]. Misorientations between 20 to 50° are normally attributed to prior austenite grain boundaries [15]. When the analysis of the EBSD images is finished an image showing the corresponding boundaries is created.

6. Experimental Results

The results obtained out of the experimental investigations performed in X12CrCoWVNb 11-2-2 steel are presented in this chapter. This section has been divided into 3 main points: optical light microscopy investigations, transmission electron microscopy investigations and scanning electron microscopy investigations.

6.1. Optical Microscopy

Optical micrographs of the as-received condition from Heat 1, Heat 2 and Heat 3 were studied. The samples were removed from the material supplied, see Figure 4.1 and prepared as defined in section 5.1.

All heats feature martensite lath structure with precipitates at the prior austenite grain boundaries and martensite laths. Differences were found regarding the amount of delta ferrite (δ-ferrite). No delta ferrite was observed in Heat 1 (see Figure 6.1). Microhardness measurements approved the interpretation as tempered martensite, according to the applied heat treatment of the sample. The tempered martensite showed microhardness between 288 and 346 HV0.010. Heat 2 (see Figure 6.2) showed some marginal amount of delta ferrite, unfeasible for quantitative examinations (below 0.5 %). The tempered martensite showed microhardness between 276 and 297 HV0.010, lower than in material Heat 1. For Heat 3 (see Figure 6.3), it was clearly possible to observe delta ferrite. The tempered martensite showed microhardness between 312 and 329 HV0.010. Via image analysis, an amount of 1-2.5 % of delta-ferrite was quantified in this Heat. The delta ferrite showed microhardness between 211 and 249 HV0.010. All microhardness measurements are presented in Figure 6.4.

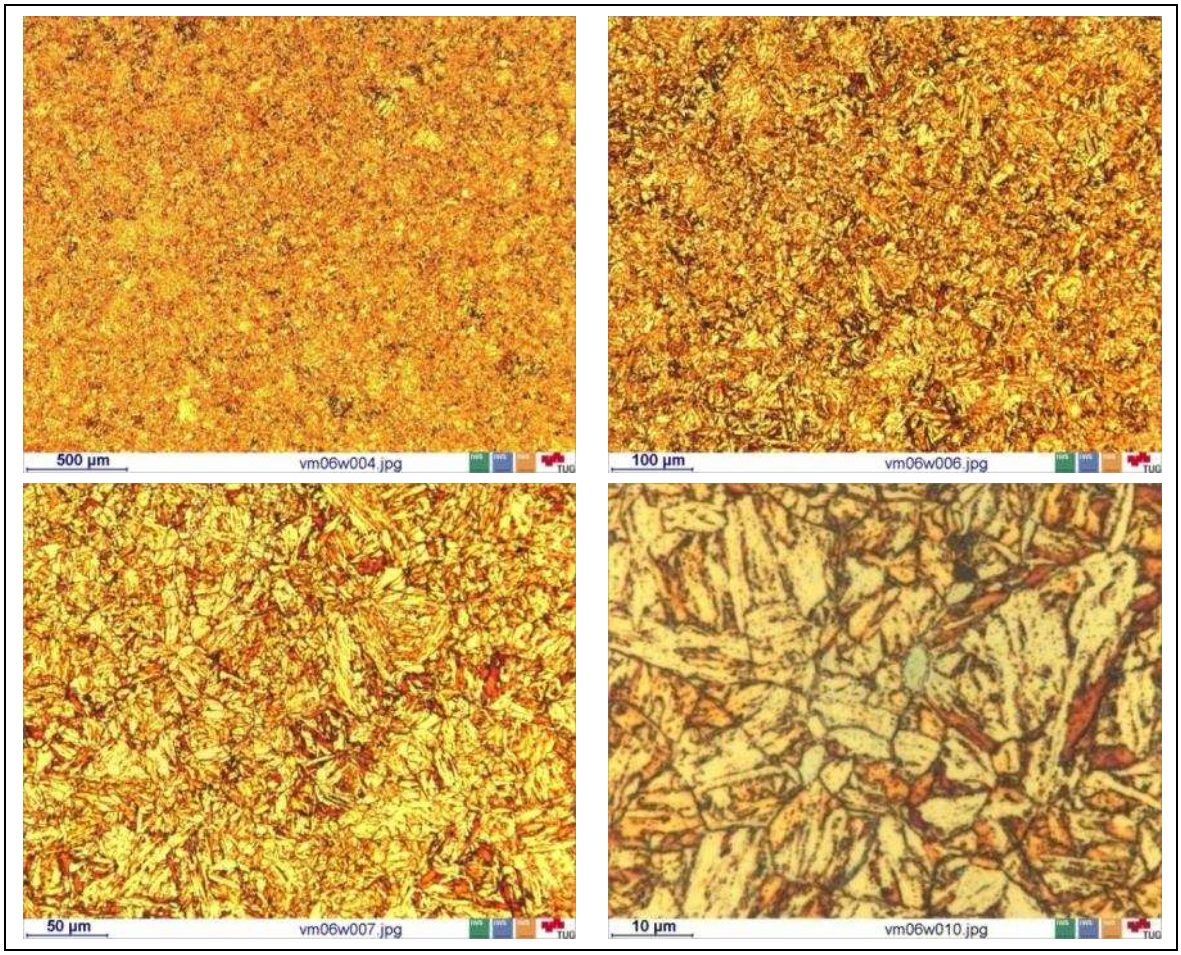

Figure 6.1. X12CrCoWVNb 11-2-2 ASH1P optical micrographs.

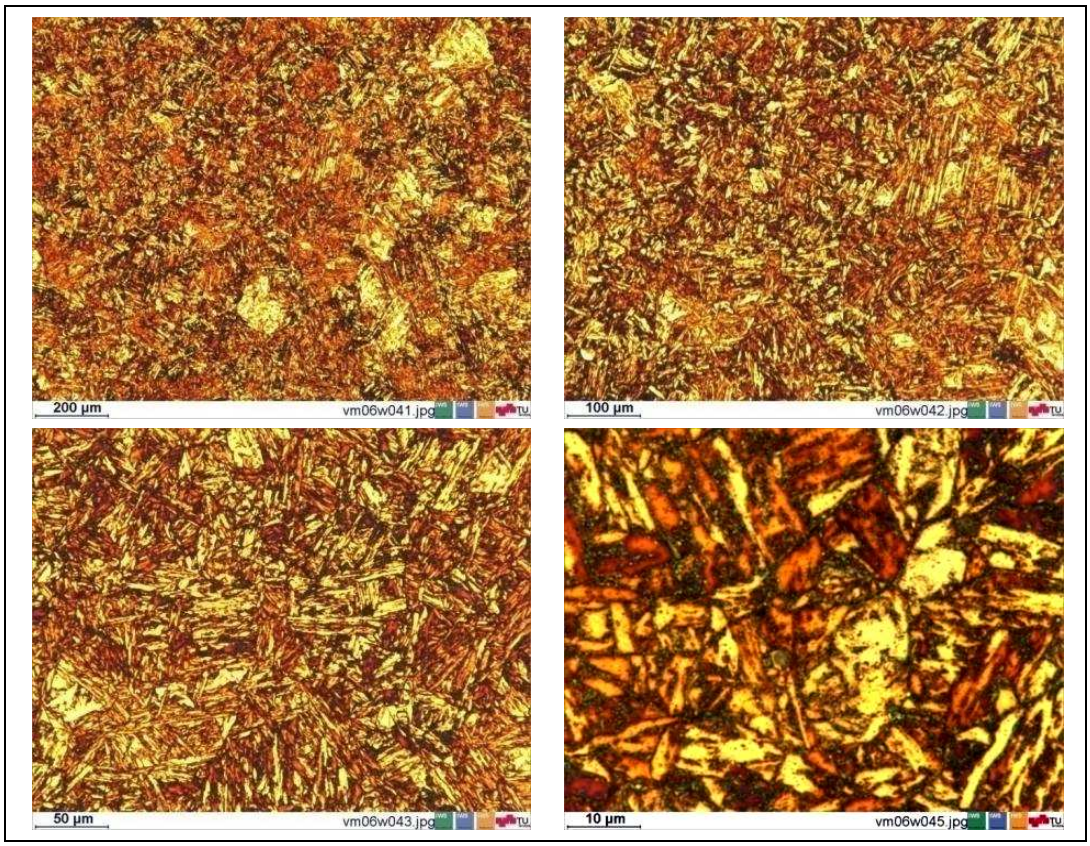

Figure 6.2. X12CrCoWVNb 11-2-2 ASH2T optical micrographs.

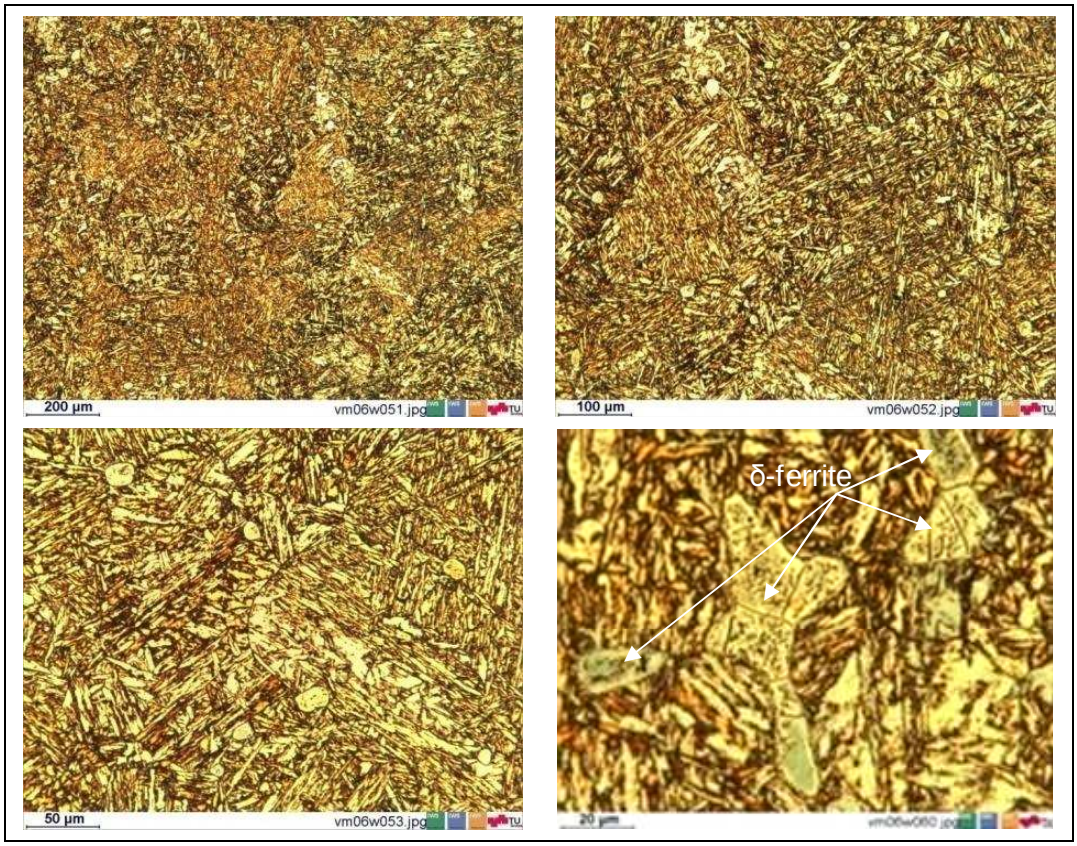

Figure 6.3. X12CrCoWVNb 11-2-2 ASH3P optical micrographs.

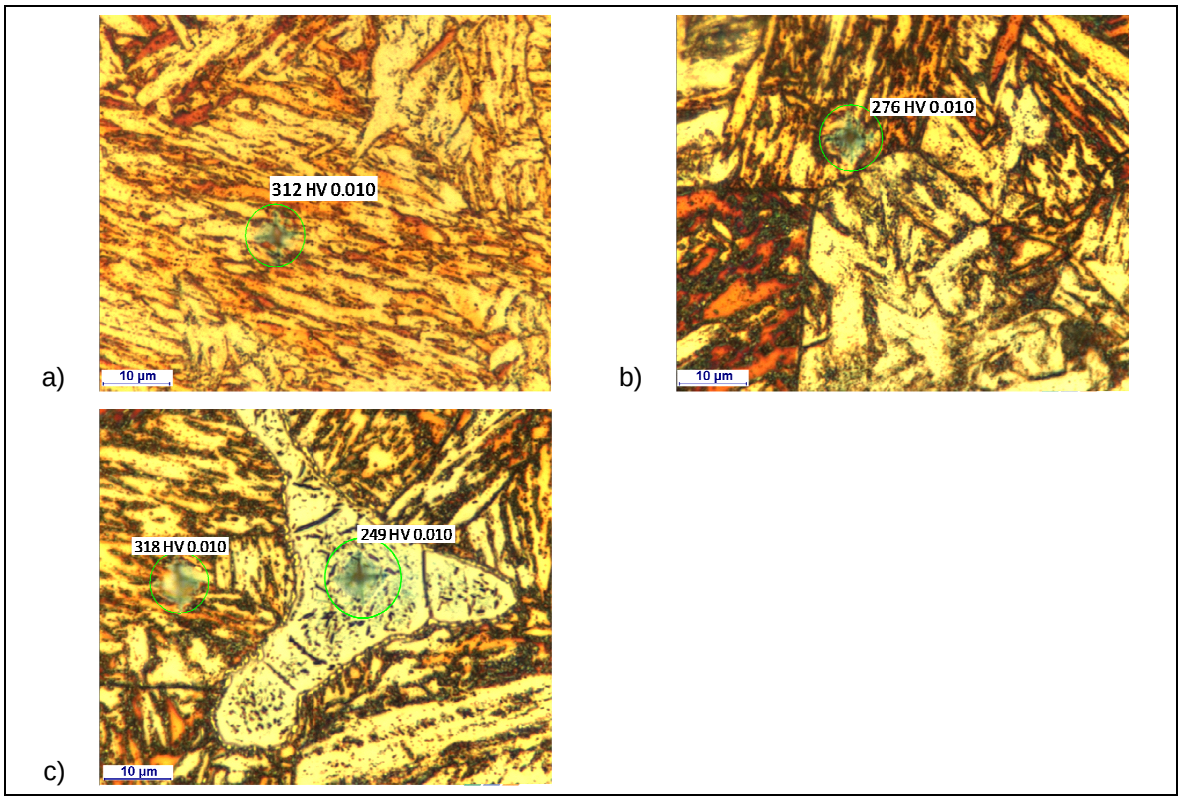

Figure 6.4. X12CrCoWVNb 11-2-2 microhardness measurements for a) ASH1P, b) ASH2T and c) ASH3P.

After thermally ageing and creep loading at 600℃ the microstructure of the X12CrCoWVNb 11-2-2 Heat 1 steel Heat 1 shows any significant difference using this technique, see Figure 6.5.

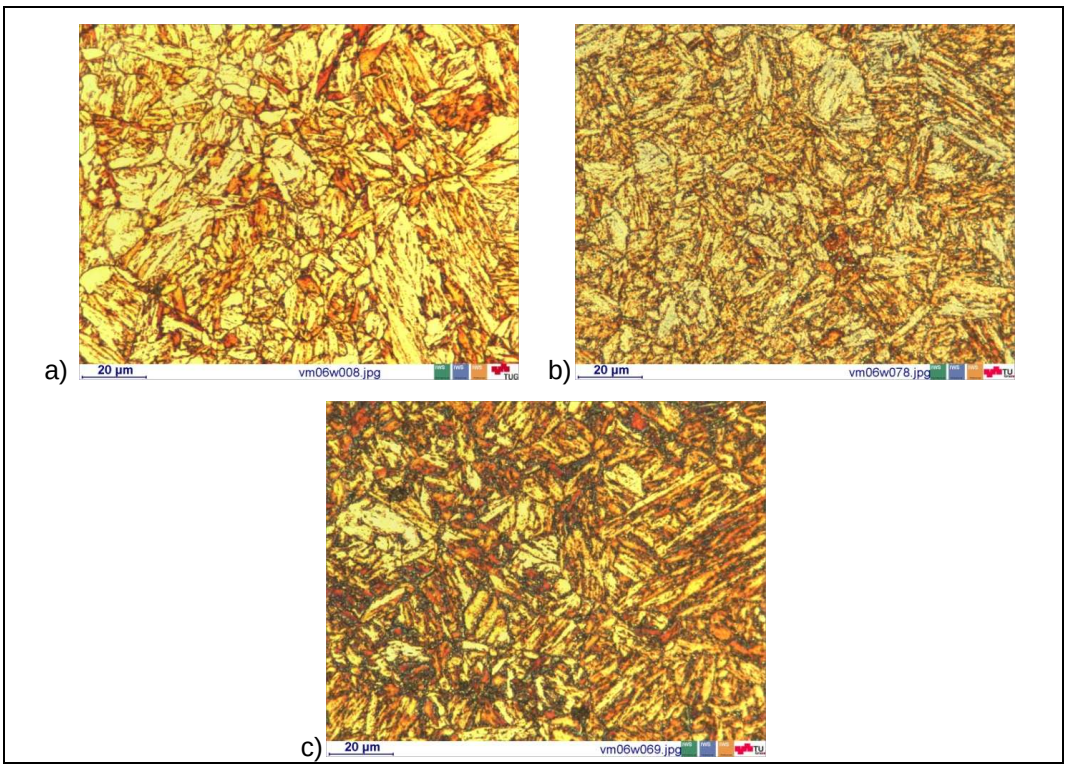

Figure 6.5. X12CrCoWVNb 11-2-2 Heat 1 optical micrographs: a) ASH1P, b) TA600H1P-24639 and c) CL600H1P-115-24639.

6.2. Transmission Electron Microscopy

TEM investigations have been employed, in order to improve the resolution limits, and thus, to work in nanometre scale. The different characterization techniques that have been used, have been already defined in previous sections, and within this section the results of the X12CrCoWVNb 11-2-2 Heat 1 steel in as-received condition as well as the different creep exposure specimens via TEM are presented.

When working with TEM two different sample preparations have been used for the chemical quantification on one side, and for the precipitate quantification on the other side. In Table 5.2 is summarized the specimens that have been characterized, their acronyms as well as the used sample condition (ion milled and/or extraction replica) for the analysis.

6.2.1. Qualitative description of the microstructure

At this section, a qualitative evaluation of the different precipitates phases evaluated in the different studied specimens is presented. Moreover, Table 6.1 summarizes the different precipitates phases of material X12CrCoWVNb 11-2-2 Heat 1 that have been identified in each sample condition out of the microstructure characterization. This table summarises the results of the TEM, EFTEM, EELS, ELNES, SAD, CBED and scatter diagrams measurements performed at each sample condition for the identification of each precipitate type.

Table 6.1. Different precipitates populations identified in X12CrCoWVNb 11-2-2 Heat 1 variant in all the investigated specimens.

Sample condition	*Acronym*	*Prepared Specimen*	*$M_{23}C_6$*	*NbC*	*VN*	*Cr_2N*	*BN*	*Mod. Z-phase*	*Laves Phase*
as-received	ASH1P	ion milled and extraction replica	X	X	X	X	X*	-	-
thermally aged 575℃ 18726h	TA575H1P-190-18726	ion milled	X	X	X	X	-	X	X
creep load 575℃ 190MPa 18726h	CL575H1P-190-18726	extraction replica	X	X	X	X	-	X	X
thermally aged 600℃ 4137h	TA600H1P-175-4137	ion milled	X	X	X	X	-	-	X
thermally aged 600℃ 24639h	TA600H1P-115-24639	ion milled and extraction replica	X	X	X	X	-	X	X
creep load 600℃ 115MPa 24639h	CL600H1P-115-24639	ion milled and extraction replica	X	X	X	X	-	X	X
thermally aged 625℃ 17487h	TA625H1P-85-17487	ion milled	X	X	X	X	-	X	X
creep load 625℃ 85MPa 17487h	CL625H1P-85-17487	ion milled and extraction replica	X	X	X	X	-	X	X
thermally aged 625℃ 28983h	TA625H1P-70-28983	ion milled and extraction replica	X	X	X	X	-	X	X

*Only detected in extraction replica specimens.

In as-received condition (ASH1P), after austenitization (1060℃, 30 min) and tempering (780℃, 2 h) **,** mainly three types of precipitates were identified in the ion milled specimen: chromium carbides ($M_{23}C_6$), vanadium nitrides (VN) and chromium nitrides (Cr_2N). In addition, in the carbon extraction replica specimens, BN and NbC were found.

$M_{23}C_6$ precipitate mostly at the prior austenite grain boundaries, martensite lath boundaries and subgrain boundaries. MX (VN) particles precipitate at the grain boundaries, subgrain boundaries and in the grain interior and M_2X (Cr_2N) particles were found mainly at the prior austenite grain boundaries, martensite lath boundaries and subgrain boundaries, but also inside the grains. Very small amount of NbC or BN were found, and they could be indentified only in the extraction replica specimens. The most likely reason for that finding was a low-number density of these phases. Figure 6.6 shows the most representative features.

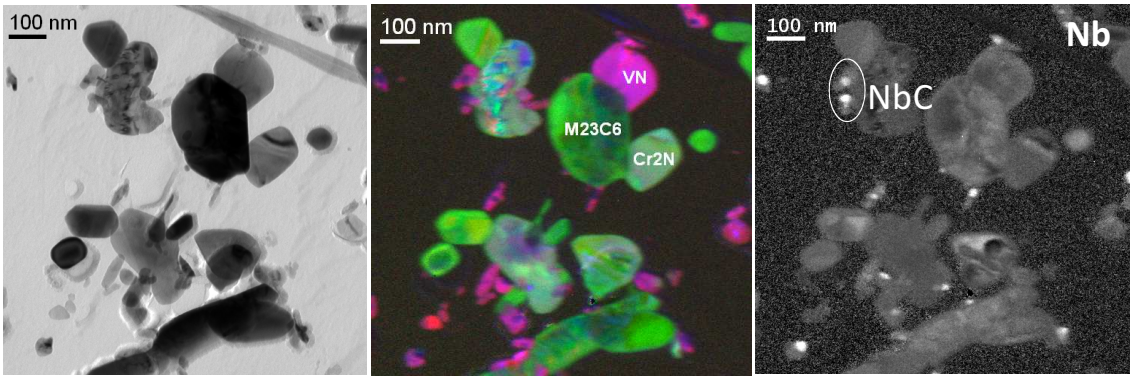

Figure 6.6. X12CrCoWVNb 11-2-2 ASH1P: TEM images for the as-received extraction replica specimen. Images from the zero loss peak (ZLP) (left image), RGB image (central image) representing Red: vanadium, Green: chromium, Blue: nitrogen and niobium ratio map (right image). M_2X (Cr_2N) particles, MX (VN), $M_{23}C_6$ and NbC were identified.

Diffraction patterns from the different particles were analysed to study the crystal structure of each phase via SAD and CBED in the extraction replica specimens. Chromium rich carbides showed a cubic crystal structure with a lattice parameter of 10.6 Å and were identified as $M_{23}C_6$. Vanadium rich particles showed a fcc crystal structure with a lattice parameter of 4.139 Å and were identified as VN (MX) particles with low-niobium content. Chromium and vanadium rich phases, identified as Cr_2N (M_2X), showed a hexagonal crystal structure with 4.760 and 4.444 Å lattice parameter, no diffraction measurements were performed for NbC phase. Together with the diffraction patterns, also EDX and EELS spectra were evaluated. The spectra and diffraction patterns are presented in Figure 6.7.

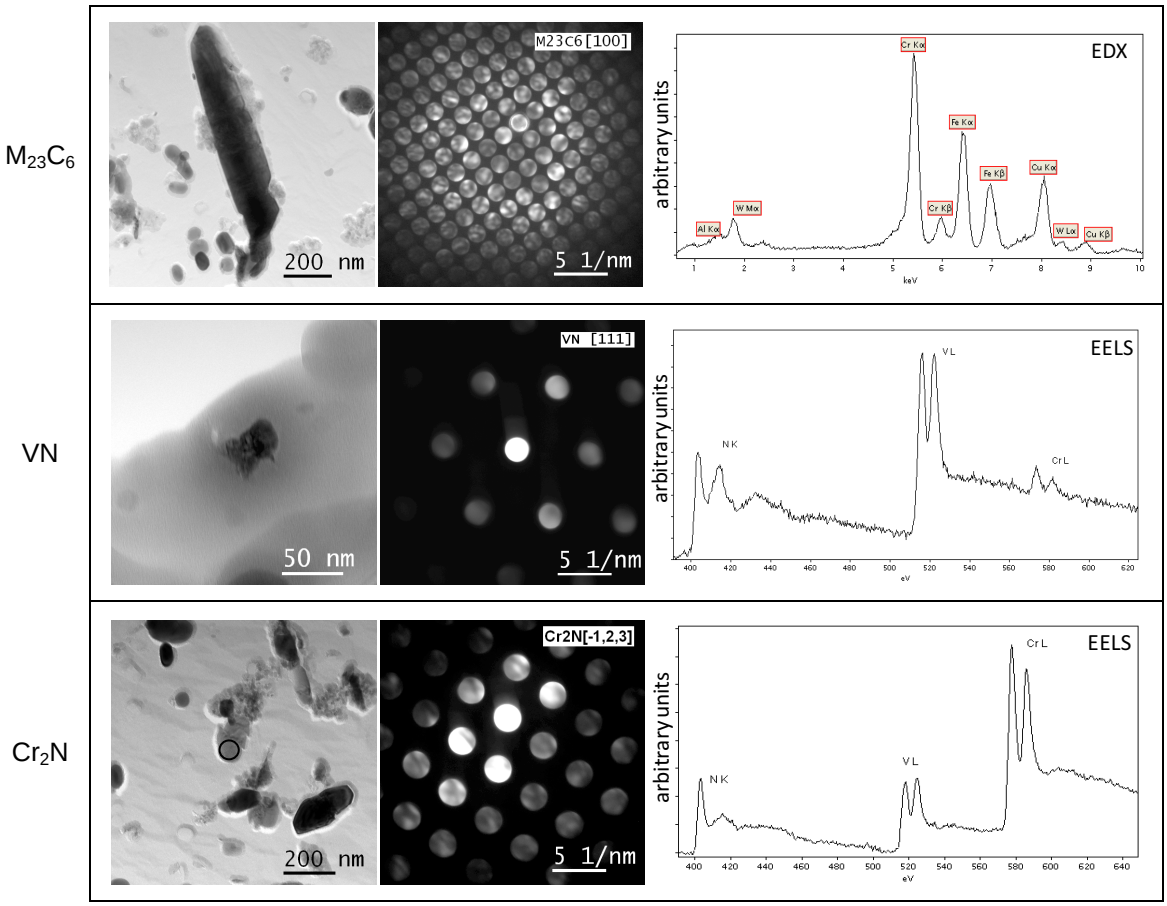

Figure 6.7. X12CrCoWVNb 11-2-2 ASH1P: ZLP image, diffraction pattern and EELS or EDX spectrum of $M_{23}C_6$, VN and Cr_2N in the as-received specimen. The measurements were performed in the extraction replica specimens to avoid matrix interferences.

Boron nitrides precipitates were also identified. They were showing different sizes, from some nanometres (50-100 nm) up to some micrometres (around 5 µm). Figure 6.8 shows the RGB image of V-Cr-Nb elements, where a BN precipitate was identified. The EEL peak fine structure of the precipitate was compared with references from the literature to study the crystal structure of the phase. The analysis revealed a characteristic hexagonal crystal structure for BN phase.

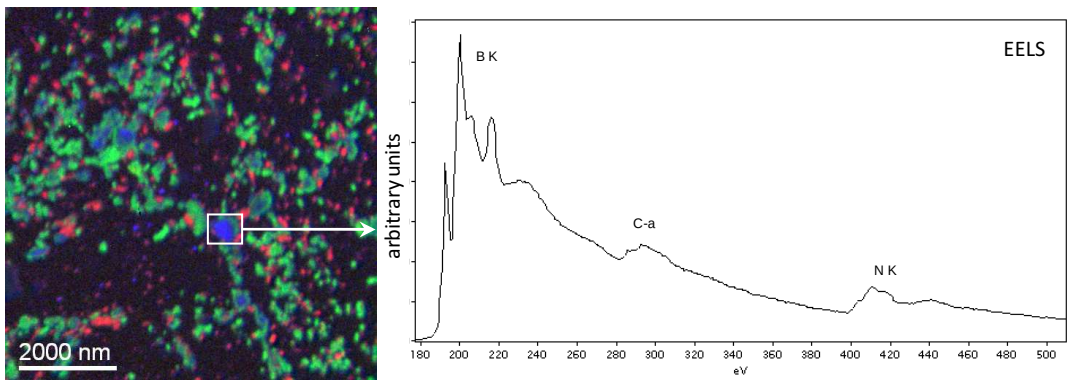

Figure 6.8. X12CrCoWVNb 11-2-2 ASH1P: BN particle RGB (Red: vanadium, Green: chromium and Blue: niobium) map (left) of the as-received specimen. EEL fine structure spectra (right) of the indicated typical for a hexagonal crystal structure.

After a full characterization of the as-received specimen, the different thermally aged and creep loaded specimens were studied.

The specimen TA575H1P-18726 was prepared as ion milled sample. A total of 10 different random positions were evaluated. $M_{23}C_6$, MX (VN and NbC), M_2X (Cr_2N) and Laves phase were identified in this sample. A low number density of mod. Z-phase was detected. Presumably, the temperature of 575°C, was too low for the formation of a high amount of mod. Z-phase. Figure 6.9 presents the zero loss image (ZLP) as well as the Fe, Cr, V, C and N ratio maps. BN precipitates were not found in this sample condition.

The creep loaded CL575H1P-190-18726 specimen was studied via extraction replica. A total number of 12 positions were evaluated. Carbides ($M_{23}C_6$), nitrides (VN and Cr_2N) and NbC were identified. Laves phase was found too, as well as a low number of mod. Z-phase precipitates. On the other hand, BN phase was not found in this sample condition. $M_{23}C_6$ and Laves phase mainly precipitated at the boundaries (prior austenite, subgrain and martensite laths boundaries). VN generally precipitated finely distributed in the matrix. Cr_2N precipitated mainly at the prior austenite grain boundaries, martensite lath boundaries and subgrain boundaries but also inside laths and subgrains, as in the as-received condition, see Figure 6.10 and Figure 6.11.

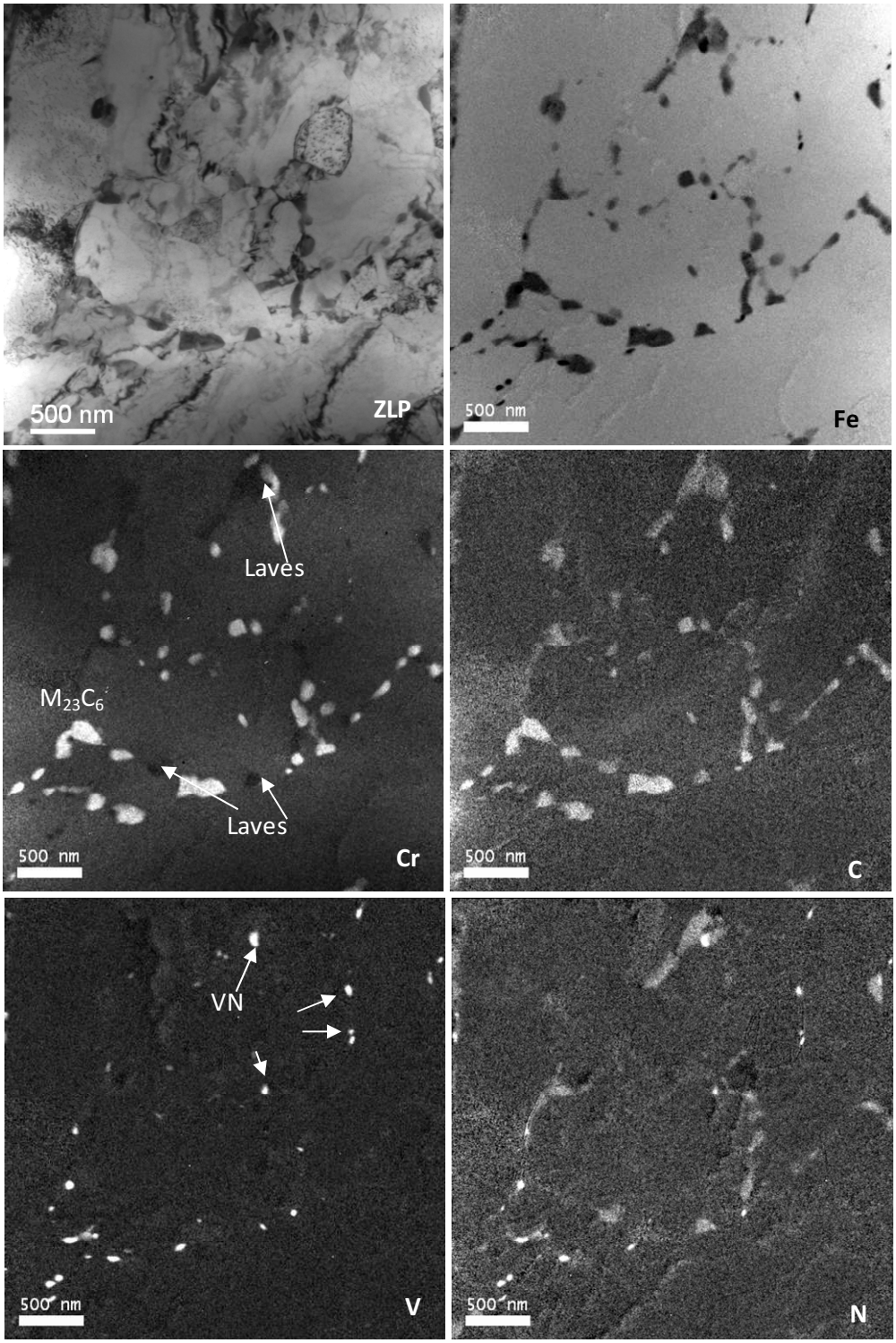

Figure 6.9. X12CrCoWVNb 11-2-2 TA575H1P-18726: EFTEM maps of Fe, Cr, V, C and N from the ion milled specimen. Dark precipitates in the Cr map were identified as Laves phase. Due to an energy overlap between the W, Mo and N some bright signal of the Laves phase precipitates can be observed in the N map. The bright precipitates from the Cr maps were identified as $M_{23}C_6$. The bright precipitates from the V ratio map were identified as VN.

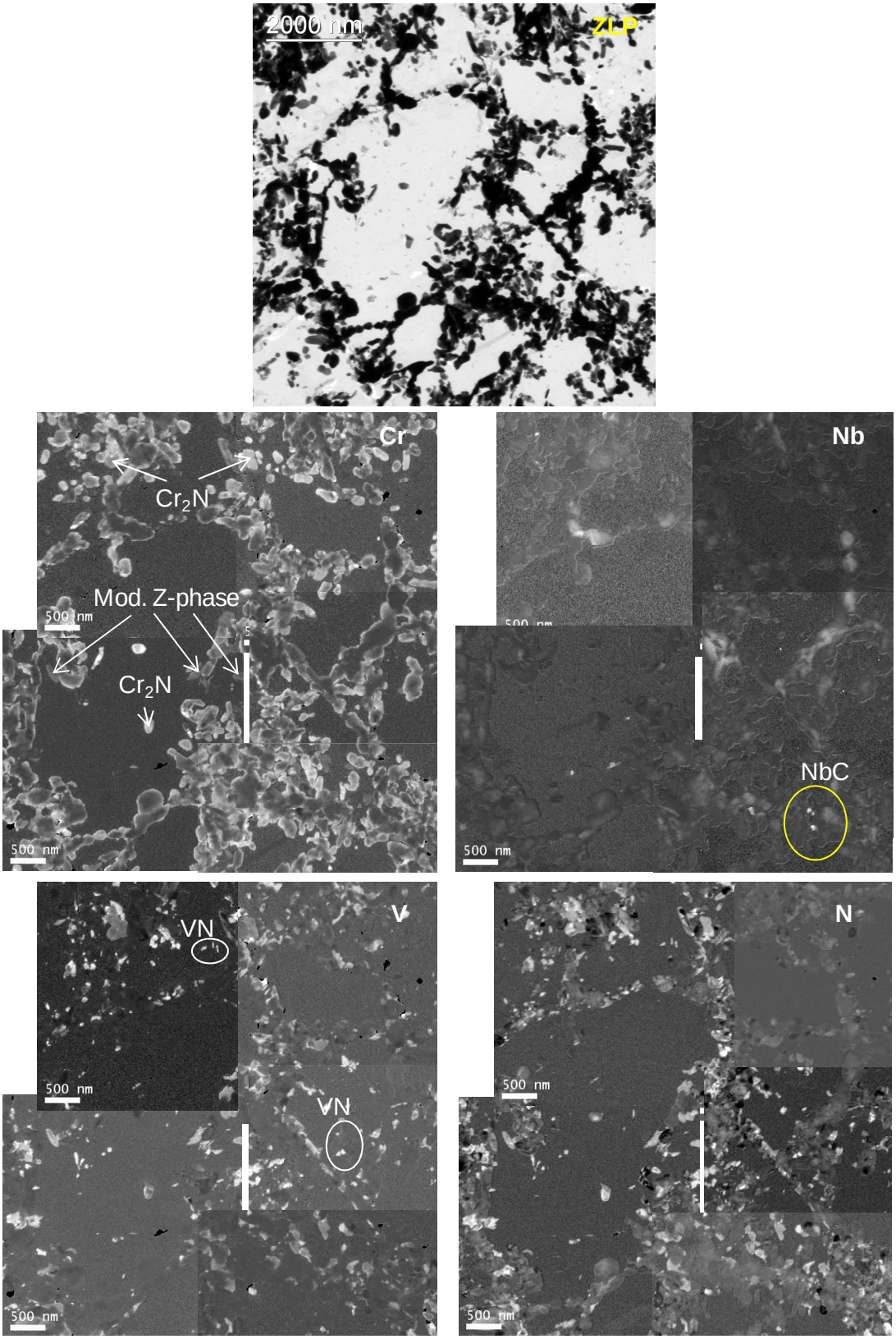

Figure 6.10. X12CrCoWVNb 11-2-2 CL575H1P-190-18726: ZLP image and EFTEM maps of Cr, Nb, V and N from the extraction replica specimen.

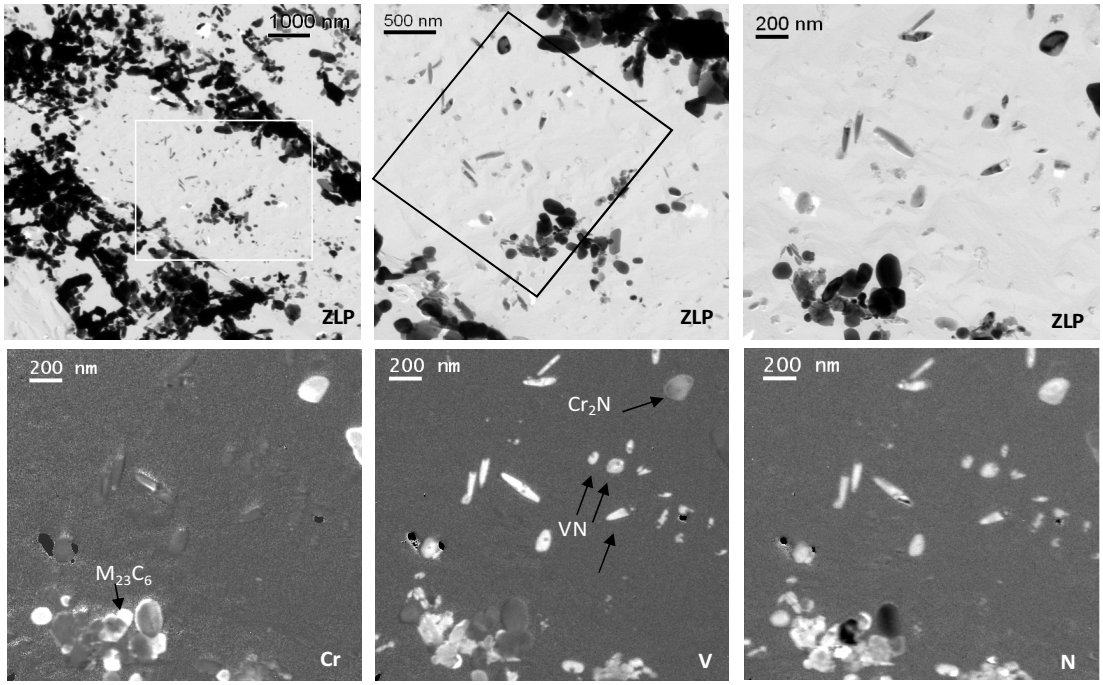

Figure 6.11. X12CrCoWVNb 11-2-2 CL575H1P-190-18726: ZLP images at different magnifications and EFTEM maps of Cr, V and N from the ion milled specimen. The bright precipitates from the Cr maps were identified as $M_{23}C_6$. The bright precipitates from the V ratio map were identified as VN. The bright precipitates from the Cr and V ratio maps are identified as Cr_2N.

Two specimens creep exposed at 600℃ were studied: The first one TA600H1P-4137 and the second one TA600H1P-24639. Some differences regarding the phase fraction of the different precipitates were found between the two specimens, as well as in the phases that were identified. In the material tested after 4137 h (TA600H1P-4137), $M_{23}C_6$, MX (VN and NbC), M_2X (Cr_2N) and Laves phase were characterized and no mod. Z-phase or BN were found, see Figure 6.12. While, in the specimen tested for longer times (TA600H1P-24639) a higher number of mod. Z-phase was found. Figure 6.13 and Figure 6.14 show different images of the studied material, the phases were indentified via EDX and EELS and the chemical composition is presented in the next section. Electron diffraction from the mod. Z-phase was evaluated, in order to avoid possible misinterpretations with M_2X (Cr_2N) phase, see Figure 6.15. The creep loaded CL600H1P-115-24639 sample (see Figure 6.16) showed the same phases as in the thermally aged condition (TA600H1P-24639): $M_{23}C_6$, MX (VN and NbC), M_2X (Cr_2N), Laves phase and mod. Z-phase were precipitated. No presence of BN precipitates was found, at any of the specimens tested at 600℃.

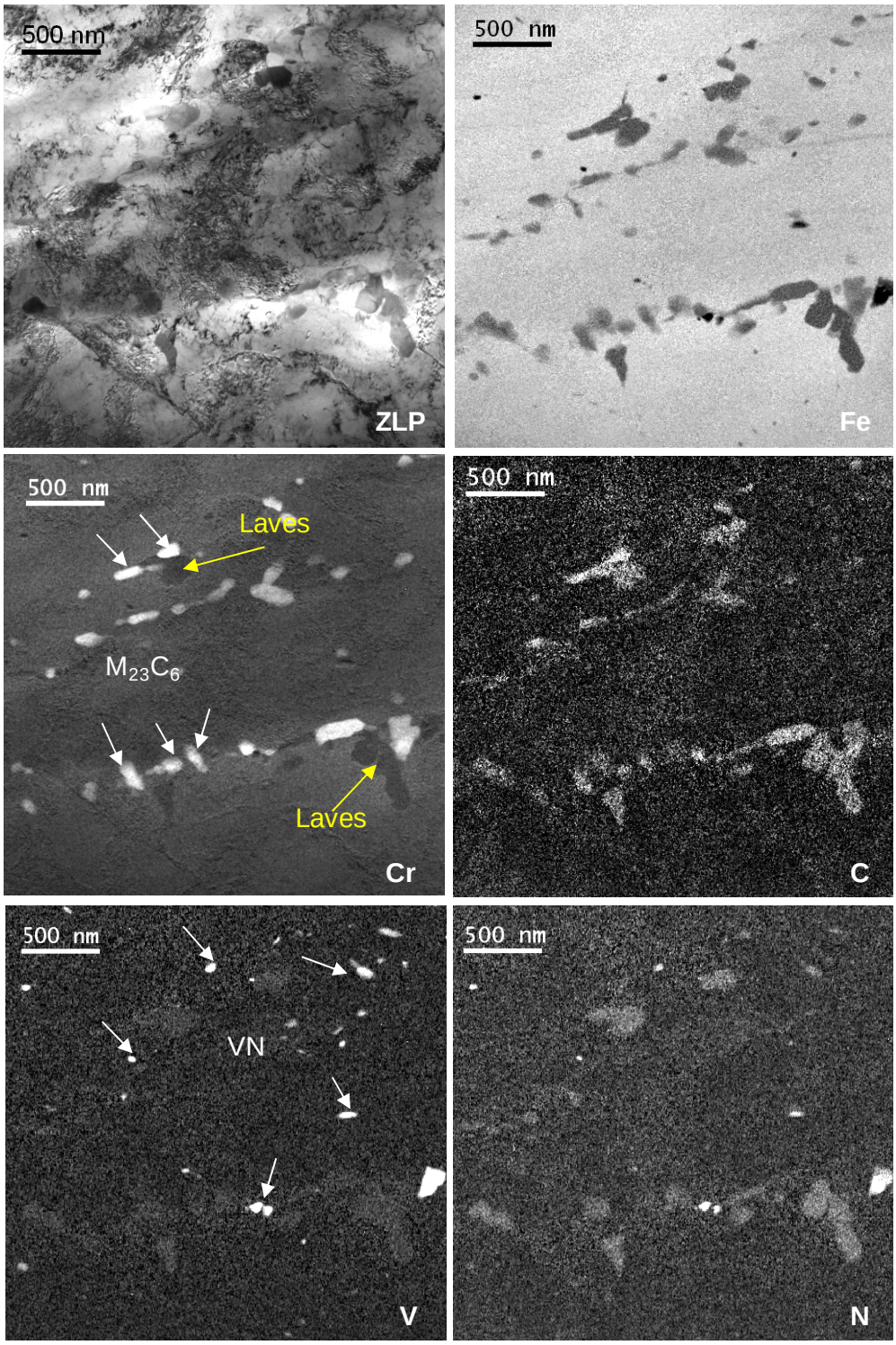

Figure 6.12. X12CrCoWVNb 11-2-2 TA600H1P-4137: ZLP image and EFTEM maps of Fe, Cr, C, V and N from the ion milled specimen. The bright precipitates from the Cr maps were identified as $M_{23}C_6$. The bright precipitates from the V ratio map were identified as VN.

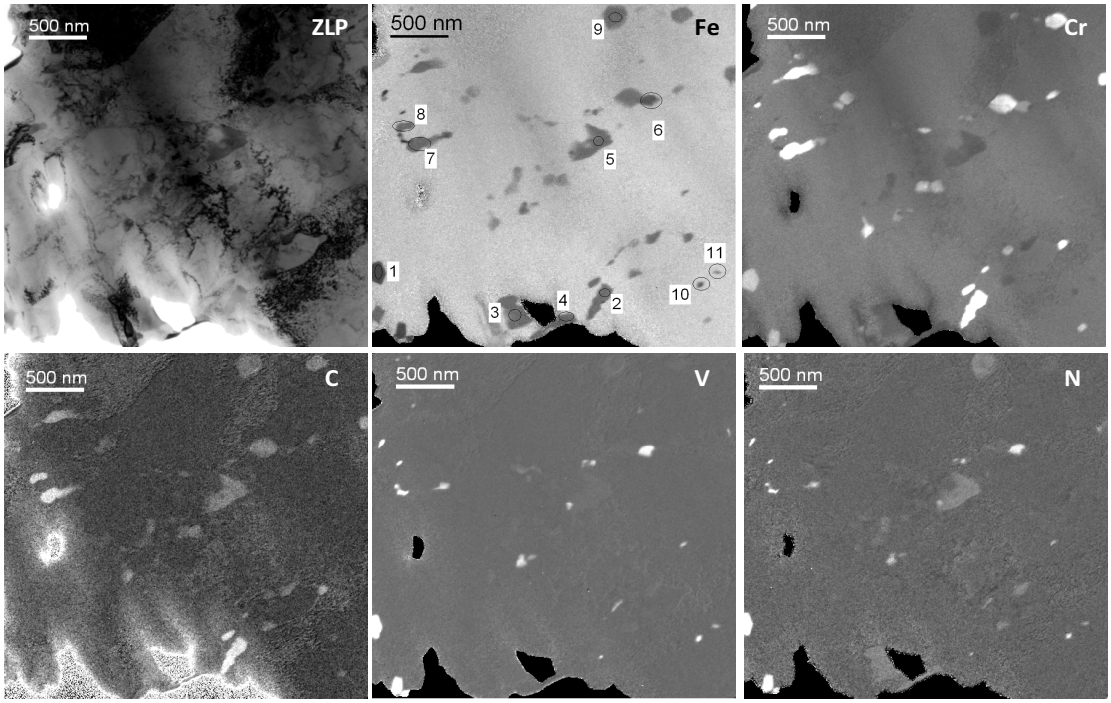

Figure 6.13. X12CrCoWVNb 11-2-2 TA600H1P-24639: ZLP image and EFTEM maps of Fe, Cr, C, V and N from the ion milled specimen. Precipitate 1 was identified as mod. Z-phase. Precipitates 2, 7 and 8 were identified as $M_{23}C_6$ particles. Precipitate 6 identified as Cr_2N. Precipitate 3, 4, 5 and 9 were identified as Laves phase particles. Precipitates10 and 11 were identified as VN.

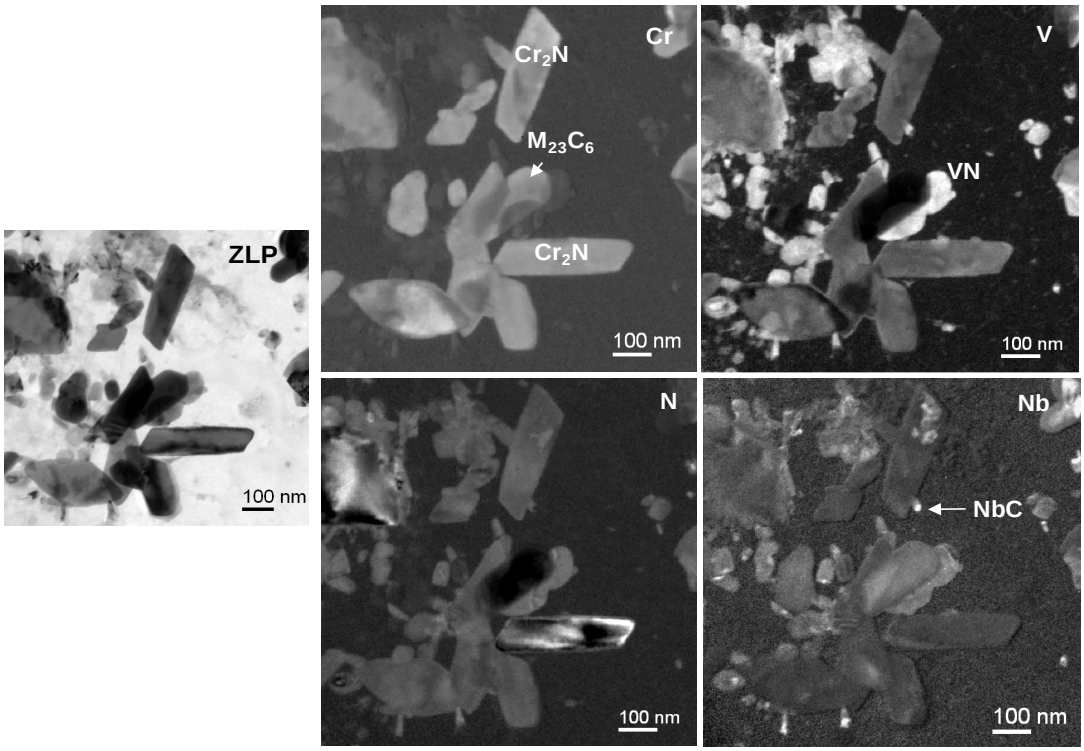

Figure 6.14. X12CrCoWVNb 11-2-2 TA600H1P-24639: ZLP and EFTEM ratio maps for Cr, V, N and Nb.

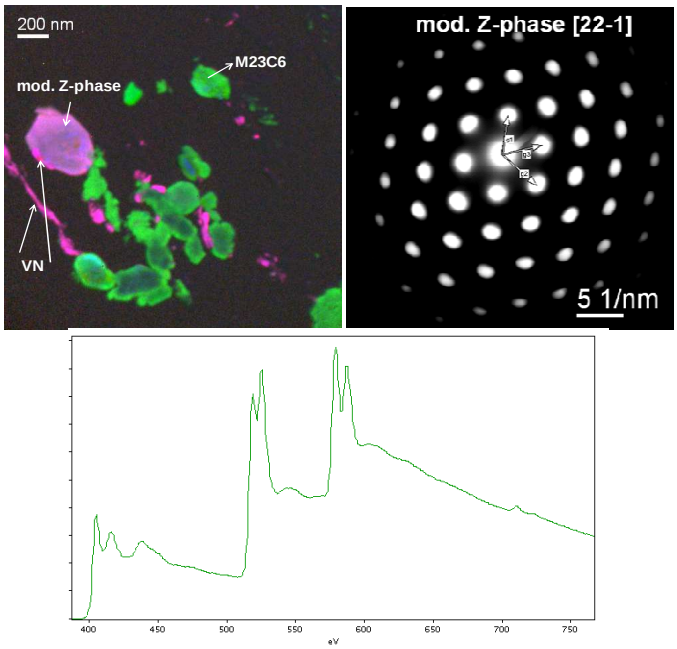

Figure 6.15. X12CrCoWVNb 11-2-2 CL600H1P-115-24639: RGB image (red=vanadium, green=chromium and blue=nitrogen), diffraction pattern and EEL spectrum from a mod. Z-phase.

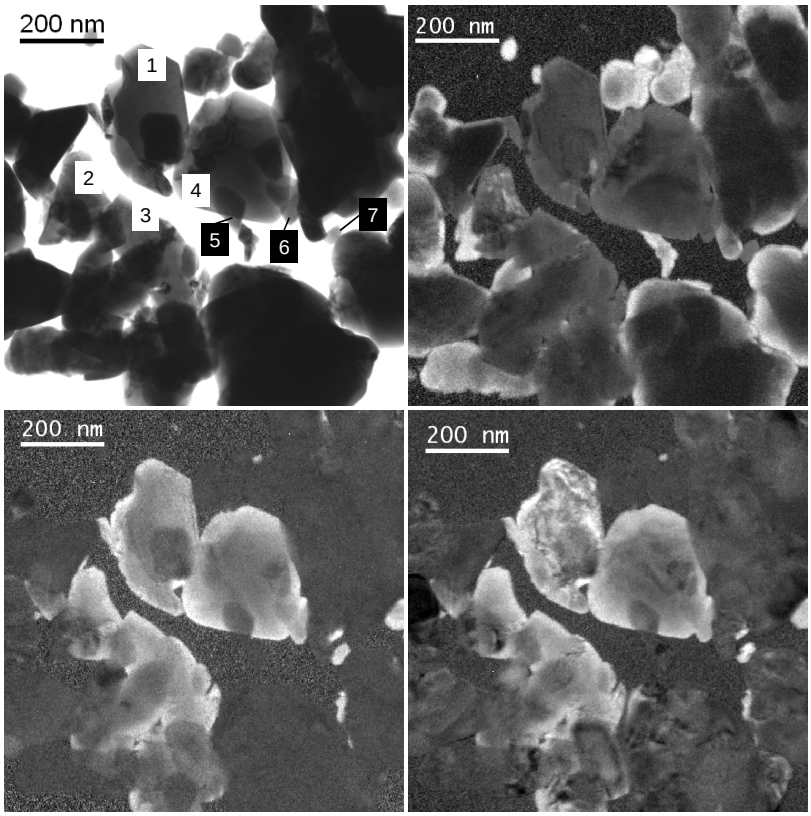

Figure 6.16. X12CrCoWVNb 11-2-2 CL600H1P-115-24639: ZLP image and EFTEM maps of Cr, V, Nb and N from the extraction replica specimen. Precipitates 1, 2, 3, 4 and 6 were identified like mod. Z-phase. Precipitate 7 was identified as M_2X particle (Cr_2N). Precipitate 5 was identified as $M_{23}C_6$.

Finally, different samples were tested at 625℃, TA 625H1P-17487, CL625H1P-85-17487 and TA625H1P-28983 were studied. For all conditions, the results were similar: carbides mainly $M_{23}C_6$ and nitrides VN, Cr_2N as well as mod. Z-phase were identified. Laves phase and NbC were identified too but no BN precipitate was found at any of the studied specimens. Figure 6.17, Figure 6.18 and Figure 6.19 show representative images of the specimens creep tested at 625℃.

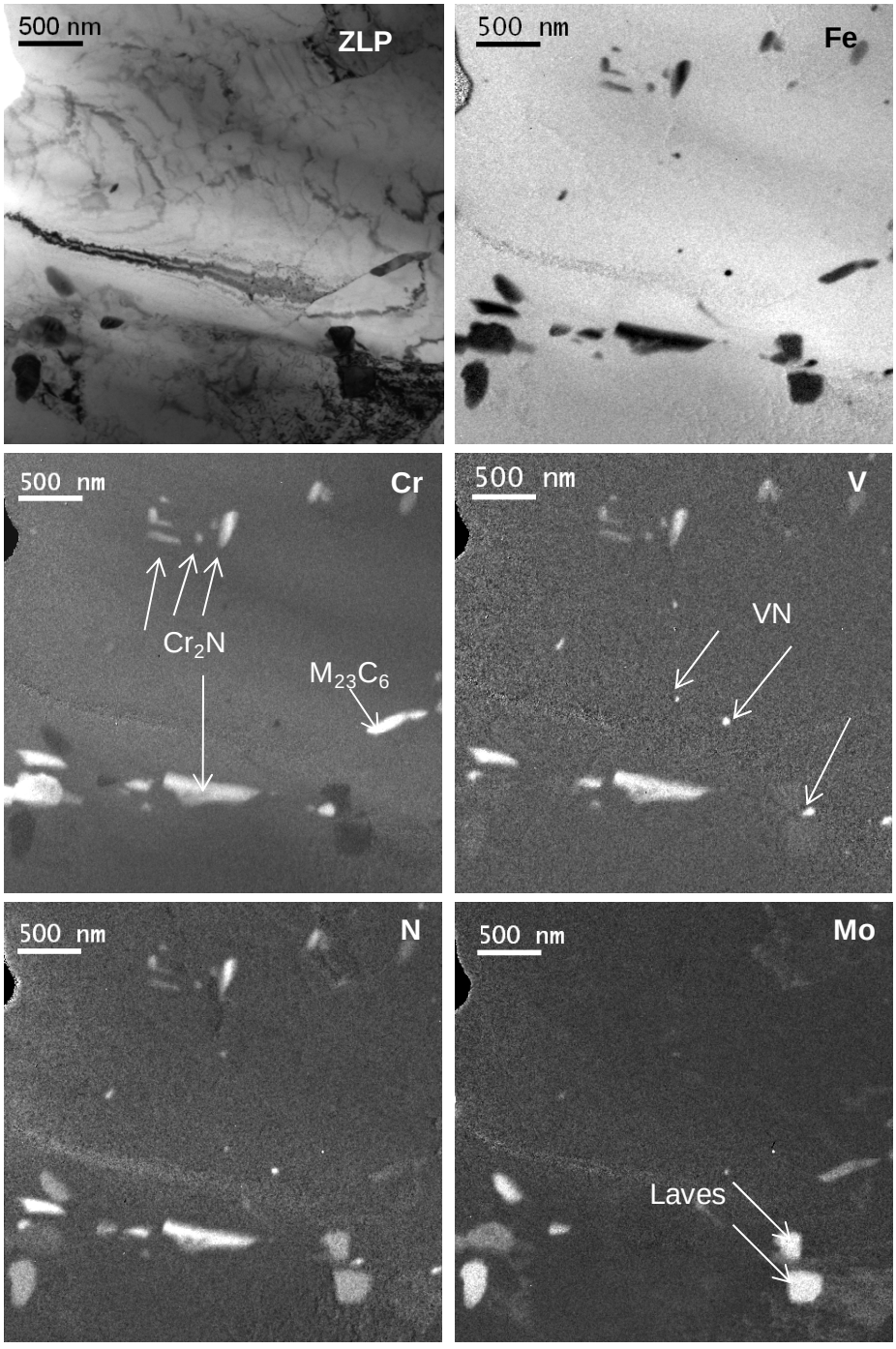

Figure 6.17. X12CrCoWVNb 11-2-2 TA625H1P-17487: ZLP image and EFTEM maps of Fe, Cr, V, N and Mo from the ion milled specimen.

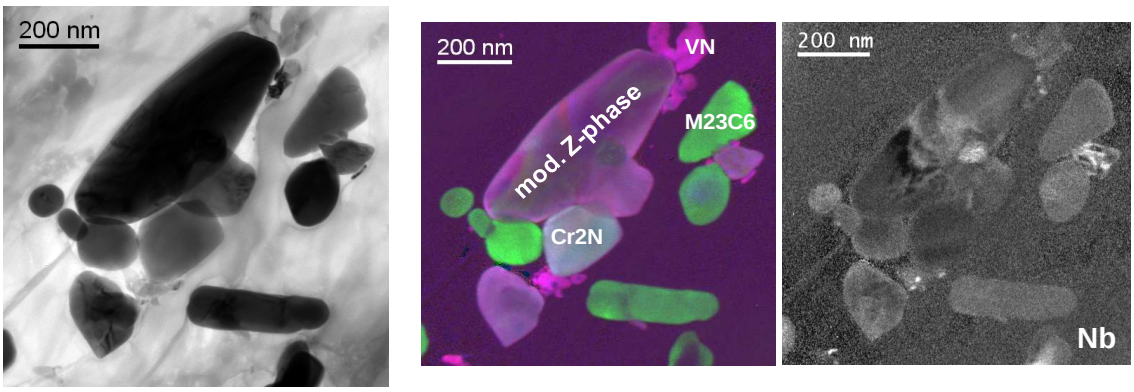

Figure 6.18. X12CrCoWVNb 11-2-2 CL625H1P-85-17487: This sample has been studied via thin foil and extraction replica. $M_{23}C_6$ and nitrides (MX (VN) and M_2X (Cr_2N) and mod. Z-phase) have been identified. Laves phase and NbC were found too.

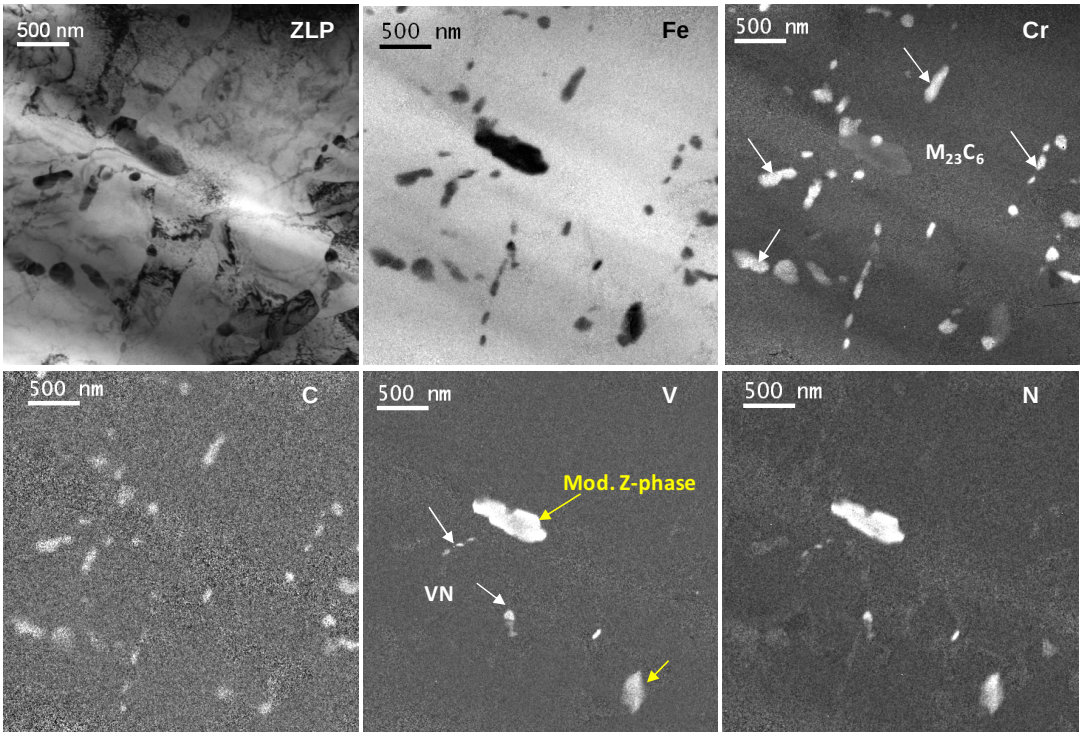

Figure 6.19. X12CrCoWVNb 11-2-2 TA625H1P-28983: ZLP image and EFTEM maps of Fe, Cr, C, V and N from the ion milled specimen.

6.2.2. Quantitative description of the microstructure

In this section, as a result from the microstructural investigations a quantitative analysis regarding chemical composition, mean diameter, number densities and volume fractions of the different precipitate populations is presented.

6.2.2.1. Chemical composition analysis of the different precipitate phases

The results for the chemical composition of the different precipitates populations analyzed via EDX in extraction replica specimens are here presented. Only the metal part of the chemical composition of the analyzed particles could be evaluated from the EDX spectra, and the values were scaled considering stoichiometric precipitates phases.

In the as-received (ASH1P) condition, $M_{23}C_6$ shows a chemical composition of: 55 at.%Cr, 18 at.%Fe, 1 at.%Mo and 5 at.%W, MX (VN) shows a chemical composition of: 38 at.%V, 9 at.%Cr, 1 at.%Fe and 2-3 at.%Nb and M_2X (Cr_2N) shows a chemical composition of: 15 at.%V, 50 at.%Cr and 1 at.%Fe and Nb or W traces. No Laves phase or mod. Z-phase were found in this condition. The results for the chemical quantification are presented in Figure 6.20.

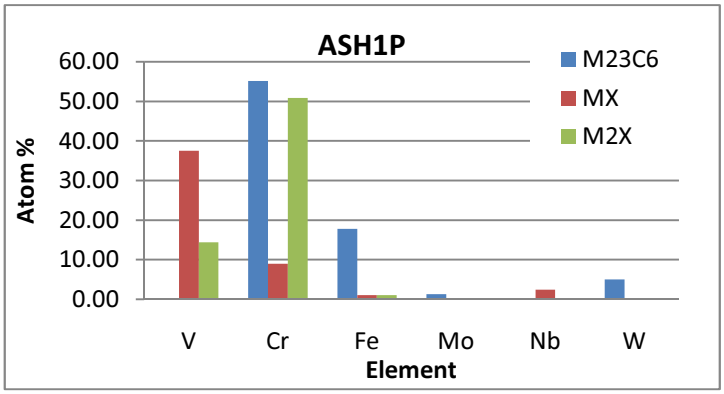

Figure 6.20. X12CrCoWVNb 11-2-2 ASH1P: Chemical quantification of the metal part of the analyzed particles via EDX.

At 575℃, in the creep loaded condition (CL575H1P-1 90-18726) similar chemical compositions for the same phases were found. Figure 6.21 shows the obtained results. Laves phases were only indentified in the ion milled specimens where the quantification is also influenced by the matrix, because of that no chemical quantification via EDX is presented. A low number of mod. Z-phase precipitates were found at this condition but no chemical quantification was performed.

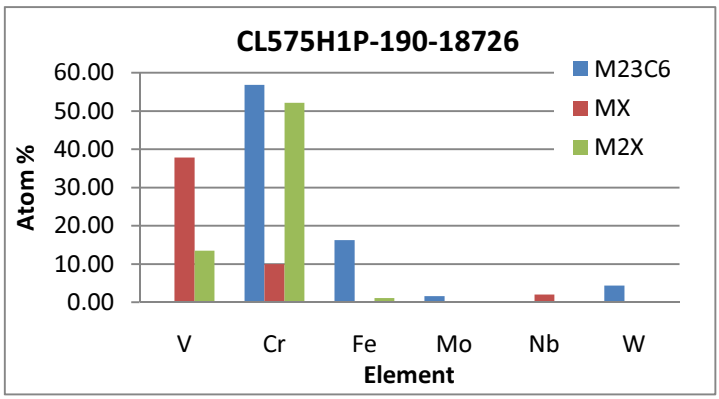

Figure 6.21. X12CrCoWVNb 11-2-2 CL575H1P-190-18726: Chemical quantification of the metal part of the analyzed particles via EDX.

$M_{23}C_6$, MX (VN) and M_2X (Cr_2N) were quantified in the thermally aged at 600℃ sample (TA600H1P-24639) with a chemical composition of: 56 at.%Cr, 17 at.%Fe, 1 at.%Mo, 5 at.%W and V traces for the $M_{23}C_6$, 38.5 at.%V, 9 at.%Cr, 0.8 at.%Fe and 3.7 at.%Nb for the MX (VN), 14 at.%V, 50 at.%Cr and 1 at.%Fe and Nb traces for the M_2X (Cr_2N). Figure 6.22 shows the corresponding chemical quantification for the different phases.

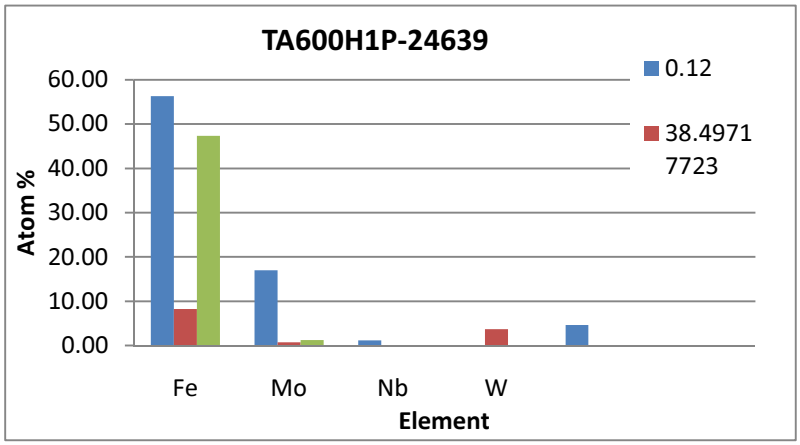

Figure 6.22. X12CrCoWVNb 11-2-2 TA600H1P-24639: Chemical quantification of the metal part of the analyzed particles via EDX.

The same specimen but creep loaded at the same temperature of 600℃ (CL600H1P-115-24639), which broke after 24639 h under 115 MPa was studied. Chemical composition of 58 at.%Cr, 15 at.%Fe, 1 at.%Mo, 5 at.%W and V traces for the $M_{23}C_6$, 37 at.%V, 10.5 at.%Cr, 1.5 at.%Nb and less than 1 at.%Fe for the MX (VN), 15 at.%V, 45 at.%Cr and 6 at.%Fe for the M_2X (Cr_2N) and 29 at.%V and 33.5 at.%Cr, 3 at.%Fe and 1.5 at.%Nb for mod. Z-phase was analyzed. Figure 6.23 shows the EDX quantification results.

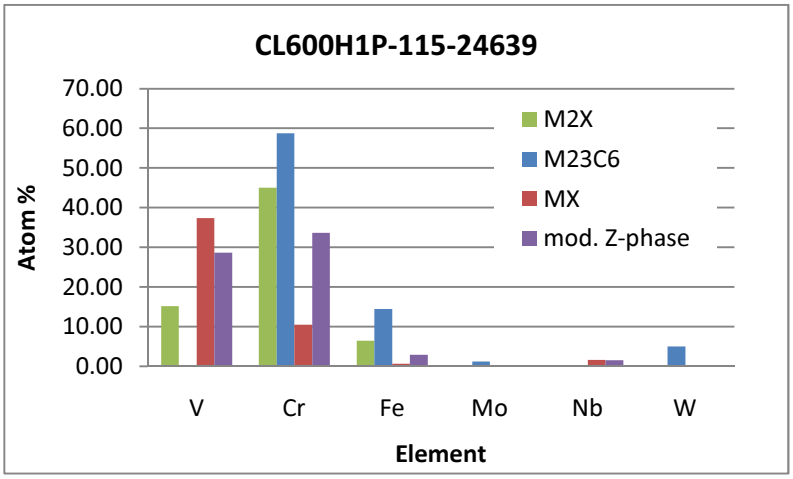

Figure 6.23. X12CrCoWVNb 11-2-2 CL600H1P-115-24639: Chemical quantification of the metal part of the analyzed particles via EDX.

In Figure 6.24, the results for the specimen *creep loaded at 625℃* which broke after 17487 h under 85MPa (CL625H1P-85-17487) are presented. In this specimen, a chemical quantification for Laves phase could be performed. They showed a high content of iron (around 45 at.%) and tungsten (around 32 at.%); also some molybdenum could be found (around 8 at.%).

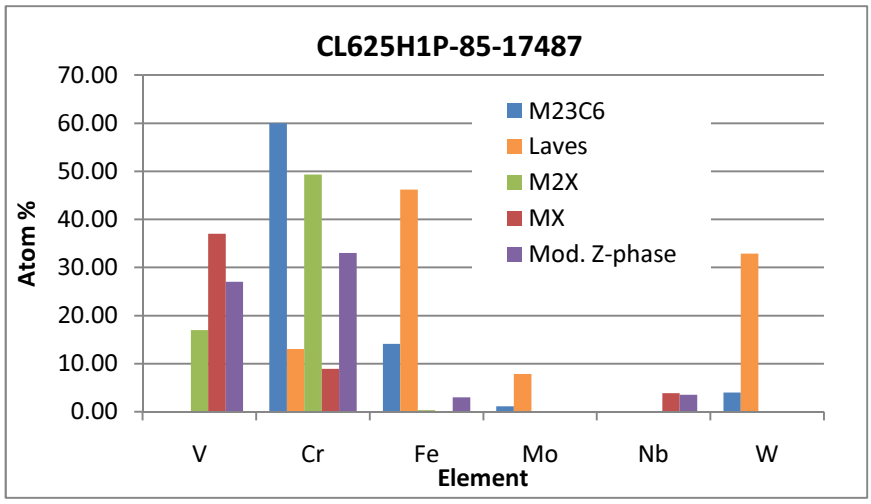

Figure 6.24. X12CrCoWVNb 11-2-2 CL625H1P-85-17487: Chemical quantification of the metal part of the analyzed particles via EDX.

Special attention was given to the chemical analysis of the mod. Z-phase. EDX analysis in different positions within this precipitate were carried out, as shown Figure 6.25. Around 33 at.% of Cr and 30 at.% of V with Nb and Fe was present in the different analysed positions, showing no significant difference in the chemical composition for each studied position.

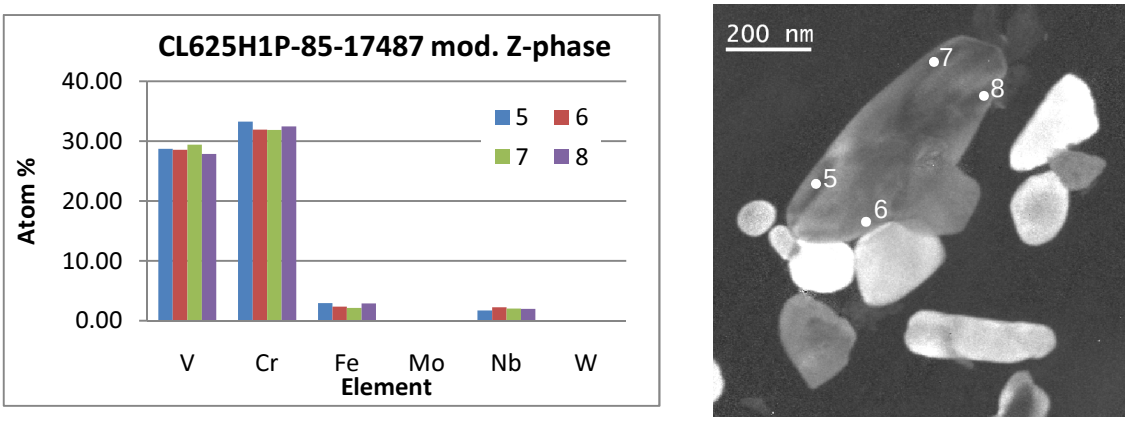

Figure 6.25. X12CrCoWVNb 11-2-2 CL625H1P-85-17487: EDX chemical quantification of the metal content at different positions in a mod. Z-phase. The micrograph (right) represents the Cr ratio map, where the analyzed positions are marked.

The results of the specimen thermal aged at 625℃ a fter 28983 h (TA625H1P-28983) are presented in Figure 6.26. The chemical quantification was performed only in two phases: carbides $M_{23}C_6$ and nitrides M_2X (Cr_2N). Special attention was given to the M_2X (Cr_2N) phase. For this phase EDX line scan analysis were performed to study the possible elemental segregation of Cr or V at the interface precipitate-matrix. As showed in Figure 6.26 these elements are equally distributed in the precipitate phase. Moreover, it is recommended to perform further investigations, with EELS at higher magnifications for the evaluation of possible segregations of chromium which could not be detected using EDX line scan.

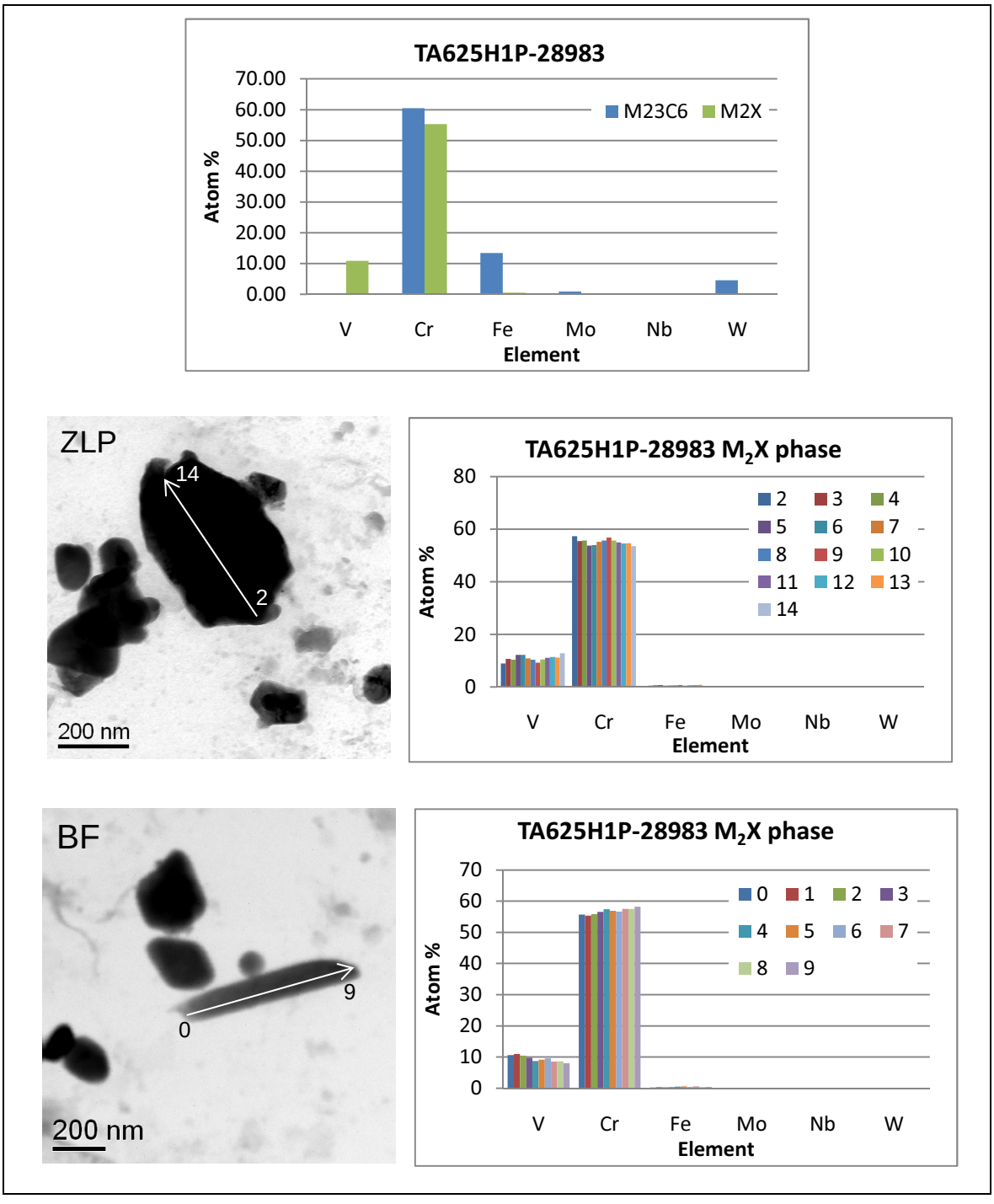

Figure 6.26. X12CrCoWVNb 11-2-2 TA625H1P-28983: Chemical quantification for the metal part of the different analyzed particles via EDX and chemical composition in different positions of two M_2X (Cr_2N) particles.

The chemical composition of all investigated samples is summarised in Figure 6.27, only for the $M_{23}C_6$, MX (VN) and M_2X (Cr_2N) precipitates. On the other hand, Figure 6.28 represents the chemical composition of the same precipitates phases but only for the creep loaded material, to have a better overview of the stress effect at these specimens.

$M_{23}C_6$ shows an increase in chromium at the specimen creep loaded at 600℃ for 24639 h and at all the specimens tested at 625℃. MX (VN) chemical composition remains unaffected at all tested specimens. On the other hand, M_2X (Cr_2N) phase shows a decrease in chromium content when comparing the thermal age and creep load specimens tested at 600°C and 625℃.

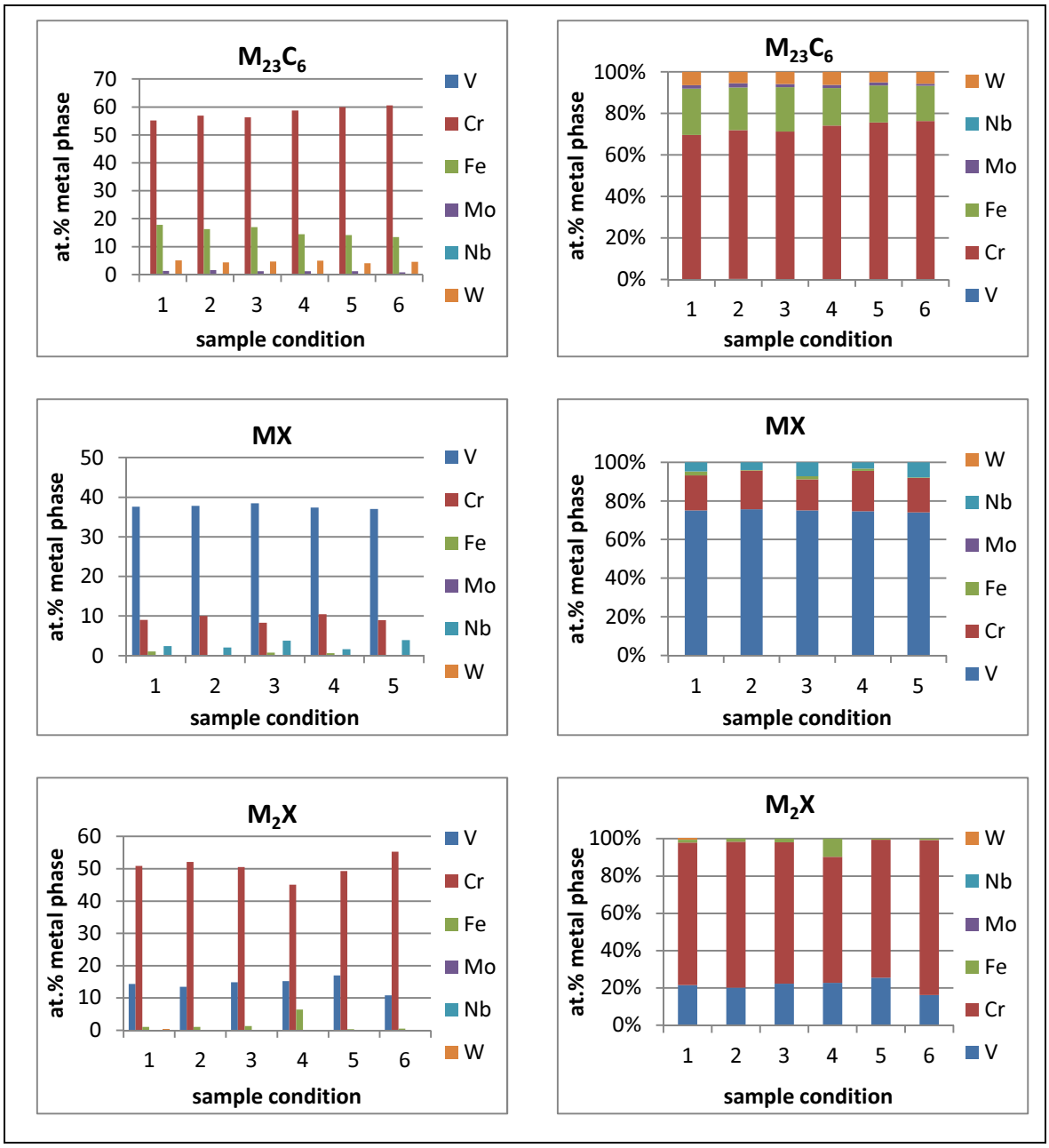

Figure 6.27. X12CrCoWVNb 11-2-2 Heat 1: Chemical composition of $M_{23}C_6$, MX (VN) and M_2X (Cr_2N) for all the studied specimens. X-axis represents the different sample conditions, corresponding to: 1=ASH1P, 2=CL575H1P-190-18726, 3=TA600H1P-24639, 4=CL600H1P-115-24639, 5=CL625H1P-85-17487 and 6=TA625H1P-28983.

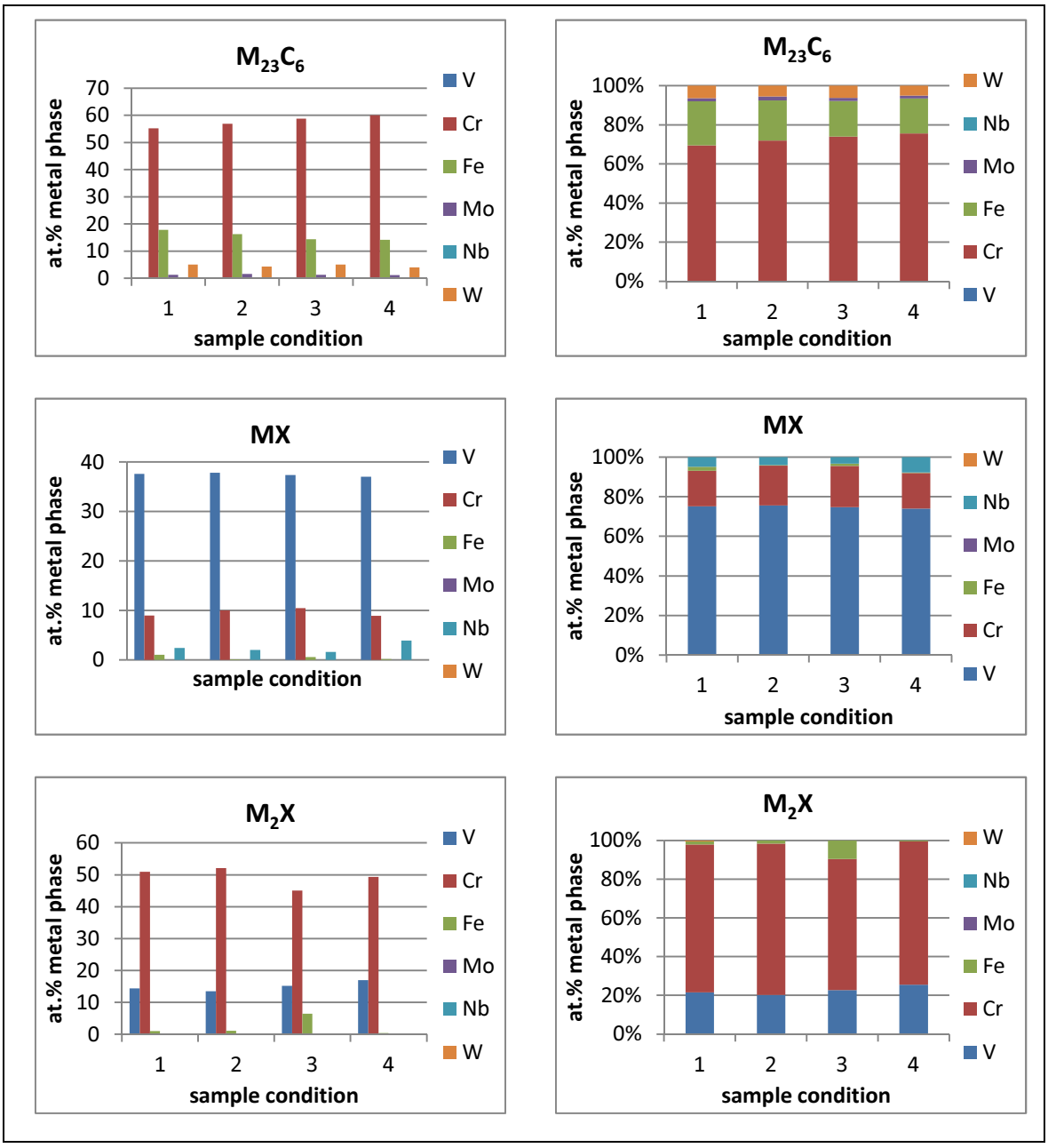

Figure 6.28. X12CrCoWVNb 11-2-2 Heat 1: Chemical composition of $M_{23}C_6$, MX (VN) and M_2X (Cr_2N) for all the studied specimens. X axis represents the different sample conditions, corresponding to: 1=ASH1P, 2=CL575H1P-190-18726, 3=CL600H1P-115-24639 and 4=CL625H1P-85-17487.

EDX technique is a well known technique for chemical analysis, although in the outgoing of this project also EELS chemical quantification of the different nitrides phases (Cr_2N, VN and mod. Z-phase) has been performed to evaluate possible chemical composition changes due to the tested conditions. Using EELS, chemical quantification of light elements like carbon and nitrogen can be quantified. For the quantification of the EEL spectra the multiple linear least squares (MLS) fit deconvolution was used [60], fitting suitable references to elemental edges [28], see Figure 6.29.

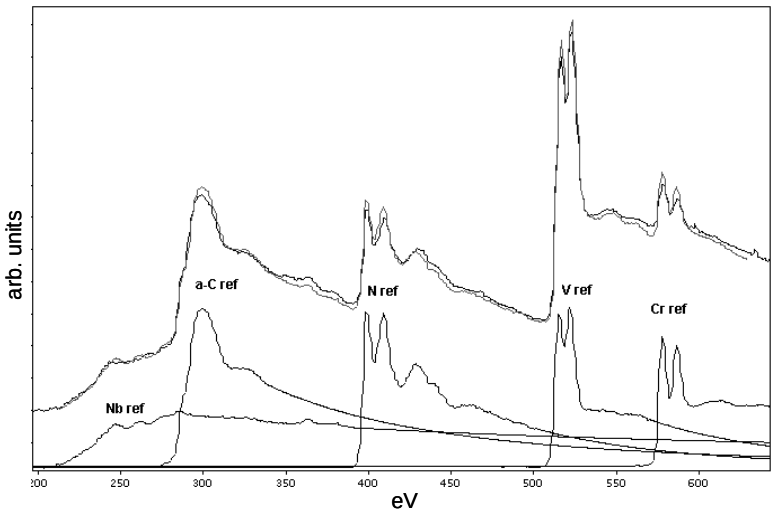

Figure 6.29. MLS fit using Nb, amorphous C, N, V and Cr references for an MX (VN) particle. With black colour is represented the experimental spectrum and with grey the MLS fit [28].

The chemical composition of the different nitride phases VN, Cr_2N and mod. Z-phase was analyzed via EELS in the as-received, thermally aged and creep loaded at 600℃ conditions. The results of this quantification are presented in Table 6.2. The EELS characterization reveals that, Cr_2N phase as well as the mod. Z-phase are rich in chromium and nitrogen. The main difference between these two phases is the vanadium and the niobium content, lower in the Cr_2N compared with mod. Z-phase. VN nitride phase has been found to be rich in vanadium and nitrogen (40 at.% each) and lower contents of chromium, niobium and iron.

Table 6.2. Chemical composition measurements using EELS, for the three identified nitrides: Cr_2N, VN and mod. Z-phase. The analysis was performed in the samples: as-received, thermally aged specimen and creep loaded at 600℃. The EDX values for each analysed particle have been scaled to the nitrogen content derived from EELS quantification [28].

EELS	Cr (at.%)	V (at.%)	Nb (at.%)	Fe (at.%)	N (at.%)
Cr_2N	49.75 ± 3.4	17.18 ± 2.1	0	2.61 ± 1.7	30.42 ± 4.25
VN	11.56 ± 4	40.01 ± 4.5	6.89 ± 2.7	2.18 ± 1.1	41.18 ± 4.8
mod. Z-phase	32.76 ± 9.5	31.27 ± 2.41	3.31 ± 1.57	3.52 ± 1.16	32.3 ± 3.42

EDX	Cr (at.%)	V (at.%)	Nb (at.%)	Fe (at.%)
Cr_2N	52.48 ± 3.7	15.44 ± 2.5	0.36	1.49 ± 1.7
VN	10.27 ± 2.8	43.01 ± 4.6	4.52 ±1.9	1.09 ± 0.3
mod. Z-phase	34.6 ± 2.4	29.79 ± 1.99	1.44 ± 0.13	2.62 ± 0.2

Detailed information about the used method is presented in appendix 1.

6.2.2.2. Quantification of the precipitates: mean radii, volume fraction and number densities

Precipitates $M_{23}C_6$, MX (VN) and M_2X (Cr_2N) were identified in as-received, tempered and creep loaded material. During aging and creep loading, the diameter of these particles increases. Coarsening of $M_{23}C_6$ carbides and changes in the MX (VN) nitrides are significant degradation mechanisms that cause softening in this type of steel grades.

The mean radius, volume fraction and number density of $M_{23}C_6$, MX (VN) and M_2X (Cr_2N) precipitates in as-received as well as after aging and creep loading were determined using EFTEM images from Cr as well as V and the corresponding thickness maps, together with the routines cited in the experimental procedure chapter.

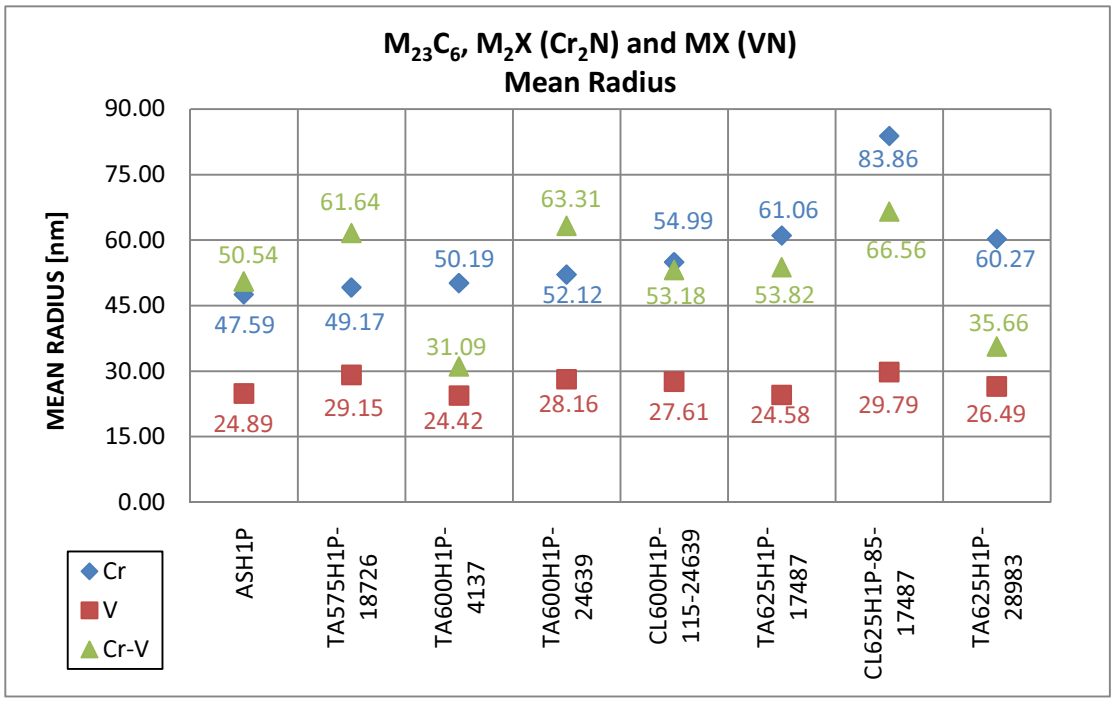

Figure 6.30. X12CrCoWVNb 11-2-2 Heat 1: Mean radius of phases rich in chromium ($M_{23}C_6$), phases rich in vanadium (MX (VN)) and phases rich in chromium and vanadium (M_2X (Cr_2N)) in all the investigated sample conditions.

The precipitates rich in chromium ($M_{23}C_6$) and the precipitates rich in chromium and vanadium (M_2X (Cr_2N)) show a smooth coarsening. The $M_{23}C_6$ showed an increase of the mean radius from 50 to 80 nm and the M_2X (Cr_2N) from 50 to 60 nm. Nevertheless, MX precipitates exhibited a constant mean radius around 25 to 30 nm (see Figure 6.30).

Figure 6.31 splits the data of Figure 6.30 into thermally aged and creep loaded specimens, respectively. The $M_{23}C_6$ precipitates have a smooth coarsening at 575℃ compared with the material in as-received condition. The same behaviour is observed at the specimens tested at 600℃ and 625℃ (thermal ageing and creep loaded) with an increase in the mean radius compared with the as-received material. The MX (VN) phase keeps almost a constant mean radius in all samples conditions and no differences were observed in size between the creep loaded or the thermal aged specimens. The M_2X (Cr_2N) phase increase its mean radius, when comparing to the thermally aged specimens (upper image from Figure 6.31) with two exceptions, the specimen thermally aged at 600℃ after 4137 h and at the specimen thermally aged at 625℃ after 28983 h. When comparing only the creep loaded specimens, (lower image from Figure 6.31), the mean radius of this phase as well as for $M_{23}C_6$ phase clearly increase due to the effect of temperature and stress.

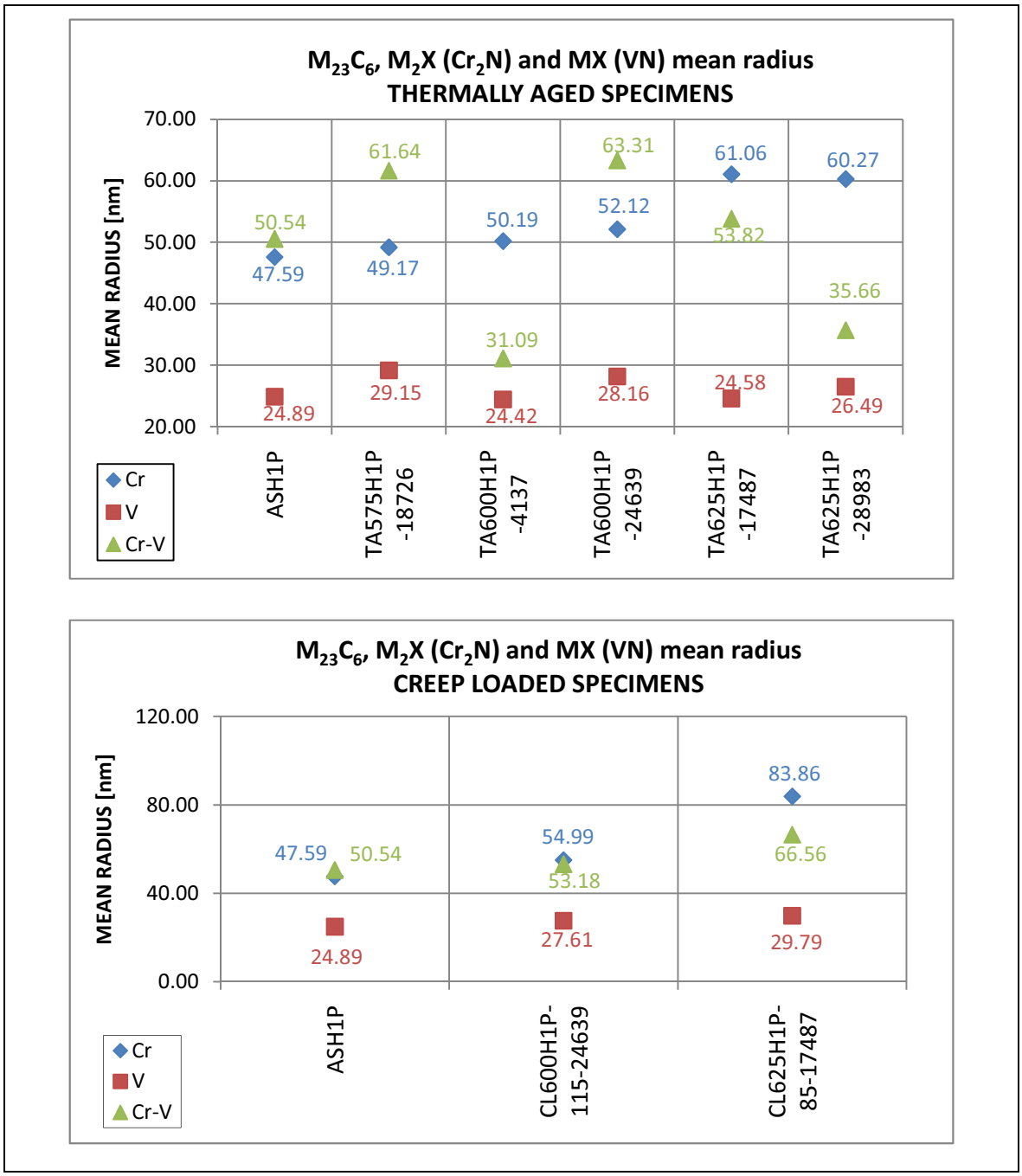

Figure 6.31. X12CrCoWVNb 11-2-2 Heat 1: Mean radius of phases rich in chromium ($M_{23}C_6$), phases rich in vanadium (MX (VN)) and phases rich in chromium and vanadium (M_2X (Cr_2N)) in the thermally aged specimens (upper image) and in the creep loaded specimens (lower image).

Since the tempering was by far sufficiently long for a full precipitation of $M_{23}C_6$ carbides the measurements systematically underestimate the volume fraction of this phase. The presumable reason can be found in thick sections of the sample. These sections contribute to the sample volume, but are too thick for detecting precipitates. To overcome these difficulties, the phase fraction of $M_{23}C_6$ is assumed to be constant at 2.5% (value predicted by MatCalc software in other similar steels) and is thus used as calibration factor for the fractions of the other phases in the following graphs. Figure 6.32 shows the volume fraction analysis for the thermally aged and creep loaded specimens when applying the mentioned correction.

The volume fraction of VN phase is roughly half of the maximum phase fraction (see samples aged at 575℃), which indicates that this phase is still precipitating. Moreover, the volume fraction of VN

decreases when aging/creep loading at 600℃ and 625℃ respectively. Parallelly, mod. Z-phase was identified at these sample conditions, which is the main reason for the dissolution of VN in these steels grades. Cr_2N precipitate act differently: it starts with a very low volume fraction, and increases its fraction in every aged and creep loaded specimen indicating further precipitation of this phase after the heat treatment. Afterwards decrease at the specimen tested at the higher temperature for longer time (625℃ and 28983 h). When comparing the thermal age and creep load specimens, the volume fraction of Cr_2N is higher for the specimens' thermal age than for the creep load at 600℃ as well as at 625℃, the stress has an influence in the dissolution of this phase. However, this phase seems to precipitate during service, showing longer stability than the VN phase.

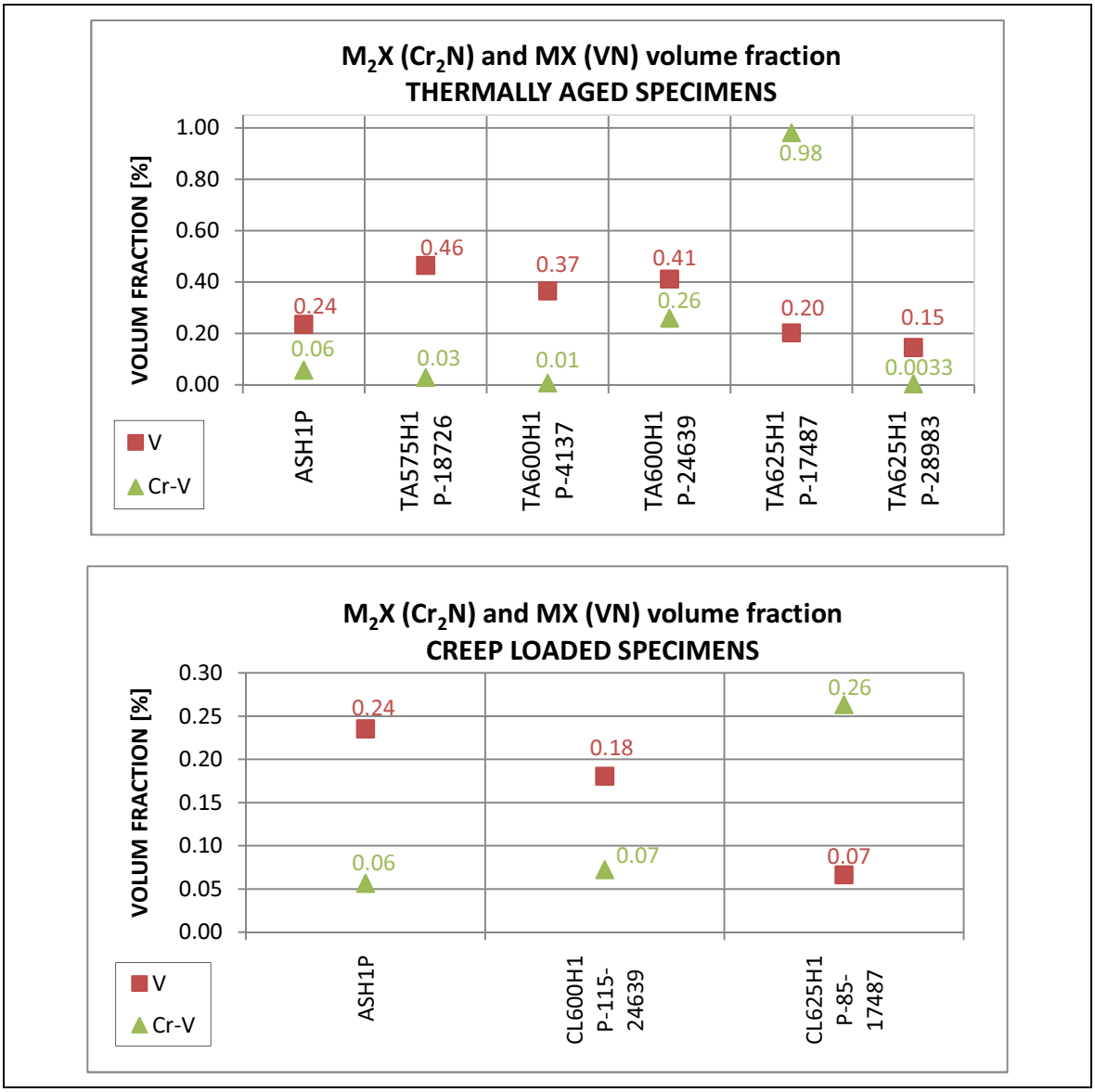

Figure 6.32. X12CrCoWVNb 11-2-2 Heat 1: Volume fraction of phases rich in vanadium (MX (VN)) and phases rich in chromium and vanadium (M_2X (Cr_2N)) in the thermally aged specimens (upper image) and in the creep loaded specimens (lower image).

The number density of the same ($M_{23}C_6$, M_2X (Cr_2N), MX (VN)) phases were also quantified assuming, that $M_{23}C_6$ had already fully precipitated after tempering. In Figure 6.33 the number density of the studied thermally aged and creep loaded specimens is presented. The number density of the $M_{23}C_6$ phase decrease in all the tested specimens when comparing with the as-received condition because of the coarsening of this phase. Moreover, a decrease of the MX (VN) phase can also be observed. The reason of this decrease is the presumable transformation of this phase to mod. Z-phase. On the other hand, the

number density of M_2X (Cr_2N) has a different behaviour. In the specimen tested at 575℃, the number density of this phase decreases because this phase coarsens. At 600℃ and 625℃ the number density increase indicating that this phase was not fully precipitated after the heat treatment. On the other hand, after very long aging times, the sample tested at 625℃ for the longest time (28983 h) the number dens ity decrease as well as its phase fraction indicating that after longer tested times dissolves.

The size distribution of the $M_{23}C_6$ as well as for MX (VN) phase has been calculated and the values are presented in Figure 6.34 and Figure 6.35. Insufficient number of particles were analysed for a size distribution of Cr_2N phase. The size distribution for $M_{23}C_6$ as well as for the MX (VN) phase at 575℃ shows insignificant differences compared with the as-received specimen. Moreover, the specimens tested at higher temperatures (600℃ and 625℃) showed tha t $M_{23}C_6$ increases its mean diameter to higher values (100-120 nm), whereas the MX(VN) phase has stable diameter.

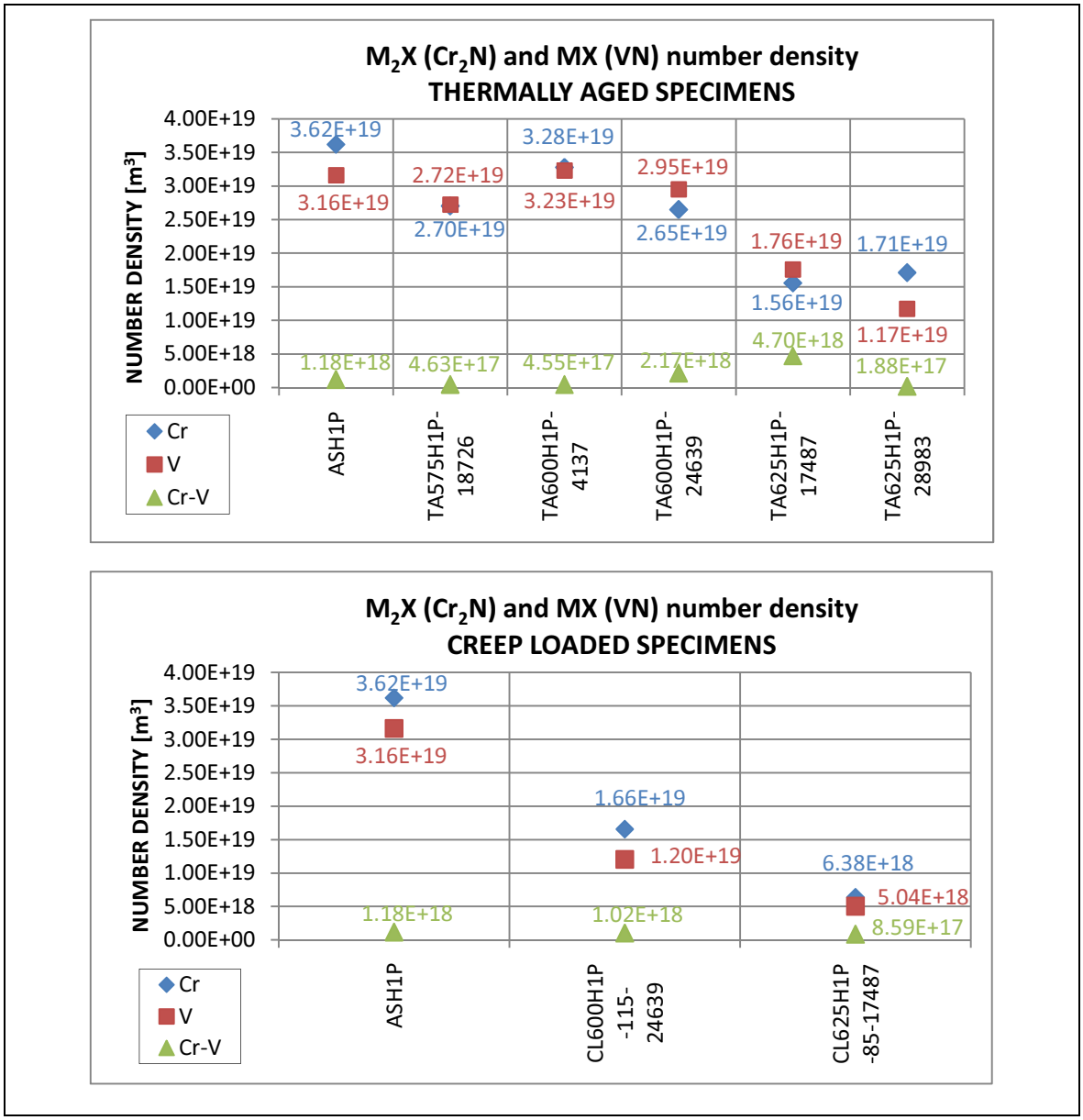

Figure 6.33. X12CrCoWVNb 11-2-2 Heat 1: Number density of phases rich in chromium ($M_{23}C_6$), phases rich in vanadium (MX (VN)) and phases rich in chromium and vanadium (M_2X (Cr_2N)) in the thermally aged specimens (upper image) and in the creep loaded specimens (lower image).

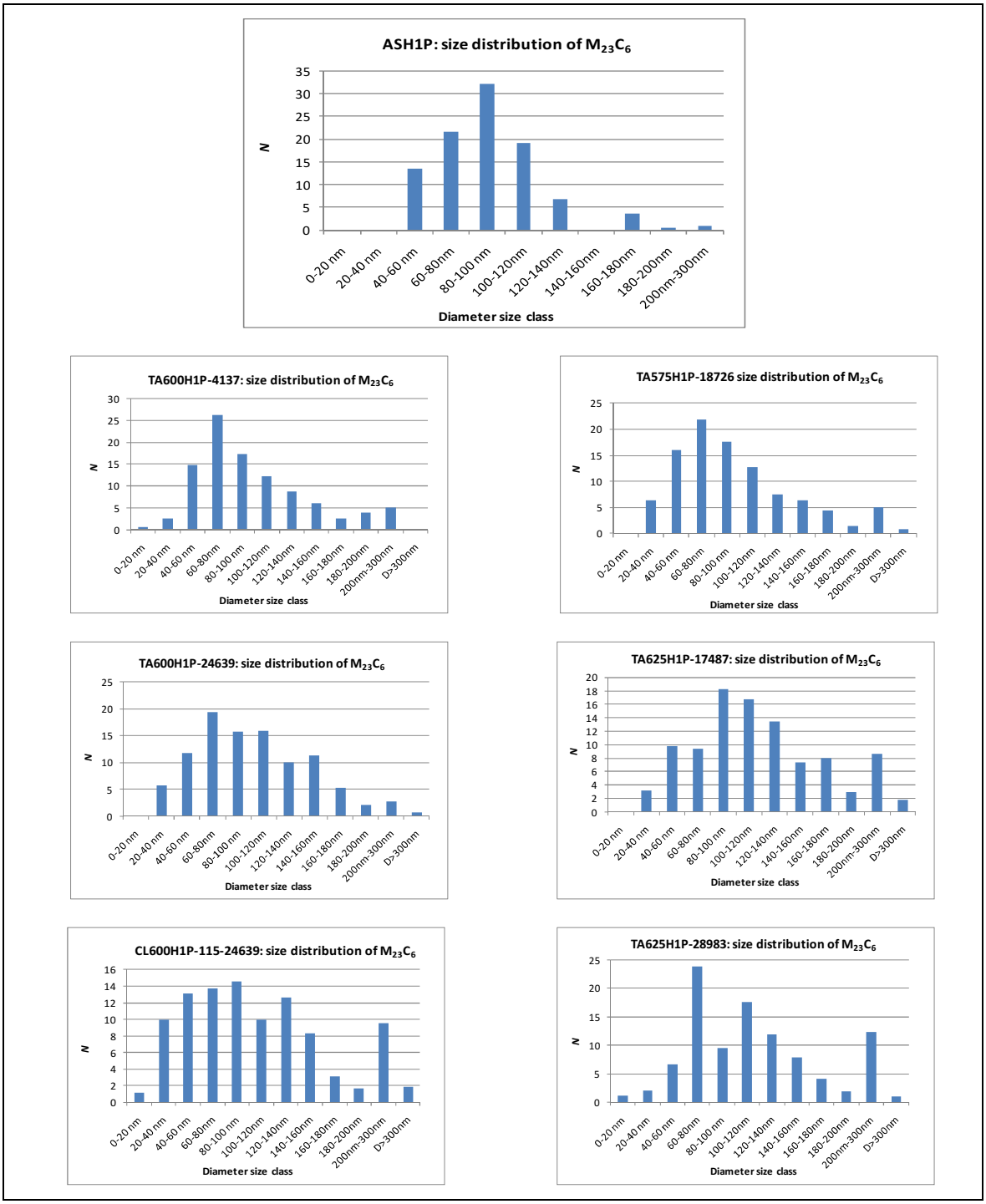

Figure 6.34. X12CrCoWVNb 11-2-2 Heat 1: Mean diameter size distribution of the $M_{23}C_6$ phase at the different studied sample conditions.

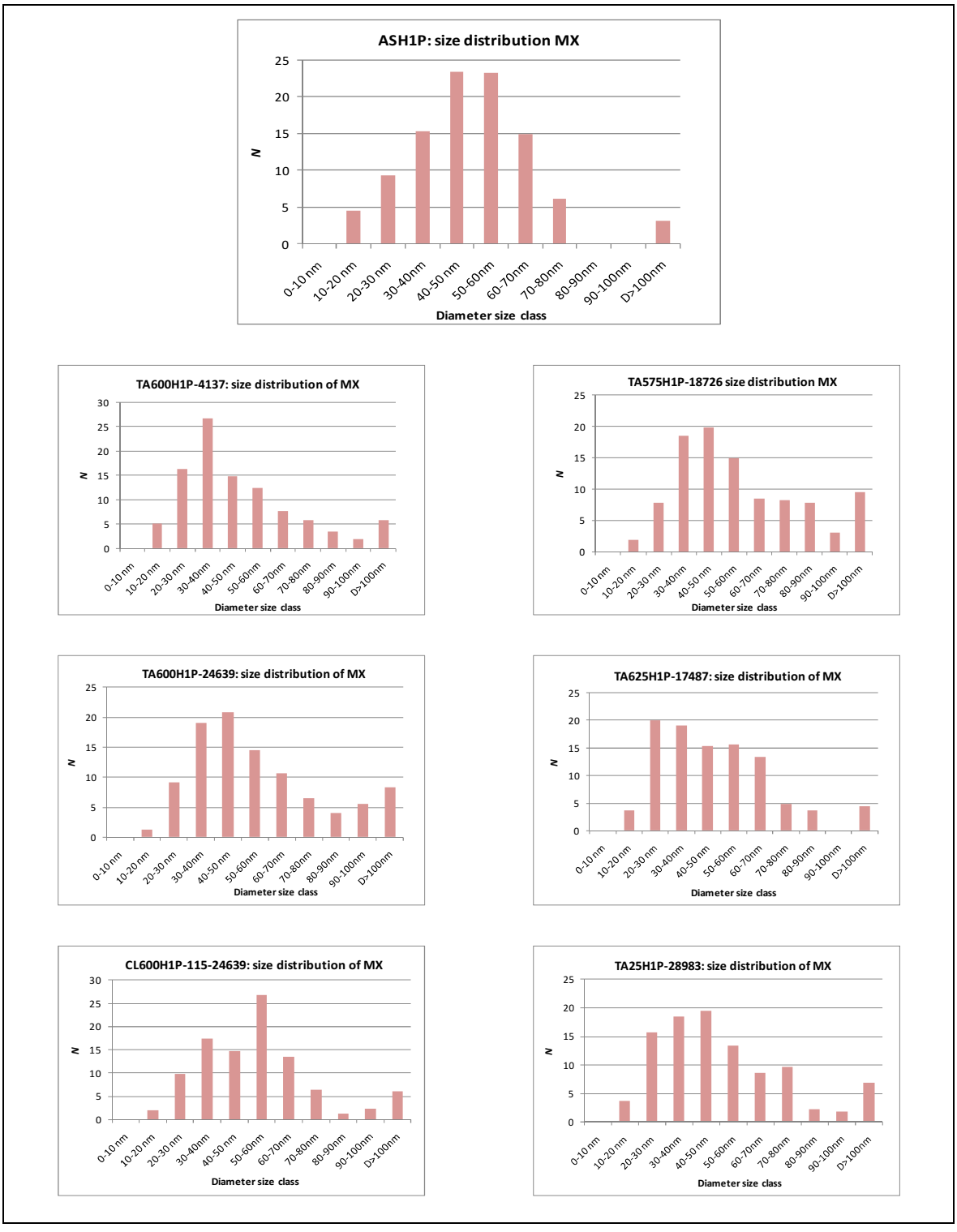

Figure 6.35. X12CrCoWVNb 11-2-2 Heat 1: Mean diameter size distribution of the MX phase at the different studied sample conditions.

6.3. Scanning Electron Microscopy: Electron Backscattered Diffraction

Electron backscattered diffraction measurements (EBSD) were used for the analysis of the prior austenite grain size, martensite lath width and subgrain size. Figure 6.36 and Figure 6.37 show the results of the EBSD measurements. On the left side, the EBSD image representing the different crystal orientations of the analysed position is presented. On the right side, the results after filtering the images with the routines defined in the experimental procedure chapter (section 5.2.3) are shown. Red colour marks the subgrains, blue colour the martensite laths and white colour the austenite grains.

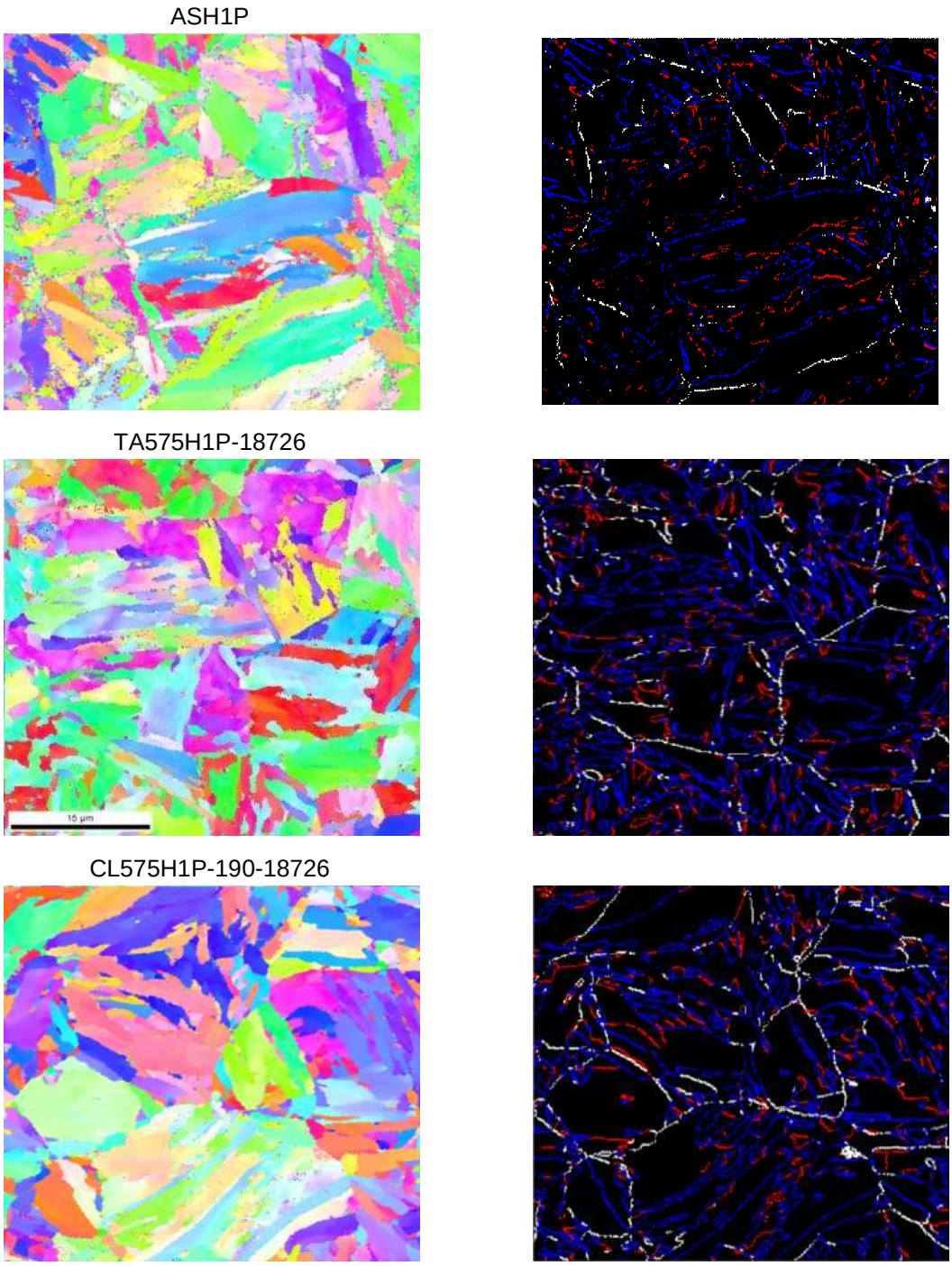

Figure 6.36. X12CrCoWVNb 11-2-2 Heat 1: EBSD images of the studied specimens (left). Filtered images (right) showing in Blue:martensite laths, Red:subgrain boundaries and White: Prior austenite grain boundaries.

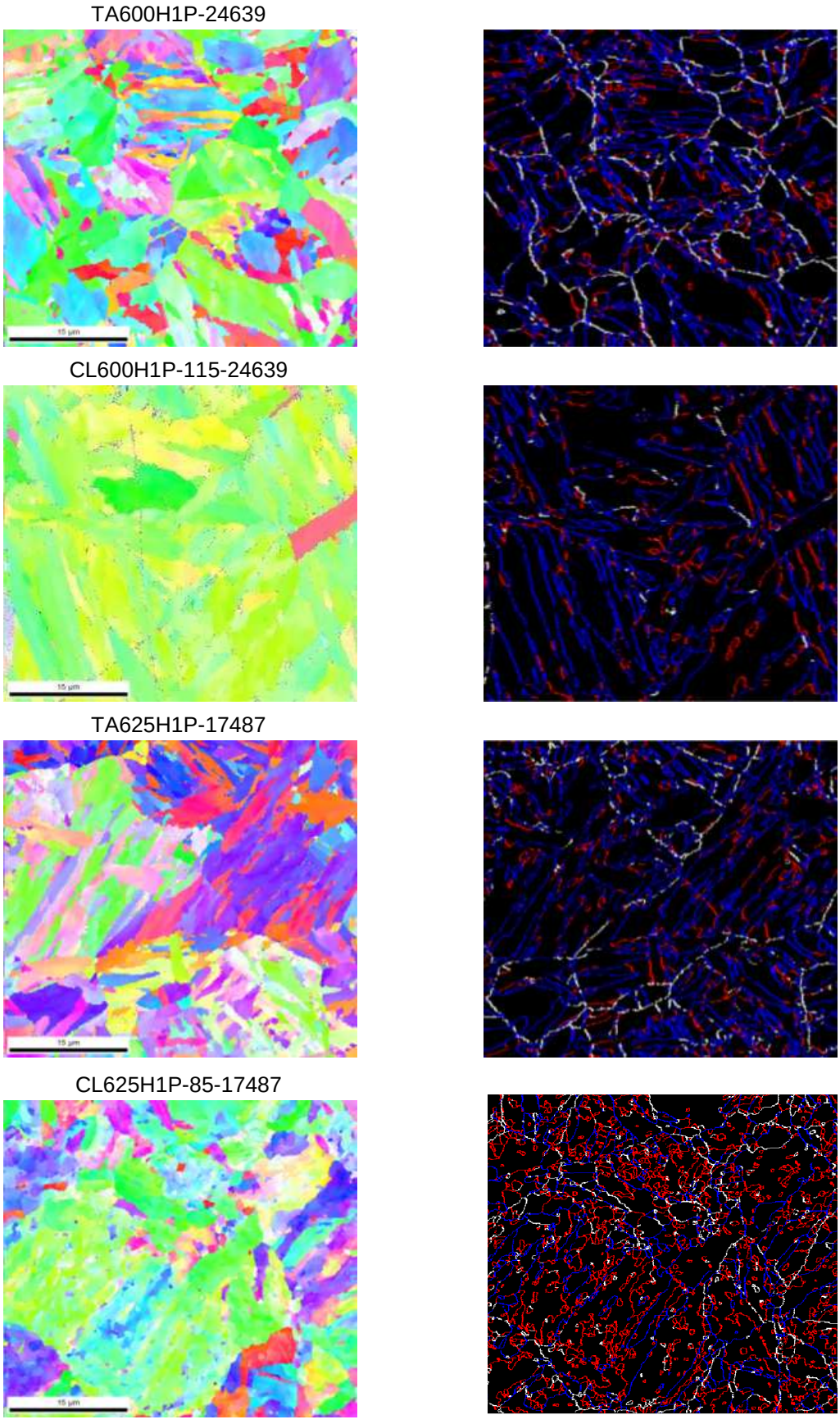

Figure 6.37. X12CrCoWVNb 11-2-2 Heat 1: EBSD images of the studied specimens (left). Filtered images (right) showing in Blue:martensite laths, Red:subgrain boundaries and White: Prior austenite grain boundaries.

Table 6.3 and Figure 6.38 show the mean size of the martensite lath width as well as the equivalent circle diameter of the subgrain size, calculated out of the EBSD image analysis.

At 575℃ martensite lath width and the equivalent circle diameter of the subgrain remains almost constant, when the values are compared with the as-received material. At 600℃, creep strength and temperature is high enough to allow coarsening, from 0.76 µm in the as-received condition to 0.97 µm in the creep loaded specimen for martensite lath width and from 1.22 µm to 1.55 µm for subgrains. For the material tested at 625℃, also smoothly coarsening of martensite lath can be observed, from 0.76 to 0.86 µm. However, a smaller subgrain size of only 0.8 µm was detected. In this sample, the particle size of Laves phase was exceeding the measurement limit of the EBSD method, and therefore, interfered with the measurement of subgrains. Figure 6.39 represents the subgrain size distribution. The specimen creep tested at 625℃ has a strong peak at the lower size class due to the interference of Laves phase precipitates in the measurements.

Table 6.3. X12CrCoWVNb 11-2-2 Heat 1: Martensite lath and subgrain size measurements.

Sample Condition	Lath Width [µm]	Equivalent Circle Diameter [µm]
ASH1P	0.76	1.22
TA575H1P-18726	0.85	1.18
TA600H1P-24639	0.87	1.12
TA625H1P-17487	0.79	1.14
CL575H1P-190-18726	0.89	1.23
CL600H1P-115-24639	0.97	1.55
CL625H1P-85-17487	0.86	0.76*

*interference of Laves phase in the measurement.

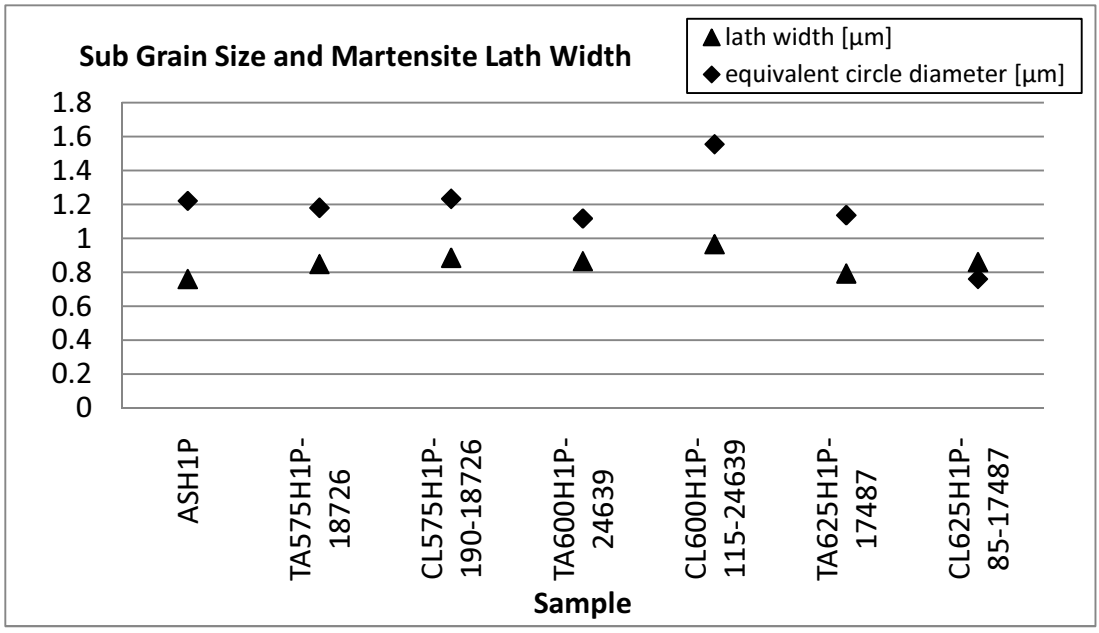

Figure 6.38. X12CrCoWVNb 11-2-2 Heat 1: Subgrain size (equivalent circle diameter) and martensite lath width size distribution.

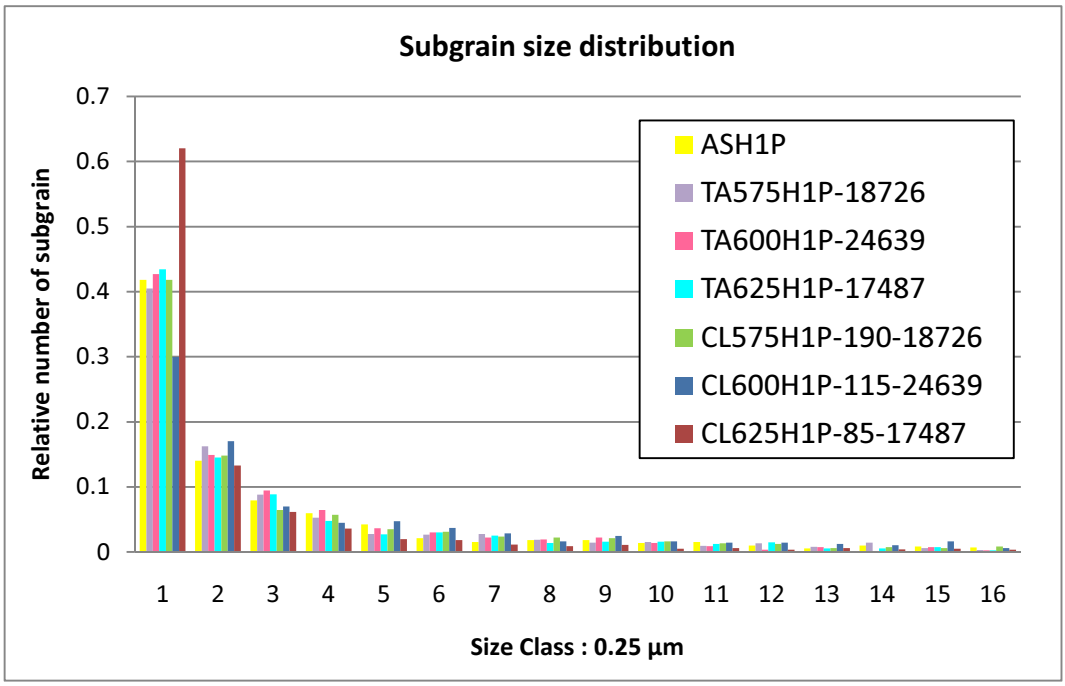

Figure 6.39. X12CrCoWVNb 11-2-2 Heat 1: Subgrain size distribution for all specimens analyzed via EBSD.

7. Thermodynamic and Kinetic Simulations with MatCalc Software for X12CrCoWVNb 11-2-2 material

The microstructure of the material X12CrCoWVNb 11-2-2 in all three variants, Heat 1, 2 and 3 (special focus is given in Heat 1), has been simulated using the Software MatCalc and three different databases versions: mc-steel[5], and modified versions for 9-12 wt.%Cr of TCFE3[6] and Fe-data6[7].

For the assessment of the MatCalc calculations, important input parameters that have to be considered, are:

- Composition of the steel and precipitates phases.
- Heat treatment: austenitization and tempering times and temperatures, as well as cooling and heating rates.
- Thermal ageing temperature and time.
- Nucleation sites of the different precipitate phases.
- Grain sizes (for the calculation of nucleation site densities).

Chemical composition, heat treatment and service temperature were defined by the investigated material and creep specimen conditions. Besides, nucleation sites for the different precipitates phases and the different simulated precipitates phases are defined in Table 7.1.

Table 7.1. Definition of the nucleation site, for each matrix phase, for the different precipitates phases considered in the MatCalc simulations, where: ge indicates grain boundary and triple points, gs indicates grain boundaries and subgrain boundaries, gsd indicates grain boundaries, subgrain boundaries and dislocations and on VN indicates precipitation on the VN phase.

Precipitate Phase	***Matrix Phase: Austenite***	***Matrix Phase: Ferrite***
$M_{23}C_6$	ge	gs
M_7C_3	ge	gs
NbC	ge	gsd
VN	ge	gsd
Cr_2N	ge	gs
Zp	on VN	on VN
Zm	ge	gs
Laves Phase	ge	gs

As a first step, thermodynamic calculations were carried out considering the phases defined in Table 7.1. For this calculations, taking into account that mod. Z-phase has long nucleation times, two thermodynamic calculations have been carried out, considering and suppressing this phase from the calculation. When mod. Z-phase is suppressed within the calculations; an accurate calculation of the status of the material after heat treatment (as-received) can be obtained. On the other hand, when mod. Z-phase is considered in the calculation; more reliable information of the phases in equilibrium that are precipitating in service can be obtained.

[5] www.matcalc.at
[6] ThermoCalc AB, Stockholm, Sweden
[7] www.thermotech.co.uk/databases.html#Fe-data with implementations of H. Danielsen [18]

As a second step, kinetic simulations were performed. In these simulations, two different mod. Z-phases were considered in order to include different nucleation processes. Zp [18] phase is a mod. Z-phase which nucleates from VN precipitates and Zm is a mod. Z-phase that nucleate in the matrix.

Equilibrium and kinetic calculations were carried out using various thermodynamic parameters, databases, heat treatments and materials. An overview is given in Table 7.2 of the different used MatCalc versions as well as the different databases and phases. Table 7.3 and Table 7.4 summarises the different cooling and heating rates used in the calculations.

Table 7.2. Summary of the different MatCalc versions, databases and materials used for the thermodynamic and kinetic calculations.

MatCalc version	Databases	Diffusion databases	Material	Phases
V5.13 beta16 V5.20 rel 12 V5.23 rel 1006	TCFE3 modified for Cr steels	mobility_v21	X12CrCoWVNb 11-2-2: Heat 1, Heat 2 and Heat 3	Austenite, Ferrite, liquid, Laves phase, M_7C_3, $M_{23}C_6$, mod. Z-phase, M_2X (Cr_2N, Mo_2C), MX (VN and NbC)
V5.13 beta16	Fe-data6 modified for Cr steels	mobility_v21	X12CrCoWVNb 11-2-2 Heat 1	Austenite, Ferrite, liquid, Laves phase, M_7C_3, $M_{23}C_6$, mod. Z-phase, M_2X (Cr_2N), MX (VN and NbC)
V5.30 rel 1042	mc_steel	mc_sample_fe and mc_steel	X12CrCoWVNb 11-2-2 Heat 1	Austenite, Ferrite, liquid, Laves phase, M_7C_3, $M_{23}C_6$, mod. Z-phase, Cr_2N, VN and NbC.

Table 7.3. X12CrCoWVNb 11-2-2 simulations: heating and cooling rates considered when using TCFE3 and FE-data6 databases.

Heat treatment: **1060℃ 30 min + 780℃ 2 h**	Cooling from casting: 0.0125 ℃/s Heating up to austenitization temperature: 0.05 ℃/ s Cooling down from austenitization temperature: 0.06 ℃/s Heating up to tempering temperature: 0.24 ℃/s Cooling down from tempering temperature:0.24 ℃/s

Table 7.4. X12CrCoWVNb 11-2-2 simulations: heating and cooling rates considered when using mc_steel database.

Heat treatment: **1060℃ 30 min + 780℃ 2 h**	Cooling from casting: 0.25 ℃/s Heating up to austenitization temperature: 0.02 ℃/ s Cooling down from austenitization temperature: 0.05 ℃/s Heating up to tempering temperature: 0.014 ℃/s Cooling down from tempering temperature:0.01 ℃/s

7.1. Preliminary simulations of X12CrCoWVNb 11-2-2 Heat 1, Heat 2 and Heat 3

MatCalc calculations were carried out on the steels Heat 1, Heat 2 and Heat 3. The calculations covered the thermodynamic equilibrium states (Equilibrium Simulations) (phase fractions and chemical composition of the phases, depending on the temperature) and calculations of the kinetic processes (Kinetic Simulations), considering austenitization, tempering and thermal ageing. For the simulations, a modified TCFE3[8] database for chromium steels was used and the cooling and heating rates presented in Table 7.3 was considered.

Equilibrium Simulations

The results of the X12CrCoWVNb 11-2-2 equilibrium simulations are presented in Figure 7.1 for Heat 1, Figure 7.3 for Heat 2 and Figure 7.4 for Heat 3.

By comparing the equilibrium calculations of the three heats, some deviations could be observed. In all steels, $M_{23}C_6$ was the predominant precipitate phase according to the phase fraction, being stable at temperatures below roughly 900°C. This phase was expected to have high Cr-content (50-65 at%, depending on T), some W (up to 5 at%) and Mo (up to 4 at%).

VN was stable at temperatures below 1200°C. The composition of these precipitates varies strongly over the temperature, with a V/Nb ratio of 4:1 at temperatures below 1000°C, and approximately 1:1 at 1200°C, see Figure 7.2, when the phase was found stable for the first time. As a consequence, MX precipitates formed during austenitization showed a much higher Nb content in the calculations as compared to MX precipitates formed during tempering or service.

For all three Heats simulations, Cr_2N was stable at different temperature regions and with different phase fractions. In Heat 2 and Heat 3, this phase had very low phase fractions, in contrast to Heat 1, where the fraction was going up to 0.38 % at 600°C and therefore, was partially replacing the VN particles.

In all Heats simulated, mod. Z-phase precipitated when considered in the calculations. The phase was stable up to roughly 750°C and totally replaced VN and Cr_2N below this temperature. However, kinetic calculations did not produce this phase at ageing times up to 100000 h.

[8] ThermoCalc AB, Stockholm, Sweden

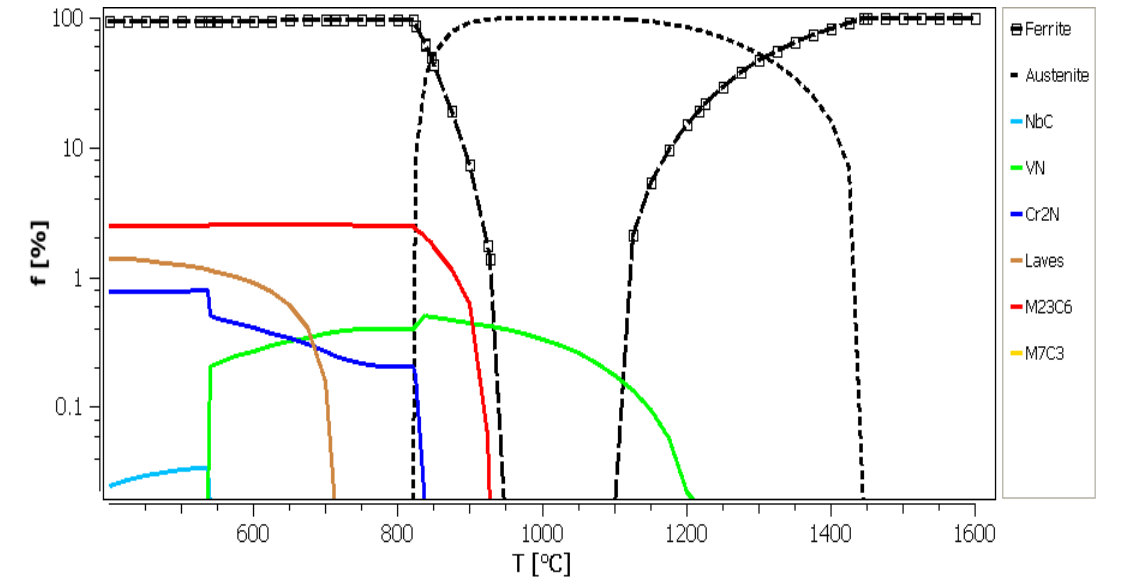

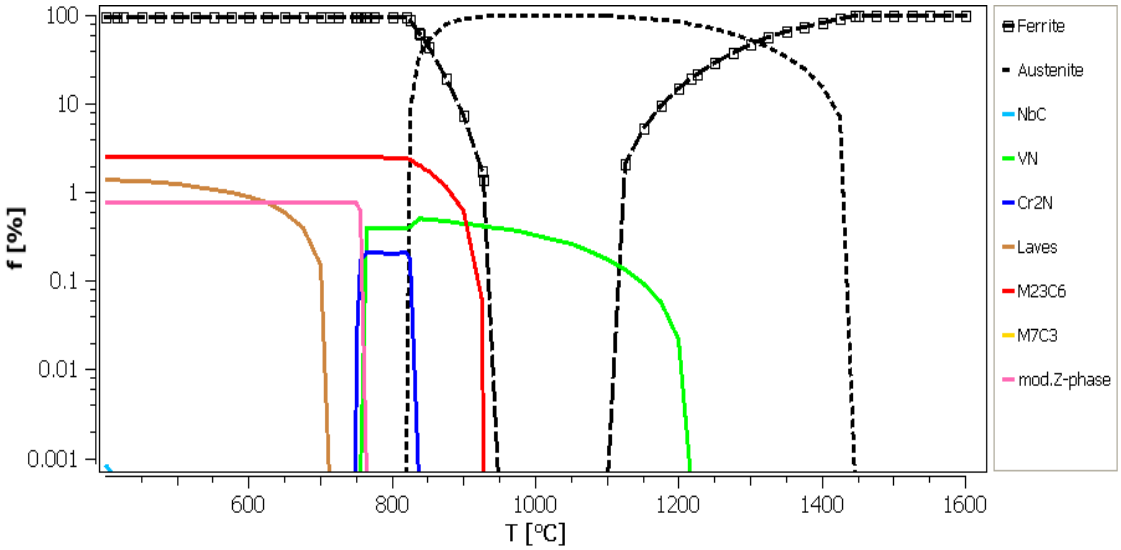

f [%]	Without Z-Phase			With Z-Phase		
T [°C]	**600**	**650**	**780**	**600**	**650**	**780**
$M_{23}C_6$	2.56	2.56	2.52	2.57	2.56	2.52
Laves	0.91	0.61	-	0.90	0.61	-
$(Cr,V)_2N$	0.38	0.34	0.16	-	-	0.16
VN	0.29	0.31	0.43	-	-	0.43
Z	-	-	-	0.78	0.78	-

Figure 7.1. X12CrCoWVNb 11-2-2 Heat 1 equilibrium simulation with TCFE3 modified for chromium steels database: Upper image suppressing mod. Z-phase from the calculation, lower image considering this phase in the calculation. Lower table summarizes the phase fraction of the different precipitates, at the different service temperatures.

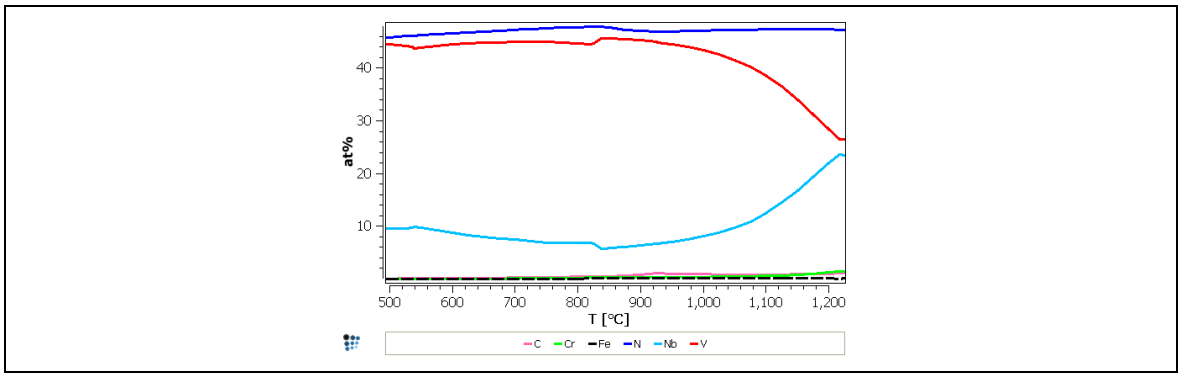

Figure 7.2. X12CrCoWVNb 11-2-2 Heat 1 equilibrium simulation with TCFE3 modified for chromium steels database: MX chemical composition evolution during time (heat treatment and service).

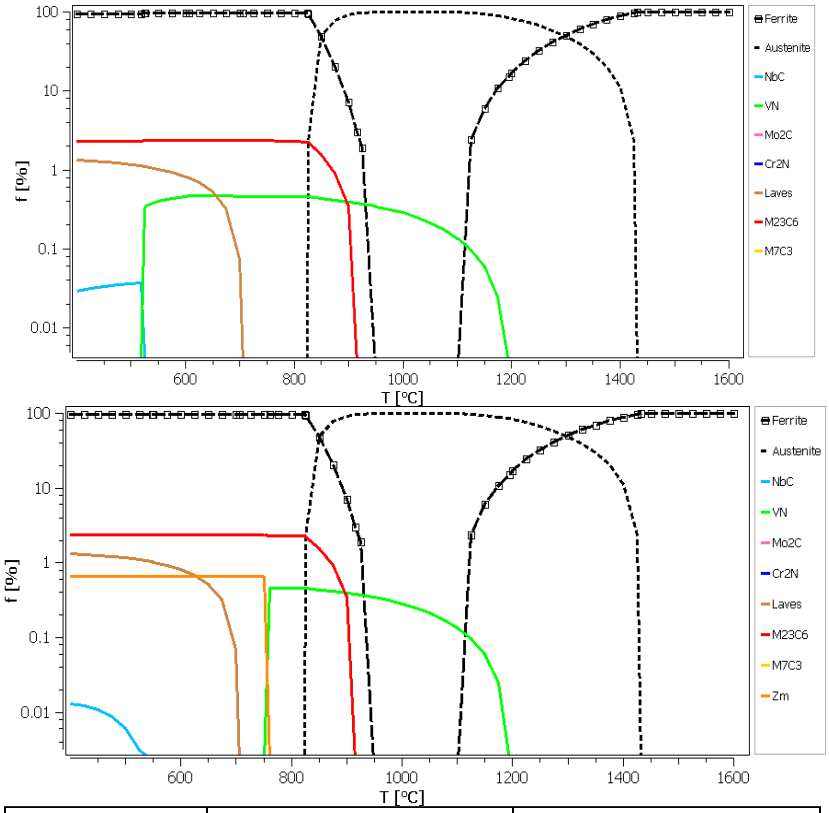

f [%]	without Z-Phase			With Z-Phase		
T [℃]	600	650	780	600	650	780
$M_{23}C_6$	2,36	2,36	2,32	2,37	2,36	2,32
Laves	0,82	0,53	-	0,82	0,52	-
$(Cr,V)_2N$	0,01	-	-	-	-	-
VN	0,46	0,47	0,46	-	-	0,46
Z	-	-	-	0,65	0,65	-

Figure 7.3. X12CrCoWVNb 11-2-2 Heat 2 equilibrium simulation with TCFE3 database modified for chromium steels: Upper graph represents the equilibrium calculation simulated without considering mod. Z-phase into the simulation and lower graph considering mod. Z-phase into the calculation. Lower table summarizes the phase fraction of the different precipitates, at the different service temperatures.

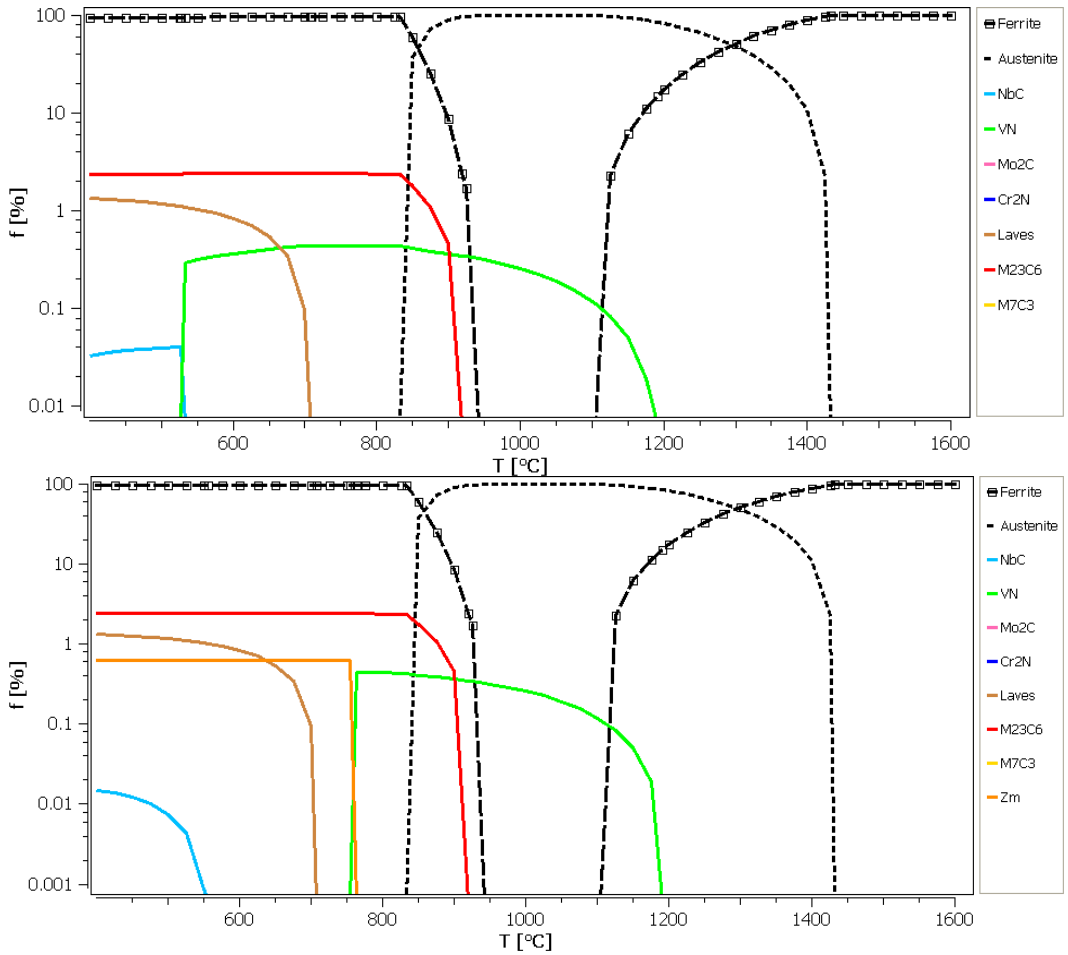

f [%] Heat 3	without Z-Phase			With Z-Phase		
T [℃]	600	650	780	600	650	780
$M_{23}C_6$	2,45	2,45	2,41	2,45	2,45	2,41
Laves	0,84	0,55	-	0,84	0,54	-
$(Cr,V)_2N$	0,12	0,06	-	-	-	-
VN	0,37	0,40	0,44	-	-	0,44
Z	-	-	-	0,63	0,63	-

Figure 7.4. X12CrCoWVNb 11-2-2 Heat 3 equilibrium simulation with TCFE3 modified database for chromium steels: Upper graph represents the calculation without considering mod. Z-phase and the lower graph considering mod. Z-phase into the calculation. Lower table summarizes the phase fraction of the different precipitates, at the different service temperatures.

Kinetic Simulations

The results of the X12CrCoWVNb 11-2-2 kinetic simulations are presented in Figure 7.5 for Heat 1, Figure 7.6 for Heat 2 and Figure 7.7 for Heat 3. Temperature-time curve, phase fraction, mean radii and number density are presented.

First surprising result by performing the kinetic calculations was, that the mod. Z-phase was not forming in any of the three steels at thermal ageing at 650°C up to times of 100000h. Instead, in the calculations of all three Heats VN stayed as the predominant N-containing phase. In Heat 1, VN was found partially replaced by $(Cr,V)_2N$ on the long run (decrease of 30 %), in Heat 2 and Heat 3, the phase fraction was staying totally constant. VN coarsened slightly, their mean radii were calculated between 20-30 nm.

The calculations showed that $(Cr,V)_2N$ was forming in Heat 1 and Heat 3. In either cases, the precipitates grew or coarsened respectively, but were keeping a relatively small radius, below 70 nm.

$M_{23}C_6$ formed with its equilibrium phase fraction (2.3-2.4 %) after tempering and coarsens strongly in all steels, starting with a radius of roughly 60-100 nm and was growing up to 200-300 nm after 100000 h of thermal ageing.

When considering the number of particles per unit volume as a first indication for good creep performance, it turned out in the calculations that VN seemed to be the most important phase in all three Heats, followed by $(Cr,V)_2N$ and $M_{23}C_6$, and Laves phase as the least significant one. For this reason, it was of particular interest to repress the formation of mod. Z-phase, as the result of the dissolution of VN at expenses of mod. Z-phase formation. Although the first kinetic calculations encourage optimistic expectations, the experimental investigations showed other results, and adjustments in the database were carried out.

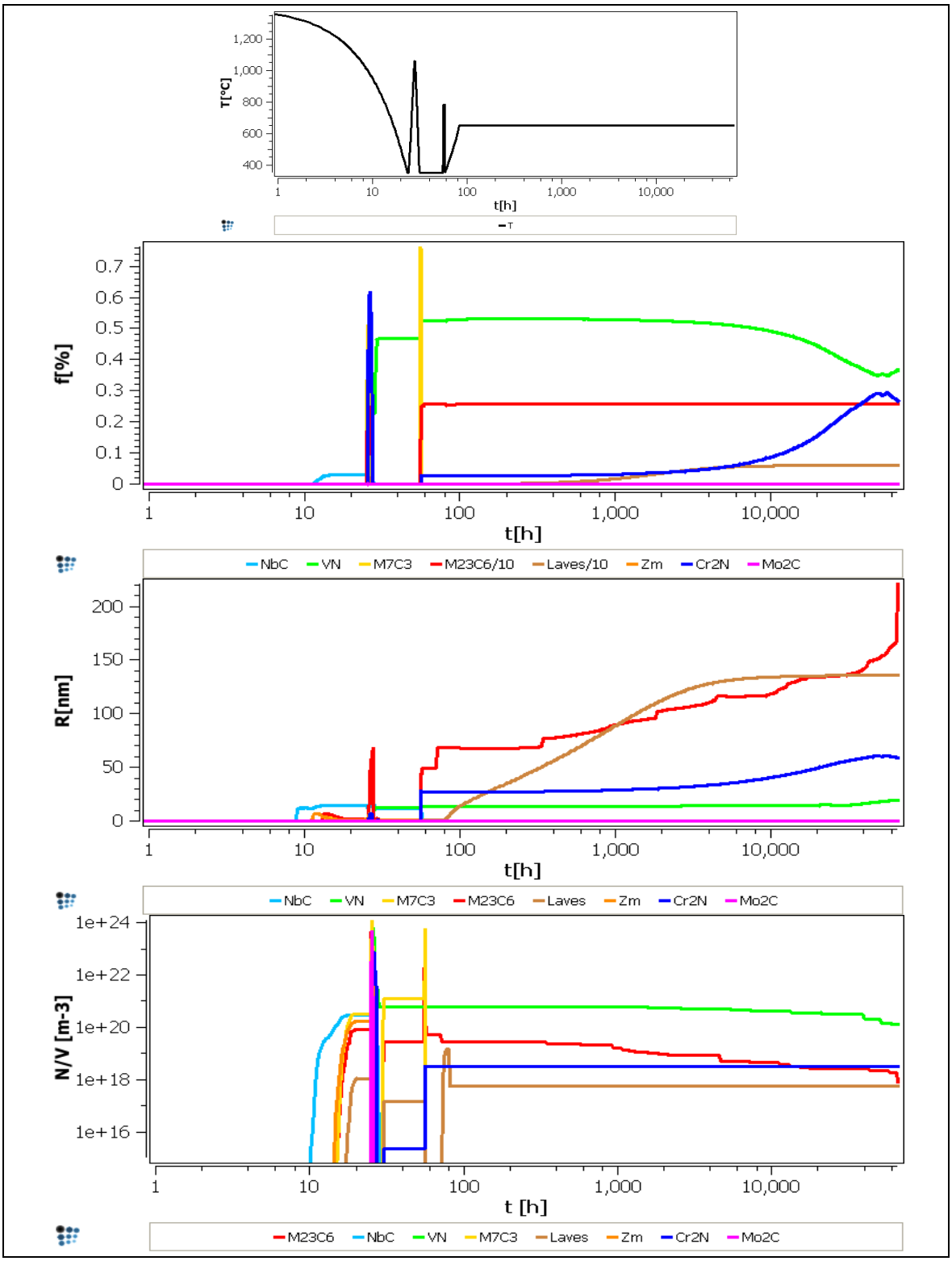

Figure 7.5. X12CrCoWVNb 11-2-2 Heat 1 kinetic simulation with TCFE3 modified for chromium steels database at 650℃: The first graph represents the temperature history applied on the material: cooling after casting, austenitization, tempering and service. The following graphs represent the phase fractions (f[%]), mean radii (R[nm]) and number densities (N/V[m^{-3}]) of the individual precipitates phases.

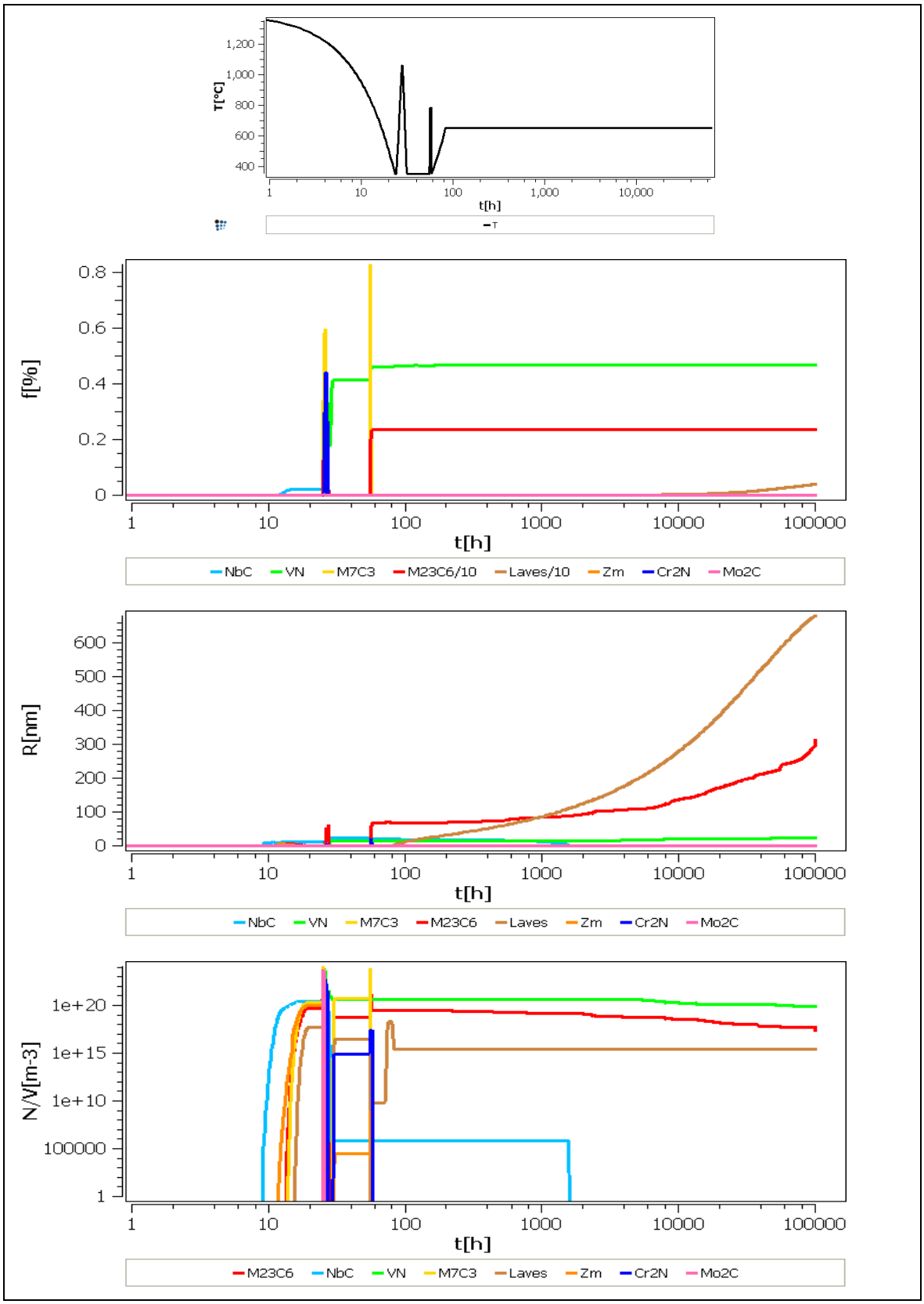

Figure 7.6. X12CrCoWVNb 11-2-2 Heat 2 kinetic simulation with TCFE3 modified for chromium steels database at 650℃: The first graph represent s the temperature history applied on the material: cooling after casting, austenitization, tempering and service. The following graphs represent the phase fractions (f[%]), mean radii (R[nm]) and number densities (N/V[m^{-3}]) of the individual precipitates phases.

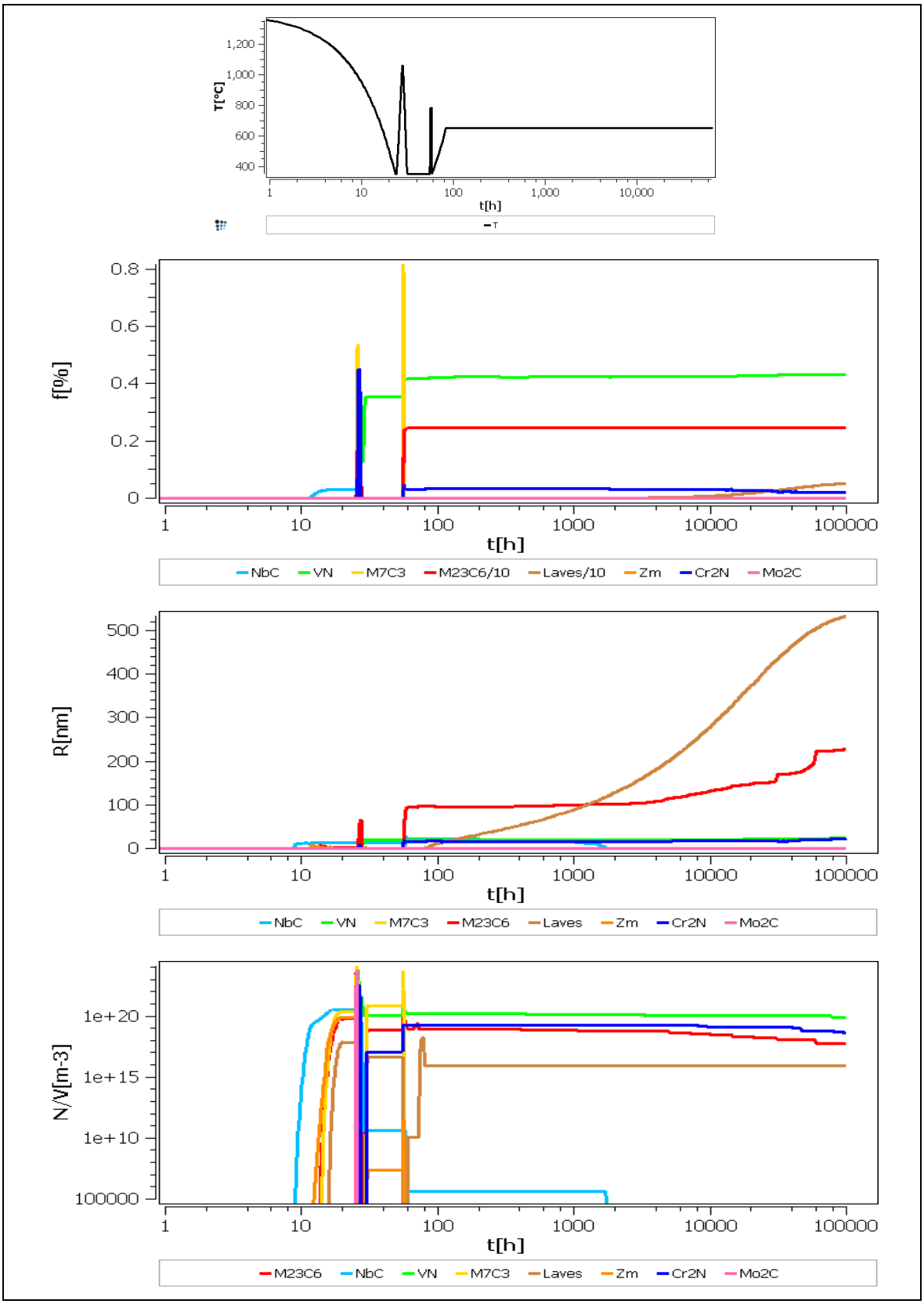

Figure 7.7. X12CrCoWVNb 11-2-2 Heat 3 kinetic simulation with TCFE3 modified for chromium steels database at 650℃: The first graph represent s the temperature history applied on the material: cooling after casting, austenitization, tempering and service. The following graphs represent the phase fractions (f[%]), mean radii (R[nm]) and number densities (N/V[m^{-3}]) of the individual precipitates phases.

7.2. Comparison of two different databases

After the results from the preliminary simulations (presented in the chapter 7.1), the further work focussed only in Heat 1 and thus complementing the experimental investigations. In order to adjust the discrepancies between the first simulations and the experimental results, two databases were chosen, with adjustments on the thermodynamics of the mod. Z-phase done by Danielsen [18]: TCFE3 and Fe-data6 modified for chromium steels, and the results were compared.

Equilibrium Simulations

The results of the X12CrCoWVNb 11-2-2 equilibrium simulations are presented in Figure 7.8 for the modified TCFE3 database and Figure 7.9 for the modified Fe-data6.

The equilibrium simulations were not showing significant differences when using the two databases. $M_{23}C_6$ was found the predominant phase showing a constant phase fraction of 2.5 % at temperatures below roughly 800℃ with high (see Figure 7.8 and Figure 7.9) Cr and C contents, 63% and 21% mole fraction respectively, and some amount of W and Mo (2% and 4% mole fraction, respectively). VN was found stable at temperatures below 1200℃. Surprisingly, Cr_2N was not found forming in either of the new simulations. Laves phase was stable at temperatures below 700℃ and its phase fraction increased with decreasing temperature. The NbC was found only stable between 1000-850℃ showing a mole fraction of 0.03%. Mod. Z-phase became a stable phase approximately below 950℃, with almost 1 % of phase fraction, see lower graphs of Figure 7.8 and Figure 7.9. As soon as the mod. Z-phase was considered into the calculations, the VN phase was only stable phase at high temperatures, 1200 to 800℃.

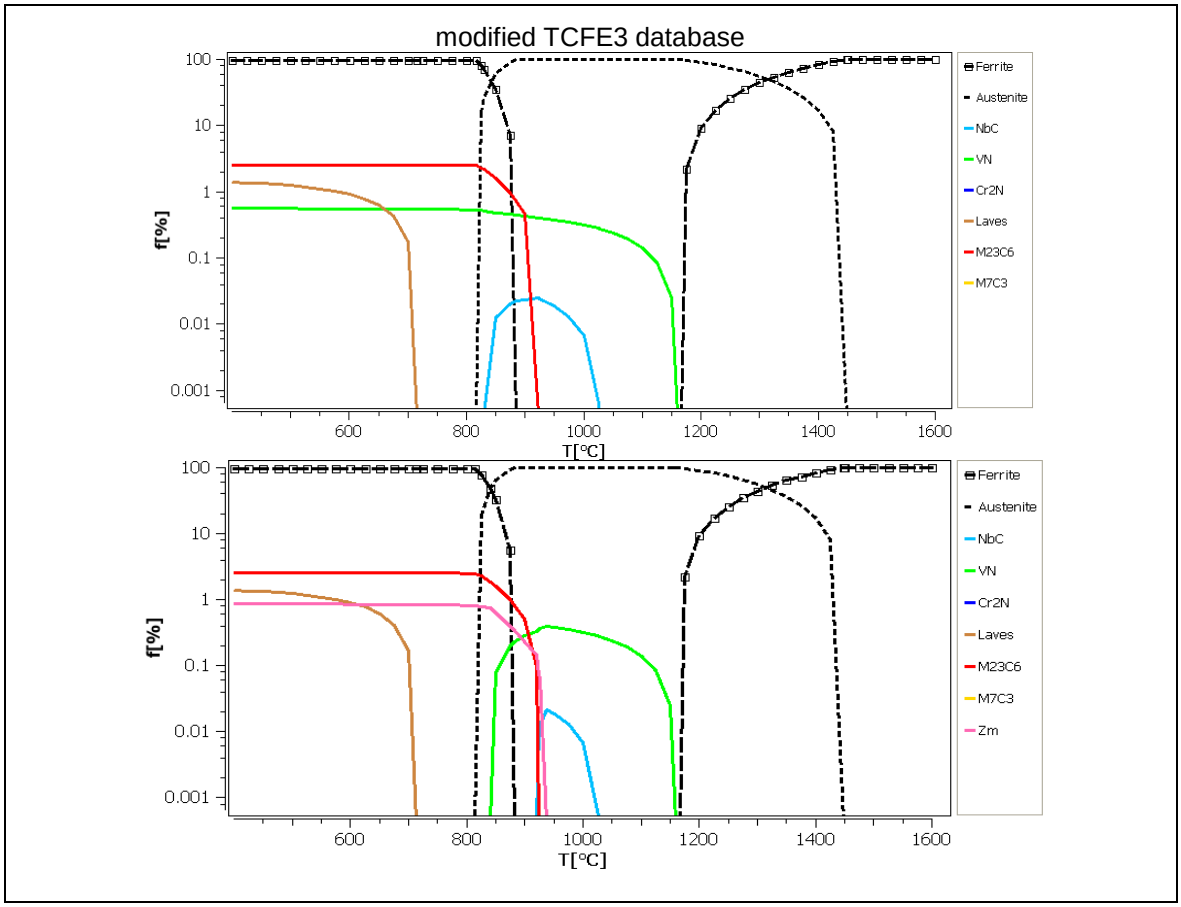

Figure 7.8. X12CrCoWVNb 11-2-2 Heat 1 equilibrium simulation using TCFE3 database modified for chromium steels with implementations on the thermodynamics of mod. Z-phase [18]: Upper graph simulated without consider mod. Z-phase and in lower graph mod. Z-phase was considered in the simulation.

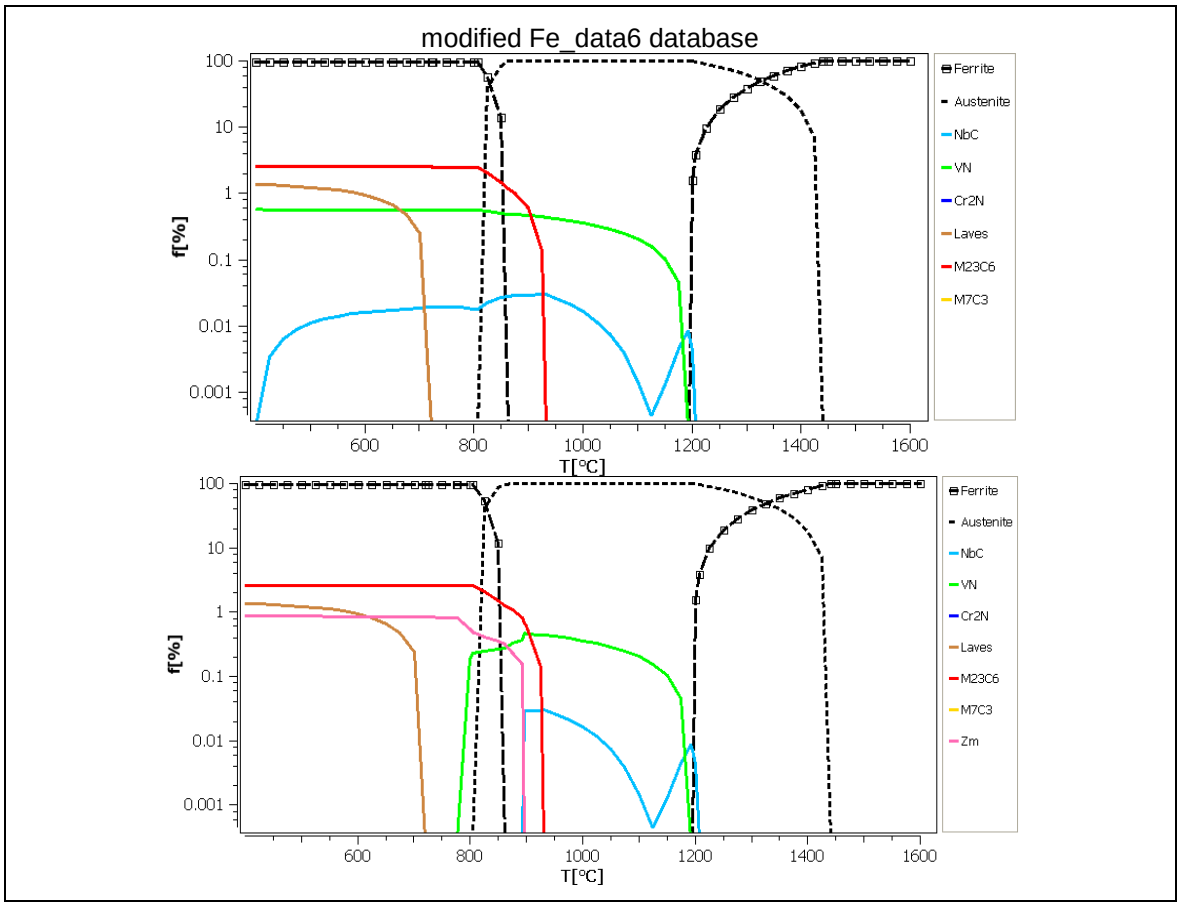

Figure 7.9. X12CrCoWVNb 11-2-2 Heat 1 equilibrium simulation using Fe_data6 database modified for chromium steels with implementations on the thermodynamics of mod. Z-phase [18]: Upper equilibrium calculation graph was simulated without consider mod. Z-phase and in lower equilibrium calculation graph mod. Z-phase was considered in the simulation.

Kinetic Simulations

The results of the X12CrCoWVNb 11-2-2 kinetic simulations are presented from Figure 7.10 to Figure 7.15. The following conclusions could be taken:

- The precipitation of mod. Z-phase started to form after 4000 h (<1year), increasing its phase fraction during aging. Parallel, VN decreased its phase fraction at the same starting point of time, whether the most of was shortcut to precipitates.
- $M_{23}C_6$ precipitates formed during the tempering and they kept their phase fraction constant at 2.5 % during the thermal aging process showing a mean radius of approximately 80 nm. After approximately 6000 h aging time, they started to coarse by increasing their mean radii to more than 100 nm.
- Laves phase particles precipitated after 200 h of service. No significant coarsening rate could be observed in this phase. The mean radius was found almost constant at 25 nm with a 1.0 % of phase fraction.
- M_7C_3 formed during the heating up in the tempering process but at tempering temperature this phase dissolved and the phase fraction becomes zero.
- Cr_2N did not form during the entire kinetic calculation, following the results obtained in the equilibrium calculations.
- By using the databases, the Z-phase (Zp) replaced VN on the long run. However, NbC and Zm behave differently depending on the applied database: When applying TCFE3 database, Zm

replaced the NbC precipitates. In the Fe_data6 database, the phase fraction of NbC precipitates after austenitization remained more or less constant, while only a small amount of Zm was formed.

When service temperature was increased in the simulations from 575 to 625℃, the diffusion in the mate rial increased and all the processes; nucleation, growth and coarsening, became faster.

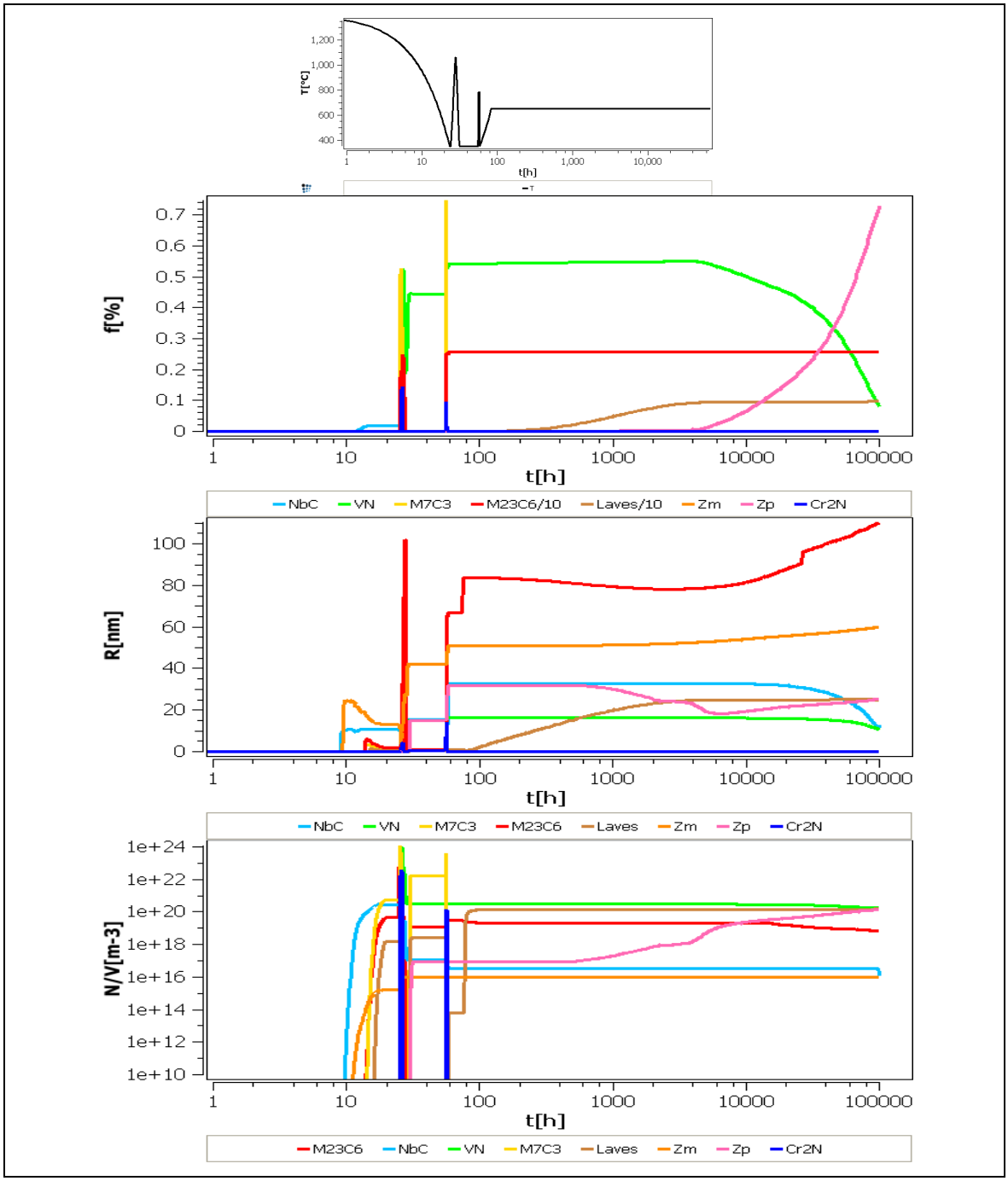

Figure 7.10. X12CrCoWVNb 11-2-2 Heat 1 kinetic simulation with TCFE3 modified for chromium steels database and with implementations on the thermodynamics of the mod. Z-phase, at 575℃: The first graph represents the temperature history applied on the material: cooling after casting, austenitization, tempering and service. The following graphs represent the phase fractions (f[%]), mean radii (R[nm]) and number densities (N/V[m^{-3}]) of the individual precipitates phases.

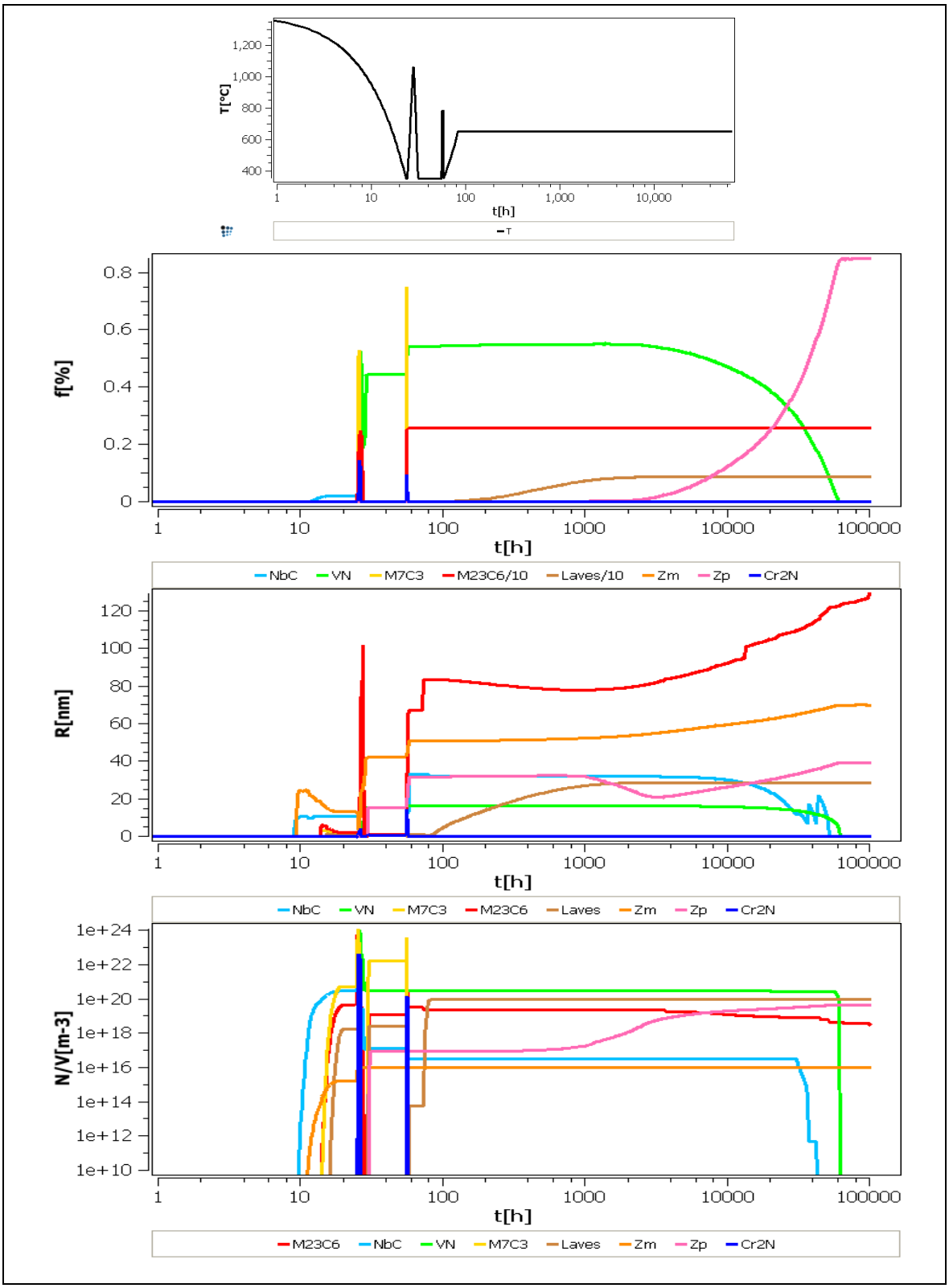

Figure 7.11. X12CrCoWVNb 11-2-2 Heat 1 kinetic simulation with TCFE3 modified for chromium steels database and with implementations of the thermodynamics of mod. Z-phase, at 600℃: The first graph represents the temperature history applied on the material: cooling after casting, austenitization, tempering and service. The following graphs represent the phase fractions (f[%]), mean radii (R[nm]) and number densities (N/V[m^{-3}]) of the individual precipitates phases.

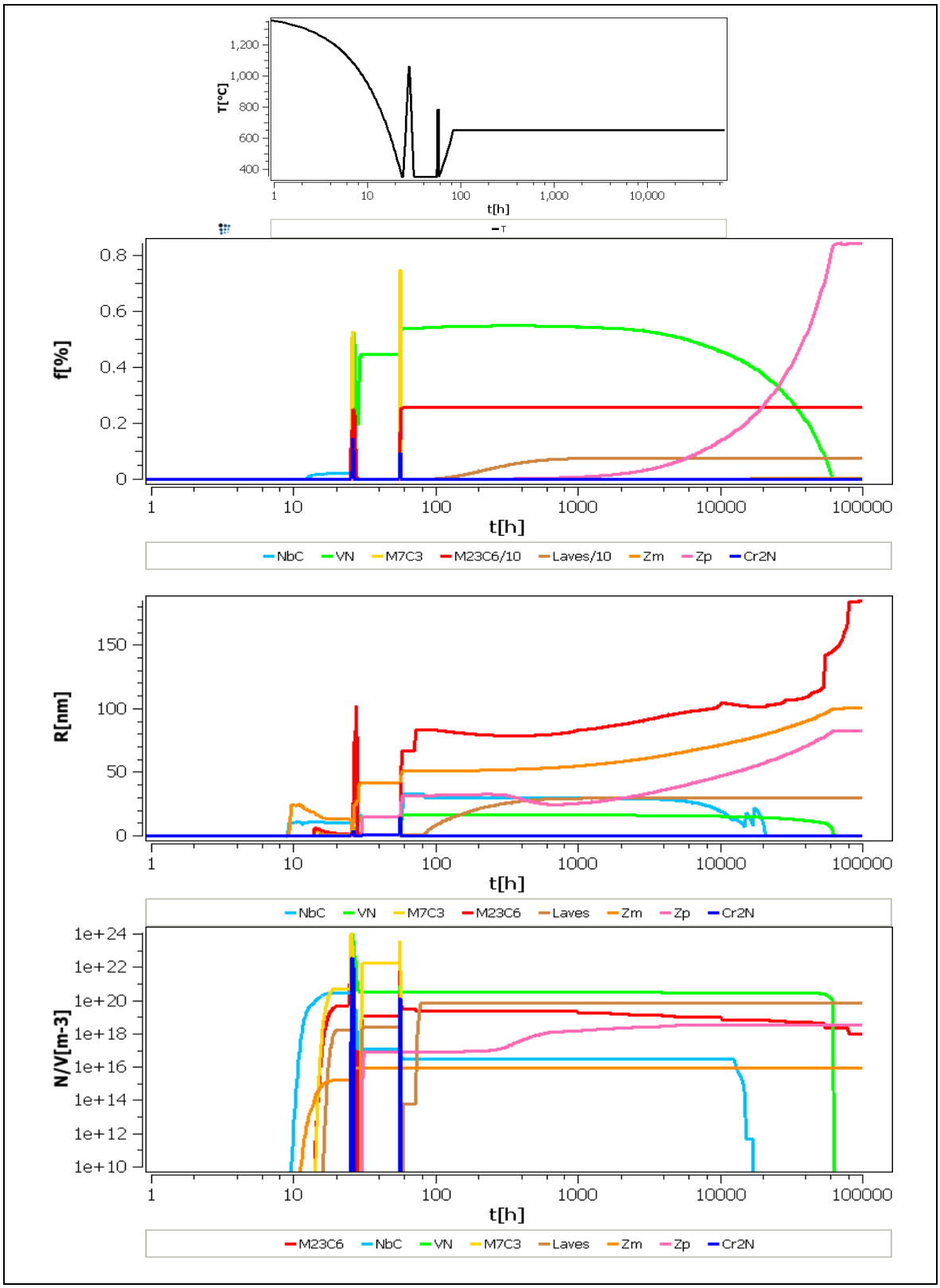

Figure 7.12. X12CrCoWVNb 11-2-2 Heat 1 kinetic simulation with TCFE3 modified for chromium steels database and with implementations of the thermodynamics of mod. Z-phase, at 625℃: The first graph represents the temperature history applied on the material: cooling after casting, austenitization, tempering and service. The following graphs represent the phase fractions (f[%]), mean radii (R[nm]) and number densities (N/V[m^{-3}]) of the individual precipitates phases.

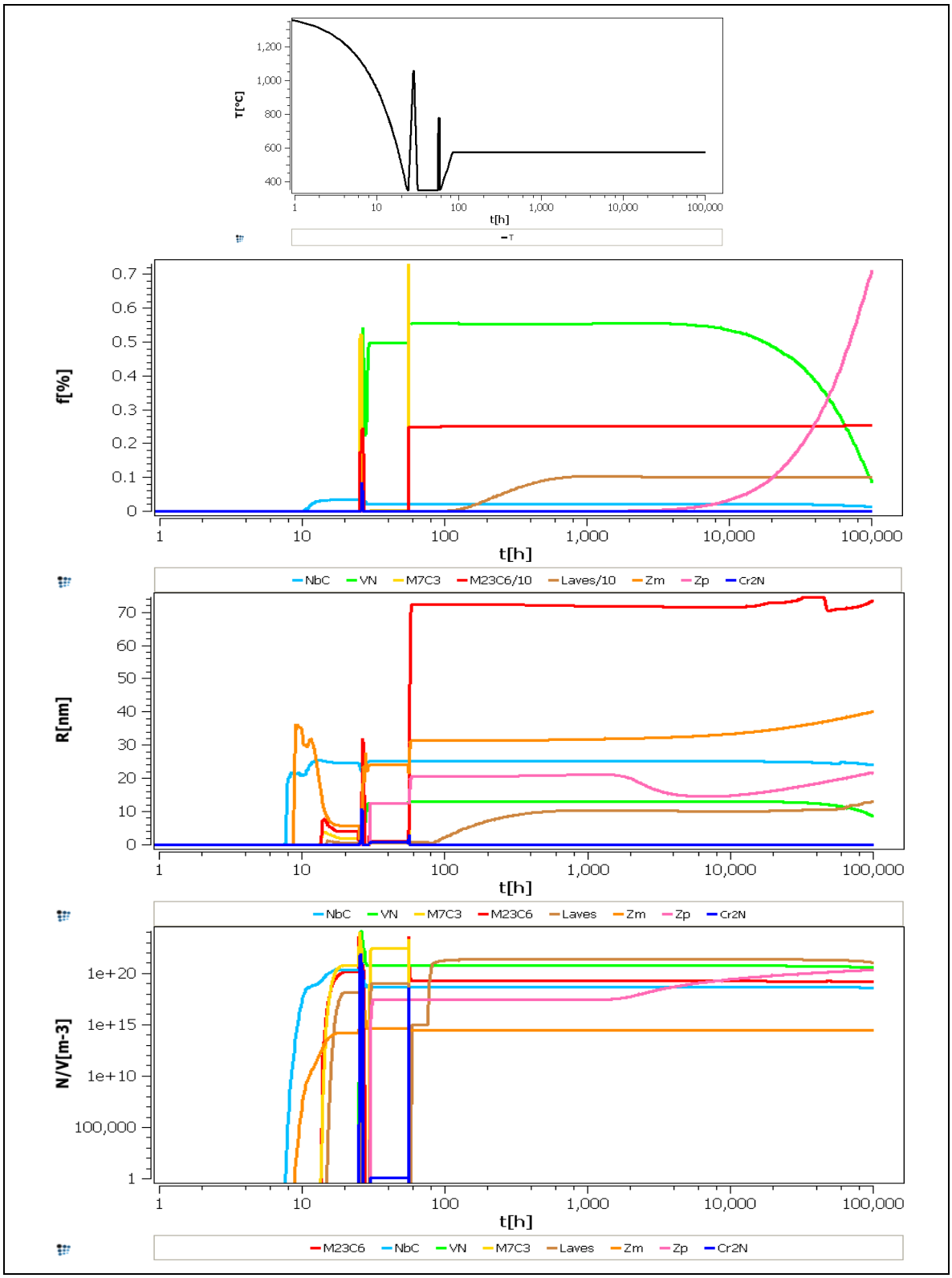

Figure 7.13. X12CrCoWVNb 11-2-2 Heat 1 kinetic simulation with Fe_data6 modified for chromium steels database and with implementations of the thermodynamics of mod. Z-phase, at 575℃: The first graph the temperature history applied on the material: cooling after casting, austenitization, tempering and service. The following graphs represent the phase fractions (f[%]), mean radii (R[nm]) and number densities (N/V[m^{-3}]) of the individual precipitates phases.

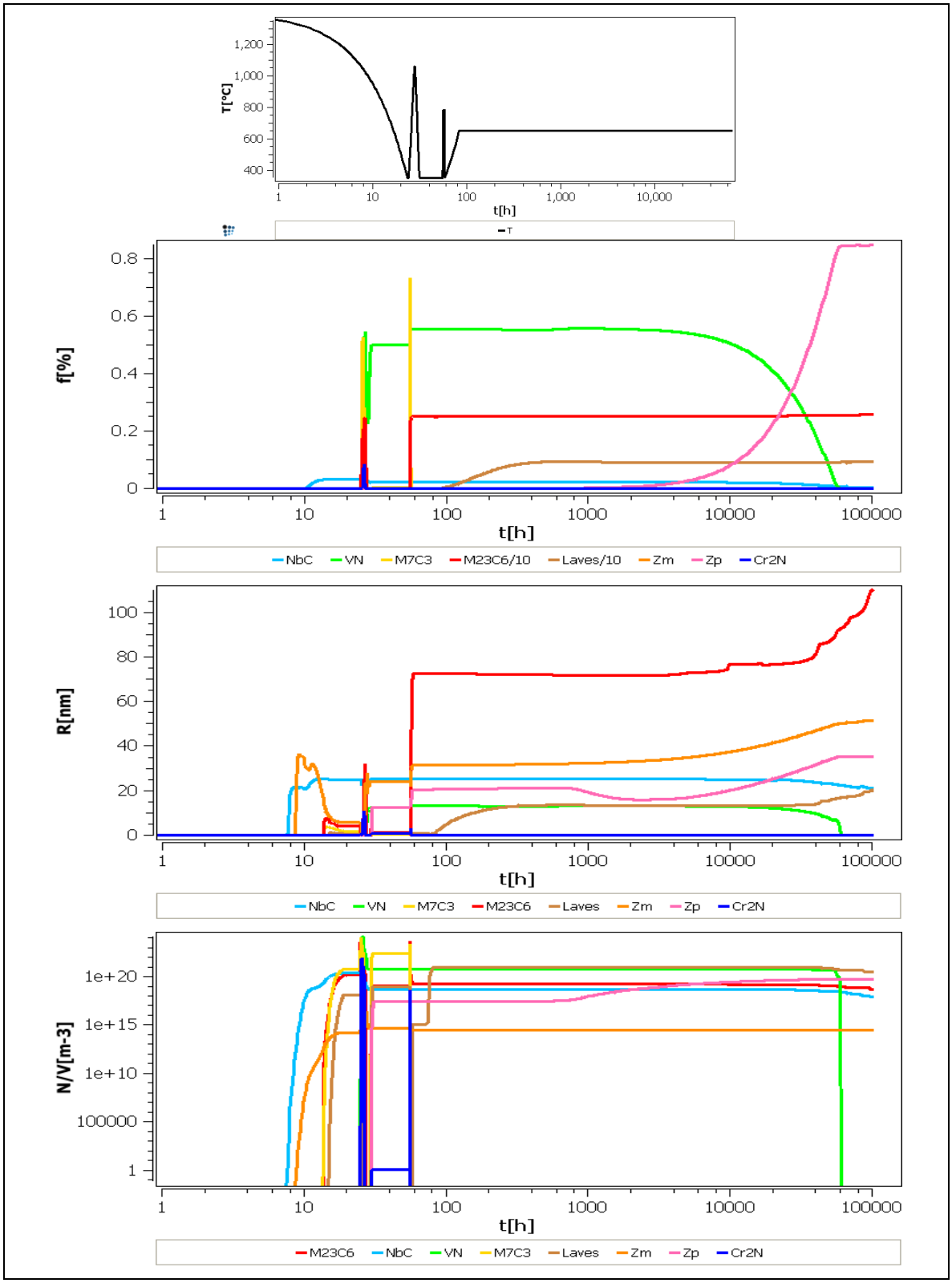

Figure 7.14. X12CrCoWVNb 11-2-2 Heat 1 kinetic simulation with Fe_data6 modified for chromium steels database and with implementations of the thermodynamics of mod. Z-phase, at 600℃: The first graph the temperature history applied on the material: cooling after casting, austenitization, tempering and service. The following graphs represent the phase fractions (f[%]), mean radii (R[nm]) and number densities (N/V[m^{-3}]) of the individual precipitates phases.

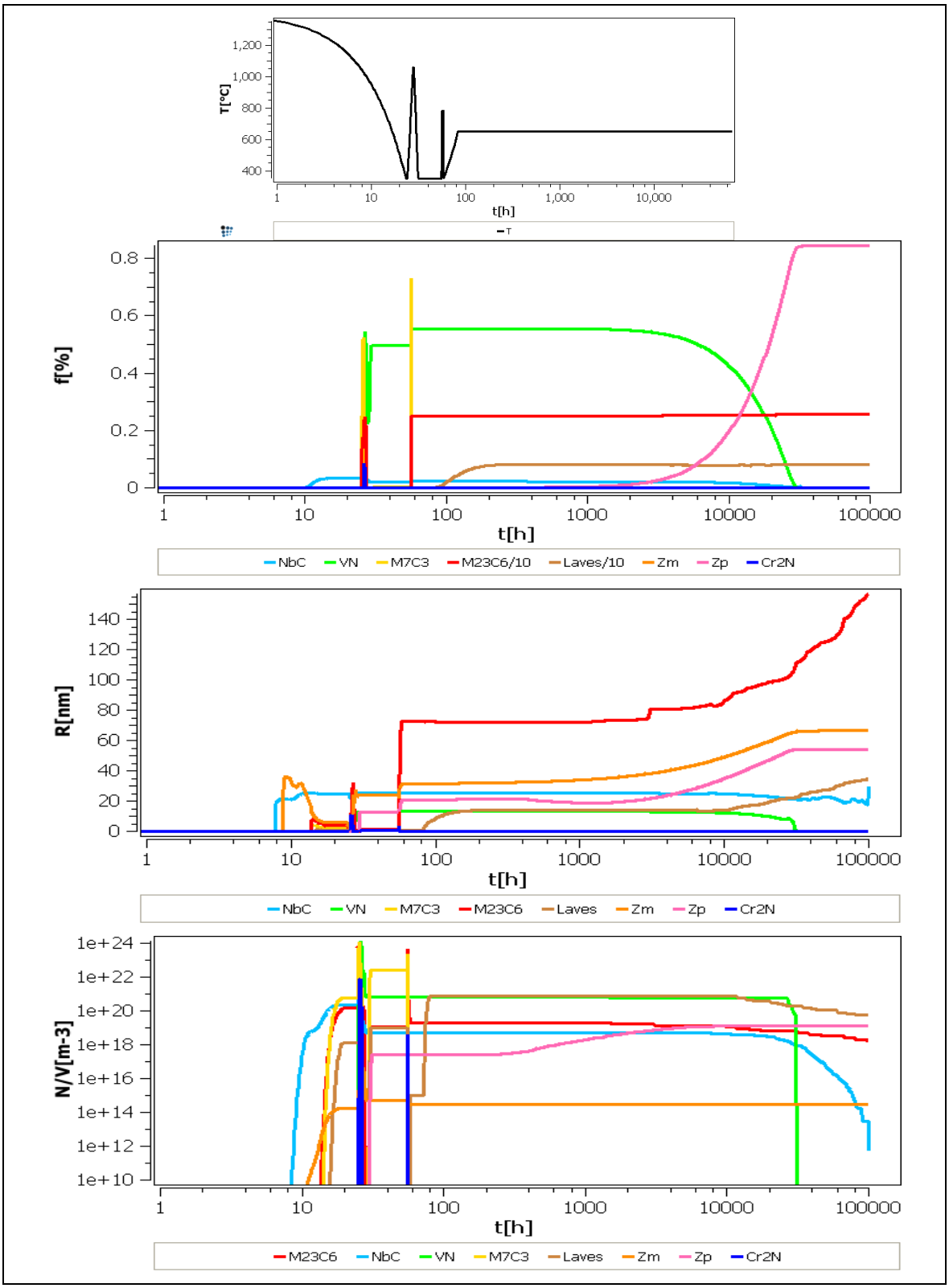

Figure 7.15. X12CrCoWVNb 11-2-2 Heat 1 kinetic simulation with Fe_data6 modified for chromium steels database and with implementations of the thermodynamics of mod. Z-phase, at 625℃: The first graph represents the temperature history applied on the material: cooling after casting, austenitization, tempering and service. The following graphs represent the phase fractions (f[%]), mean radii (R[nm]) and number densities (N/V[m^{-3}]) of the individual precipitates phases.

7.3. Optimization of database

The results presented in the previous simulations (section 7.1 and 7.2) showed discrepancies in the behaviour of Cr_2N and mod. Z-phase, revealing the need to perform adjustments in their thermodynamics. The TCFE3 database was selected for further simulations and implementations on the thermodynamics of Cr_2N and mod. Z-phase were done. Afterwards the simulations were compared with the experimental results performed in this work.

7.3.1. Changes of Gibbs energy for M_2X: -2500 J/mol

Changes in the thermodynamics parameters of the M_2X (Cr_2N) were performed. Following the experimental results, the setting of the Gibbs energy for M_2X (Cr_2N) phase was decreased to -2500J/mol, making this phase more stable. Taking into account the new thermodynamic parameters, new equilibrium and kinetic calculations were carried out.

Equilibrium Simulations

Table 7.5 and Table 7.6 together with Figure 7.16 to Figure 7.19 summarize the results of the equilibrium simulations.

Calculated $M_{23}C_6$ and Laves phases showed the no influence when introducing the thermodynamic changes in the database of the Gibbs energy for chromium nitrides. $M_{23}C_6$ forms roughly at 900ºC increasing its phase fraction until 2.5 % keeping this value constant at lower temperatures. Laves phase precipitate at 700ºC increasing its phase fraction until 1.5 % at 400ºC.

M_2X (Cr_2N), MX (VN and NbC) and mod. Z-phase, the nitrides phases, showed different behaviour when the thermodynamics parameters were adjusted for M_2X (Cr_2N). When Gibbs energy of the M_2X (Cr_2N) phase remained like in previous calculations, mod. Z-phase became the equilibrium phase from 950ºC until 400ºC keeping its phase fraction constant at 0.85 % and replacing VN phase. When the Gibbs energy of the M_2X was modified (-2500 J/mol), making this phase more stable (according to the experimental results), the mod. Z-phase became stable from 550ºC until 400ºC with a phase fraction of approximately 0.8 %. M_2X (Cr_2N) precipitated at 850ºC with a constant phase fraction approximately of 0.2 %. Because of the changes in the thermodynamics of the M_2X (Cr_2N) phase, NbC particles formed at 1000ºC and its phase fraction decreased to totally dissolution after 575ºC.

Following the results of the equilibrium simulations, due to the decrease of the Gibbs energy of M_2X, this phase became stable at the service temperature of our samples (575ºC, 600ºC and 625ºC). Therefore, the mod. Z-phase was not predicted as stable phase at those temperatures.

Table 7.5. X12CrCoWVNb 11-2-2 Heat 1 equilibrium calculation: The TCFE3 database modified for chromium steels, with implementations on the thermodynamics of the mod. Z-phase, considering thermodynamic changes of the M_2X phase (-2500 J/mol) was used for the calculation.

f [%]	**Without Z-Phase**			**With Z-Phase**		
T [℃]	**575**	**600**	**625**	**575**	**600**	**625**
$M_{23}C_6$	2.54	2.54	2.54	2.54	2.54	2.54
Laves	1	0.95	0.8	1.02	0.91	0.78
$(Cr,V)_2N$	0.17	0.17	0.17	0.17	0.17	0.16
VN	0.43	0.43	0.43	0.43	0.42	0.43
NbC	0.01	0.01	0.01	0.008	0.008	0.008
mod. Z-phase	-	-	-	0	0	0

Table 7.6. X12CrCoWVNb 11-2-2 Heat 1 equilibrium calculation: The TCFE3 database modified for chromium steels, with implementations on the thermodynamics of the mod. Z-phase, without considering the changes in the thermodynamics of M_2X phase was used for the calculation.

f [%]	Without Z-Phase			With Z-Phase		
T [℃]	**575**	**600**	**625**	**575**	**600**	**625**
$M_{23}C_6$	2.56	2.56	2.56	2.56	2.56	2.56
Laves	1.02	0.90	0.78	1.01	0.90	0.77
$(Cr,V)_2N$	0	0	0	0	0	0
VN	0.55	0.55	055	0	0	0
NbC	0	0	0	0	0	0
mod. Z-phase	-	-	-	0.85	0.85	0.85

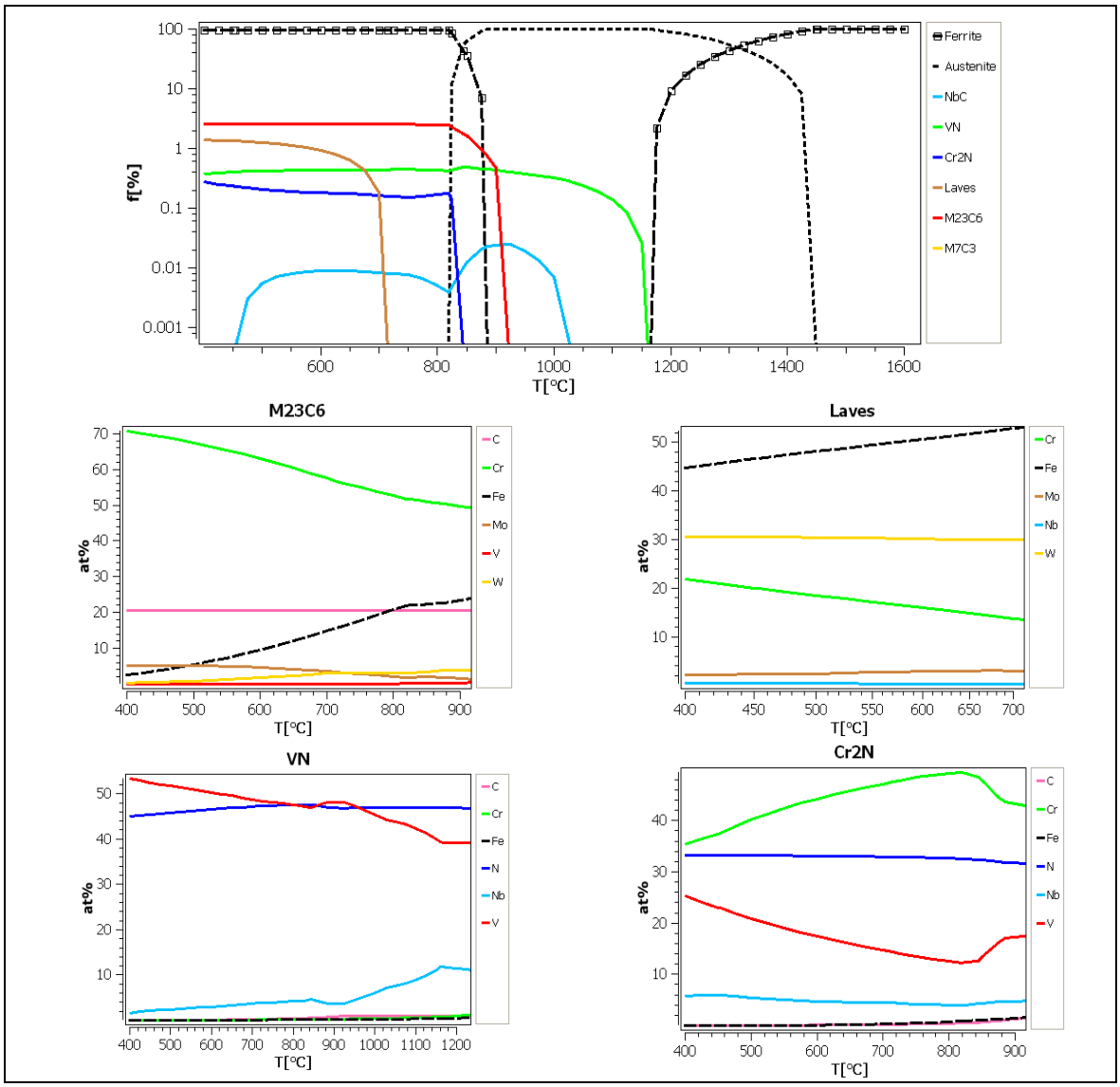

Figure 7.16. X12CrCoWVNb 11-2-2 Heat 1 equilibrium simulation: Equilibrium phase fraction and composition diagram for each phase with TCFE3 modified for chromium steels database, with implementations of the thermodynamics of mod. Z-phase, without considering the mod. Z-phase and changing the Gibbs energy to -2500J/mol for M_2X phase.

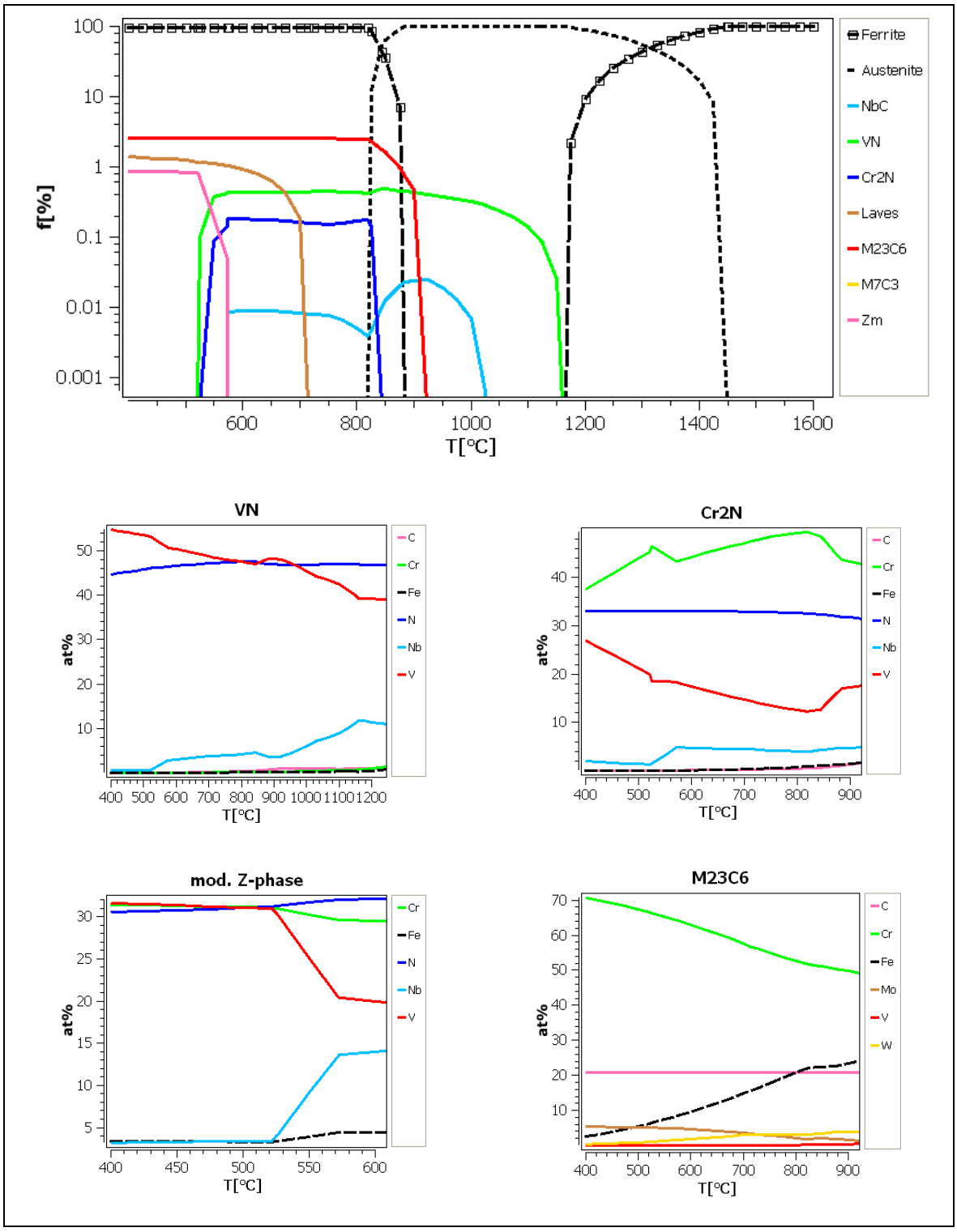

Figure 7.17. X12CrCoWVNb 11-2-2 Heat 1 equilibrium simulation: Equilibrium phase fraction and composition diagram for each phase with TCFE3 modified for chromium steels database, with implementations of the thermodynamics of mod. Z-phase, considering the mod. Z-phase and changing the Gibbs energy to -2500J/mol for M_2X phase.

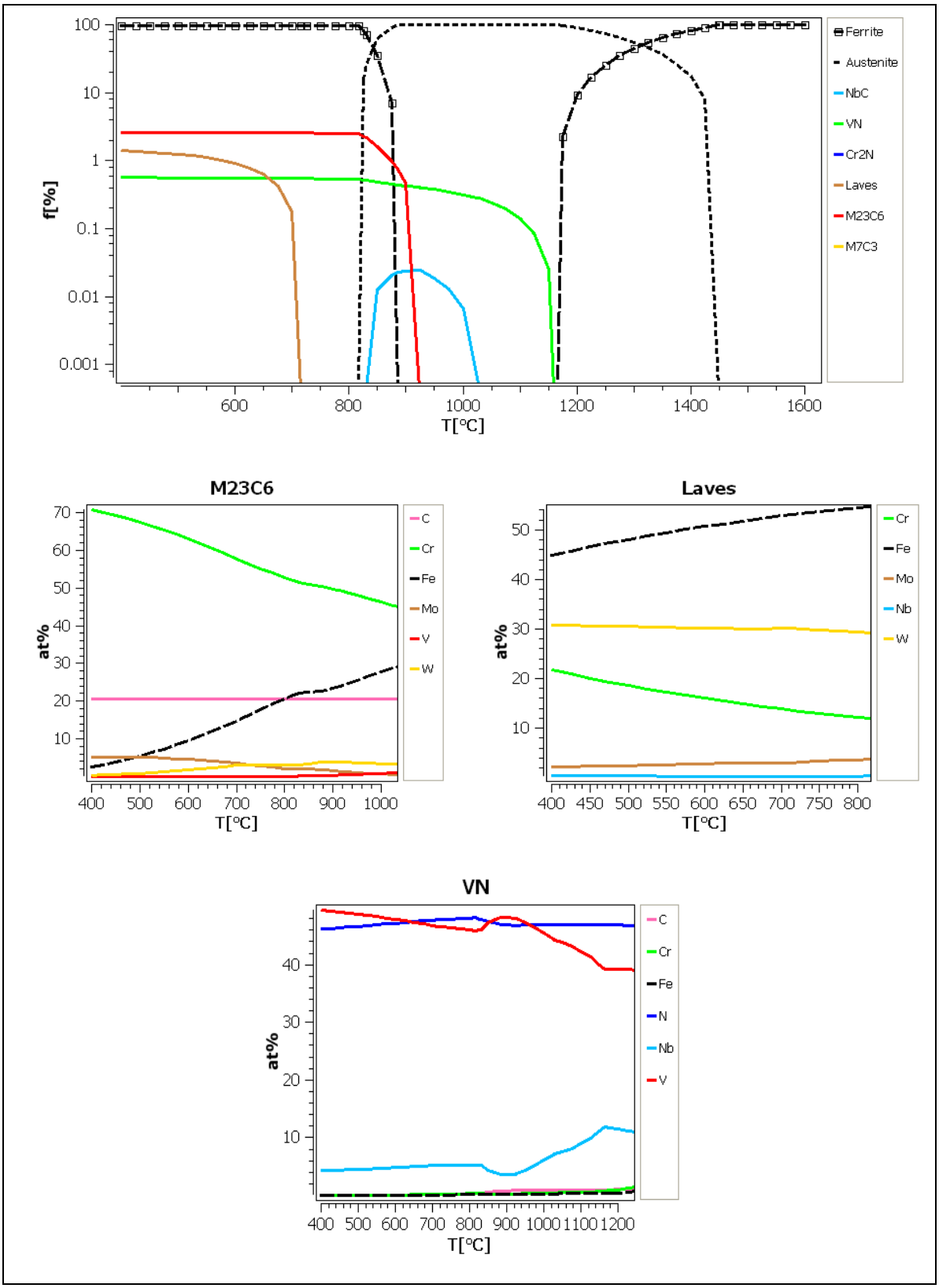

Figure 7.18. X12CrCoWVNb 11-2-2 Heat 1 equilibrium simulation: Equilibrium phase fraction and composition diagram for each phase with TCFE3 modified for chromium steels database, with implementations of the thermodynamics of mod. Z-phase, without considering the mod. Z-phase and without changing the Gibbs energy for M_2X phase.

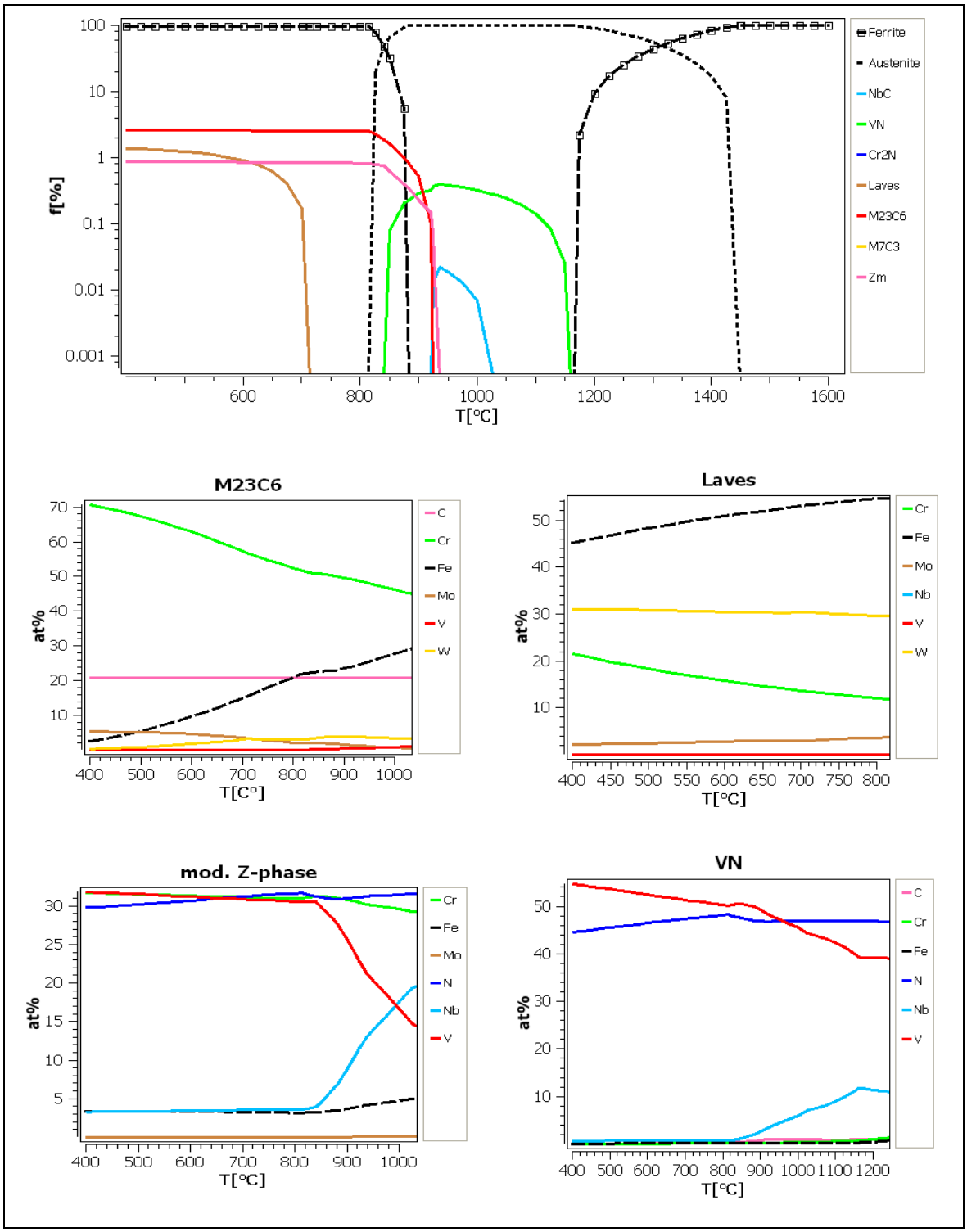

Figure 7.19. X12CrCoWVNb 11-2-2 Heat 1 equilibrium simulation: Equilibrium phase fraction and composition diagram for each phase with TCFE3 modified for chromium steels database, with implementations of the thermodynamics of mod. Z-phase, considering the mod. Z-phase and without changing the Gibbs energy for M_2X phase.

Kinetic Simulations

Figure 7.20, Figure 7.21 and Figure 7.22 represent the kinetic simulations of X12CrCoWVNb 11-2-2 Heat 1 with the TCFE3 modified for chromiun steels, with implementations on the thermodynamics of the mod. Z-phase, and the thermodynamic adjustments of the Gibbs energy for M_2X phase.

The Gibbs energy of M_2X (Cr_2N) phase has been decreased in the databases to stabilize this phase up to -2500 J/mol. When this change is considered, the $M_{23}C_6$, VN, Cr_2N as well as mod. Z-phase are stable phases up to 10000 h at 575℃, up to 4000 h at 600° C and up to 2000 h at 625℃. Precipitation of Laves phase occurs after 200 h, 400 h and 2000 h of service at 575℃, 600℃ and 625℃, respectively. Moreover, the mean radius of this phase at the end of the calculation is 35 nm at 575℃ and 600℃, 220 nm at 625℃, see Figure 7.20, Figure 7.21 and Figur e 7.22.

VN showed higher phase fraction as the M_2X, 0.4 and 0.2 % respectively. The highest phase fraction was predicted for $M_{23}C_6$ phase with 2.5 %, thereupon of Laves phase with 1 %. When mod. Z-phase precipitate, VN phase dissolves as first, followed by Cr_2N. Afterwards, mod. Z-phase is the stable nitride phase, see see Figure 7.20, Figure 7.21 and Figure 7.22.

The mean radii was also calculated. $M_{23}C_6$ phase increases its mean radius from 80 nm to 85 nm, 100 nm and 200 nm at 575℃, 600℃ and 625℃, respective ly. VN and Cr_2N have a constant mean radius of 5 and 15 nm respectively at all simulated temperatures. Laves phase shows a mean radii of 35 nm at 575℃ and 600℃; however, at 625℃ it was 200 nm, s ee see Figure 7.20, Figure 7.21 and Figure 7.22. The Laves phase showed a strong coarsening in the calculations that was not observed in the experimental investigations.

In all the kinetic simulations graphs also the experimental results are ploted (see Figure 7.20, Figure 7.21 and Figure 7.22). The predicted radius of the $M_{23}C_6$ phase was higher as the experimental results showed. Contrary, for the Cr_2N and VN it was lower. The calculations predicted faster dissolution of the VN and Cr_2N and faster precipitation of the mod. Z-phase. Moreover, the siumlated number densitiy of the Cr_2N and VN was higher than the experimental values, contrary $M_{23}C_6$ had good agreement between the number density simulated and the experimentally obtained.

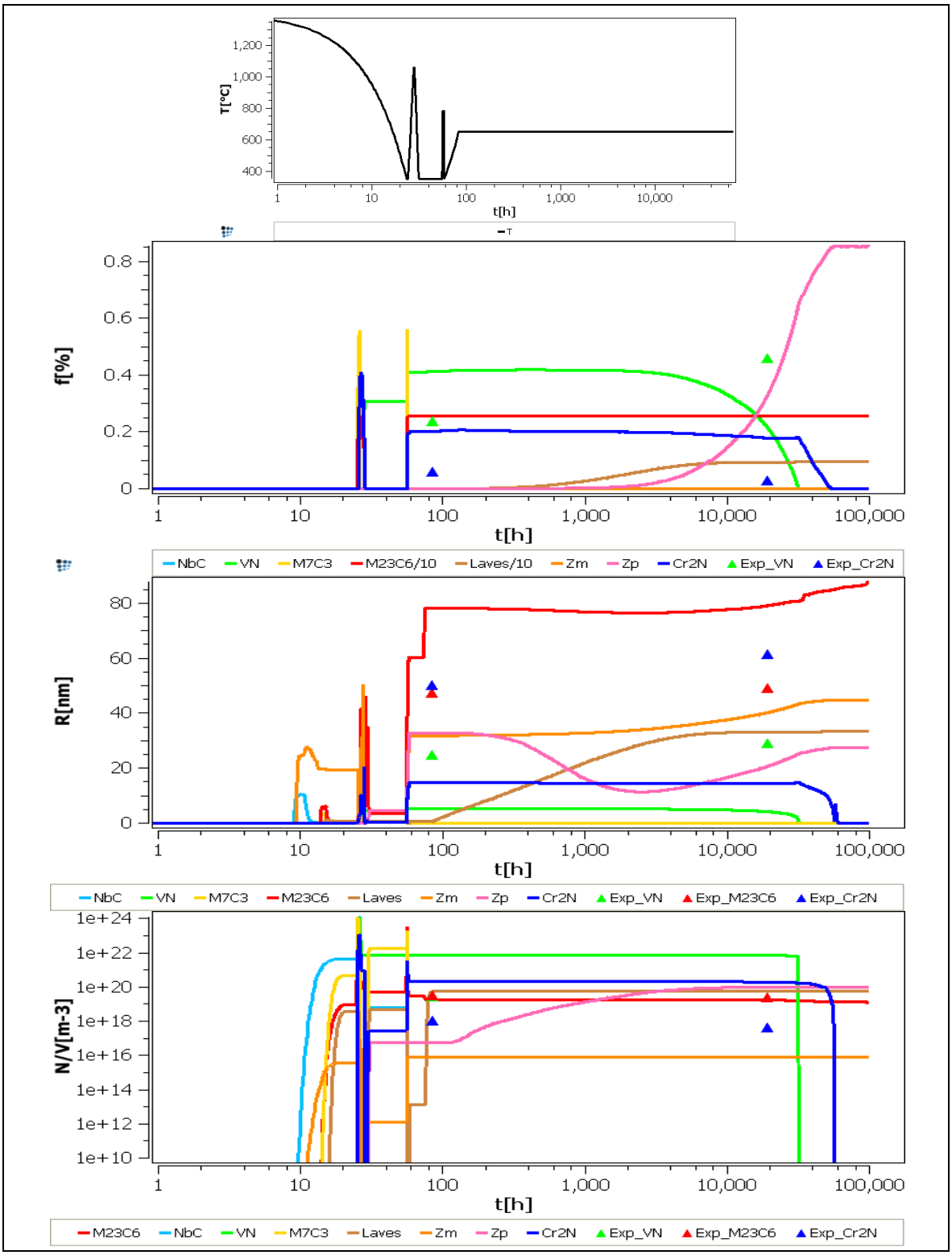

Figure 7.20. X12CrCoWVNb 11-2-2 Heat 1 kinetic simulation with TCFE3 modified for chromium steels database, with implementations of the thermodynamics of mod. Z-phase, at 575℃: The first graph represents the temperature history applied on the material: cooling after casting, austenitization, tempering and service. The following graphs represent the phase fractions (f[%]), mean radii (R[nm]) and number densities (N/V[m^{-3}]) of the individual precipitates phases. The Gibbs energy for M_2X (Cr_2N) phase is changed to -2500J/mol of M_2X phase. The experimental results are plotted as triangles.

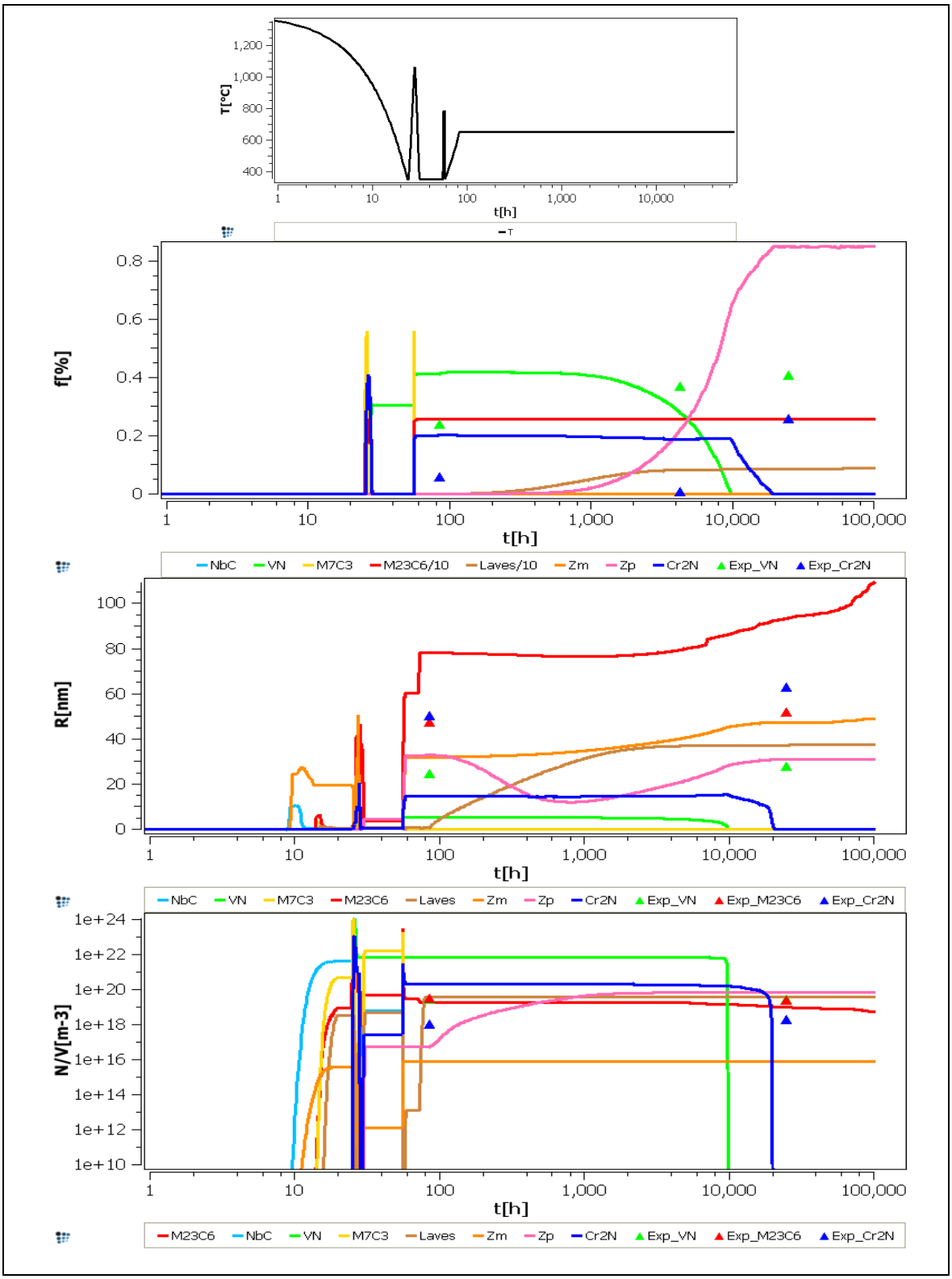

Figure 7.21. X12CrCoWVNb 11-2-2 Heat 1 kinetic simulation with TCFE3 modified for chromium steels, with implementations on the thermodynamics of the mod. Z-phase, considering new thermodynamics parameters for M_2X phase at 600℃: The first graph represents the te mperature history applied on the material: cooling after casting, austenitization, tempering and service. The following graphs represent the phase fractions (f[%]), mean radii (R[nm]) and number densities (N/V[m^{-3}]) of the individual precipitates phases. The experimental results are plotted as triangles.

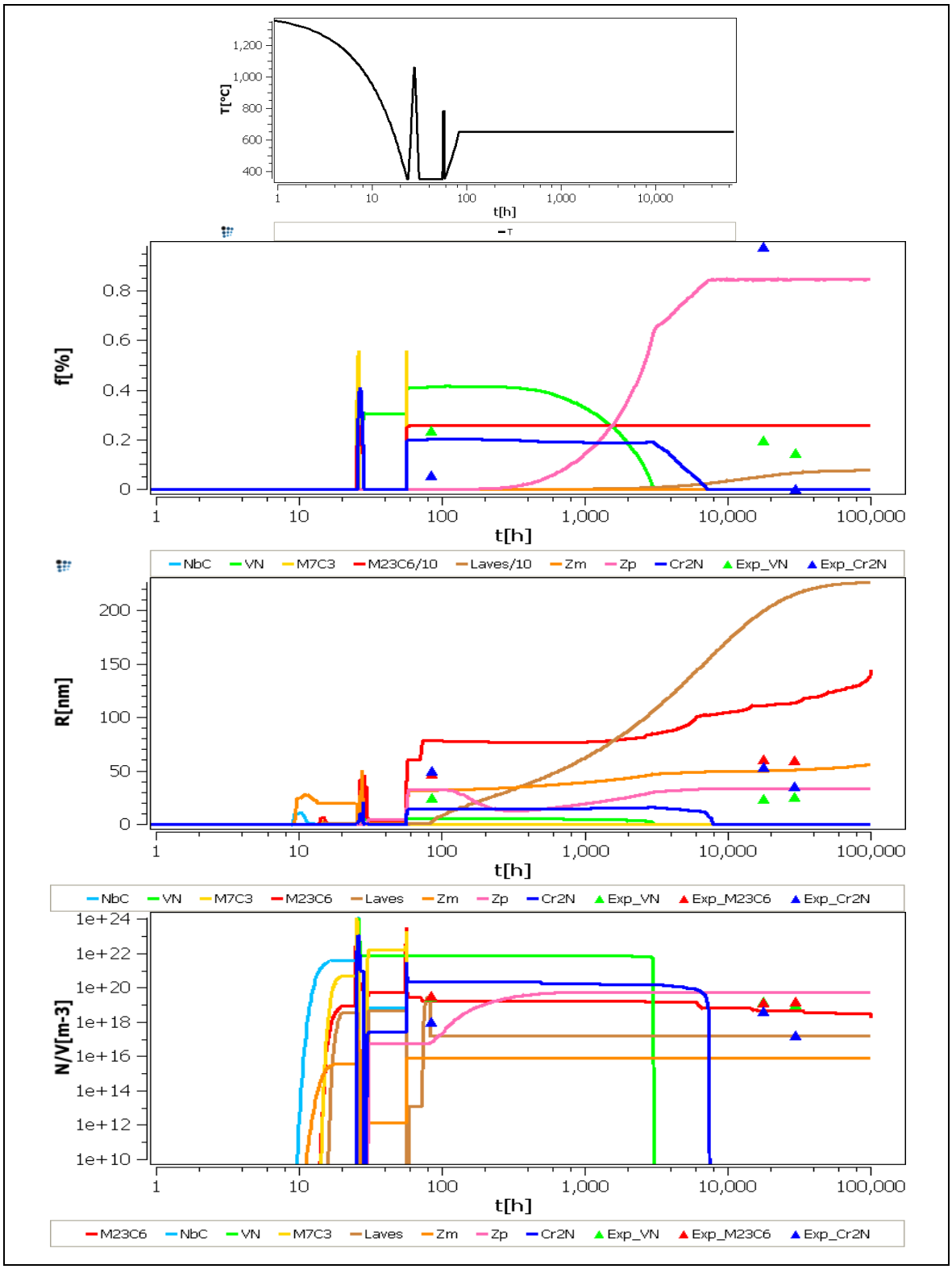

Figure 7.22. X12CrCoWVNb 11-2-2 Heat 1 kinetic simulation with TCFE3 modified for chromium steels database, with implementations of the thermodynamics of mod. Z-phase, at 625℃: The first graph represents the temperature history applied on the material: cooling after casting, austenitization, tempering and service. The following graphs represent the phase fractions (f[%]), mean radii (R[nm]) and number densities (N/V[m^{-3}]) of the individual precipitates phases. The Gibbs energy for M_2X (Cr_2N) phase is changed to -2500J/mol of M_2X phase. The experimental results are plotted as triangles.

7.3.2. Changes of Gibbs energy for M_2X -1950 J/mol and interfacial energy for Zp

The modification of the Cr_2N Gibbs energy described in 7.3.1. to a value of -2500 J/mol was improving the results of the calculations. However, the results still were showing discrepancies, especially regarding phase fractions and number densities, compared with the experimental investigations. Because of that, further implementations were performed in the thermodynamic of Cr_2N and mod. Z-phase. The Gibbs energy was increased to -1950J/mol, in order to destabilize this phase. Moreover, for these calculations also, the nucleation constant and the equivalent interfacial energy, for the mod. Z-phase precipitating on the VN phase (Zp), were adjusted to 10^{-07} and 0.12 respectively, to adjust the prediction of the calculations with the experimental results.

Equilibrium Simulations

Figure 7.23 represents the equilibrium simulations.

$M_{23}C_6$ was found the predominant precipitate phase together with Laves phase, being stable at temperature roughly below 950℃ and 700℃ respectiv ely. VN was stable at temperatures below 1200℃ and no presence of NbC precipitation was predicted. M_2X (Cr_2N) was stable at temperatures below 900℃ with 0.8 % of phase fraction replacing the VN phase at temperatures lower than 700℃. However, when mod. Z-phase was considered in the simulations, this phase replaced M_2X and VN phases. VN phase was stable only at high temperatures (750 to 850℃) with a very low phase fraction, 0.3 %.

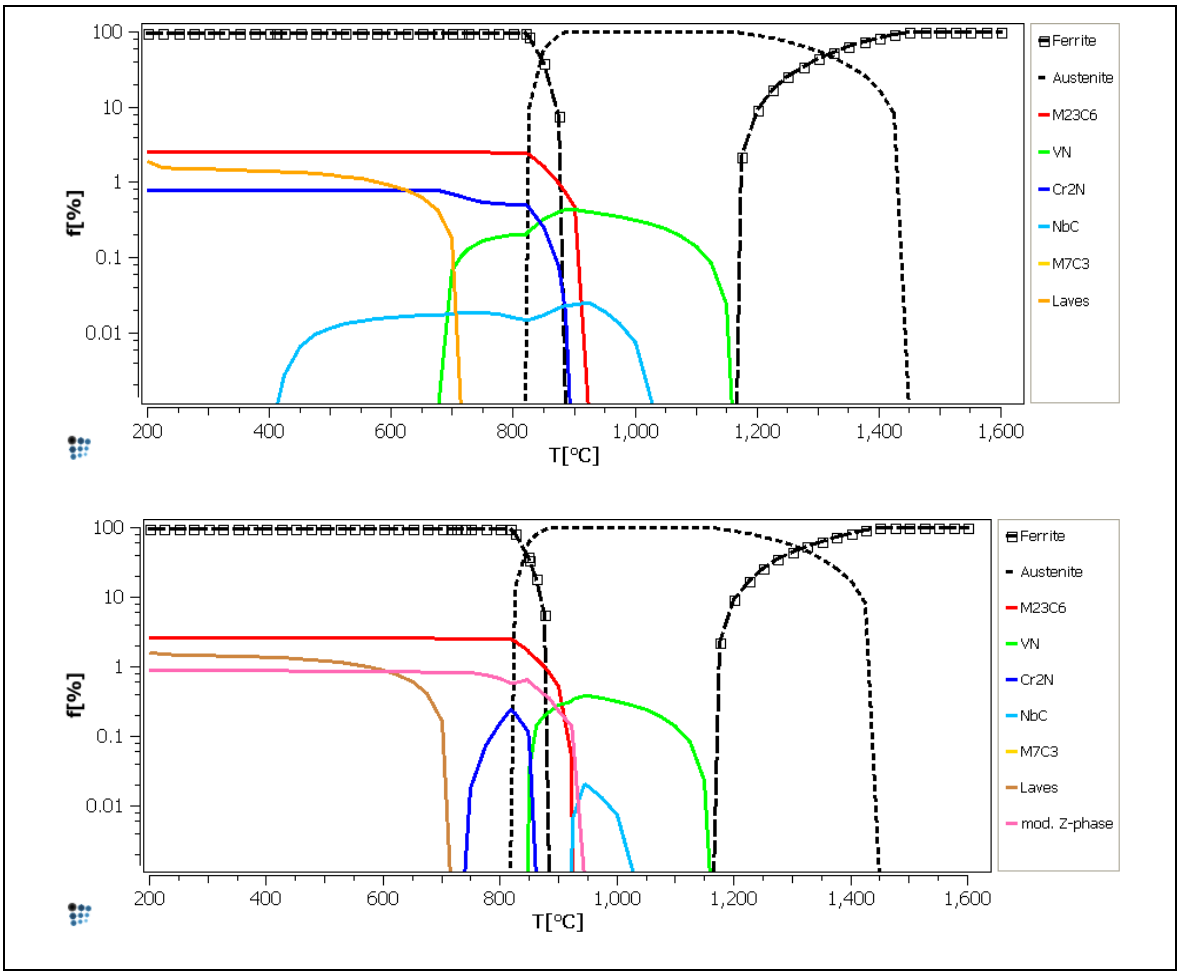

Figure 7.23. X12CrCoWVNb 11-2-2 Heat 1 equilibrium simulation with TCFE3 modified for chromium steels database, with implementations on the thermodynamics of the mod. Z-phase, was used. Gibbs energy of M_2X (Cr_2N) was increased to -1950J/mol: Equilibrium calculations without considering mod. Z-phase (upper image) and considering mod. Z-phase (lower image).

Kinetic Simulations

The simulations (presented in Figure 7.24) predicted $M_{23}C_6$ phase as fully precipitated phase after the heat treatment with a phase fraction of 2.5 %, who remains constant in the entire calculation. VN phase was also fully precipitated after the heat treatment with a phase fraction of 0.32 %. After roughly 4000 h of service the VN phase fraction decrease, together with a phase fraction increase of mod. Z-phase and M_2X phases. M_2X showed, after the heat treatment, a phase fraction of 0.25 % which increase until a maximum of 0.56 %. However, the mod. Z-phase was predicted as the predominant phase together with $M_{23}C_6$ and Laves phase. Laves phase precipitates shortly after start of aging and slowly increases its phase fraction to almost 0.1 %. NbC phase was not predicted in the calculation.

The mean radius of the $M_{23}C_6$ was calculated to approximately 25 nm after the heat treatment, coarsening up to 80 nm at the end of the simulation, together with a slowly number density decrease. VN phase showed a constant mean radius of 10 nm. M_2X showed a constant radius of 15 nm up to 40000 h then slightly increase its radius to 20 nm before dissolution. Laves phase increased its size up to 40 nm. Mod. Z-phase (Zp) had an initial size of 10 nm coarsening up to 80 nm.

M_7C_3 phase has been considered also in the calculation. This phase was dissolving always during the heat treatment, remaining $M_{23}C_6$ as the stable carbide during service.

Mod. Z-phase was considered to have to different nucleation sites: in the matrix (Zm) and on a VN precipitate (Zp). The Zm phase showed long nucleation times, almost not affecting the other precipitates populations.

The calculations performed at the different services temperatures are presented in Figure 7.25. For the material tested at lower temperatures the calculations predicted lower coarsening rates and longer stabilities.

In Figure 7.24 as well as in Figure 7.25 the experimental results are plotted in the results of the kinetic simulation. The change of the Gibbs energy of the Cr_2N as well as the changes in the interfacial energy parameters of the mod. Z-phase, improved the concordance between experimental and calculated results. The phase fraction of the Cr_2N phase is predicted to increase as the experimental results, however the predicted values are much higher as the simulated. For the MX (VN) phase, the calculation shows a faster dissolution as in the experimental results. Regarding the mean radii and number densities, the predicted values of the $M_{23}C_6$ are in good agreement with the experimental results. Nevertheless, for the VN and Cr_2N phase the predicted mean radii are lower as in the experimental investigations, and consequently the predicted number densities are higher as in the experimental.

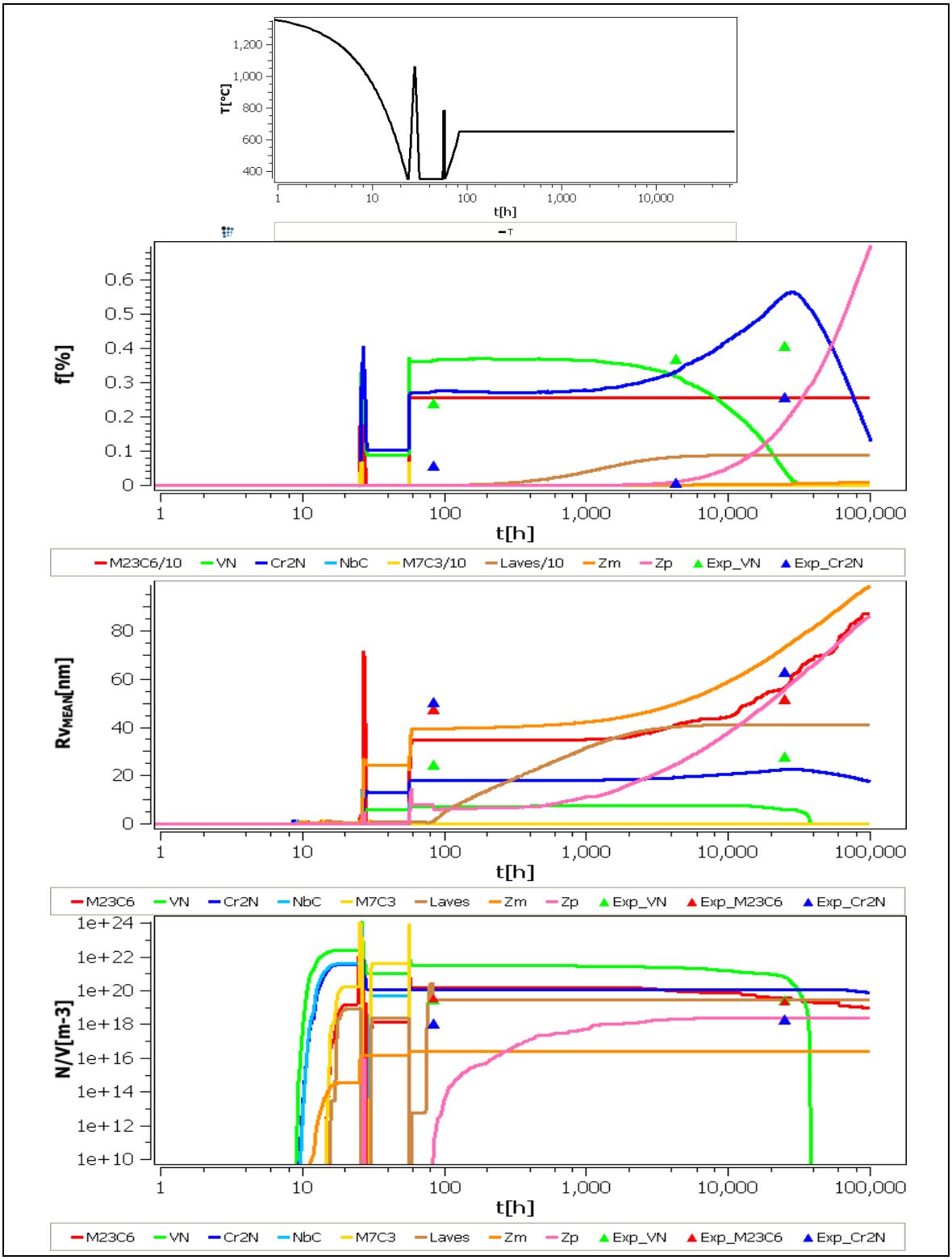

Figure 7.24. X12CrCoWVNb 11-2-2 Heat 1 kinetic simulation with TCFE3 modified for chromium steels database, with implementations on the thermodynamics of the mod. Z-phase and the new thermodynamics parameters of Gibbs energy for M_2X at -1950J/mol, and the nucleation constant and the equivalent interfacial energy, for the mod. Z-phase precipitating on the VN phase (Zp) at 600℃: The graphs represent the phase fractions (f[%]), mean radii (R[nm]) and number densities ($N/V[m^{-3}]$) of the individual precipitates phases. Open simbols represent the experimental values of $M_{23}C_6$, M_2X (Cr_2N) and MX(VN). The experimental results are plotted as triangles.

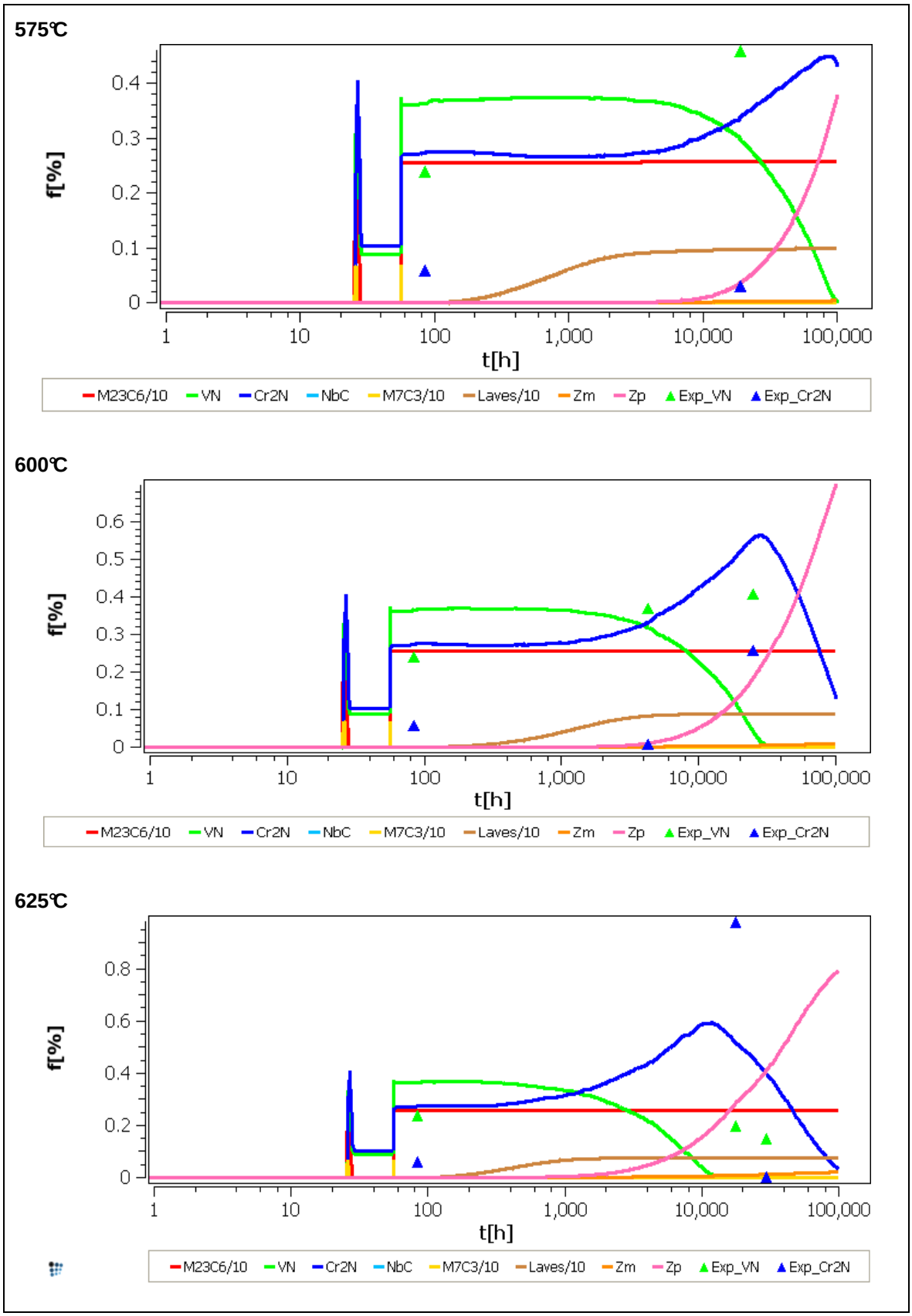

Figure 7.25. X12CrCoWVNb 11-2-2 Heat 1 kinetic simulation with TCFE3 modified for chromium steels database, with implementations on the thermodynamics of the mod. Z-phase and the new thermodynamics parameters: Phase fraction (f[%]) diagrams calculated at 575℃, 600℃ and 625℃. The experimental results are plotted as triangles.

7.4. Optimization of mc_steel database

According with the obtained results from the previous calculations with TCFE3 modified for chromium steels and the experimental results presented in the previous sections, the newest MatCalc database was used for the last calculations with X12CrCoWVNb 11-2-2 Heat 1 steel: mc_steel[9] implemented with the changes of the thermodynamics for mod. Z-phase and the adjustments performed for the thermodynamics of the M_2X phase. Moreover, a new heat treatment was considered in the kinetic calculations: longer cooling and heating rates, which are more reliable with the real production process of the steel (values presented in Table 7.4).

Equilibrium Simulations

The results of the equilibrium simulations presented in Figure 7.26 showed $M_{23}C_6$ as the predominant precipitate phase together with Laves phase, being stable at temperatures roughly below 1000℃ and 700℃ respectively. VN was stable at temperatures b elow 1200℃ as well as NbC, with a phase fraction of 0.4 and 0.1 % respectively. M_2X was stable, together with VN, at temperatures below 900℃ with 0.3 % of phase fraction. However, when mod. Z-phase was considered in the calculations; Cr_2N, VN and NbC phases were replaced. Mod. Z-phase became the stable nitride phase up to 1000℃ with almost 1 % of phase fraction.

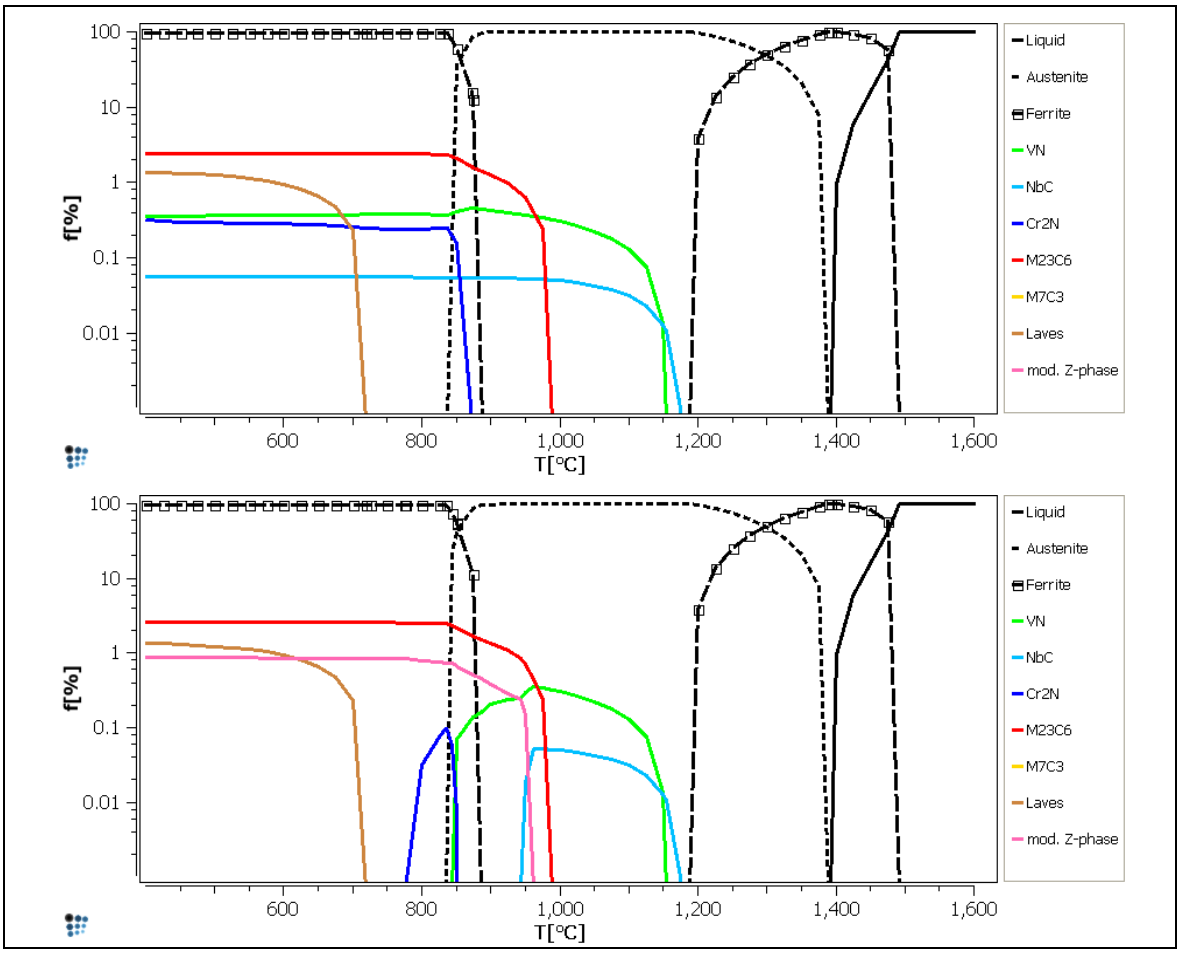

Figure 7.26. X12CrCoWVNb 11-2-2 Heat 1 equilibrium simulation with mc_steel database: Upper graph without consider mod. Z-phase and lower graph considering mod. Z-phase into the calculation.

[9] www.matcalc.at

Kinetic Simulations

The results of the kinetic simulation at 600℃ are presented in Figure 7.27. The calculation reveals $M_{23}C_6$ as fully precipitated phase after the heat treatment with a phase fraction of 2.5 %, which remains constant during aging, the entire simulation. Together with $M_{23}C_6$, Laves phase shows around 1 % of phase fraction. NbC phase precipitated in the austenitic regime and kept its phase fraction constant in the entire simulation, with a phase fraction of less than 0.1 %. VN phase was also fully precipitated after the heat treatment showing a phase fraction of 0.48 %. Although this phase decreased its phase fraction to totally dissolution, when mod. Z-phase precipitates. Similar behaviour showed Cr_2N phase. This phase precipitates during the heat treatment, with a relative low phase fraction of 0.1 %. It kept its phase fraction during the simulation Cr_2N almost constant until VN phase starts to dissolve, due to the precipitation of mod. Z-phase. At this point of time, Cr_2N phase increased its phase fraction to a value of 0.3 %, to afterwards dissolve.

In Figure 7.28, the evolution of the chemical composition of the different nitride phases, VN, Cr_2N and mod. Z-phase is presented. VN phase presents a decrease in its vanadium during its dissolution, related with the increase of vanadium content in the mod. Z-phase. On the other hand, Cr_2N phase kept almost unchanged its chemical composition in the entire calculation. For all three phases, the chemical composition shows an unusual behaviour in the first 100 h of service exposure, which is related with the nucleation process. When these phases have been already nucleated, a defined chemical composition can be observed in the simulations.

The mean radius of the $M_{23}C_6$ was 50 nm after the heat treatment keeping it almost constant in the entire simulation as well as its number density. VN phase showed a constant mean radius of 20-25 nm. Cr_2N (M_2X) showed a radius of 40 nm up to 20000 h which slightly increases it to 50 nm before start of its dissolution. NbC phase show a mean radius of 15 nm constant in the entire simulation as well as its number density. Laves phase increases its size up to 40 nm, where it stays constant. Mod. Z-phase (Zp and Zm) showed an initial size of 35 nm and 60 nm respectively which coarsening up to values higher than 100 nm.

M_7C_3 phase has been considered also in the calculation. This phase was dissolving always during the heat treatment, remaining $M_{23}C_6$ as the stable carbide during service.

The calculations performed at the different services temperatures are presented in Figure 7.29. The calculations predict lower coarsening rates and longer stabilities for the material tested at lower temperatures.

The experimental values are presented in the kinetic simulation graphs, see Figure 7.27 and Figure 7.29. The mean radii and number densities calculated out of the experimental results, is in good agreement with the values than that predicted by the calculations with software MatCalc. Nevertheless, the phase fraction after heat treatment (100h) is much lower that it was the predicted by MatCalc.

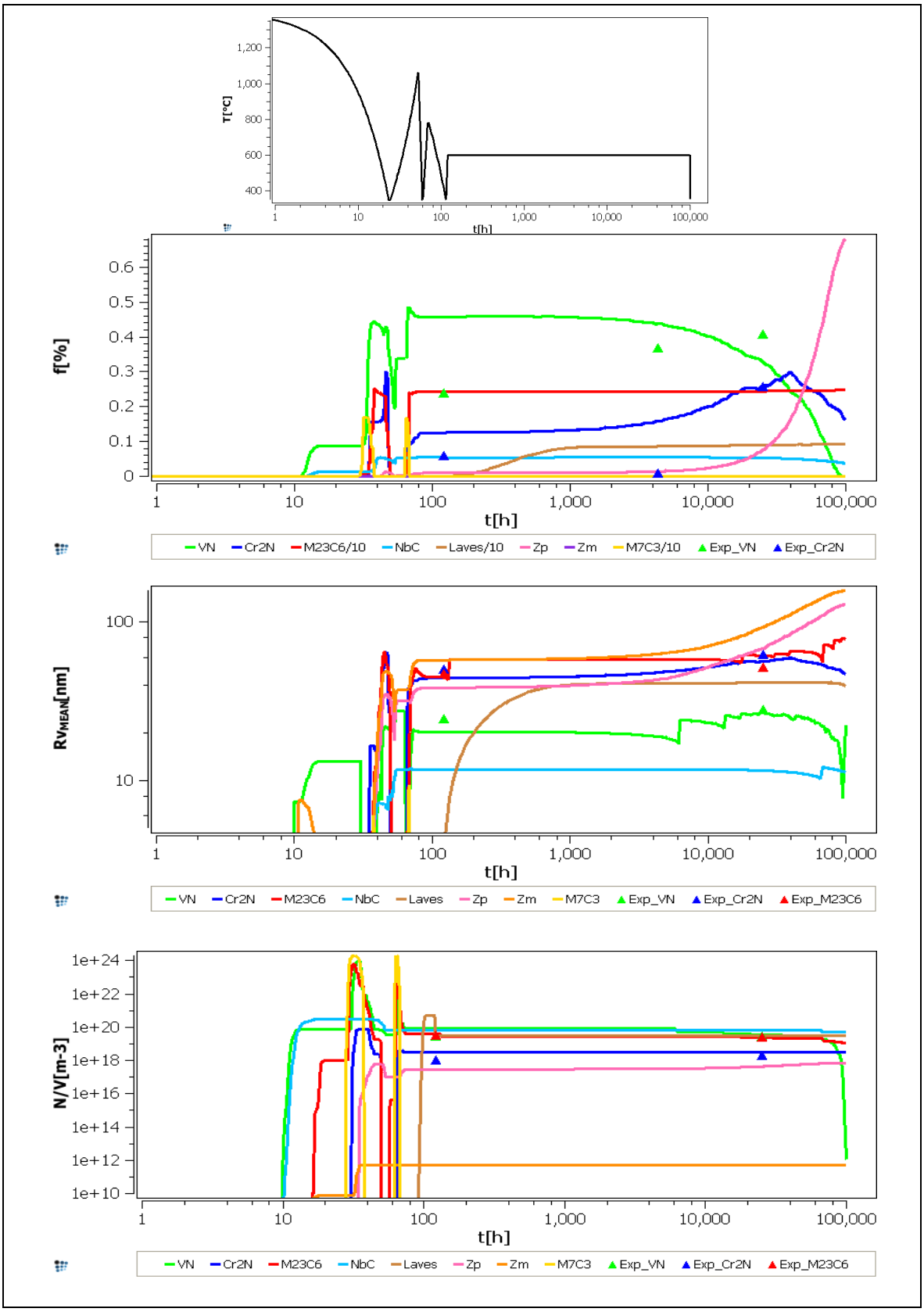

Figure 7.27. X12CrCoWVNb 11-2-2 Heat 1 kinetic simulation with mc_steel database at 600℃: The first graph represents the temperature history applied on the material: cooling after casting, austenitization, tempering and service. The following graphs represent the phase fractions (f[%]), mean radii (R[nm]) and number densities (N/V[m^{-3}]) of the individual precipitates phases. The experimental results are plotted as triangles.

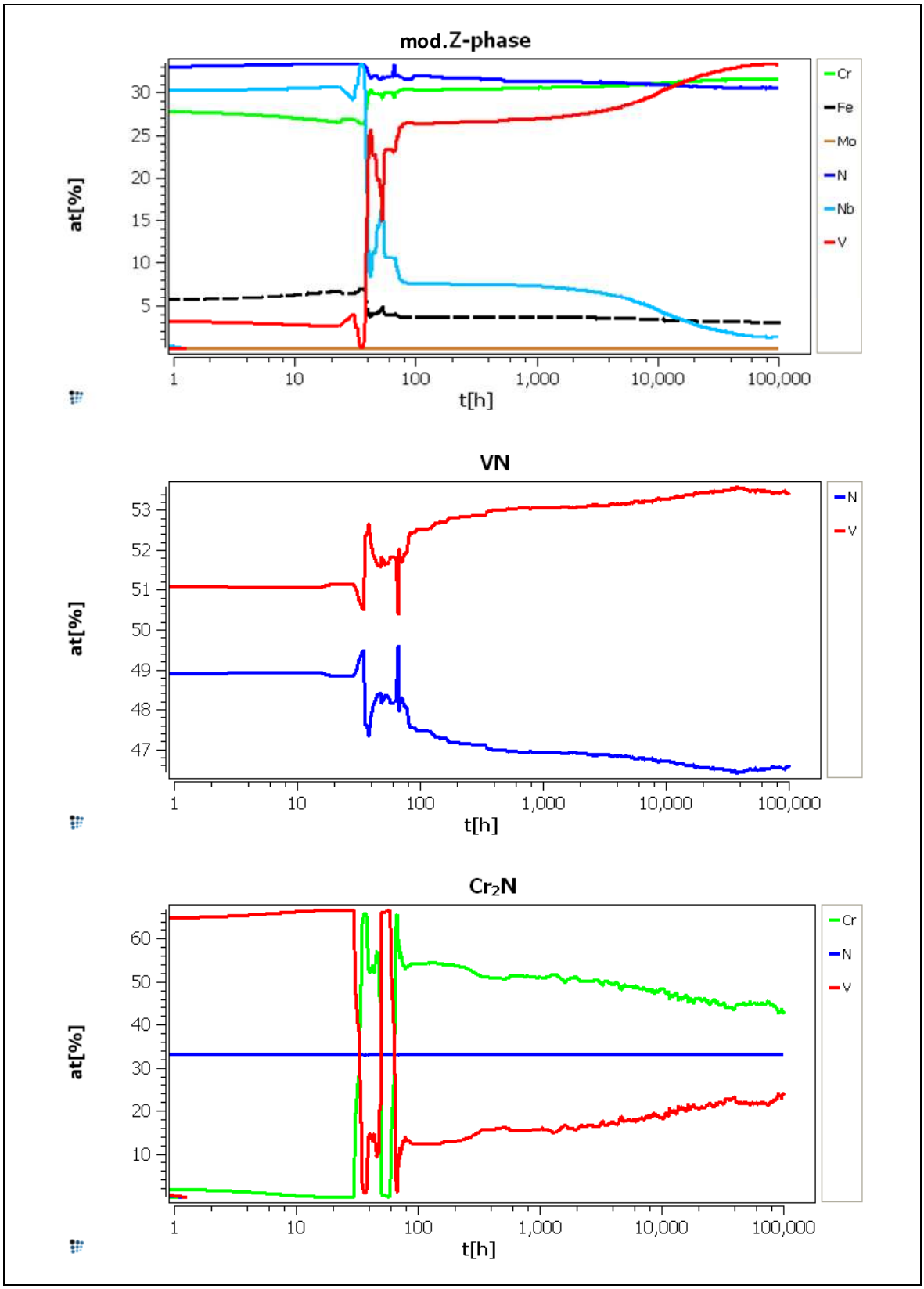

Figure 7.28. X12CrCoWVNb 11-2-2 Heat 1 kinetic simulation with mc_steel database at 600℃: Evolution of the chemical composition in the different nitride phases during time (heat treatment and service).

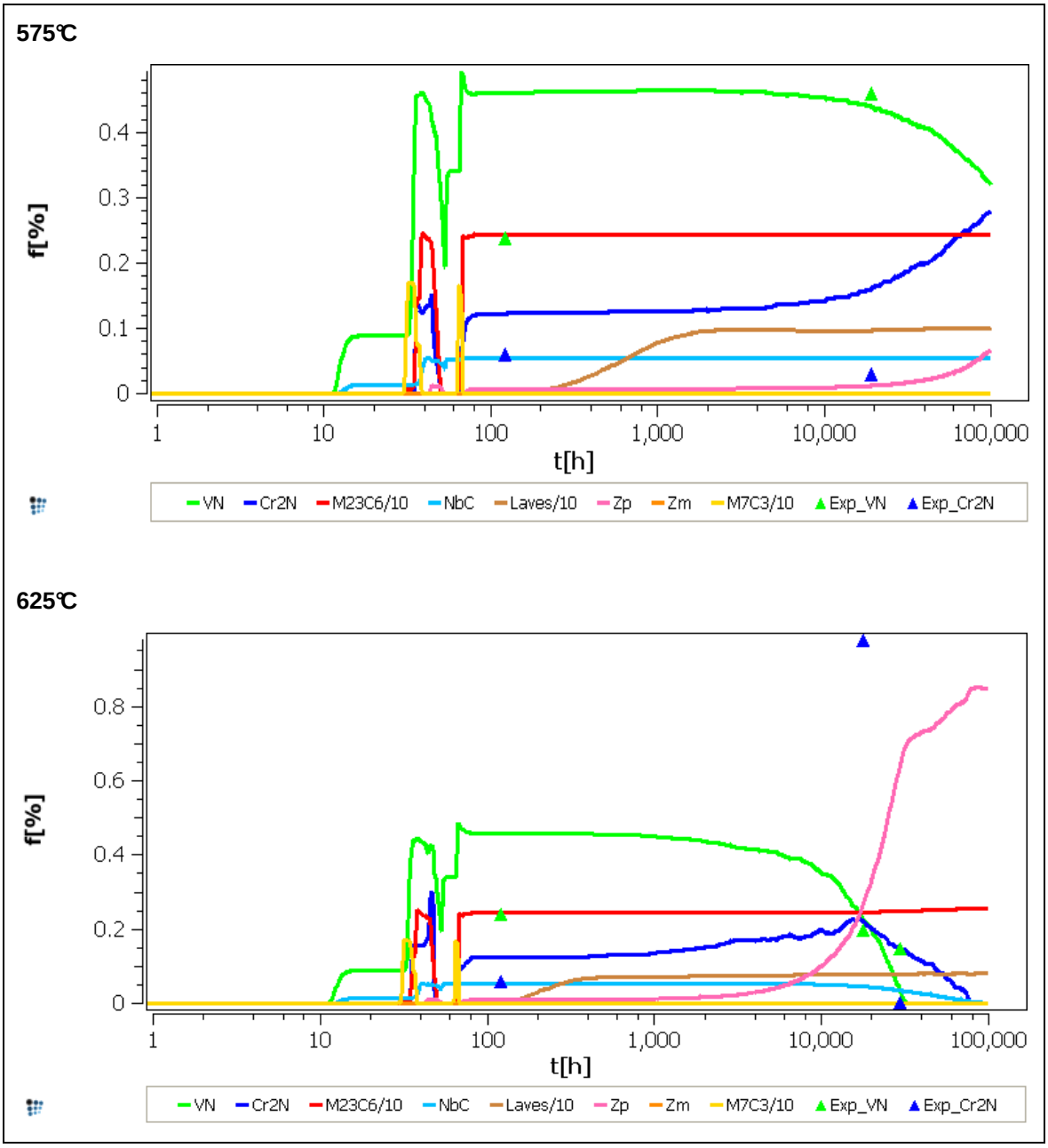

Figure 7.29. X12CrCoWVNb 11-2-2 Heat 1 kinetic simulation with mc_steel database at different service temperatures: Phase fraction (f[%]) diagrams calculated at 575℃ and 625℃. The experimental results are plotted as triangles.

8. Experimental Heat

X12CrCoWVNb 11-2-2 alloy concept is based on precipitation strengthening by carbides (mainly $M_{23}C_6$ and NbC), Laves phase and also nitrides (Cr_2N, VN). However, the transformation of the finely distributed VN precipitates to the low distributed and large mod. Z-phase decreases the creep strength of the material at high temperatures. Because of that fact, a simulation of a vanadium free variant of X12CrCoWVNb 11-2-2 to prevent the precipitation of VN was performed. In this variant the strengthening precipitates are: $M_{23}C_6$, NbC, Laves phase and also Cr_2N.

Equilibrium and kinetic simulations have been performed to evaluate the behaviour of the X12CrCoW[V]Nb 11-2-2 steel vanadium free content. The chemical composition (except V) and heat treatment used for the simulations have been the same as for the original X12CrCoWVNb 11-2-2 steel, presented in Table 4.1 and Table 4.2. Moreover, the mc_steel optimised database was used together with the same phases and cooling rates as presented in Table 7.1 and Table 7.4 for the original X12CrCoWVNb 11-2-2 steel.

Equilibrium Simulations

Figure 8.1 presents the equilibrium simulation of the X12CrCoW[V]Nb 11-2-2 material with a 0.000001 wt.%V. The calculation predicts as stable phases in a temperature range of 600℃ to 700℃, $M_{23}C_6$, Laves phase, Cr_2N and NbC in a fully martensitic matrix. The highest phase fraction corresponds to $M_{23}C_6$ phase with 2.5 %, followed by laves phase with 1.4 % and Cr_2N with 0.8 %. NbC has the lowest phase fraction with 0.06 %.

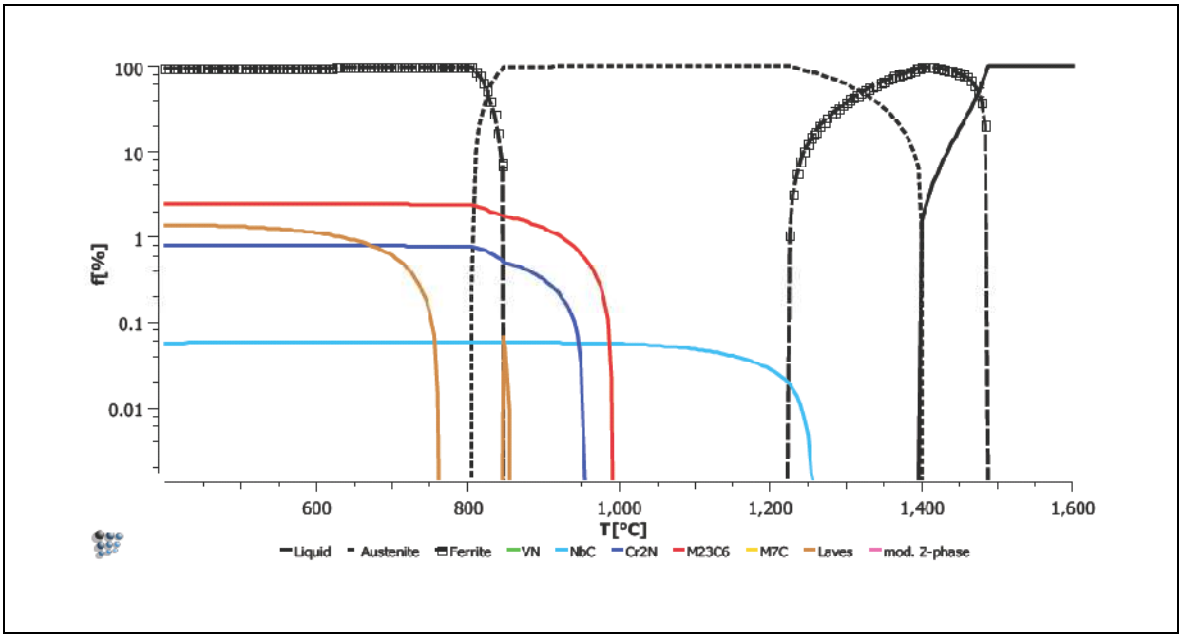

Figure 8.1. X12CrCoW[V]Nb 11-2-2 Heat 1 vanadium free equilibrium simulation with mc_steel database.

Kinetic Simulations

Figure 8.2 represents the kinetic calculation of the X12CrCoW[V]Nb 11-2-2 material vanadium free content (0.000001 wt.%).

The kinetics simulation reveals that during cooling from 1400℃ to 350℃, the first precipitation corresponds to NbC, Cr_2N and M_7C_3. During the heating up from 350℃ to the austeniti zation temperature (1060℃) the matrix is switched from martensite (fe rrite with high dislocation number) to austenite at 824℃, the calculate Ae1 temperature. The Cr_2N and M_7C_3 increase their phase fraction during the heating up to austenitization temperature to afterwards dissolve at temperatures above the Ae1, whereas the NbC remains with a constant phase fraction. During the cooling down from the austenitization temperature to 350℃, the Cr_2N increases its phase fraction to the level of the NbC phase (0.05 % with a men radius of 5 nm and a number density of $1.2x10^{20}$), at this point of the simulation the matrix is switched again to martensite (ferrite with high dislocation number). During the tempering (at 780℃) t he M_7C_3, Cr_2N and $M_{23}C_6$ increase their phase fraction. The $M_{23}C_6$ increases its phase fraction to a value of 2.5 % with at mean radius of 52 nm, parameters that remain constant in the entire calculation (service at 600℃). Contrary, the M_7C_3 carbide dissolves during tempering. The Cr_2N phase increases also its phase fraction to 0.8 % with a mean radius of 54.4 nm. After, tempering the service is simulated at 600℃ an d the Cr_2N as well as the $M_{23}C_6$ are the stables phases with 0.8 % and 2.4 % phase fraction, respectively. After 300 h of service precipitation of laves phase occurred, increasing its phase fraction progressively during the calculation to a stable value of 1.1 %, a mean diameter of 123 nm and a number density of $1.7x10^{18}$. Moreover, after around 10000 h of service the Cr_2N phase increase its mean radius from 54.4 nm to 123 nm at the end of the calculation, decreasing its number density form $1.1x10^{19}$ to $8.3x10^{18}$, after 10000 h of service, this phase coarses. NbC phase remains constant during the service with a 0.06 % phase fraction, 10 nm mean radius and $4.6x10^{19}$ of number density.

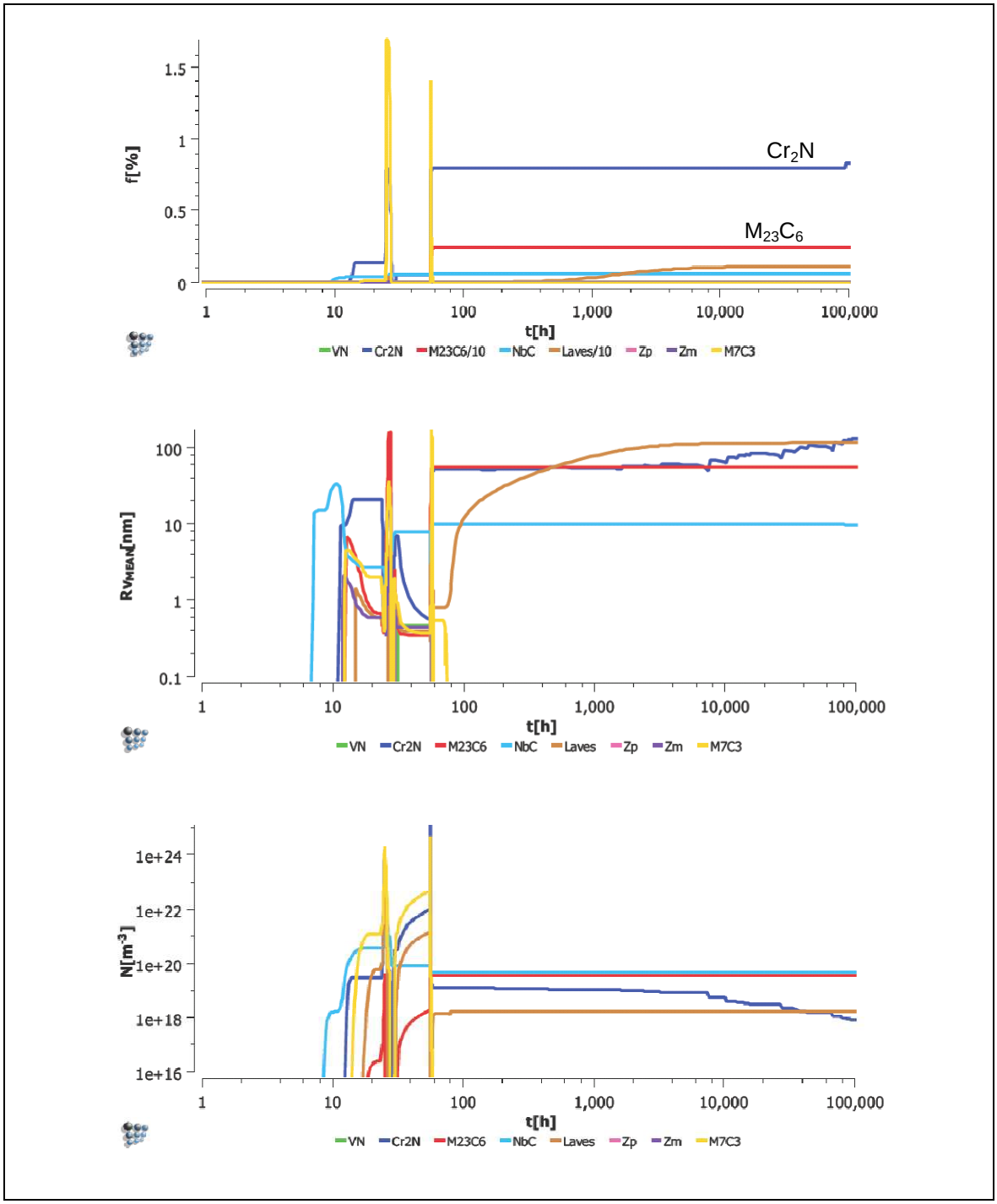

Figure 8.2. X12CrCoW[V]Nb 11-2-2 Heat 1 vanadium free kinetic simulation with steel with mc_steel database at 600℃. The first graph represents the temperature history applied on the material: cooling after casting, austenitization, tempering and service. The following graphs represent the phase fractions (f[%]), mean radii (R[nm]) and number densities (N/V[m^{-3}]) of the individual precipitates phases.

Because of the promising simulation results of the appearance of stable phases, an experimental test heat was produced and investigated by the same method as the previous Heat X12CrCoWVNb 11-2-2

However, the experimental investigations reveal some discrepancies with the simulations. By using the same experimental techniques and same quantifications methods as for the original X12CrCoWVNb 11-2-2 steel, the microstructure of the X12CrCoW[V]Nb 11-2-2 vanadium free steel was investigated.

The material X12CrCoW[V]Nb 11-2-2 vanadium free was studied by ion milled specimens and showed a martensitic structure with different precipitates types, mainly distributed at the boundaries. The precipitates were identified as $M_{23}C_6$, Laves phases, NbC and Cr_2N in as received condition (after heat treatment). Also creep exposure material was investigated. The sample was creep exposure at 60 MPa and 650℃ and broke after 3403 h. The different typ es of precipitates found, were classified as: chrome carbides (mainly $M_{23}C_6$), Laves phase, Cr_2N and chrome-niobium rich particles. Figure 8.3 shows two images of the material tested in as-received condition and after creep exposure. Out of the TEM investigations, precipitate quantification analyses were performed. The quantification was carried out in the thin foil samples using the different elemental maps. The mean diameter, number density and volume fraction were calculated and the results are presented in Table 8.1.

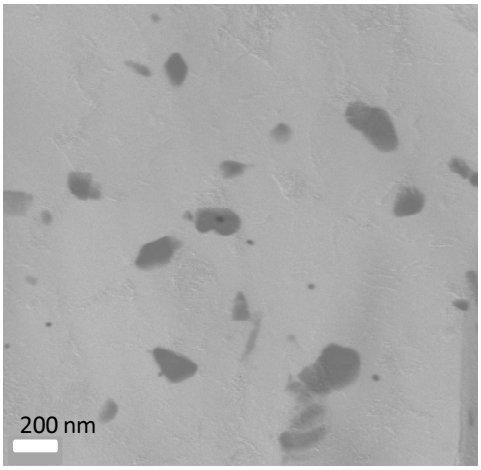

as-received material

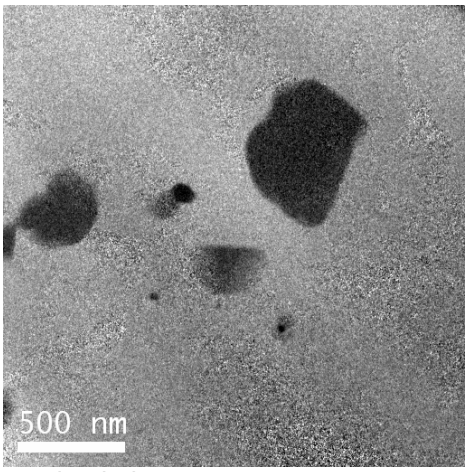

creep loaded: stress 60 MPa, temperature 650℃, time to fracture 3403 h

Figure 8.3. X12CrCoW[V]Nb 11-2-2 vanadium free: Fe EFTEM images.

Table 8.1. X12CrCoW[V]Nb 11-2-2 vanadium free: Values of mean diameter, volume fraction and number density obtained from the experimental investigations.

	mean radii [nm]	volume fraction [%]	number density [m-3]
M23C6			
as-received	51.59	1.19	1.09E+19
creep exposure	167.54	0.61	1.08E+18
Laves			
as-received	24.70	0.05	4.63E+18
creep exposure	32.68	0.06	1.63E+18
NbC			
as-received	15.59	0.00	1.63E+18
creep exposure	-	-	-
Cr2N			
as-received	50.91	0.43	2.40E+18
creep exposure	82.46	0.08	1.68E+17

The experimental investigations on the X12CrCoW[V]Nb 11-2-2 vanadium free revealed an unexpected strong coarsening behaviour of the $M_{23}C_6$ and Cr_2N not predicted by the simulations. The volume fraction of these two phases dramatically decrease after only 3403 h of creep test at 650℃ and 60 MPa. Laves phase precipitates were already identified in as received condition and no NbC were found after creep test.

The experimental investigations showed strong discrepancies with MatCalc simulations, indicating that further implementations, on the Cr_2N and mod. Z-phase thermodynamic, have still to be studied intensively.

9. Discussion and Summary

Currently, the increase of operation temperatures and pressures in USC power plants is one worldwide goal to increase their efficiency. For the achievement of this goal, new materials must be developed that can resist the high service temperatures and pressures. Tempered martensitic 9-12 wt.%Cr steels are excellent candidates for components in USC power plants, due to its price and its properties compared with austenitic steels. For the use of these materials at the defined service temperatures and pressures, important characteristics have to be satisfied such as: oxidation resistance, high ductility, fabricability, weldability but also long life expectancy and creep resistance strength. Several European, Asian and American projects have been created for the development of these materials and it has been demonstrated that the creep resistance is one of the most critical parameters in these steels. Different alloy variants have been investigated in worldwide projects to improve the creep resistance of these tempered martensitic steels, and many theories were coming out to explain the reason of the drop in creep strength of these materials, creep tested at high temperatures. Microstructure instabilities as precipitates dissolution-transformations, coarsening, recovery and recrystallization of the matrix have been found the main reason for the drop in creep of these materials.

In the completion of this thesis a fully microstructure characterization of the 12 wt.%Cr steel X12CrCoWVNb 11-2-2, which was developed to increase oxidation resistance keeping the creep resistance in the level of P91 and P92, has been performed using the most advances microscopy techniques. Optical microscopes, transmission electron microscopes and scanning electron microscopes have been used for the microstructure characterization of the material, in as-received condition of three different X12CrCoWVNb 11-2-2 Heats (Heat 1, 2 and 3) as well as in 10 different thermally aged and creep loaded specimens for the X12CrCoWVNb 11-2-2 Heat 1 variant. Moreover, using upgraded databases of MatCalc software based in the extensive performed investigations, the microstructure changes of X12CrCoWVNb 11-2-2 are described satisfactory.

Experimental investigations

Three different heats of the X12CrCoWVNb 11-2-2 steel: Heat 1, Heat 2 and Heat 3 were characterized via optical microscopy in as-received condition. A fully tempered martensitic microstructure was identified in all three heats with exception of Heat 3. In addition to the martensitic structure, in this heat, 1-2.5 % of δ-ferrite was quantified. This phase has a strong effect in the properties of the material as grain size and hardness, tensile strength, toughness and ductility or creep rupture strength. The defined effects of δ-ferrite in the mentioned properties are excellent summarised in [9].

Because of the promising results on the creep tests of X12CrCoWVNb 11-2-2 Heat 1 steel, further investigations in this project were performed in this material heat only. A total of 11 sample conditions, as-received and creep tested specimens were investigated via TEM, EDX, EFTEM, EELS, ELNES, Scatter diagrams, CBED, SAD, SEM, EBSD.

In the as-received condition (ASH1P) $M_{23}C_6$, VN, NbC and Cr_2N were identified and their chemical composition was analysed. $M_{23}C_6$ showed a chemical composition of: 55 at.%Cr, 18 at.%Fe, 1 at.%Mo and 5 at.%W. MX (VN) showed a chemical composition of: 38 at.%V, 9 at.%Cr, 1 at.%Fe and 2-3 at.%Nb and M_2X (Cr_2N) showed a chemical composition of: 15 at.%V, 50 at.%Cr and 1 at.%Fe together with Nb or W traces. At any of the investigated positions no Laves phase or mod. Z-phase could be found. The mean diameter, volume fraction and number density of $M_{23}C_6$, VN and Cr_2N were also calculated from the extensive experimental investigations. $M_{23}C_6$ had a mean diameter of 95 nm similar to Cr_2N (100 nm). The VN phase showed lower size, 50 nm of mean diameter. Volume fractions as well as number densities were also calculated. The $M_{23}C_6$ phase had a phase fraction and number density of 1.79 % and 3.62×10^{19} m^3. For the VN phase it was calculated 0.07 % and 3.16×10^{19} m^3 and, 0.02 % and 1.18×10^{18} m^3 for Cr_2N. BN as well as NbC were also identified in this condition. However, these precipitates were only identified in the extraction replica specimens, and a quantification of the data was not possible. Moreover,

BN precipitates had different sizes, from some nanometres diameter (50-100 nm) until some microns in diameter. NbC precipitates with a size of roughly 50 nm in diameter were identified.

The following investigations were performed in creep exposed specimens to observe the behaviour of these phases at high temperature and different stresses. Specimens creep tested at 575℃, 600℃ and 625℃, at different stresses, were characterized an d are in the following lines described.

Creep specimens at 575℃

The specimen creep tested at 575℃ was studied at g rip (thermally aged material) and the gauge (creep loaded material portion. $M_{23}C_6$, MX (VN and NbC), M_2X (Cr_2N) and Laves phase were identified together with a low number density of mod. Z-phase. Presumably, the temperature, of 575℃, was too low for the formation of the mod. Z-phase. Moreover, no BN has been found at these specimens.

$M_{23}C_6$ were mainly distributed at the prior austenite grain boundaries, martensite lath boundaries and subgrain boundaries, whereas the vanadium rich phases indentified as MX (VN) were found also to be finely distributed in the matrix.

Creep specimens at 600℃

Two different specimens tested at 600℃ were studie d. The first one was tested at 175 MPa, broke after 4137 h and the second one, tested at 115 MPa after 24639 h. After thermal ageing at 600℃ for 4137 h (TA600H1P-4137), $M_{23}C_6$, MX (VN and NbC), M_2X (Cr_2N) and Laves phase were identified. For the specimen tested after longer time (24639 h), in the thermally aged (TA600H1P-24639) as well as in the creep loaded (CL600H1P-115-24639) higher quantity of mod. Z-phase was found. No presence of boron nitride precipitates were found at the specimens exposed at 600℃.

Creep specimens at 625℃

Two samples creep exposure at 625℃ were studied. T he first studied specimen was studied after thermal aging (TA625H1P-17487) and creep load for 17487 h (CL625H1P-85-17487) condition via thin foil and extraction replica, the second sample thermal aged at 625℃ after 28983 h (TA625H1P-28983) via thin foil and extraction replica. For all the studied positions and specimens conditions, the same phases were identified: carbides $M_{23}C_6$ and NbC, as well as nitrides VN, Cr_2N and mod. Z-phase. Laves phase was identified too with a high content of iron (around 45 at.%) and tungsten (around 30 at.%); also some % of molybdenum (around 10 at.%). No presence of boron nitride precipitates were found at the specimens tested at 625℃

Out of the chemical quantification from the $M_{23}C_6$, M_2X (Cr_2N) as well as MX (VN) phases some relevant differences were found, between the material in as-received condition, the thermally aged and creep loaded at the tested temperatures (575℃, 600℃ and 625℃). $M_{23}C_6$ shows an increase in chromium content at the specimens creep loaded at 600℃ and in all the specimens tested at 625℃ creep loaded and thermally aged compared to the as-received condition. Moreover, MX (VN) phase has constant vanadium content at all tested conditions. The M_2X (Cr_2N) phase shows a decrease in chromium only in the creep loaded specimens tested at 600℃ and 625° C.

These changes in chemical composition reveal that these phases evolve during the creep tests. The increase of chromium observed in the $M_{23}C_6$ is related with the availability of chromium in the matrix, out of the dissolution of M_2X (Cr_2N) phase at the higher creep tested temperatures.

The number density, volume fraction and mean radius of the $M_{23}C_6$, M_2X (Cr_2N) and MX (VN) were calculated using the EFTEM images of Cr and V and the corresponding thickness maps.

The $M_{23}C_6$ and the M_2X (Cr_2N) phases showed a smooth coarsening when comparing all the studied specimens, in as-received, thermally aged or creep loaded condition. The $M_{23}C_6$ precipitates showed a soft coarsening at 575℃ compared with the material in as-received condition. The same behaviour was observed at the specimens tested at 600℃ and 625℃ (thermal aging and creep load) with an increase in the mean radius compared to the as-received material. The MX (VN) phase keeps almost a constant mean radius in all samples conditions and no differences were observed in size between the creep load and the thermal age specimens. The M_2X (Cr_2N) phase increased its mean radius, when comparing between the thermally aged specimens, with 2 exceptions, the specimen thermally aged at 600℃ after 4137 h and at the specimen thermally aged at 625℃ after 28983 h. This is related with the low number of studied particles, which were having a negative influence on the statistics. When comparing only the creep loaded specimens, the mean radius of M_2X (Cr_2N) phase and $M_{23}C_6$ phase clearly increased due to the effect of temperature and stress. The aging temperature seems not to have a strong influence on the mean radii of the studied phases, however the stress seems to accelerate the coarsening of $M_{23}C_6$, followed by the M_2X (Cr_2N) phase, and VN remained almost unaffected by the stress.

When evaluating the volume fraction measurements, the VN phase in the sample in as-received condition is roughly half of the maximum phase fraction represented at the aged condition at 575℃. This indicat es that this phase is still precipitating. Moreover, the volume fraction of VN decreases when aging/creep loading at 600℃ and 625℃ respectively. Parallelly , mod. Z-phase was identified at these sample conditions, which is the main reason for the dissolution of VN in these steels grades. Cr_2N precipitates act differently, this phase started with a very low volume fraction, and increased its fraction in every aged and creep loaded sample indicating the further precipitation of this phase after the heat treatment. However, during the longer time exposure decrease. When comparing the thermal aging and creep load specimens, the volume fraction of Cr_2N was higher for the specimens' thermal aged compared to the creep loaded at 600℃ as well as at 625℃ sample, t he stress has an influence in the dissolution of this phase. However, this phase seems to precipitate during service, showing longer stability than the VN phase. Cr_2N showed an increase of the phase fraction, which can be related with the availability of nitrogen, out of the dissolution of VN.

When comparing the number densities, $M_{23}C_6$ decreased its number density when comparing the different tested specimens related with its coarsening. Similar decrease of number density was found for the VN phase. This phase decreased its number density and volume fraction, although its mean diameter remain constant, which is related with the precipitation/transformation of this phase to mod. Z-phase. It has been found that at the lower creep testing temperature (575℃), lower amount of mod. Z-phase were found, showing at this condition a insignificant decrease of the phase fraction. Nevertheless, at the specimens tested at higher temperatures where high number of mod. Z-phase particles were identified; the phase fraction and number density of VN strongly decrease. The Cr_2N phase showed a different behaviour, this phase increased its volume fraction and its number density remained constant. This can indicate that some chromium and nitrogen could be available during the dissolution/transformation of the VN phase. According to the experimental results, the precipitates quantifications showed that VN and Cr_2N were not fully precipitating after the heat treatment. When comparing the results from the as-received specimen and the specimens thermally aged or creep loaded, it turns out that there is an increase of the volume fraction of these two phases. After long term service, it was observed VN volume fraction decreases again, contrary to the behaviour of Cr_2N. Therefore, it is concluded, that Cr_2N is more stable compared to VN.

Electron backscattered diffraction measurements were used for the analysis of the prior austenite grain size, martensite lath width and subgrain size. At 600℃, creep strength and temperature is high enough to allow coarsening of martensite lath width and of subgrains. For the material tested at 625℃, also

smoothly coarsening of martensite lath was observed. However, a smaller subgrain size because the particle size of Laves phase was exceeding the measurement limit of the EBSD method, and therefore, interfering with the measurement of subgrains. Therefore, the expected increase in the subgrain size could not be observed.

For all creep loaded and thermally aged specimens two additional phases were identified that were not present in the as-received state, Laves phase and mod. Z-phase. The first, as intermetallic phase rich in Mo and W, reduce the strengthening of the martrix, because Mo and W improve the creep strength of these materials by solid solution hardening. However, due to its size and distribution in X12CrCoWVNb 11-2-2 steel, it is assumed that this phase is improving the creep resistance of the material hindering the movement of the dislocations (precipitation hardening). However, different is the effect of the mod. Z-phase precipitation. At the specimen tested at 575°C lower amount of this phase have been found, as well as no change in the chemical composition of VN phase. Moreover, in the specimens tested at 600℃ and 625℃, higher amounts of mod. Z-phase were identified, and changes in the number density and volume fraction of VN phase were observed, mod. Z-phase was consuming the VN phase or VN phase was transforming to mod. Z-phase.

Special attention was paid in the possible transformation of the Cr_2N phase to mod. Z-phase. However, no evidence has been found. This phase as well as the VN phase was not fully precipitate in the as-received condition and furthermore the volume fraction of Cr_2N phase increase in the specimen tested at 600℃ and 625℃.

Interaction between MX, M_2X and mod. Z- phase

The results demonstrated that neither MX (VN) nor M_2X (Cr_2N) was fully precipitated in the as-received sample. Volume fraction of VN phase was roughly half of the maximum phase fraction (see samples aged at 575℃), whereas the volume fraction of Cr_2N was very low. Compared to this sample, the volume fraction of VN decreases when tempering/creep loading at 600℃ and 625℃ respectively. Parallelly, mod. Z-phase formed, which is the reason for the dissolution of VN. Cr_2N precipitate act differently: it started with a very low volume fraction, and increased its fraction in every tempered and creep loaded sample. This increase has two reasons: (i) nitrogen is still available in the matrix and precipitates as M_2X (Cr_2N) and MX (VN) (sample TA575H1P, TA600H1P). (ii) N is taken from dissolving VN precipitates. This second case makes sense in the interpretation of the measured values for sample TA600H1P, CL600H1P and TA625H1P.

The mod. Z-phase formation consumes the VN carbonitrides as has been reported in several publications (some example [18] [21]). In X12CrCoWVNb 11-2-2 steel, the formation of the mod. Z-phase fits to the decrease in the phase fraction of VN, too. But in X12CrCoWVNb 11-2-2 steel, the situation is more complicated due to the M_2X (Cr_2N) precipitation. A model for the interaction of VN, Cr_2N and mod. Z-phase, is presented in Figure 9.1.

The phases VN, Cr_2N and mod Z-phase are extremely dependent of the N, Nb, V and Cr content in the steel. For steels with higher chromium content, Cr_2N phase seems to be preferably than VN at the investigated service temperatures (575℃, 600℃ and 625℃). Cr_2N will also dissolve, and the nitrogen available will be used for the formation of mod. Z-phase. However, two points are important in this context: First, Cr_2N does not directly transform into mod. Z-phase. Second, the dissolution of Cr_2N takes longer compared to VN.

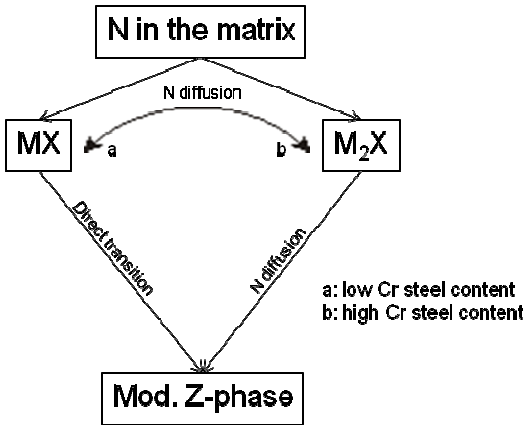

Figure 9.1. Distribution of nitrogen in the 9-12 %Cr steels. This helps to interpret the interaction of the nitrides phases during creep test.

Boron effect

The BN precipitates were only found at the first status of our material, as-received condition. After that in no other sample were BN particles found. Boron element has been reported to decrease the coarsening rate of the $M_{23}C_6$ [12][16][17]. However, to gain this objective boron has to remain in solution in the matrix. Neither in $M_{23}C_6$ or in any other precipitate phase, any boron could be characterized.

MatCalc simulations

All the experimental results have been implemented in MatCalc software in order to improve the existing databases on one side, but also to have a tool to predict the behaviour of the precipitates phases during aging. The calculations covered equilibrium states (phase fractions and chemical composition of the phases, depending on the temperature) and kinetic simulations, considering austenitization, tempering and thermal ageing. Following this aim, different databases have been used in the outgoing of this project: TCFE3 modified for chromium steels, Fe-data6 modified for chromium steels and mc_steel database.

As a first step, MatCalc calculations were carried out on the X12CrCoWVNb 11-2-2 Heat 1, Heat 2 and Heat 3. For the first simulations, a modified TCFE3 database for chromium steels was used. The first calculations performed with this database predicted as stable phases during the kinetic simulations VN, Cr_2N, $M_{23}C_6$ and Laves phase. The software predicted no precipitation of mod. Z-phase. Although the kinetic simulations were very optimistic the experimental investigations showed the precipitation of the mod. Z-phase at 600℃ and because of that, adjustme nts in the database were carried out.

The following calculations were performed with two different databases: TCFE3 and Fe-data6 modified for chromium steels but with implementations of the thermodynamics of mod. Z-phase done by Danielsen [18]. The equilibrium calculations were predicting for both databases, $M_{23}C_6$, VN, NbC, Laves phase but no Cr_2N. As soon as the mod. Z-phase was considered into the calculations, the VN were dissolved. When analysing the kinetic simulations, for any of both databases Cr_2N was not forming. Out of the results of these simulations the TCFE3 modified for chromium steels, with implementations of the thermodynamics of mod. Z-phase, was used for the further simulations and the Gibbs energy of the M_2X was modified, simulating this phase more stable (according to the experimental results). The changes of the thermodynamic data of M_2X (Cr_2N) were making this phase more stable than the mod. Z-phase and in the equilibrium calculations mod. Z-phase was predicted to be stable phase at temperature lower than 575℃ . Moreover, in the kinetic calculation mod. Z-phase was forming, but the phase fraction of the Cr_2N was predicted to be constant by the entire calculation. This fact was not representing the experimental results. Furthermore, Laves phase was predicted to have a mean radius at the end of the calculation of 200 nm,

not representing the experimental findings either. To adjust the prediction of the calculations with the experimental results the Gibbs energy of the Cr_2N phase as well as the nucleation constant and the equivalent interfacial energy for the mod. Z-phase, When performing these changes, it was determined that the phase fractions experimentally calculated were lower than the predicted by MatCalc.

According with the obtained results from the previous calculations with TCFE3 modified for chromium steels with implementations of the thermodynamics of mod. Z-phase and the experimental results, the newest MatCalc database mc_steel was used for the last simulations. Moreover, a new heat treatment was considered in the kinetic simulations: lower cooling and heating rates, which were more reliable to the real production process of the steel. The equilibrium simulations predicted $M_{23}C_6$ as the predominant precipitate phase together with Laves phase. VN was stable at temperatures below 1200℃ as well as NbC, and M_2X (Cr_2N) was stable at temperatures below 900℃. However, when mod. Z-phase was considered in the equilibrium simulations; M_2X (Cr_2N) and VN phases were replaced. Mod. Z-phase became the stable nitride phase. The kinetic simulations showed $M_{23}C_6$ as fully precipitated phase after the heat treatment, which remained constant in the entire calculation together with Laves phase. NbC phase precipitated in the austenitic regime and kept its phase fraction constant in the entire simulation. VN phase was also fully precipitate after the heat treatment, although this phase decreases its phase fraction, to totally dissolution, when mod. Z-phase precipitated. Similar behaviour was found for the Cr_2N phase. This phase precipitated during the heat treatment, with a relative low phase fraction but during the simulation kept its phase fraction almost constant until VN phase starts to dissolve, due to the precipitation of mod. Z-phase. At this point of time Cr_2N phase, increased its phase fraction, to dissolve afterwards.

Comparison of the experimental results with the simulations

When comparing the experimental results with MatCalc simulations, the performed changes on the thermodynamics of the Cr_2N and adjustments in the interfacial energy of the mod. Z-phase improved the prediction capability of the calculations to more accurate values. The predicted mean radii as well as the number densities were observed now in good agreement with the experimental results. However, the phase fraction experimentally observed in the as-received condition was much lower than one predicted by MatCalc.

X12CrCoWVNb 11-2-2 alloy concept is based on precipitation strengthening by carbides (mainly $M_{23}C_6$ and NbC), Laves phase and also nitrides (Cr_2N, VN). However, the transformation of the finely distributed VN precipitates to the low distributed and large mod. Z-phase will decrease the creep strength of the material at high temperatures. A new tested alloy, X12CrCoW[V]Nb 11-2-2 vanadium free was simulated with the updated mc_steel database, to determine if this new alloy could show better properties as the original steel.

Thermodynamic and kinetic simulations were performed and the results reveal high stability for M_2X phase and $M_{23}C_6$ together with Laves phase and NbC. Because the steel is vanadium free, the simulations were not predicting mod. Z-phase precipitation.

Out of the positive results from the simulations a experimental Heat was create with the same chemical composition and heat treatment as X12CrCoWVNb 11-2-2, but vanadium free. The experimental investigations on the X12CrCoW[V]Nb 11-2-2 vanadium free reveal a strong coarsening of the $M_{23}C_6$ and Cr_2N. The volume fraction of these two phase dramatically decrease after only 3403 h of creep test at 650℃ and 60 MPa. Laves phase precipitates were alr eady identified in as received condition and no NbC was found after creep test.

The experimental investigations showed strong discrepancies with MatCalc simulations, indicating that further implementations, on the Cr_2N and mod. Z-phase thermodynamic, have still to be performed.

10. Conclusions

In this PhD thesis, a very extensive quantitative microstructure characterization of the X12CrCoWVNb 11-2-2 steel has been performed using the most advanced microscopy techniques. Optical microscopy investigations were used to characterize the matrix and quantify possible retained δ-ferrite. TEM investigations, using EFTEM, EELS, ELNES, EDX, SAD and CBED for the identification of each type of precipitates presented in this thesis were performed. SEM-EBSD investigation has been used for the characterization of the subgrain size and martensite lath width.

It has been found that EELS and ELNES techniques are the most convenient way for the characterization of the different nitride precipitates without the need to performed diffraction measurement.

Chemical quantification of the precipitates by EDX has been performed and it has been found that during thermal aging and creep loaded, $M_{23}C_6$ increase its chromium content whereas in Cr_2N phase decreases it.

The main goal for increase the long time creep behaviour of these types of steels is to design a material, which remains with a stable microstructure at higher service conditions. By using EFTEM investigations mean radius, number density and volume fraction of $M_{23}C_6$, Cr_2N and VN has been quantified. $M_{23}C_6$ and Cr_2N increase their mean radius at all the investigated specimens, whereas VN remains stable. $M_{23}C_6$ as well as VN decrease their number density at the thermal age and creep load samples compared with the material in as-received condition. However, the reason for this decrease is different for each phase. $M_{23}C_6$ decreases its number density due to the increase of its mean radius; this phase coarsens during the creep tests.

Microstructure instabilities, precipitates dissolution, coarsening, recovery and recrystallization of the matrix, have been defined as the main reasons of the decrease in creep strength of 9-12 %Cr tempered martensitic steels. The dissolution of VN is causing a drop in the internal back-stress and leading to the deterioration of creep strength, which has been found one of the main reason for the drop in creep strength in the 12 %Cr tempered martensitic steels. VN phase, due to its similar chemical composition as its similar crystallographic structure, transforms to mod. Z-phase.

Out of the experimental results a model for the interaction of VN, Cr_2N and mod. Z-phase was presented, where the transformation of VN to mod. Z-phase plus the dissolution of the Cr_2N is defined.

MatCalc software package has been used for the prediction of new chemical compositions and heat treatments. The experimental results obtained have been compared with the results obtained by MatCalc software. The obtained results showed discrepancies on the predictions of VN, mod. Z-phase and Cr_2N between simulations and experimental investigations. Because of that, adjustments in the used databases have been performed. The Gibbs energy of Cr_2N has been adjusted as well as the interfacial energy parameters for mod. Z-phase. Out of these modifications a more reliable database was obtained, showing good agreement between experimental and simulation.

Based on the good agreement between experimental and simulations a new X12CrCoW[V]Nb 11-2-2 alloy vanadium free was simulated. The main goal of this steel grade is to avoid the precipitation of mod. Z-phase by the decrease of the vanadium content. The thermodynamic and kinetic simulations predicted a high stability for M_2X phase and $M_{23}C_6$ together with Laves phase and NbC. Because the steel is vanadium free, the simulations were not predicting mod. Z-phase precipitation. However, after the production of the experimental heat and the first TEM investigations the material showed strong discrepancies with MatCalc simulations, indicating that further studies, on the Cr_2N and mod. Z-phase thermodynamic have still to be studied.

11. Outlook

The X12CrCoWVNb 11-2-2 steel has been fully characterized using different microscopy techniques, and applying methods as a first time in this types of steels grades, like the ELNES fingerprint method for the characterization of the different nitrides without the need to perform diffraction measurements.

The obtained experimental results have been implemented in thermodynamic databases and a new chemical composition was simulated. Out of the positive predictions of the simulations a new experimental heat was developed. However, the experimental results show singular discrepancies with the calculations.

It has to be considered when working with thermodynamic models that it is of vital importance to have thermodynamic quantitative data, because modelling without experimental information will reveals unrealistic results. Microstructure instabilities as precipitates dissolution-transformations, coarsening, recovery and recrystallization of the matrix have been found the main reason for the drop in creep of these materials. Recrystallization processes, the effect of boron in the coarsening of $M_{23}C_6$ as well as in the prior austenite grain boundaries, together with dislocation density, are mechanisms that still have to be clarified and quantified in order to full the thermodynamics databases with reliable experimental measurements. Afterwards a tool, which will be able to predict precipitation kinetics in a realistic way, will be obtained.

12. Acronyms

General

IWS	*Institute for materials science and welding*
V&M	*Vallourec & Mannesmann Tubes*
SZMF	*Salzgitter Mannesmann Forschung*
FELMI	*Institute for electron microscopy*
EPRI	*Electric power research institute*
EPDC	*Electric power development center*
COST	*Community of science and technology of the European communities*
AGH	*Akademia Górniczo-Hutnicza*

Experimental Techniques

OM	*Optical Microscopy or Light Microscopy*
TEM	*Transmission Electron Microscopy*
STEM	*Scanning Transmission Electron Microscopy*
SEM	*Scanning Electron Microscopy*
EBSD	*Electron Backscatter Diffraction*
EDX or EDS	*Energy Dispersive X-ray Spectroscopy*
EFTEM	*Energy Filtering Transmission Electron Microscopy*
EELS	*Electron Energy Loss Spectroscopy*
ELNES	*Electron Energy-Loss Near Edge Structure*
EXELFS	*Extended Energy Loss Fine Structure*
CBED	*Convergent Beam Electron Diffraction*
SAD	*Selected Area Electron Diffraction*

13. References

[1] Beer J., *Fossil fuel power plant*, http://www.eoearth.org/article/Fossil_fuel_power_plant, (2008), (accessed June 2009).

[2] Kern T.U., Wieghardt K. and Kirchner H., Material and design solutions for advanced steam power plants, in int. conf. Advances in materials technology for fossil power plants, ASM International South Carolina, (2004), 20-34.

[3] Zachary J., *Options for reducing a coal-fired plant's carbon footprint Part II*, http://www.powermag.com/coal/, (accessed November 2009).

[4] Armor A. F. and Viswanathan R., *Supercritical fossil steam plants: Operational issues and design needs for advanced plants*, in int. conf. Advances in materials technology for fossil power plants, ASM International South Carolina, (2004), 138-151.

[5] Viswanathan R., Henry J. F., Tanzosh J., Stanko G., Shingledecker J. and Vitalis V., *U.S. Program on materials technology for USC power plants*, in 4th int. conf. Advances in materials technology for fossil power plants, ASM International South Carolina, (2004), 3-19.

[6] Masuyama F., *Alloy development and material issues with increasing steam temperature*, in int. conf. Advances in materials technology for fossil power plants, ASM International South Carolina, (2004), 35-50.

[7] Blum R., Vanstone R. W. and Messelier-Gouze C., *Materials development for boilers and steam turbines operating at 700℃*, in int. conf. Advances in materials technology for fossil power plants, ASM International South Carolina, (2004), 116-136.

[8] Staubli M., Bendick W., Orr J., Deshayes F. and Henry C., *European collaborative evaluation of advanced boiler materials*, in int. conf. Materials for advanced power engineering, Liege, (1998), 87-103.

[9] Mayr P., *Evolution of microsturcture and mechanical properties of the heat affected zone in B-containing 9 % chromium steels*, Doctoral Thesis, Graz University of Technology, (2007).

[10] Cerjak H., Holzer I., Mayr P., Pein C., Sonderegger 'B. and Kozeschnik E., *The relation between microstructure and creep properties of martensitic 9-12% Cr steels*, in int. conf. New developments on metallurgy and applications of high strength steels 2008, Buenos Aires, (2008), 247-265.

[11] Ruttmann W., *Untersuchungen and Schraubenblozen*, Mitteilungen der VGB, 65, (1937), 395-396.

[12] Abe F., Kern T.U. and Viswanathan R., *Creep-resistant steels*, chapters 1, 2, 6 and 9, (2008), ISBN 978-1-84569-178-3.

[13] Masuyama F., *Steam plant material developments in Japan*, in int. conf. Materials for advanced power engineering, Liege, (1998), 1807-1824.

[14] Badeshia H. K. D. H., *Martensitic Transformations: Crystallography and Nucleation*, (2001), ISBN 0-08-0431526, 5203-5206.

[15] Sonderegger B., *Charakterisierung der Substruktur in modernen 9-12% Cr Stählen mittels der EBSD Methode*, Doctoral Thesis, Graz University of Technology, (2005).

[16] Abe F., Horiuchi T., Taneike M., Sawada K., *Stabilization of martensitic microstructure in advanced 9Cr steel during creep at high temperature*, Materials and engineering A, 378, (2004) 299-303.

[17] Abe F., *Alloy Design of creep and oxidation resistant 9Cr steels for thick section boiler components operating at 650℃*, in int. conf. Advances in materials technology for fossil power plants, ASM International South Carolina, (2004), 202-216.

[18] Danielsen H., *Z-phase in 9-12 %Cr Steels*, Doctoral Thesis, Technical University of Denmark, (2007).

[19] Schäfer L., *Influence f delta ferrite and dendritic carbides on the impact and tensile properties of a martensitic chromium steel,* Journal of nuclear materials, 258-263, (1998), 1336-1339.

[20] Jenkins M., http://courses.washington.edu/mengr354/jenkins/notes/chap8.pdf (accessed june 2009)

[21] Danielsen H. K. and Hald J., *Behaviour of Z phase in 9–12%Cr steels*, Energy Materials, 1, (2006), 49–57.

[22] Sawada K, Taneike M, Kimura K and Abe F, *Effect of nitrogen content on microstructural aspects and Creep behavior in extremely low carbon 9Cr heat-resistant steel*, ISIJ International, 44, (2004), 1243–1249.

[23] Sklenicka V., Kucharova K., Svoboda M., Kloc L., Bursik J. and Kroupa A., *Long-term creep behavior of 9–12%Cr power plant steels*, Materials Characterization, 51, (2003), 35–48.

[24] Plumbridge W.J., *The analysis of creep data for solder alloys*, Soldering & Surface Mount Technology, 15/1, (2003), 26-30.

[25] Nembach E., *Particle strengthening of metals and alloys,* John Wiley & Sons, New York (1997).

[26] Mitterbauer C., *Fine-structure resolved electron energy-loss spectroscopy measurements of transition metal oxides in the transmission electron microscope*, Doctoral Thesis, Graz University of Technology, (2003).

[27] Williams D. B. and Carter C. B., *Transmission electron microscopy*, (2009), ISBN 978-0-387-76502-0.

[28] Albu M., Méndez Martín F., Kothleitner G., Sonderegger B., *Compositional characterisation and thermodynamic modelling of nitride precipitates in a 12 %Cr steel*, International Journal of Materials Research., 99, (2008), 422-427.

[29] Hofer F., Grogger W., Kothleitner G., Warbichler P., *Quantitative analysis of EFTEM elemental distribution images*, Ultramicroscopy, 67, (1997), 83-103.

[30] Grogger W., Krishnan K.M., Scatter diagram analysis of Cr segregation in Co-Cr based recording media, IEEE transactions on magnetic, 37, (2001), 1465-1467.

[31] Goodhew P. J., Humphreys J., Beanland R., *Electron microscopy and analysis*, third edition (2001) IBSN 0-74840968-8.

[32] Schwartz A. J., Kumar M. and Adams B. L., *Electron backscatter diffraction in materials science*, (2000), IBSN 0-306-46487-X.

[33] http://www.dstu.univ-montp2.fr/spip/spip.php?article104 (accessed Mai 2010).

[34] Rajek H. J., *Computer simulation of precipitation kinetics in solid metals and application to the complex power plant steel CB8,* Doctoral Thesis, Graz University of Technology, (2005).

[35] Kozeschnik E. and Buchmayr B., *MatCalc a simulation tool for multicomponent thermodynamics, diffusion and phase transformations*, in int. conf. Mathematical modelling of weld phenomena 5, (2001), 349-361.

[36] Kozeschnik E., Svoboda S., Fratzl P. and Fischer F. D., *Modelling of kinetics in multicomponent multi-phase systems with spherical precipitates II. – Numerical solution and application*, Materials Science Engineering A, 385(1-2), (2004), 157-165.

[37] Svoboda J., Fischer F. D., Fratzl P. and Kozeschnik E., *Modelling of kinetics in multicomponent multi-phase systems with spherical precipitates I. – Theory*, Materials Science Engineering A, 385(1-2), (2004) 166-174.

[38] Kozeschnik E., Svoboda J. and Fischer F. D., *Modified evolution equations for the precipitation kinetics of complex phases in multi-component systems*, CALPHAD, 28(4), (2005), 379-382.

[39] Borgenstam A., Engstrom A., Hoglund L., and Agren J., *DICTRA, a tool for simulation of diffusional transformations in alloys*, Journal of Phase Equilibria, 21, (2000), 269-280.

[40] Andersson J. O., Helander T., Höglund L., Shi P. and Sundman B., *Thermo-Calc & DICTRA, computational tools for materials science,* CALPHAD, 26, (2002), 273-312.

[41] Andersson J.O., Höglund L., Jönsson B., and Agren J., *Computer simulations of multicomponent diffusional transformations in steel,* in int. conf. Fundamentals and applications of ternary diffusion, Sweden, (1990), 153-163.

[42] Kozeschnik E., Holzer I. and Sonderegger B., *On the potential for improving equilibrium thermodynamic databases with kinetic simulations,* Journal of Phase Equilibria and Diffusion, 28, (2007), 64-71.

[43] Janssens K.G.F., Raabe D., Kozeschnik E., Miodownik M.A. and Nestler B., *Computational materials engineering, first edition*, (2007), ISBN 13: 978-0-12-369468-3.

[44] Holzer I., Rajek J., Kozeschnik E. and Cerjak H., *Simulation of the precipitation kinetics during heat treatment and service of creep resistant martensitic 9-12% Cr steel*, in int. conf. Materials for advanced power engineering, Liege, (2006), 1191-1198.

[45] Vandenberghe B., Lefebvre B., Gabrel J. and Vaillant J.-C., *Development of a new 12 % Cr steel for tubes and pipes in power plants with steam temperatures up to 650℃,* La Revue de Métallurgie-CIT, (2005), 263-268.

[46] Gabrel J., Bendick W., Vandenberghe B. and Lefebvre B., *Status of development of the VM12 steel for tubular applications in advanced power plants*, in int. conf. Materials for advanced power engineering, Liege, (2006), 1065-1075.

[47] Zielinska-Lipiec A., Bendick W., Cempura G., Vandenberghe B., Ennis P. J. and Czyrska-Filemonowicz A., *Microstructural development of VM12 steel caused by creep deformation at 625℃,* in int. conf. Materials for advanced power engineering, Liege, (2006), 1077-1086.

[48] Bendick W., Gabrel J., Vaillant J.-C., Vandenberghe B., *Development of a new 12 %Cr steel for tubes and pipes in power plants with steam temperatures up to 650℃* , in 28th MPA-Seminar, Band 2 Vol 2, (2002), 50.1-50.15.

[49] Czyrska-Filemonowicz, A., Zielińska-Lipiec, A., Cempura, C.,*TEM microstructure characterization of annealed and creep deformed VM12 steel*, 2nd annual report, COST Action 536_Alloy Design Group (2005).

[50] Danielsen, H., *Investigation methods, Experimental results, Modelling efforts*, TUD Report, COST Action 536, Model alloys (2006).

[51] Katrakova D. and Mücklich F. *Specimen Preparation for Electron Backscatter Diffraction Part 1: Metals*, Praktische Metallographie, 38(10), (2001), 547-565.

[52] Pun T., Ellis J.R., Eden M., *Optimized acquisition parameters and statistical detection limit in quantitative EELS imaging*, Journal of Microscopy, 135, (1984), 295-316.

[53] Grogger W., *Quantitative Mikrobereichsanalyse im Analytischen Elektronenmikroskop unter Verwendung eines HPGe-Röntgendetektors*, Doctoral Thesis, Graz University of Technology, (1994).

[54] Hofer F., Warbichler P., Scott A., Brydson R., Galesic I. and Kolbesen B. *Electron energy loss near edge structure on the nitrogen K-edge in vanadium nitrides,* Journal of Microscopy, 204, (2001), 166-171.

[55] Cahn J.W., Nutting J., *Transmission quantitative metallography*, Transaction of the metallurgical society of AIME, 215, (1959), 526-528.

[56] Hättestrand M., Andren H.O., *Evaluation of particle size distributions of precipitates in a 9% chromium steel using energy filtered transmission electron microscopy*, Micron, 32, (2001), 789-797.

[57] Sonderegger B., *Modifications of stereological correction methods for precipitate parameters using transmission microscopy*, Ultramicroscopy, 106, (2006), 941-950.

[58] Sonderegger B., Mitsche S. and Cerjak H., *Microstructural analysis on a creep resistant martensitic 9-12% Cr steel using the EBSD method*, Materials Science and Engineering A, 481-482, (2008), 466-470.

[59] Sonderegger B., Mitsche S. and Cerjak H., *Martensite laths in creep resistant martensitic 9-12% Cr steels - Calculation and measurement of misorientations*, Materials Characterisation, 58 (2007), 874-882.

[60] Leapman R.D., Hunt J.A., *Comparison of detection limits for EELS and EDXS*, Microscopy, Microanalalyis, Microstructure, 2, (1991), 231-244.

APPENDIX 1

Mihaela Albu[a], Francisca Méndez Martín[b], Gerald Kothleitner[a], Bernhard Sonderegger[b]
[a]Institute for Electron Microscopy, Graz University of Technology, Graz, Austria
[b]Institute for Materials Science, Welding and Forming, Graz University of Technology, Graz, Austria

Compositional characterisation and thermodynamic modelling of nitride precipitates in a 12% Cr steel

Dedicated to Professor Dr. Horst Cerjak on the occasion of his elevation to Emeritus status

In 9–12% Cr steels, nitrides (MX, M_2X) and modified Z-phase ((Cr, V, Nb, Fe)N)) are of special interest because of their different contribution to the creep strength of the material. The changes in the chemical composition of complex nitrides and their crystallography were investigated using transmission electron microscopy. A method based on multiple linear least squares fit procedures was applied to extract the complete element content of the nitrides from the electron energy loss spectra. These results, augmented by X-ray spectroscopic data, were compared with the outcomes of the thermodynamic model implemented in the software package MatCalc. The elemental concentrations of precipitates under study i.e. the M_2X, MX and modified Z-phase are in good agreement with simulations.

Keywords: Nitride precipitates; Chromium steels; EELS; Quantification; Thermodynamic modelling

1. Introduction

Microstructure and precipitation in 12% Cr martensitic steels for steam power plants are mainly determined by the chemical composition and heat treatment parameters. During the service life, the microstructure of these materials changes: grains coarsen and precipitates form, grow or dissolve. These changes in the microstructure decrease the creep properties and limit the possible increase in the operating steam temperature at the power plants [1].

The microstructure of the 12% Cr martensitic steels consists of a material with a tempered martensite matrix with a fine distribution of carbides and nitrides that provides the high creep strength. However, long-term creep properties decrease and several explanations have been proposed for this breakdown. Local recovery along prior austenite grain boundaries, loss of solid solution hardening or transition from ductile transgranular fracture to brittle intergranular fracture are some explanations for this decrease in creep properties. These microstructural effects are summarised by Lee et al. [2]. The MX ((V, Nb)N or NbC) particles are important strengtheners for these steels. VN precipitates as small and densely distributed particles and increases the strength of the material by hindering dislocation movements. Nevertheless, the modified (mod.) Z-phase (Cr(V, Nb, Fe)N) is likely to form as a stable phase after creep exposure of about 10000 h at 600 °C, and consumes the VN particles [3, 4]. M_2X ($(Cr, V)_2N$) precipitation results from tempering below 700 °C. The composition of this phase is also similar to the mod. Z-phase. Consequently, it can be assumed that M_2X is also interlinked with the precipitation of the mod. Z-phase. It is expected that the mod. Z-phase grows at the expense of finer V-rich phases, like VN and M_2X. Because of the larger precipitate diameters and thus lower number density, the mod. Z-phase hinders dislocation movements much less compared to VN and M_2X particles, thus its formation leads to a decrease of the creep properties [5, 6].

Due to the importance of these nitride phases, their identification in the material should be unambiguous. For this reason, composition measurements have been accompanied by thermodynamic modelling with the simulation tool MatCalc [7, 8]. MatCalc is a software tool which can calculate the evolution of precipitates and their equilibrium states. In order to get the equilibrium phase fraction and chemistry, the Gibbs energies for each phase have to be calculated while considering various compositions. As a result one can compute the phase fractions and specific compositions of each phase with the lowest possible Gibbs energy, which is equivalent to the system equilibrium. For this task, MatCalc involves CALPHAD type databases [9]. These databases compile the outcomes of numerous solution experiments and provide the Gibbs energies needed. When comparing experimental results with the prediction of the thermodynamic calculations, one can test the reliability of the experiments as well as the accuracy of the applied databases [10]. In this paper, equilibrium calculations have been carried out with varying system composition and temperature, in order to calculate the nitride compositions and their variations.

The different nitrides present have been identified using the energy filtered transmission electron microscopy (EFTEM) technique [11, 12] and their elemental composition has been established both with electron energy loss spectroscopy (EELS) and energy dispersive X-ray spectroscopy (EDX). Nevertheless the light elements are not easily quantifiable with EDX, for which reason EELS was involved. Furthermore, the energy-loss near edge structure (ELNES) of the nitrogen ionisation K edge has been used to identify the type of different nitride particles [13].

Table 1. Elemental contents of the investigated steel (wt.%) and heat treatment (air cooling (a.c.)).

Chemical Comp.:	C: 0.115	Cr: 11.50	V: 0.26	Nb: 0.050	N: 0.066	Mo: 0.29	W: 1.50
Heat Treatment:	1060 °C 30 min a.c. + 780 °C 2 h a.c.						

2. Experimental procedure

The investigation was performed on a 12 % Cr martensitic steel available in three different conditions: as-received (after tempering at 780 °C), thermally aged and creep loaded at 600 °C for 24639 h at 115 MPa. Table 1 summarises the chemical composition and the heat treatment of the steel.

For TEM analysis, the specimens were prepared by extracting the precipitates from the matrix into an amorphous carbon film. For removing the matrix, a gentle Villela etch solution (45 ml Glycerine, 30 ml HCl, 15 ml HNO_3) at room temperature was used, with varying etching times ranging from 12 to 48 h.

Analytical investigations were carried out on a Philips CM20/Scanning TEM (STEM) equipped with a Gatan imaging filter (GIF). The microscope was operated at 200 kV with an LaB_6 cathode. The spectra were recorded in image mode, to minimise sample contamination, with the slow scan CCD camera integrated in the GIF at a dispersion of 1 eV/channel and an energy resolution of about 1.5 eV. All images and spectra were processed with Gatan's Digital Micrograph, and were corrected for dark current and gain variations. A good compromise in terms of signal to noise ratio was found by using a 200 µm condenser aperture (beam convergence angle $\alpha = 6.4$ mrad) and a 40 µm objective aperture (acceptance half angle $\beta = 7.6$ mrad). To reduce the effect of plural scattering, the spectra were acquired only from very thin particles, which were then analysed with the log-ratio technique [14]. The thicknesses were in the range 0.2–0.5 times the inelastic mean free path. For core-loss analysis the elemental edges of Nb-M45, C-K, N-K, V-L23, O-K, Cr-L23 and Fe-L23 were used. The EDX spectra were recorded in STEM mode, with a probe diameter of about 7 nm, using a Noran HPGe detector with an ultra thin window.

Equilibrium calculations were carried out with the MatCalc software package. The simulations include calculations with fixed chemical composition and varying temperatures, and simulations at a specific temperature while varying the Cr-, Nb- V- and N-content of the system. The thermodynamic parameters for the calculation are taken from a modified version of the TCFE3 database [9]. The modifications include the implementation of the mod. Z-phase with data coming from Danielsen and Hald [15], and a modification concerning the Si-content of Laves phase, investigated by Kroupa [16, 17]. Apart from the chemical composition and the thermodynamic database, no other input parameters were used in the simulation.

The chemical composition of MX, M_2X and mod. Z-phase for fixed system composition at 600 °C and 780 °C were simulated, as well as changes in the precipitate composition when varying the steel composition from 9 to 12 wt.% Cr, from 0.025 to 0.1 wt.% N, 0.02 to 0.4 wt.% Nb and 0.15 to 0.3 wt.% V, while keeping all the other element concentrations constant. Because of the aim of this paper (identification of the nitrides), the influence of the carbon content of the steel was not studied.

At 600 °C, the chemical compositions of VN and M_2X precipitates were simulated by suppressing the mod. Z-phase. With this technique, the (metastable) VN and M_2X get stable nitrides, and their compositions can be investigated. NbC is not stable at the temperatures under consideration even when suppressing the mod. Z-phase, so it was therefore not included in the following discussions.

3. Results and discussion

3.1. Elemental quantifications

Analysis was carried out on a total of 60 thin particles from the three differently treated samples. RGB (red-green-blue) energy filtered TEM pictures from one position in each sample are shown in Fig. 1a–c (only relevant precipitates shown). $M_{23}C_6$, BN, MX ((V, Nb)N or NbC) and M_2X ($(Cr, V)_2N$) particles were identified in the as-received sample. In addition, in the thermally aged and creep loaded samples mod. Z-phases and Laves phases also appear. Ac-

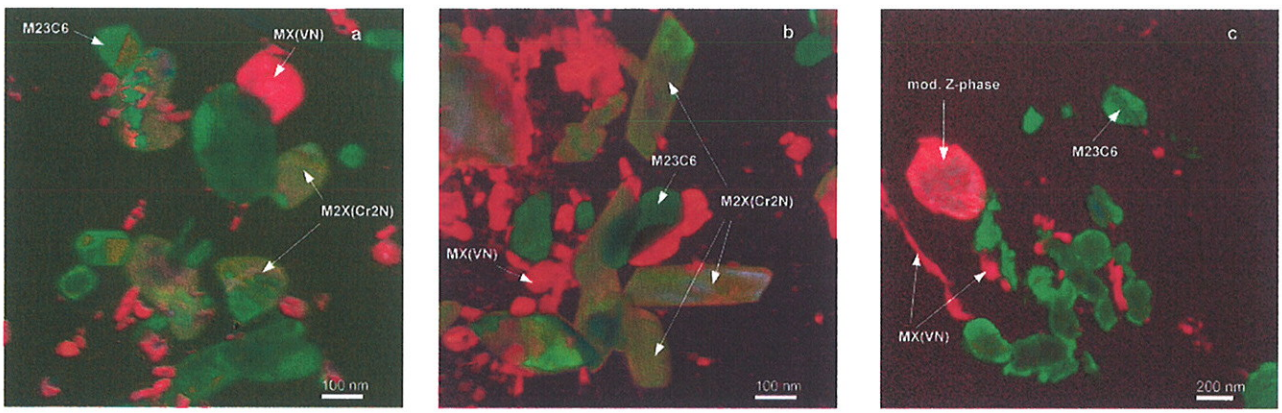

Fig. 1. (a) RGB map from the as-received specimen, (b) thermally aged specimen, and (c) the creep loaded specimen. The colours correspond to the signals extracted from the Cr-L23 (green), N-K (blue) and V-L23 (red) edges respectively.

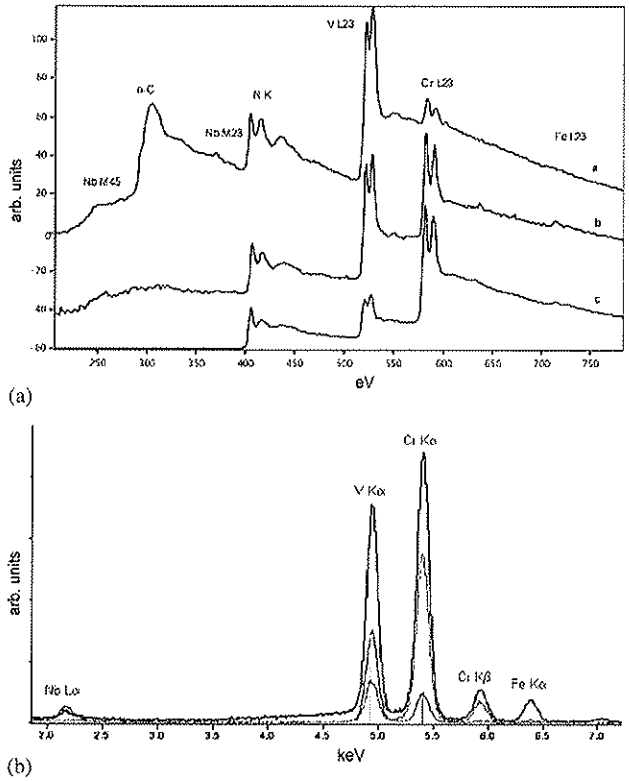

Fig. 2. (a) Background subtracted EEL spectra from a-VN, b-Cr_2N, and c-mod. Z-phase. The ELNES for N-K edge was used as a fingerprint for particle identification. (b) EDX spectra for mod. Z-phase (black), M_2X (light grey) and MX (dark grey).

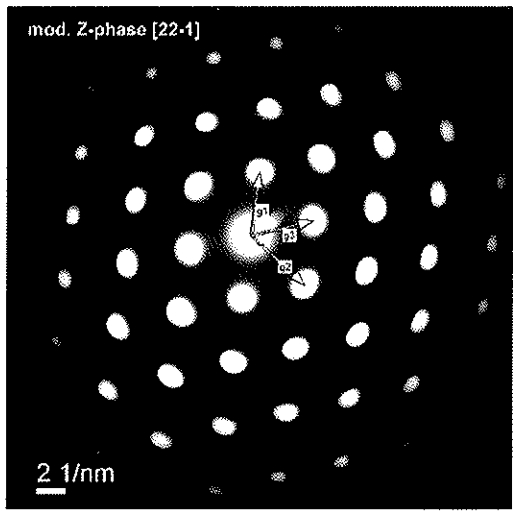

Fig. 3. Selected Area Electron Diffraction from the Z-phase particle in the creep loaded sample.

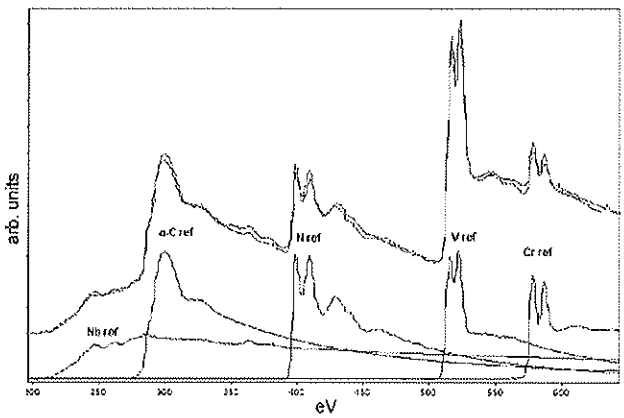

Fig. 4. MLS fit using Nb, amorphous C, N, V and Cr references for an MX (VN) particle. Black – the experimental spectrum and grey – the MLS fit.

cording to theory, VN precipitates in the thermally aged and creep loaded sample should disappear when mod. Z-phase is present, however, many VN precipitates were still identified.

In Fig. 2a and b three representative background subtracted EELS and the respective EDX from VN, M_2X ($(CrV)_2N$) and mod. Z phase are shown. In the VN EEL spectra, edges coming from Nb(M45, M23), N(K), V(L23), Cr(L23) and Fe(L23) can be recognised in addition to amorphous carbon from the extraction film. In the M_2X the niobium content is too low to be detected, instead, the iron content is marginally higher. From other work [18] it is known that the ELNES of the nitrogen K edge in certain nitrides can differ according to the crystallographic structure. While VN is face centred cubic, Cr_2N is hexagonally close packed and the mod. Z-phase features a tetragonally distorted bcc lattice with double layers of identical atoms alternating along the c axis to give a stacking sequence of the type AABBAABB [19]. In the case of VN and Cr_2N the differences in the N-K ELNES are obvious (doublet vs. single peak at edge onset) [20]. The mod. Z phase shows a fine structure resembling that of a VN particle, explicable and consistent with the electron diffraction pattern from Fig. 3. However, the edges from Nb, N, V and Cr are energetically too closely spaced and a conventional edge intensity extraction, based on a power-law background subtraction is not possible. To overcome this problem the multiple linear least squares (MLS) fit deconvolution has been employed [21], fitting suitable references to all overlapping edges. These references ideally should have identical fine structure and should be ac-

Table 2. Experimental partial cross-section for C-K, V-L_{23}, Cr-L_{23} and Fe-L_{23} (200 kV, $\beta = 7.1$ mrad, $\Delta = 100$ eV). Hartree–Slater calculated cross-sections for N-K and O-K. EDX experimental k-factors determined relative to Si [21].

Element	eV	σ (10^{-25} m^2)
Nb M45	205	17.82 ± 1.73
C K	282	4.05 ± 0.16
N K	401	2.14 ± 0.21
V L23	513	3.86 ± 0.62
O K	532	1.20 ± 0.12
Cr L23	575	3.30 ± 0.08
Fe L23	708	1.80 ± 0.03
Element	**keV**	**k factor relative to Si**
Nb L	2.17	1.43
V K	4.95	1.14
Cr K	5.41	1.17
Fe K	6.40	1.23

quired from positions of equal thicknesses. Such an MLS fit together with the references used is shown as an example for an VN particle in Fig. 4. Computing the relative fit weights and integrating the references over an energy range of 100 eV, allows calculation of the atomic percentages of each element quite accurately, provided experimentally determined cross-sections [22, 23] are available (see Table 2). The EELS cross-section values derived from stoichiometric oxides or carbides are summarised in Table 2. In terms of signal extraction, EDX was less sophisticated, using standard background modelling and peak area integration. However, for conversion into concentrations, experimental sensitivity factors, also shown in Table 2, measured relative to silicon were used to obtain higher accuracy [24]. The EDX values for each analysed particle have been scaled to the nitrogen content derived from EELS quantification. Table 3 contains the mean compositions of 60 particles analysed by EELS and EDX.

Elemental concentrations in the Cr_2N precipitates lie around 50 at.% for Cr, 15 to 20 at.% for V (no Nb present), 2 to 5 at.% for Fe and around 30 at.% for N, across all specimens with very little scatter.

On the other hand the various VN phases have contents of 40 to 50 at.% for V, 4 to 13 at.% for Nb, 10 to 15 at.% for Cr, 0.5 to 2.5 at.% for Fe and 30 to 50 at.% for N. The mod. Z-phase element contents vary for Cr from 40 to 20 at.%, for V + Nb from 20 to 40 at.% and for N from 26 to 39 at.%. Traces of iron are also present. The ELNES of the nitrogen K edge (see Fig. 2a) taken from the VN, Cr_2N and mod. Z-phase particles confirm this assessment. Moreover, the diffraction pattern from the mod. Z-phase in Fig. 3 ($g_1 = (\bar{1}10)$, $g_2 = (\bar{1}02)$, $g_3 = (102)$ verify it as well.

3.2. MatCalc calculations

The simulations with MatCalc were carried out in two stages: evaluations where the steel composition was kept fixed and evaluations where the temperature of the system was kept fixed.

Table 4 contains the chemical composition of MX, M_2X and mod. Z-phase for fixed system composition at 600 °C and 780 °C, which can be compared to the experimentally found values. Table 5 shows the variation of the precipitate composition when varying the steel composition, and Table 6 summarises the impact of varying system composition on the elemental contents of the precipitates.

The calculations yield that M_2X increases its vanadium and niobium contents from 16 to 28 at.% and from 0.5 to 8 at.%, respectively, when the niobium content of the steel is increased from 0.02 to 0.4 wt.%. When the nitrogen content in the steel is increased from 0.025 to 0.1 wt.%, the precipitate enriches in chromium, see Table 5. At an N-content of around 0.05 wt.%, the composition of M_2X gets close to mod. Z-phase. In this case, additional diffraction measurements should support EELS quantification to differentiate between the phases. The same conclusion can be drawn for very high (0.4 wt.%) Nb-contents. An increase in the system's V-content also enriches M_2X in vanadium at the cost of Cr, whereas a change in the steel's Cr-content leaves the M_2X composition nearly unaffected.

Table 3. Mean concentrations and their standard deviations from EELS and EDX measurements of 60 M_2X, MX and mod. Z-phase particles.

EELS	Cr (at.%)	V (at.%)	Nb (at.%)	Fe (at.%)	N (at.%)
M_2X	49.75 ± 3.4	17.18 ± 2.1	0	2.61 ± 1.7	30.42 ± 4.25
MX	11.56 ± 4	40.01 ± 4.5	6.89 ± 2.7	2.18 ± 1.1	41.18 ± 4.8
mod. Z-phase	32.76 ± 9.5	31.27 ± 2.41	3.31 ± 1.57	3.52 ± 1.16	32.3 ± 3.42

EDX	Cr (at.%)	V (at.%)	Nb (at.%)	Fe (at.%)
M_2X	52.48 ± 3.7	15.44 ± 2.5	0.36	1.49 ± 1.7
MX	10.27 ± 2.8	43.01 ± 4.6	4.52 ± 1.9	1.09 ± 0.3
mod. Z-phase	34.6 ± 2.4	29.79 ± 1.99	1.44 ± 0.13	2.62 ± 0.2

Table 4. Simulated compositions of M_2X, MX and mod. Z-phase at two different temperatures 600 °C and 780 °C.

600 °C						
at.%	Cr	N	V	Nb	Fe	C
M_2X	50.69	32.87	14.75	1.04	0.09	0.04
MX	0.05	46.61	47.39	5.40	0.02	0.52
Mod. Z-phase	31.31	30.70	31.20	3.45	3.30	0.00
780 °C						
at.%	Cr	N	V	Nb	Fe	C
M_2X	53.90	32.50	11.00	0.88	0.80	0.25
MX	0.27	46.60	45.60	5.60	0.08	1.50
Mod. Z-phase	31.05	31.40	30.50	3.70	3.22	0.00

According to Table 4, the MX-phase (V, Nb) (N, C) is close to a stoichiometric VN. A variation in the system's Cr-content does not affect the precipitate composition significantly. An increase in N or V moves the MX precipitates even closer towards an ideal VN. However, increase in the system's Nb-content also increases the Nb- and C-content of MX phase, leading to a mixed (V, Nb) (N, C) phase.

According to the simulation, the composition of the mod. Z-phase does not depend significantly on variations in the system composition. Moreover, in all simulations the iron content of the MX and M_2X is slightly lower than in the experimental findings.

The measured composition of the precipitates is in good agreement with the calculated values. This indicates that the tempering time for this steel was long enough to establish the equilibrium composition of the precipitates.

There was a small deviation in the precipitates' iron content between calculation and measurements. The simulations were predicting less iron, roughly 0–0.5 at.% of iron in the simulations and 1–2.5 at.% in the experiments (for M_2X and MX phases). This deviation is believed not to be an effect of residual matrix material surrounding the precipitate, as the matrix is removed very rapidly by the etching procedure. There is evidence that this small deviation can be overcome by adequate adjustments to the thermodynamic database.

Altogether, both calculations and measurements show that the three classes of nitrides can be differentiated clearly by their chemical composition in this steel. Identification of the precipitates via ELNES and quantitative EELS in this work was largely possible without involving any extra diffraction measurements.

The simulations with varying steel composition allow the extrapolation of this result to other 9–12 % Cr steels. The thermodynamic data reveal that with deviating chemical compositions of the system, the individual nitride classes can still be differentiated entirely by their chemical composition. With the exception of steels that have high Nb-content and/or N-contents of around 0.05 wt.%. In this case, the composition of the M_2X approaches the mod. Z-phase, and additional diffraction data are necessary for unambiguous identification.

Table 5. Calculated chemical composition for M_2X, MX and mod. Z-phase at 600 °C. Cr-, N-, Nb- and V-content of the steel were varied systematically. The table shows the upper and lower value of the outcomes.

600 °C	9 wt.% Cr						12 wt.% Cr					
at.%	Cr	N	V	Nb	Fe	C	Cr	N	V	Nb	Fe	C
M_2X	52.08	32.93	13.23	0.88	0.13	0.05	50.17	32.86	15.26	1.09	0.09	0.04
MX	0.05	46.78	47.22	5.25	0.02	0.65	0.05	46.55	47.42	5.44	0.02	0.51
Mod. Z-phase	31.11	30.82	31.12	3.46	3.47	0.00	31.35	30.67	31.21	3.44	3.31	0.00
	0.025 wt.% N						0.1 wt.% N					
M_2X	19.69	31.92	41.61	5.28	0.04	1.37	51.09	32.88	14.20	1.15	0.10	0.04
MX	0.03	39.84	45.57	8.82	0.01	5.72	0.05	46.68	46.51	6.17	0.01	0.55
Mod. Z-phase	31.99	28.51	30.40	5.33	3.74	0.00	30.95	31.58	30.80	3.39	3.25	0.00
	0.02 wt.% Nb						0.4 wt.% Nb					
M_2X	50.41	32.84	15.64	0.47	0.09	0.04	30.01	32.67	28.34	8.17	0.05	0.60
MX	0.04	46.49	50.64	2.37	0.05	0.41	0.18	31.83	24.80	27.87	0.00	15.31
Mod. Z-phase	31.32	31.25	32.95	1.42	3.05	0.00	31.08	30.05	26.62	8.35	3.89	0.00
	0.15 wt.% V						0.3 wt.% V					
M_2X	51.57	32.92	12.93	1.91	0.10	0.04	41.77	32.94	23.17	1.64	0.07	0.10
MX	0.08	46.80	41.68	10.68	0.006	0.75	0.03	45.57	48.47	4.95	0.03	0.94
Mod. Z-phase	30.64	31.75	28.54	5.57	3.48	0.00	31.69	29.79	31.86	3.24	3.40	0.00

Table 6. Influence of the steel composition on the precipitates' elemental content.

		changes of the element at.% in MX					changes of the element at.% in M_2X				
		Cr	N	V	Nb	C	Cr	N	V	Nb	C
increasing wt.% of element in steel	Cr	×	×	×	×	×	×	×	×	×	×
	N	×	+	×	–	–	+	×	–	–	–
	Nb	×	–	–	+	+	–	×	+	+	×
	V	×	×	+	–	×	–	×	+	×	×

× = no change; + = increase; – = decrease

4. Conclusions

Quantitative EELS analysis, supported by EDX data, on three types of complex nitrides (M_2X, MX and mod. Z-phase) in a 12% Cr-steel delivered the full elemental composition, enabling clear identification of the phases. These data have been further confirmed by ELNES fingerprinting and electron diffraction.

MatCalc simulations offer a way to predict changes in the composition of the MX, M_2X and mod. Z-phase depending on temperature and steel composition. With the exception of steels that have high Nb-content and/or N-contents of around 0.05 wt.%, it was shown that ELNES and quantitative EELS measurements already give sufficient information to distinguish between the nitrides in many 9–12% Cr steel variants.

The authors wish to acknowledge Manuel Paller from the FELMI TU Graz laboratory group for the preparation of the specimens analysed in this paper.

References

[1] J. Hald, in: J. Lecomte-Beckers, M. Carton, F. Schubert, P.J. Ennis (Eds.), Materials for Advanced Power Engineering 2006, Liege, Proceedings part II (2006) 917.
[2] J.S. Lee, H.G. Armaki, K. Maruyama, T. Muraki, H. Asahi: Mater. Sci. Eng. A 428 (2006) 270.
[3] H.K. Danielsen, J. Hald: Energy Materials 1 (2006) 1748.
[4] K. Sawada, H. Kushima, K. Kimura: ISIJ International 46 (2006) 769.
[5] R. Agamennone, W. Blum, C. Gupta, J.K. Chakravartty: Acta Mater. 54 (2006) 3003.
[6] G. Götz, W. Blum: Mater. Sci. Eng. A 348 (2003) 201–207.
[7] J. Svoboda, F.D. Fischer, P. Fratzl, E. Kozeschnik: Mater. Sci. Eng. A 385 (2004) 166.
[8] J. Svoboda, F.D. Fischer, P. Fratzl, E. Kozeschnik: Mater. Sci. Eng. A 385 (2004) 157.
[9] ThermoCalc AB, Stockholm, Sweden.
[10] I. Holzer, J. Rajek, E. Kozeschnik, H. Cerjak, in: J. Lecomte-Beckers, M. Carton, F. Schubert, P.J. Ennis (Eds.), Materials for Advanced Power Engineering 2006, Liege, Proceedings part III (2006) 1191.
[11] I. Letofsky-Papst, P. Warbichler, F. Hofer, E. Letofsky, H. Cerjak: Z. Metallk. 95 (2004) 18–21.
[12] F. Hofer, P. Warbichler, B. Bucjmayr, S. Kleber: Journal of Microscopy 184 (1996) 163.
[13] F. Hofer, P. Warbichler, A. Scott, R. Brydson, I. Galesic, B. Kolbesen: Journal of Microscopy 204 (2001) 166.
[14] T. Pun, J.R. Ellis, M. Eden: Journal of Microscopy 135 (1984) 295.
[15] H. Danielsen, J. Hald: Internal Report Värmeforsk Service AB (2004).
[16] A. Kroupa, private communication.
[17] J. Rajek: PhD. Thesis (2005).
[18] M. MacKenzie, A.J. Craven, C.L. Collins: Scripta Mater. 54 (2006) 1.
[19] H.D. Jack, K.H. Jack: Iron Steel Inst., London (1972) 210.
[20] C. Mitterbauer, C. Hebert, G. Kothleitner, F. Hofer, P. Schattschneider, H.W. Zandbergen: Solid state communications 130 (2004) 209.
[21] R.D. Leapman, J.A. Hunt: Microsc. Microanal. Microstruct. 2 (1991) 231.
[22] F. Hofer, G. Kothleitner: Microsc. Microanal. Microstruct. 4 (1993) 539.
[23] F. Hofer: Microsc. Microanal. Microstruct. 2 (1991) 215.
[24] W. Grogger: PhD. Thesis (1994).

(Received October 10, 2007; accepted January 30, 2008)

Bibliography

DOI 10.3139/146.101644
Int. J. Mat. Res. (formerly Z. Metallkd.)
99 (2008) 4; page 422–427

ISSN 1862-5282

Correspondence address

Dipl.-Ing. Dr. techn. Mihaela Albu
Institute for Electron Microscopy
Graz University of Technology
Steyrergasse 17, A-8010 Graz
Tel.: +43 316 873 8348
Fax: +43 316 811 596
E-mail: mihaela.albu@felmi-zfe.at

APPENDIX 2

Appendix II: List of publications

Publications

Mendez Martin F., Gabriela Panait C., Bendick W., Albu M., Sonderegger B., Kothleitner G., Sommitsch C., Gourgues-Lorenzon A., Besson J., Fuchsmann A.: *Creep strength and microstructural evolution of 9-12% Cr heat resistant steels during creep exposure at 600℃ and 650℃* . – in: int. conf. Materials for advanced power engineering, Liege, (2010).

Albu, M.; Mayr, P.; Mendez Martin, F.; Kothleitner, G.: *The boron influence on the microstructure of a 9 %-Cr martensitic steel*. - in: High Temperature Defect Assessment, pp 1 – 8, International HIDA Conference (2010)

Mayr, P.; Mendez Martin, F.; Albu, M.; Cerjak, H.-H.: *Correlation of creep strength and microstructural evolution of a boron alloyed 9Cr3W3CoVNb steel in as-received and welded condition.* - in: Creep and Fracture in High Temperature Components - Design & Life Assessment Issues, pp 1029 – 1037, ECCC International Conference on Creep and Fracture in High Temperature Components: Design & Life Assessment Issues, (2009).

Mayr, P.; Mendez Martin, F.; Holzer, I.; Agüero, A.; González, V.; Baumgartner, S.; Cerjak, H.-H.: *Experience with 9Cr3W3CoVNbBN base material and crosswelds at 650℃ for implementation in USC power plants.* - in: Proc. of the 3rd Symposium on Heat Resistant Steels and Alloys for High Efficiency USC Power Plants 2009, In Press, (2009).

Mendez Martin, F.; Sonderegger, B.; Albu, M.: *Microstructure Evolution of 12% Cr Steel.* - in: Werkstofftagung, pp 83 – 85, 10 (2008).

Albu, M.; Mendez Martin, F.; Kothleitner, G.; Sonderegger, B.: *Compositional characterization and thermodynamic modeling of nitride precipitates in a 12 % Cr steel.* - in: International journal of materials research, pp 422 – 427, 4 (2008).

Mayr, P.; Holzer, I.; Mendez Martin, F.; Kozeschnik, E.; Cerjak, H.-H.: *Weldability study of boron containing 9% chromium steels.* - in: International Charles Parsons Turbine Conference - Power Generation in an Era of Climate Change 2007, pp 417 – 426, International Charles Parsons Turbine Conference, (2007).

Mendez Martin, F.; Albu, M.; Sonderegger, B.; Mitsche, S.: *Precipitation in 9-12% Cr steels.* Performance report 2005/2006, pp98, (2007).

Presentations

Mendez Martin, F.; Albu, M.; Sonderegger, B.: *Microstructure stability on 12%Cr steels for fossil power plants: Experimental research and simulations.* - in: Materials day 2009. (2009).

Mendez Martin, F.; Albu, M.; Sonderegger, B.; Sommitsch, C.: *Microstructure characterization and simulations of 12%Cr martensitic steel for fossil power plants.* - in: PhD Seminar, Prague (2009).

Mendez Martin, F.; Sonderegger, B.; Albu, M.; Kothleitner, G.: *Experimental investigations on nitrides stability in a 12CrWMoVNb steel.* - in: MS&T'08, Pittsburgh (2008).

Mendez Martin, F.: *Precipitation in 12% Cr steels.* – in: IWS internal seminar (2007).

Posters

Mendez Martin, F.; Albu, M.; Sonderegger, B., Mayr P., Sommitsch, C.: *Transmission electron microscopy investigations of a 12 wt.% martensitic Cr steel designed for high temperature service.* - in: International Microscopy Congress, Brazil (2010).

Mendez Martin, F.; Albu, M.; Sonderegger, B.; Sommitsch, C.: *Microstructure evaluation of 12% Cr steel using TEM technique.* - in: Microscopy Conference MC2009, pp 233 – 234, Multinational Congress on Microscopy, (2009).

Albu, M.; Mendez Martin, F.; Mayr, P.; Kothleitner, G.: *Comprehensive TEM studies on Cr -rich martensitic steels.* - in: Microscopy Conference MC2009, pp 215 – 216, Multinational Congress on Microscopy, (2009).

Albu, M.; Mendez Martin, F.; Kothleitner, G.: *EELS quantification of complex nitrides in a 12 % Cr steel.* - in: EMC2008, Aachen (2008).

IWS Books

Mendez Martin, F.; Sonderegger, B.: *Publikationen IWS 2004-2006.* (2008).

Sonderegger, B.; Mendez Martin, F.: *Publikationen IWS 2007-2008.* (2008).